Université de Montréal

La maladie d'Alzheimer :

de son origine aux perspectives thérapeutiques

par Anthony Flamier

Programme de biologie moléculaire, Faculté de Médecine, Université de Montréal

Thèse présentée à la Faculté de Médecine en vue de l'obtention du grade de doctorat en biologie moléculaire

Mai, 2018

Résumé

La maladie d'Alzheimer (MA) est une maladie neurodégénérative incurable affectant les principales fonctions cérébrales incluant la mémoire et la motricité. Bien que la forme familiale de la maladie (fMA) soit bien caractérisée, l'origine de la forme proéminente (sMA) reste à être élucidée. Le vieillissement est le facteur de risque le plus important pour le développement de la maladie. De plus, il a été montré que le niveau de la protéine BMI1 diminuait dans le cerveau avec l'âge. BMI1 est un membre du complexe répressif de polycomb 1 (PRC1) qui est responsable de l'ubiquitination de l'histone H2A ce qui conduit à la répression de certains gènes. Par ailleurs, les souris hétérozygotes pour *BMI1* développent, avec l'âge, une neurodégénérescence ressemblant à la MA. Ce travail montre la perte de BMI1 dans les cerveaux de patients Alzheimer ainsi que dans les neurones Alzheimer dérivés de cellules souches pluripotentes induites (iPS). Cette diminution n'est cependant pas observée chez les patients atteints de fMA ou d'autres démences. L'inactivation de BMI1 au moyen d'un shARN ou de la technologie CRISPR/Cas9 conduit à une tauopathie et une amyloïdopathie similaire à la MA. Au niveau moléculaire, la perte de BMI1 induit une dérepression de *MAPT* et une stabilisation de GSK3β et p53 conduisant à la neurodégénérescence. La restauration des niveaux physiologiques de BMI1 chez les patients atteints de la MA ouvre la voie vers de nouvelles thérapies.

Mots clés : Maladie d'Alzheimer ; BMI1 ; GSK3β ; p53 ; Tau ; Amyloïde.

Abstract

Alzheimer's disease (AD) is an incurable neurodegenerative disorder affecting major brain functions including memories and motility. Although the familial form of the disease (FAD) is well characterized, the origin of the prominent form (sporadic AD) remains to be elucidated. Aging is the strongest risk factor for developing the disease. Previous results from the lab and others showed that BMI1 is downregulated in the brain with age. BMI1 is a protein member of the polycomb repressive complex 1 (PRC1) which mediates ubiquitination of the histone H2A which leads to gene silencing. As of note, *BMI1* heterozygous mice develop, with age, a neurodegeneration resembling to AD pathology. This work shows BMI1 loss in AD brains and AD neurons derived from induced pluripotent stem cells. This reduction is however not observed in patients with FAD or other dementia. BMI1 knockdown using a shRNA or Knockout using CRISPR/Cas9 technology gave rise to a tauopathy and amyloidopathy similar to AD. Mechanistically, BMI1 loss induces a de-repression of *MAPT* and a stabilization of GSK3β and p53 leading to neurodegeneration. Restoration of BMI1 physiological levels in AD patients provides new therapeutic avenues.

Keywords: Alzheimer's disease; BMI1; GSK3β; p53; Tau; Amyloid.

TABLE DES MATIÈRES

Index des figures

Liste des acronymes et abréviations

AAV: Adeno-Associated Virus

ADAM : Disintegrin and metalloproteinase domain-containing protein

ADN: Acide DésoxyriboNucléique

AKT1: protéine kinase B

APOE: Apolipoprotéine E

APP: Amyloid Precurssor Protein

ARF: ADP-ribosylation factor 1

ARN: Acide RiboNucléique

ARNseq : Séquencage de l'ARN

Aβ40: Amyloïde béta 40

Aβ42: Amyloïde béta 42

BACE1 : beta-site APP cleaving enzyme 1

BACE2 : beta-site APP cleaving enzyme 2

BIN1: Bridging Integrator-1

BMI1: B lymphoma Mo-MLV insertion region 1 homolog

BMP4: Bone Morphogenic Protein 4

CDK4: cyclin-dependent kinase 4

CDK6: cyclin-dependent kinase 6

CDKN2A: cyclin-dependent kinase inhibitor 2A

CERAD: Consortium to Establish a Registry of Alzheimer Disease

COMMD3: COpper Metabolism gene MURR1 Domain 3

DFT: Démence Fronto-temporale

EGF: Epidermal Growth Factor

ELISA : Enzyme-Linked ImmunoSorbent Assay

ES: Embryonic Stem

ESC: Extra Sex Comb

EZH2 : enhancer of zeste 2

FACS: Fluorescent Activated Cell Sorting

FDA: Food and Drug Administration

FGF: Fibroblast Growth Factor

fMA: Maladie d'Alzheimer familiale

GSK3β: Glycogène Synthase Kinase-3

H2A: Histone 2 A

H2Aub: H2A ubiquitiné

H2B: Histone 2 B

H2O2: Peroxyde d'hydrogène

H3: Histone 3

H3K27me3: Histone 3 tri-méthylé à la Lysine 27

H3K9ac: Histone 3 acétylé à la Lysine 9

H3K9me3: Histone 3 tri-méthylé à la Lysine 9

H4: Histone 4

HDAC: histone déacétylasses

HEK293T: Human embryonic kidney cells 293 Transformed

HOX: Homeotic gene

iPS: induced Pluripotent Stem

LCR : Liquide Céphalo-Rachidien

lncRNA: long non-coding RNA

LRP1: low-density Lipoprotein Receptor-related Protein 1

MA: Maladie d'Alzheimer

MAP: Microtubule Associated Protein

MAP1: Microtubule Associated Protein 1

MAP2: Microtubule Associated Protein 2

MAPK: Mitogen-activated serine/threonine protein kinase

MAPT: Microtubule Associated Protein Tau

MDM2 : Mouse double minute 2

NF-κB: Nuclear Factor-κB

PcG: Polycomb

PI3K: Phosphatidylinositol 3-kinase

PICALM: Phosphatidylinositol Binding Clathrin Assembly Protein

PRC1: PcG Repressive Complex 1

PRC2: PcG Repressive Complex 2

PSEN1: Préséniline 1

PSEN2: Préséniline 2

PSP: progressive supranuclear palsy

REST: RE1-Silencing Transcription factor

ROS: Reactive Oxygen Species

sgARN: synthetic guide ARN

shARN : short hairpin ARN

SLA: Sclérose Latérale Amyotrophique

sMA: Maladie d'Alzheimer sporadique

SORL1: Sortilin Related Receptor 1

SUZ12: suppresseur de zeste 12

TGFβ: Transforming Growth Factor beta

TREM2: triggering receptor expressed on myeloid cells 2

UTR: Untranslated region

À mon père Jean-Pierre Flamier

Remerciements

Je souhaite avant tout remercier mon directeur de recherche Dr. Gilbert Bernier de m'avoir permis d'être dans les meilleures conditions pour réaliser mon doctorat et de m'avoir fait partager tout son savoir-faire. Je serai toujours reconnaissant pour le soutien qu'il m'a apporté ainsi que pour m'avoir tant enseigné.

Je suis très reconnaissant envers Roy Hanna et Andrea Barabino pour leur soutien moral et technique de tous les jours.

Je souhaite également remercier l'ensemble de mon jury de thèse Dr. Nicole Leclerc, Dr. Massimiliano Paganelli et Dr. Jean-Pierre Julien pour leur aide dans la réalisation de mon doctorat et leurs conseils avisés.

Enfin, je remercie tout particulièrement ma mère, ma sœur, ma compagne, mes amis et toute ma famille sans qui je n'aurais pu accomplir cette thèse.

CHAPITRE 1: INTRODUCTION

Le chapitre 1 vous présente une revue de la littérature sur le vieillissement du cerveau et les pathologies qui en sont associées tel que la maladie d'Alzheimer. Afin de mettre en contexte mon projet de doctorat, les sections 2 et 3 vous présentent notamment la technologie des cellules souches pluripotentes et la protéine BMI1 qui est au cœur de mon sujet de doctorat. Enfin, je décris mes hypothèses de travail et mes principaux objectifs.

SECTION 1: Le vieillissement du cerveau et les maladies associées

1.1.1 Le vieillissement du cerveau

1.1.1.1 Concept de vieillissement du cerveau

Le vieillissement physiologique du corps humain correspond à un ensemble de processus biologiques entrainant, avec le temps, des modifications irréversibles tant au niveau structurel qu'au niveau fonctionnel [1]. Appliqué au cerveau, le vieillissement physiologique se traduit par des changements neuro-anatomiques avec la diminution de la masse cérébrale, neurophysiologiques avec la perte et l'atrophie des neurones corticaux et neurochimiques avec la baisse des neurotransmetteurs tels que l'acétylcholine ou la dopamine [2, 3]. Ces changements physiologiques se ressentent sur le plan cognitif en fonction de l'âge mais est très variable selon les individus [3]. Il existe ainsi différents troubles cognitifs pouvant apparaître selon l'âge dépendamment des zones du cerveau affectées et de la vitesse de la progression. La frontière entre un vieillissement du cerveau normal et le diagnostic d'une pathologie neurologique est très difficile à établir. En effet, il faut différencier des troubles cognitifs associés à une démence par rapport au vieillissement normal du cerveau [1, 3]. En outre, l'âge est un facteur de risque connu dans bon nombre de maladies neurodégénératives telles que la maladie de Parkinson, la maladie d'Alzheimer ou la maladie de Lou Gehrig [3-8].

1.1.1.2 Les marqueurs du vieillissement du cerveau

1.1.1.2.1 Le locus Ink4A/Arf

Un des premiers biomarqueurs de l'âge à avoir été identifié fut celui de la dérepression du locus Ink4A/Arf situé sur le chromosome 9 [9, 10]. Le locus Ink4A/Arf comprend un gène, cyclin-dependent kinase inhibitor 2A (*CDKN2A*) codant pour les protéines p16(Ink4A) et p14(ARF) qui, comme son nom l'indique, inhibe les kinases cycline-dépendantes CDK4 et CDK6 [11]. Par le biais de cette inhibition, p16 a un impact significatif sur la prolifération. En inhibant l'entrée dans le cycle cellulaire, p16 a été tout d'abord identifié comme un suppresseur de tumeurs et est devenu le marqueur d'une senescence de la cellule [11]. C'est en 1997 que la dérepression progressive en fonction de l'âge du locus Ink4A/Arf a été rapportée [10]. Cette augmentation dépendante de l'âge a pu être observée aussi bien chez l'homme que chez la souris et dans la plupart des tissus incluant le cerveau. Bien que mal caractérisé, ce phénomène peut s'expliquer d'une part par une augmentation de l'expression de *ETS1* (un activateur transcriptionnel de *p16*) et d'autre part par la diminution de l'expression de *BMI1* (un répresseur transcriptionnel du locus Ink4A/Arf) en fonction de l'âge [12-15].

1.1.1.2.2 Le stress oxydatif

L'air que nous respirons est chargé en oxygène à 21% ce qui est par la suite métabolisé par les cellules pour former des radicaux libres. Les radicaux libres sont donc présents de façon physiologique dans la cellule et leur présence est essentielle à la lutte contre les agents infectieux mais leurs régulations à un impact directe sur la santé de l'organisme [16]. Autre que l'apport naturel de radicaux libres par la respiration, leurs niveaux sont grandement influencés par le mode de vie incluant l'alimentation, l'anxiété, le tabac et la pollution. Au-delà de cet apport, il existe des agents pro- et anti-oxydants chargés de limiter ou d'amplifier l'accumulation de

radicaux libres. Les radicaux libres les plus communs et les plus étudiés sont les espèces réactives d'oxygène (ROS). Comme leur nom l'indique, les ROS comprennent des radicaux d'oxygènes ou des agents capables de former des radicaux d'oxygènes tel que le peroxyde d'hydrogène (H_2O_2). Les radicaux libres tels que les ROS arrachent des électrons à des molécules stables ce qui a pour conséquence de propager en chaine le taux de radicaux libres dans la cellule [16-22]. Cette réaction d'oxydation peut être contrecarrée par des agents anti-oxydants mais lorsqu'il y a un débalancement des molécules pro- et anti-oxydantes, cela induit un stress pour la cellule appelé « stress oxydatif ». Le stress oxydatif peut conduire à des dommages irréversibles dans la cellule incluant des dommages à l'ADN, l'oxydation des lipides et protéines membranaires, la rupture des lysosomes et l'inhibition de récepteurs membranaires [23, 24]. Il a été rapporté très tôt un lien entre les radicaux libres et le vieillissement physiologique [25]. Il est proposé notamment que la rupture d'un équilibre entre pro- et anti-oxydants est un facteur clé du vieillissement. Quand le stress oxydatif est trop fort, le vieillissement peut se transformer en condition pathologique comme c'est le cas dans les maladies neurodégénératives [26, 27].

1.1.1.2.3 Les dommages à l'ADN

Comme mentionné précédemment, le stress oxydatif est une source importante de dommages à l'ADN. Cependant, les dommages à l'ADN peuvent aussi subvenir naturellement avec l'âge et entrainer une mort cellulaire ou la répression de l'expression de certains gènes [28]. Les dommages à l'ADN correspondent à l'ensemble des altérations induisant un défaut dans la structure de l'ADN. Si ces altérations ne sont pas réparées elles peuvent conduire à l'apparition de mutations, un blocage de la réplication ou l'entrée en apoptose. Le cerveau est

tout particulièrement impacté par l'accumulation de dommages à l'ADN car la plupart des cellules qui le compose ne se divisent plus. En effet, la division cellulaire favorise la réparation de l'ADN [28]. Il a été rapporté dans plusieurs études une accumulation progressive des dommages à l'ADN dans le cerveau en fonction de l'âge ce qui perturberait l'expression d'un répertoire de gènes impliqués dans la plasticité synaptique, la mémoire, l'apprentissage et la survie neuronale [28]. Dans la plupart des maladies neurodégénératives, il est rapporté une augmentation des niveaux de dommages à l'ADN en comparaison à un cerveau sain âgé et ce phénomène prend une place importante dans le processus pathologique [28-38].

1.1.2 La maladie d'Alzheimer (MA)

1.1.2.1 Les différentes formes de l'Alzheimer

La maladie d'Alzheimer (MA) est une maladie neurodégénérative associée à l'âge se caractérisant par une perte majeure de fonctions primaires du cerveau que sont la mémoire, la cognition et le contrôle de la motricité [39]. Cette maladie a été décrite pour la première fois par le psychiatre, neurologue et neuropathologiste Allemand Alois Alzheimer en 1901 après le suivi d'une patiente nommée Auguste Deter présentant des troubles de la mémoire, une démence exacerbée par des hallucinations ainsi qu'un déficit du langage à seulement 51 ans [40]. C'est à la mort d'Auguste Deter 5 ans plus tard qu'Alois Alzheimer sera à même de faire un examen anatomopathologique de son cerveau. Il note tout d'abord une atrophie sévère du cerveau en général avec un rétrécissement encore plus substantiel du cortex, une zone du cerveau riche un matière grise et responsable de la mémoire, l'élocution, la pensée et la conscience [39]. Par la suite, c'est au moyen de méthodes d'imprégnations argentiques sur des tranches de cerveau qu'Alois Alzheimer rapporte pour la première fois la présence de dépôts anormaux intra- et extra-cellulaires formant des fibrilles ou des plaques caractéristiques de ces patients [40]. Ce sont ces travaux qui poseront les bases diagnostics de cette démence alors appelée « maladie d'Alzheimer ».

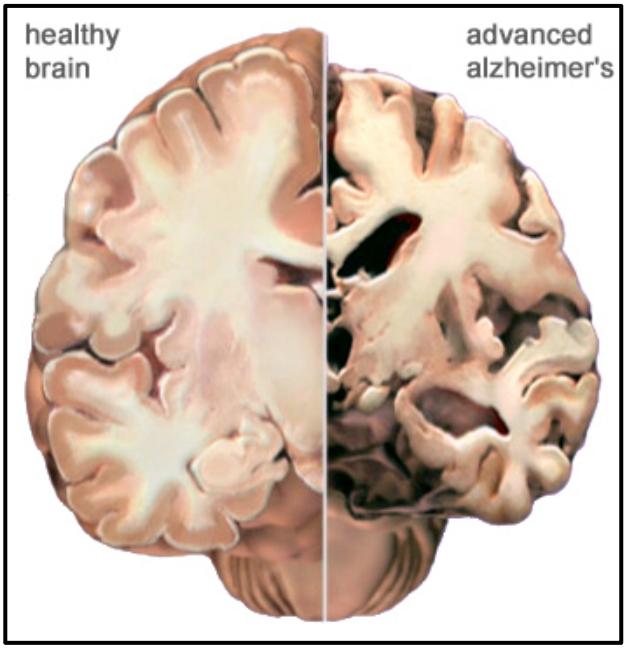

Figure 1 : Coupe transversale d'un cerveau sain âgé et d'un cerveau de patient Alzheimer.

On peut noter une atrophie cérébrale ainsi que la présence de cavités.

Adapté de la société américaine de l'Alzheimer.

Au fil des années, c'est principalement avec l'analyse anatomopathologique post-mortem de coupes de cerveaux issues de patients souffrant de démence que le diagnostic de la maladie a pris de l'ampleur. En effet, avec le vieillissement des populations, le nombre de cas rapportés chaque année est en constante augmentation [41, 42]. C'est avec le suivi de cohortes de patients et l'avènement des techniques de génie génétique que deux formes bien distinctes de la maladie ont pu être établies : la forme dite précoce et la forme dite tardive.

Comme dans le cas d'Auguste Deter, la forme précoce de la maladie présente l'ensemble des marqueurs de la pathologie mais se caractérise par le développement d'une sénilité vers l'âge de 40 ans et un décès avant 65 ans. Cette forme de la maladie étant bien souvent héréditaire, les généticiens se sont penchés sur la présence de mutations dans des gènes associés à l'Alzheimer et ont pu faire la dichotomie entre la forme familiale (fMA) et la forme sporadique (sMA). C'est en séquençant l'ADN génomique de familles impactées par la maladie que des chercheurs ont pu mettre en évidence des mutations autosomales dominantes dans le gène codant pour une protéine précurseur de l'amyloïde (*APP*) et les gènes codant pour les protéines préséniline 1 et 2 (*PSEN1* ; *PSEN2*) [43-45]. Le gène APP se trouve sur le chromosome 21 et code pour une protéine transmembranaire de 115 kDa pouvant être clivée à 3 endroits distincts par des α-sécrétases, β-sécrétases et γ-sécrétases. C'est selon le clivage de cette protéine que des peptides amyloïdes sont sécrétés et s'agrègent pour former des dépôts insolubles neurotoxiques. La voie de clivages par les α-sécrétases est considérée comme non-amyloïdogénique tandis que les coupures par les β-sécrétases et γ-sécrétases entraine la sécrétion de peptides amyloïdes béta de 40 (Aβ40) ou 42 (Aβ42) acides aminés. Dans de rares cas, des patients présentent plusieurs copies du gène APP, notamment dans le cas de trisomie

21, ce qui a pour conséquence un développement très précoce de la maladie. Les gènes PSEN1 et PSEN2 se trouvent quant à eux sur les chromosomes 14 et 1 respectivement et codent pour des γ-sécrétases responsables en partie de la libération de peptides Aβ hautement pathogéniques via leurs agrégations. Plus de 100 mutations distinctes sur les gènes PSEN1 et PSEN2 ont pu être identifiées et associées à la maladie d'Alzheimer [43]. Le lien direct entre une mutation dans ces gènes et le développement de la maladie n'est pas clair mais plusieurs hypothèses ont été formulées. La première hypothèse repose sur l'étude clinique de patients fMA ainsi que de modèles transgéniques murins. Dans les deux cas, les mutations dans *PSEN1* ou *PSEN2* furent associées à une augmentation des niveaux d'Aβ42 dans le sang incitant à penser que l'activité γ-sécrétases est perturbée et entraine un clivage accru de APP. Avec le développement des modèles de la pathologie et les contradictions qui s'en sont suivies, cette hypothèse a été mise à mal et a donné naissance à une seconde hypothèse selon laquelle les γ-sécrétases PSEN1 et PSEN2 régulent les ratios Aβ42/Aβ40. Ainsi, ces mutations entraineraient une perte de fonction enzymatique pour la production d'Aβ40 ce qui induit une augmentation du ratio Aβ42/Aβ40 [44, 46].

Enfin, dans de très rares cas, la forme précoce de la MA n'est pas familiale mais apparaît de façon sporadique. Il y a plusieurs hypothèses pour expliquer ces formes de la maladie. Tout d'abord, ces formes précoces non familiales peuvent s'expliquer, pour la plupart, par des erreurs de diagnostic. En effet, il est parfois difficile pour les cliniciens de diagnostiquer une MA précoce par rapport à d'autres démences telles que les démences vasculaires proches phénotypiquement de la MA. Par ailleurs, il n'est pas à exclure que ces cas soient en fait des cas familiaux pour lesquels il n'y a pas d'historique familial disponible et pas de mutations connues.

Afin de mettre en perspective la prévalence des formes précoces en comparaison aux formes tardives, des cliniciens et épidémiologistes ont suivi de larges cohortes de patients depuis plusieurs décennies. Il est admis que la forme précoce familiale représente 5 % de la totalité des cas de la MA et affecte ainsi environ 250.000 personnes aux États-Unis [44]. D'autres épidémiologistes préfèrent contraster ces chiffres et parlent même de 2-3 % de la totalité des cas de la MA (soit environ 100.000 cas aux États-Unis) mettant en cause des diagnostics erronés (Figure 2). Bien que cette forme de la MA soit minoritaire par rapport à l'ensemble des cas de MA, cela représente un grand nombre de personnes affectées, égalant les cas de maladie de Huntington, de Démence Fronto-Temporale (DFT) et de Sclérose Latérale Amyotrophique (SLA) combinés (Figure 2).

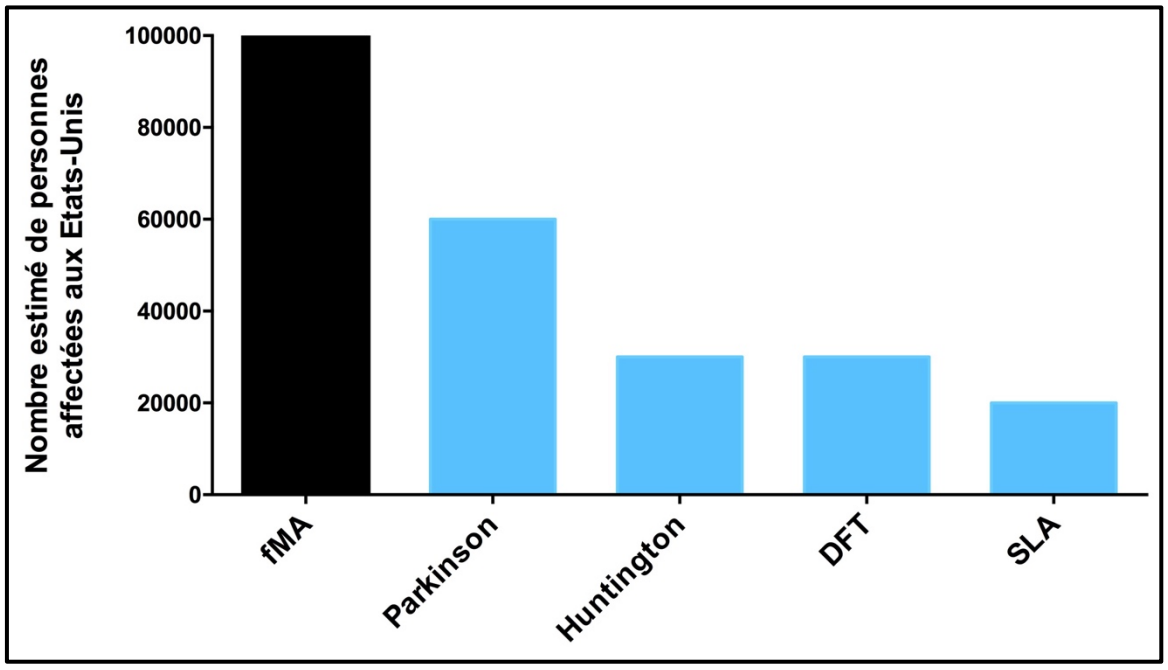

Figure 2: Nombre de cas estimé aux États-Unis pour 5 maladies neurodégénératives.

À l'inverse, la forme tardive de la MA présente l'ensemble des marqueurs de la pathologie mais se caractérise par le développement d'une sénilité vers l'âge de 65 ans et un décès après 75 ans. Cette forme prédominante touche environ 5,7 millions d'américains et ce nombre devrait passer à 14 millions d'ici 2050. Au-delà de 90 ans, il est estimé qu'une personne sur deux est atteint de la MA. Notamment, le nombre de cas diagnostiqués est en constante augmentation (123% entre 2000 et 2015) contrairement à la plupart des maladies pouvant causer un décès (Figure 3). Cette augmentation peut s'expliquer partiellement par un meilleur diagnostic de la maladie mais aussi par un vieillissement global des populations et l'absence de traitements curatifs.

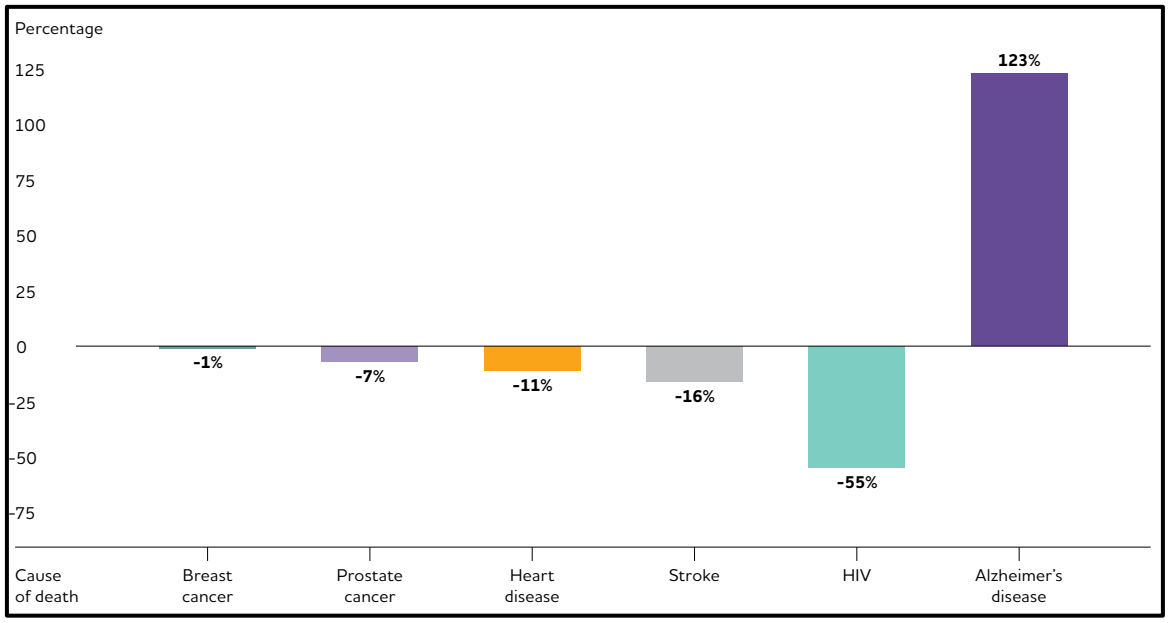

Figure 3: Évolution du pourcentage de morts pour 6 causes de décès entre 2000 et 2015 [47, 48].

Bien que les principaux facteurs de risque pour développer une MA tardive soient l'âge et le fond génétique, d'autres facteurs peuvent entrer en considération. D'une part, il y a des facteurs de risques qui sont influençables comme l'activité physique ou l'alimentation saine. D'autres facteurs aggravants comme l'obésité, l'évènement d'un traumatisme crânien ou la consommation de cigarettes ont pu être associés à la MA [49]. Enfin, une étude a rapporté un lien entre le niveau d'étude et la prévalence de la MA. Ainsi, les personnes ayant poursuivies de hautes études universitaires auraient une protection naturelle contre la MA. Les auteurs avancent l'hypothèse qu'une stimulation intellectuelle fréquente induit la formation d'une « réserve cognitive » qui a pour but de renforcer le réseau de neurones et protéger contre un éventuel dommage [50-53]. Des observations similaires ont pu être établies avec des personnes ayant un emploi les stimulant mentalement [54]. Nous pouvons également noter que 2/3 des personnes atteintes de la MA sont des femmes [55]. Cela peut s'expliquer par le fait que les hommes soient plus propices aux maladies cardiovasculaires qui sont la première cause de mortalité chez les hommes avant 65 ans. Ainsi, les hommes au-delà de 65 ans ont en moyenne une meilleure santé cardiovasculaire et donc une protection naturelle contre l'Alzheimer [56]. Il est aussi proposé que la faible proportion de femmes ayant accès à l'éducation au début du 20ème siècle pourrait expliquer ce biais pour les raisons évoquées précédemment [57]. Bien que plusieurs hypothèses aient été formulées pour expliquer l'origine de la forme tardive de la MA, il y a à l'heure actuelle aucun consensus.

1.1.2.2 Les étapes de la maladie

Afin de catégoriser au mieux les différentes étapes de la maladie, des cliniciens et neuropathologistes ont divisé le processus pathologique en plusieurs phases distinctes. Le premier à définir des phases de la maladie fut l'anatomiste Allemand Heiko Braak en 1991 qui analysa 83 cerveaux de personnes ayant souffert ou non de démence. Sa classification reposant uniquement sur l'abondance de dépôts amyloïdes extra-cellulaires et de neuro-fibrilles intra-neuronaux sur des coupes de cerveaux, cela ne participe pas au diagnostic de la maladie mais pose les bases de l'enchainement du processus pathologique [39]. Par la suite, des cliniciens tel que Barry Reisberg en 1987 associeront les phases de Braak à l'évolution de la démence chez le patient [58]:

- Phase 1 : aucune déficience mentale détectée.
- Phase 2 : faibles troubles cognitifs pouvant être associés à l'âge.
- Phase 3 : stade précoce de la MA, les patients ont des pertes de mémoire à très court terme et ont des difficultés d'organisation.
- Phase 4 : trouble cognitif modéré, les patients ont des pertes de mémoire sur des évènements récents et commencent à avoir des changements d'humeurs fréquents.
- Phase 5 : stade intermédiaire de la MA se caractérisant par une désorientation et l'oubli d'éléments du quotidien tels que l'adresse ou le numéro de téléphone. À ce stade, les patients ont besoin d'un soutien extérieur au quotidien.
- Phase 6 : stade sévère de la MA où les patients oublient leur nom et ceux de leurs proches, ont régulièrement des hallucinations et changent drastiquement de comportement.
- Phase 7 : stade terminal de la maladie où la personne n'est plus capable d'interagir avec son environnement. Au-delà de la perte des gestes, de la parole et du sourire,

les patients ont des troubles de la déglutition ce qui entraine dans la majeure partie des cas la mort du patient par pneumonie.

Enfin, il existe une dernière méthode de classification appelée le CERAD (Consortium to Establish a Registry of Alzheimer Disease). Cette méthode fut établie en 1989 par l'Institut national Américain de l'âge et regroupe à la fois des tests psychiatriques, de la neuro-imagerie mais aussi des analyses anatomo-pathologiques sur des coupes de cerveaux. Le score CERAD se divise en 4 catégories en fonction des tests et analyses effectués : normale, MA possible, MA probable, MA établie. Ce score est à ce jour le plus reconnu et utilisé par la communauté scientifique et médicale [59-62].

1.1.2.3 Les marqueurs diagnostics et pathologiques de l'Alzheimer

1.1.2.3.1 Amyloïdopathie

Le marqueur principal de la MA est la présence d'une pathologie liée à l'amyloïde. Dans le cas d'une fMA, l'origine de cette amyloïdopathie est connue et directe avec des mutations dans les gènes APP, PSEN1 et PSEN2. Cependant, dans le cas de la sMA, les niveaux d'expression de ces gènes sont normaux et leurs séquences ne présentent aucune mutation. La manière dont l'amyloïdopathie dans la sMA apparaît avec l'âge reste à être élucidé.

Comme vu précédemment, la protéine APP peut être clivée à des endroits bien distincts par des α-sécrétases, β-sécrétases et γ-sécrétases. Les metalloproteases de type ADAM ont été les premières α-sécrétases à être identifiées. La coupure par des α-sécrétases est considérée

comme non-amyloïdogénique car elle induit la libération d'un fragment appelé APPsα ayant des effets neurotrophiques ainsi que du fragment C83, la portion restante de APP. Les β-sécrétases telles que les protéines BACE1 et BACE2 vont quant à elles cliver APP pour former dans un premier temps un fragment APPsβ ainsi qu'un fragment C99 restant transmembranaire. Par la suite, les γ-sécrétases telles que les protéines préséniline 1 et 2 clivent la portion C99 ce qui libère des peptides amyloïdes appelés $A\beta_{42}$ et $A\beta_{40}$ (Figure 4) [63-66].

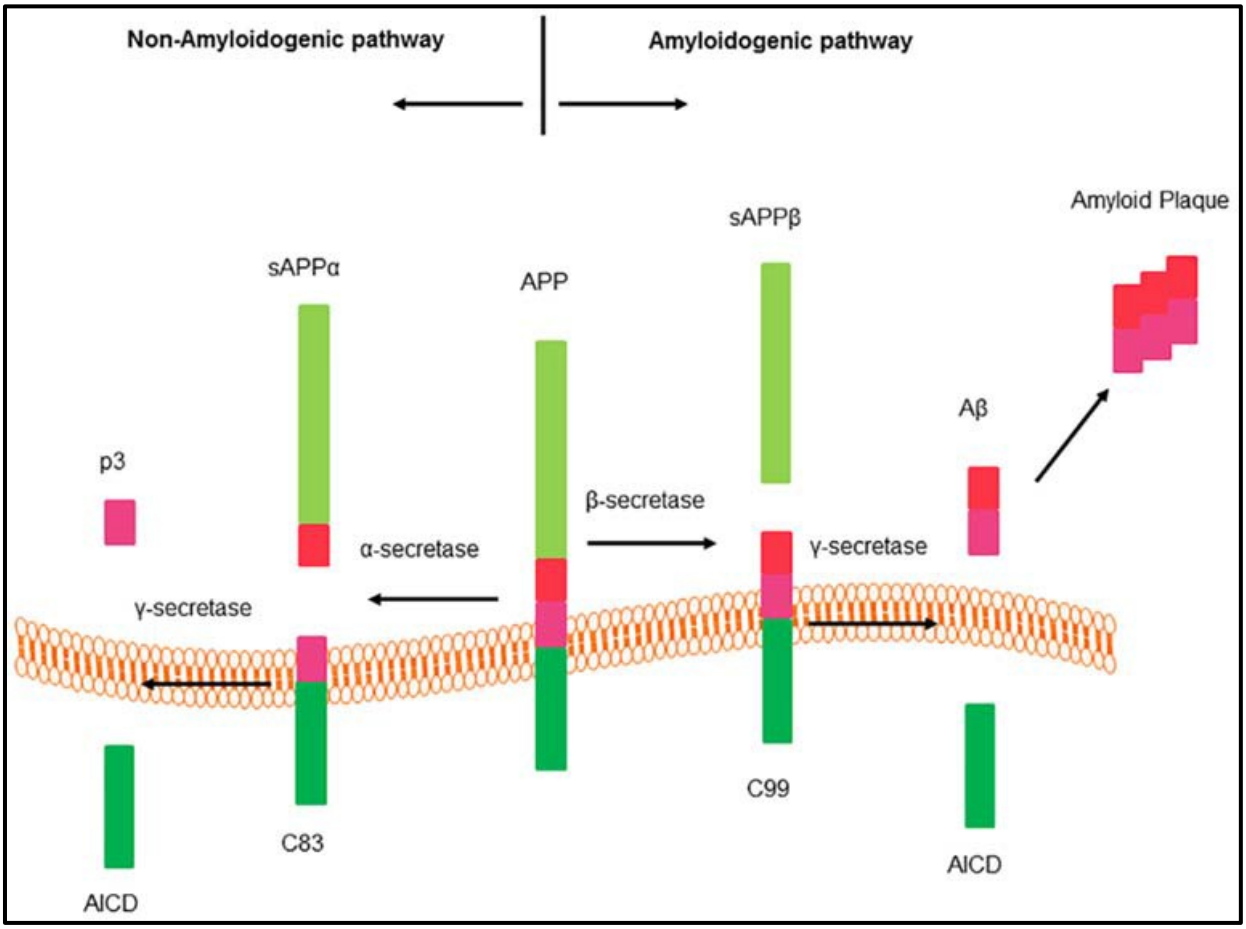

Figure 4 : Clivage de la protéine APP par les α-sécrétases, β-sécrétases et γ-sécrétases [66].

La protéine APP est exprimée de façon systémique mais son métabolisme est de loin plus abondant dans les neurones. À ce jour, la fonction de la protéine APP dans la cellule reste à

établir mais les conséquences de son métabolisme ont de lourdes répercutions. En effet, les peptides amyloïdes $A\beta_{42}$ et $A\beta_{40}$ sont rapidement secrétés par les neurones et s'agrègent pour former des dépôts extra-cellulaires insolubles. Ce sont ces dépôts qui sont à l'origine des plaques amyloïdes (Figure 5). $A\beta_{42}$ est détectable dans le Liquide Céphalo-Rachidien (LCR) au moyen d'essais de type Enzyme-Linked ImmunoSorbent Assay (ELISA). Cette mesure est diagnostique et représentative du taux de plaques amyloïde dans le cerveau. Il est attendu que les patients ayant une MA ont un taux d'$A\beta_{42}$ dans le LCR inférieur à celui des personnes âgées sans pathologie ce qui peut être expliqué par une séquestration d'$A\beta_{42}$ au niveau des plaques amyloïdes dans le cerveau. Enfin, la détection d'$A\beta_{42}$ dans le sang n'a pas fait ses preuves car elle corrèle très peu avec l'amyloïdopathie dans le cerveau probablement à cause de la sécrétion de peptides Aβ par d'autres tissus que celui-ci, ce qui a pour conséquence de fausser les résultats.

1.1.2.3.2 Tauopathie

Bien qu'étant une composante essentielle de la MA, la présence d'une Tauopathie n'est pas exclusive à cette maladie. En effet, une pathologie de Tau est retrouvée dans bon nombre de démences telles que la démence Fronto-temporale ou la maladie de Pick. La protéine Tau est encodée par le gène MAPT sur le chromosome 17 et est exprimée principalement dans le cerveau tout comme les deux autres protéines de la même famille, MAP1 et MAP2. Les Microtubule Associated Protein (MAP) ont pour fonction de se lier à la tubuline afin de promouvoir la formation de microtubules et renforcer le réseau de microtubules [67] (Figure 5). Il existe plusieurs isoformes de la protéine Tau en fonction de son épissage qui sont

caractéristiques du degré de maturation des neurones. Ainsi, il est reconnu que la présence des formes 3R et 4R soit un bon indicateur de maturité neuronale [68]. Dans l'Alzheimer, la pathologie de Tau se caractérise par son hyperphosphorylation par des kinases telle que la glycogène synthase kinase-3 (GSK-3) ce qui a pour conséquence d'altérer sa fonction primaire. En effet, Tau hyperphosphorylé dans l'Alzheimer a tendance à s'agréger dans le soma des neurones et forme ainsi des enchevêtrements de Tau (aussi appelés « Tau tangles » en Anglais) (Figure 5 et 6). Ces enchevêtrements séquestrent alors Tau normal, MAP1 et MAP2 ce qui cause une déstructuration complète des microtubules et donc du cytosquelette. Ces oligomères de Tau peuvent perturber également le transport axonal lorsqu'ils s'accumulent le long de l'axone [67] (Figure 6).

Enfin, il y a des évidences que des oligomères de Tau puissent être secrétés par les neurones, croiser la barrière hémato-encéphalique et se retrouver dans le LCR. Il est également proposé que le Tau soluble excrété dans le LCR soit capable de se propager et être toxique pour les autres cellules [69]. La mesure de la quantité de Tau dans le LCR des patients est par ailleurs un outil diagnostic intéressant. Étonnamment, la MA est une des rares Tauopathie pour laquelle Tau hyperphosphorylé se retrouve dans le LCR et est donc mesurable par des techniques d'ELISA [70-72]. Il est à noter que Tau hyperphosphorylé n'est cependant pas détectable dans le plasma.

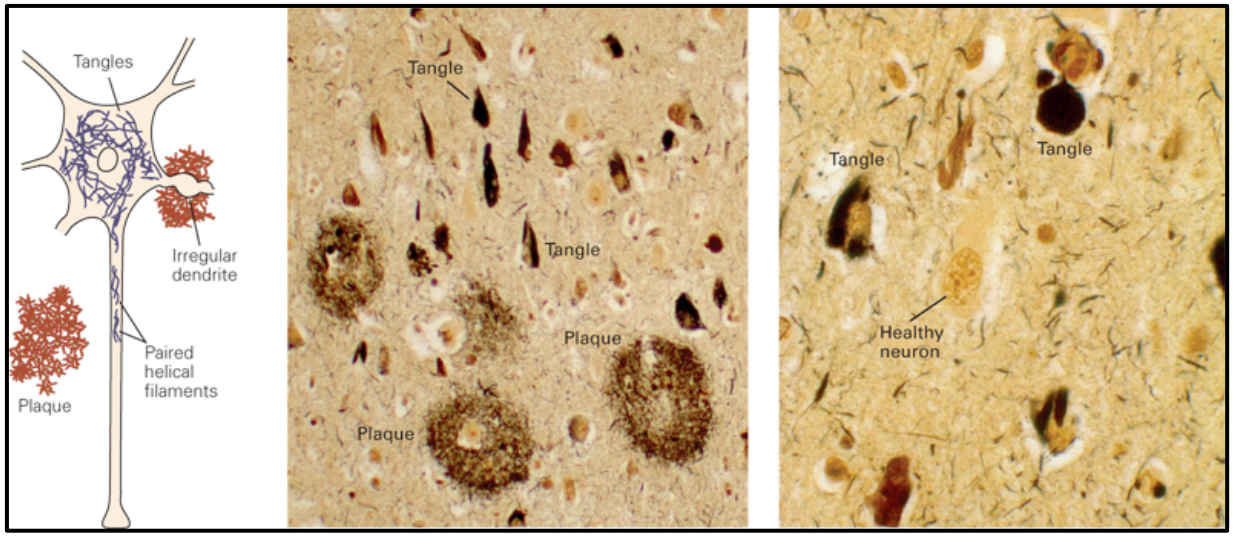

Figure 5 : Schéma et coupe de cerveau de patients Alzheimer montrant la structure de plaques amyloïdes et d'enchevêtrement de Tau (Tangle).

Principles of Neural Science, Chapter 59 : the aging brain

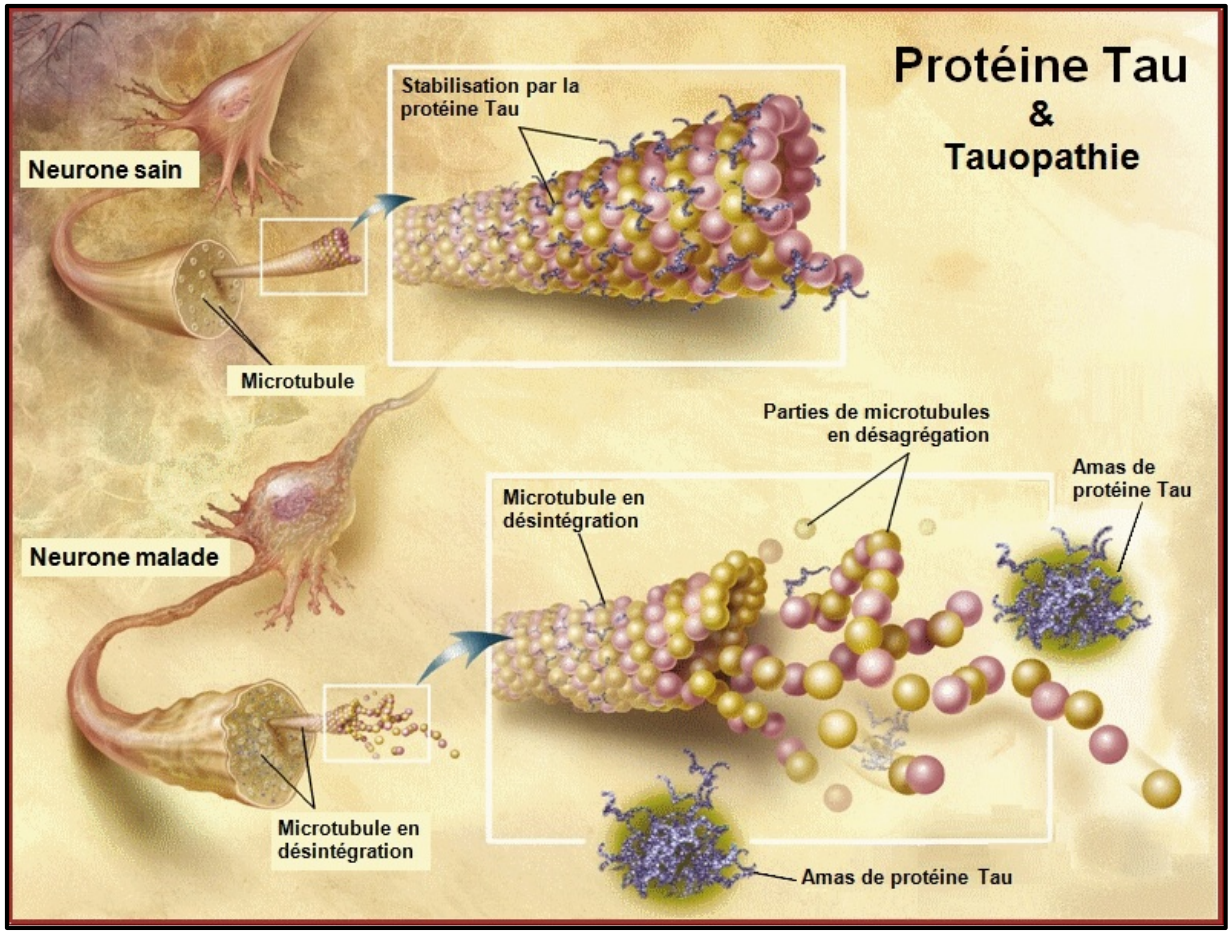

Figure 6 : Fonction de la protéine Tau et dommages engendrés par son hyperphosphorylation. Image adaptée du National Institute of Aging.

1.1.2.3.3 Neuroinflammation et perte de plasticité neuronale

Un cerveau humain sain contient en moyenne 100 milliards de neurones à l'âge adulte et chaque neurone contient environ 1000 synapses responsables de l'échange d'informations entre les neurones. La plasticité du cerveau se définit par la capacité du réseau neuronale à être malléable en fonction de l'âge, des traumatismes ou de l'apprentissage. Les cellules de la microglie sont des cellules immunitaires du cerveau jouant un rôle très important dans la synaptogénèse et donc dans la plasticité du cerveau. Il a été rapporté qu'Aβ induit directement une activation de la microglie et une neuroinflammation au site des plaques amyloïdes [73]. Suite à cela, des cytokines inflammatoires sont produites comme les interleukines et se retrouvent dans le plasma. Ainsi, l'augmentation d'immunoglobulines M, de chemokines ligand 13, d'interleukines 17, de protéines d'adhésion de cellules vasculaires, de macroglobulines et d'apolipoproteines A1 dans le plasma ont pu être associés à la présence d'une amyloidopathie dans le cerveau [74-76]. L'activation de la microglie peut également induire l'apoptose des neurones via la production de ROS [77]. La neuroinflammation n'est pas exclusive à la MA mais est néanmoins très caractéristique de la MA.

1.1.2.4 Susceptibilité génétique

Afin de trouver l'origine potentielle de la forme sporadique de la MA, de nombreux groupes et consortiums internationaux ont entrepris de séquencer le génome de plusieurs milliers de patients Alzheimer et d'individus contrôle. Cet effort n'ayant pas permis d'identifier des mutations pouvant causer la maladie, l'emphase a été mise sur la découverte de polymorphismes ou de variants alléliques pouvant conférer une susceptibilité ou une protection contre le développement de la maladie. Le meilleur exemple de variant allélique associé à la MA concerne le gène APOE. *APOE* code pour une protéine impliquée dans le transport du cholestérol et exprimée dans le foie, le cerveau et le tissu endocrinien. Chaque individu hérite d'un variant de *APOE* de la part de chaque parent. Il existe 3 variants de *APOE* nommés ε2, ε3 (la plus commune) et ε4. C'est le variant *APOE*ε4 qui est à ce jour le variant allélique le plus associé à la MA. À l'inverse, les individus ayant uniquement le variant *APOE*ε2 semblent avoir une protection naturelle contre la MA. Il est estimé que le fait d'avoir 2 copies du variant *APOE*ε4 entraine un risque 8 à 12 fois supérieur de développer une MA par rapport au reste de la population [78-80]. Aux États-Unis, 2 % et 23 % de la population possède une paire du gène APOE ε4/ε4 et ε3/ε4 respectivement. Pour mieux se rendre compte du lien entre les variants de APOE et la MA, il faut comparer ces pourcentages avec la proportion de patients diagnostiqués possédant au moins une copie de *APOE*ε4 étant de 56 % [81-83]. Cependant, ce lien n'est pas systématique. En effet, il est à noter que 44 % des patients n'ont quant à eux aucune copie de *APOE*ε4 et, à l'inverse, de nombreuses personnes porteuses de 2 copies de *APOE*ε4 ne développeront jamais la maladie même avec l'âge.

D'autres facteurs génétiques ont pu être associés à la MA mais avec une pénétrance moindre par rapport aux variants de *APOE*. Par exemple, des variants de *SORL1*, codant pour une protéine impliquée dans l'endocytose, ont pu être associés à la MA mais aussi à la maladie de Parkinson [84]. Enfin, des variations dans la séquence génomique des gènes TREM2, BIN1 et PICALM ont pu être identifiés mais avec une faible pénétrance.

Pour conclure, bien que la susceptibilité génétique semble jouer un rôle majeur, la présence ou l'absence de ces variants ne peuvent expliquer à eux seuls l'apparition de la maladie. De plus la pénétrance de ces variations reste relativement faible. Afin de quantifier cette pénétrance, les épidémiologistes ont mis au point un coefficient appelé « odds ratio » et exprime la susceptibilité de développer une maladie par rapport à un trait génétique. Le lien entre la présence de *APOE*ε4 et la MA possède un odds ratio de 3,1 pour les personnes hétérozygotes et 34,1 pour les personnes homozygotes [85]. À titre de comparaison, le odds ratio entre le fait de fumer 30 cigarettes par jour et le développement d'un cancer du poumon est de 111,3 [86].

1.1.2.5 Les traitements

Il est tout d'abord important de noter qu'il n'existe à ce jour aucun traitement curatif de la MA. De plus, aucun traitement ne permet d'arrêter ou ralentir le processus de la maladie. Les seuls médicaments étant prescrits à l'heure actuelle, comme le Donepezil, réduisent temporairement la persistance des symptômes mais leur efficacité varie selon les individus. Entre 2002 et 2012, 244 traitements sont entrés en phase clinique pour le traitement de la MA. Cependant, seulement 1 molécule fut acceptée par l'agence de régulation des médicaments Américaine, la Food and Drug Administration (FDA). De nombreux espoirs reposaient sur

l'utilisation d'inhibiteurs des β-secretases et γ-secretases pour empêcher la progression de la maladie. Ce fut la stratégie employée par la société Eli Lilly en association avec AstraZeneca en 2014 avec le développement d'un inhibiteur de β-secretase avec une prévision de mise sur le marché en 2019 et un revenu estimé à 10 milliards de dollars américains en cas de succès. L'essai clinique de phase 3 comparant 1.057 patients traités par la molécule et 1.072 patients traités avec un placebo n'a montré en 2018 aucune amélioration significative due au traitement. Cet échec notoire met à mal le développement de nouvelles molécules contre la MA en général et le développement d'inhibiteurs des β-secretases en particulier. Ainsi, des acteurs majeurs de la pharmacologie tels que Pfizer, Sanofi, Eli Lilly et Johnson & Johnson ont fermé leur développement de molécules contre l'Alzheimer. D'autres compagnies pharmaceutiques ont misé sur le développement d'anticorps reconnaissant l'Aβ ou Tau pour réduire les taux de protéines agrégées. Certaines stratégies consistent à cibler la protéine p38 MAPK (mitogen-activated serine/threonine protein kinase) afin de réduire la neuroinflammation et la perte synaptique. Malgré l'augmentation constante de cas de la MA, le développement de thérapies innovantes peine à croître. Ce manque de perspective peut s'expliquer par une mauvaise compréhension de l'origine même de la maladie et également d'un manque de modèles adéquats.

1.1.2.6 Les modèles existants

Le premier modèle à avoir été développé sur la MA fut un modèle murin en 1995. Cette souris, appelée PDAPP, consiste en une surexpression du cDNA de APP humain de façon systémique ce qui a pour conséquence d'augmenter grandement le taux d'amyloïde. Cette souris développe

avec l'âge une pathologie ressemblant à l'Alzheimer avec une amyloïdopathie se traduisant par la présence de plaques insolubles et par conséquent, une perte de la mémoire [87-89]. Les premiers tests de surexpression de APP murins n'ont pas été concluant du fait que l'amyloïde murin ne soit pas capable de s'agréger [90]. Par la suite, Karen Hsiao développa en 1996 un nouveau modèle transgénique consistant en la surexpression de APP humain porteur de la double mutation Swedish (K670N et M671L), connue chez certains patients de fMA [91, 92]. Cette souris transgénique (*APP*^{swe}) développe la même amyloïdopathie que la souris PDAPP mais plus rapidement et avec la présence de Tau hyperphosphorylé avec l'âge. Afin d'aggraver la pathologie, la souris *APP*^{swe} fut croisée avec une souris surexprimant *PSEN1* humain muté et ainsi fut créer le modèle *APP*^{swe}/*PSEN1*^{M146V} [93]. Bien que développant une pathologie très agressive, ces 2 dernières ne présentent qu'une faible pathologie de Tau. Pour parer à cette problématique, il fut créé en 2003 une souris triple transgénique en croisant le modèle *APP*^{swe}/*PSEN1*^{M146V} avec une souris surexprimant MAPT humain muté codant pour la protéine Tau hyperphosphorylée (souris *APP*^{swe}/*PSEN1*^{M146V}/*MAPT*^{P301L}) [94]. C'est à ce jour le seul modèle présentant à la fois une pathologie de Tau et de l'amyloïde au bout d'un an. Il existe enfin des modèles de vieillissement accéléré permettant d'étudier la perte de la mémoire sans avoir d'amyloïdopathie ou de Tauopathie [95, 96] (Figure 7). Le principal inconvénient de ces modèles autre que le fait que le modèle murin soit éloigné de l'homme, réside dans le fait que ces modèles ne soient pas physiologiques et peu représentatifs de la MA. Comme évoqué précédemment, les mutations utilisées dans ces modèles ne correspondent qu'à 2-3% des cas de l'Alzheimer dans le monde [90, 97].

Afin d'être plus fidèle à la pathologie, d'autres modèles non transgéniques ont été créés. Ces modèles reposent principalement sur l'injection d'Aβ ou de Tau directement dans

l'hippocampe ou le cortex de souris ou macaques [98-100]. Cette méthode permet d'une part d'étudier les effets d'Aβ ou de Tau chez des animaux pour lesquels il n'existe pas de modèle transgénique tel que le primate mais aussi d'investiguer des formes particulières d'Aβ et de Tau (monomérique, insoluble, oligomérique). Il a également été rapporté en 2017 un modèle naturel de l'Alzheimer sur le singe vert d'Afrique âgé présentant, chez certains singes, des marques pathologiques de l'Alzheimer [101]. Au niveau cellulaire, peu de modèles existe pour la MA autre que la surexpression des protéines APP, PSEN1 et Tau dans des cellules HEK293T et Hela [49, 99]. Nous pouvons tout de même noter une étude parue en 2015 portant sur la transdifférenciation de fibroblastes de patients ayant la fMA en neurones post-mitotiques sans l'ajout de transgène. Cette nouvelle technologie présente une stratégie alternative pour modéliser les maladies neurodégénératives. Cependant, nous ne savons pas si cette technologie est applicable à la modélisation de la MA en générale [102].

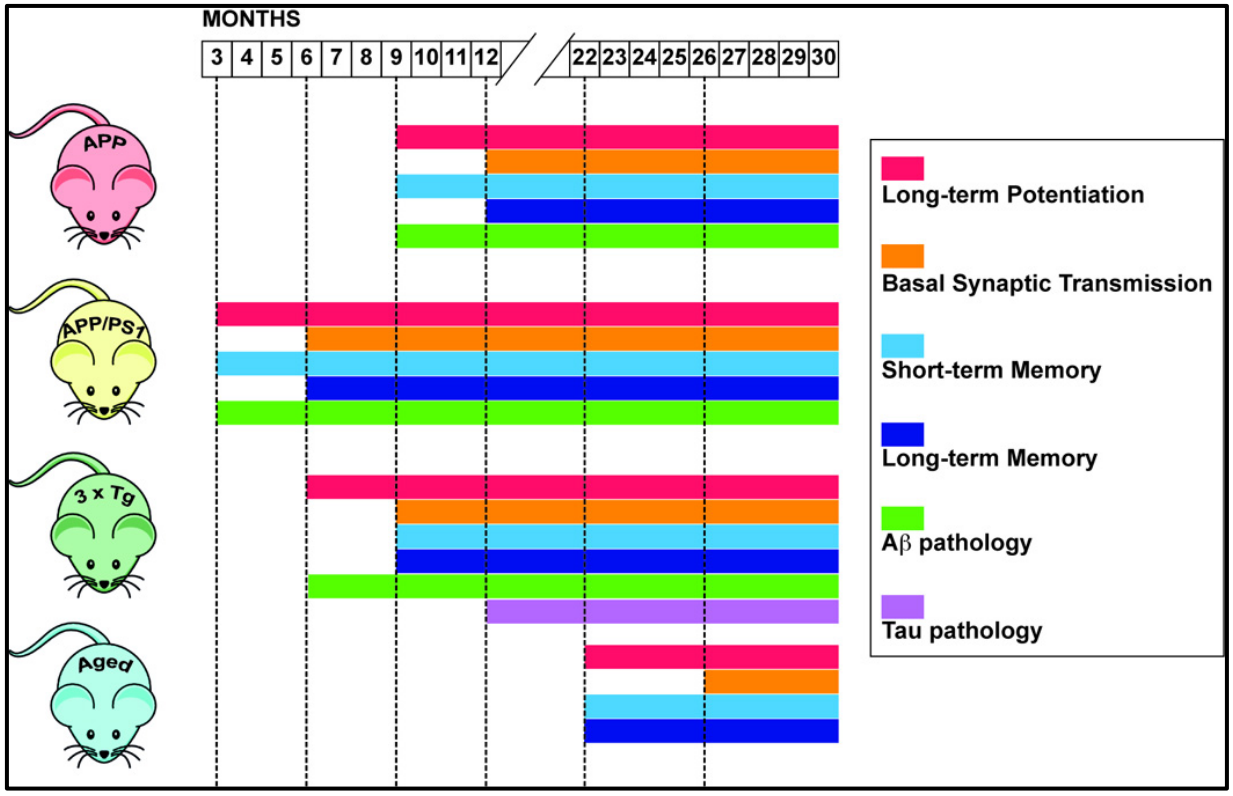

Figure 7 : Modèles transgéniques murins de la MA [97].

SECTION 2: Différenciation de cellules souches pluripotentes humaines en neurones corticaux

1.2.1 Les cellules souches pluripotentes

1.2.1.1 Isolation et propriétés des cellules souches embryonnaires humaines

Les cellules souches pluripotentes sont des cellules primitives avec une identité embryonnaire pouvant se différencier en n'importe quel type cellulaire du corps. À l'inverse des cellules totipotentes, les cellules pluripotentes ne peuvent cependant pas former du trophoblaste pour recréer un placenta. Les premières cellules souches pluripotentes ont été isolées par Martin Evans et Matthew Kaufman en 1981 à partir de la masse interne d'un blastocyste de souris [103]. Chez l'homme et la souris, le blastocyste se forme 4-5 jours après fertilisation et contient environ 100 cellules. La même année, Gail R. Martin confirmera leurs résultats et introduira pour la première fois le terme de cellules souches embryonnaires (ES) [104]. C'est en 1998 que James Thomson fit une découverte majeure en isolant des cellules ES humaines et en découvrant la méthode pour cultiver ces cellules *in vitro* [105]. Bien que révolutionnaire, cette technique provoquant une rupture du blastocyste et donc de l'embryon a suscité des interrogations dans la population et a mis en exergue des problèmes éthiques ou religieux quant à l'utilisation de ces cellules. Dans la plupart des pays dans le monde, la dérivation et/ou l'utilisation de cellules ES issues d'embryons humains sont possibles uniquement si la recherche est à visée thérapeutique (Figure 8). Pour certains pays comme le Brésil, les cellules ES humaines peuvent être isolées seulement à partir d'embryons surnuméraires lors de fertilisation *in vitro* et après 3 ans de congélation.

Une fois mises en culture, les cellules ES peuvent s'auto-renouveler indéfiniment tout en maintenant leur pluripotence. Le maintien de la pluripotence se fait en culture principalement en inhibant leurs capacités de différenciation au moyen de protéines recombinantes. Les cellules ES peuvent être cultivées soit sur un lit de fibroblastes inactivés mitotiquement ou sur des matrices contenant des facteurs de croissance tel que l'EGF. Dans les deux cas, du basic fibroblast growth factor (bFGF) est requis afin de préserver l'auto-renouvèlement et la prolifération des cellules. En particulier, le lit de fibroblastes inactivés a pour fonction de sécréter du bFGF et de garder un contact cellule-cellule avec les ES. Cette dernière fonction est importante car les cellules ES perdent rapidement leur pluripotence lorsqu'elles sont individuelles. Une fois le bFGF retiré du milieu, les cellules ES se différencient dans les trois feuillets embryonnaires que sont les couches de l'endoderme, le mésoderme et l'ectoderme [106].

1.2.1.2 La reprogrammation de cellules somatiques en cellules souches pluripotentes

Comme évoqué précédemment, l'isolation et l'utilisation des cellules ES posent des problèmes éthiques et cela rend impossible l'obtention de cellules pluripotentes humaines à partir de n'importe quel individu. De plus, les cellules ES sont difficilement utilisables dans le cadre de la transplantation de cellules différenciées pour cause de rejet immunitaire. Ainsi, la solution retenue fut de trouver une méthode capable de reprogrammer des cellules somatiques humaines en cellules ayant les mêmes propriétés que les cellules ES. Par conséquent, depuis la découverte et l'utilisation des cellules ES en 1998, de nombreux laboratoires dans le monde se sont penchés sur le moyen de convertir des cellules somatiques en cellules ayant les mêmes

propriétés que les cellules souches embryonnaires. Cependant l'idée et la démonstration d'une première reprogrammation est apparue bien avant grâce aux premiers travaux de John Gurdon en 1962 qui réalisa une transplantation de noyaux de cellules épithéliales dans des œufs énucléés de *Xénope* et qui démontra que ces noyaux transplantés étaient par la suite capables de donner naissance à des têtards normaux. Ce fut la preuve que des cellules différenciées possédaient l'information génétique nécessaire pour récapituler un développement embryonnaire [107]. Suite à ces travaux et avec la possibilité de cultiver les cellules souches pluripotentes humaines, démonstration fut faite que la fusion entre une cellule ES humaine et un fibroblaste humain permettait à cette dernière d'être reprogrammée en cellule pluripotente [108-111].

C'est en 2006 que la dernière étape fut franchie par Shinya Yamanaka qui a réussi à induire artificiellement un état de pluripotence à partir de cellules somatiques murines telles que des fibroblastes. Pour faire cette reprogrammation, Dr. Yamanaka étudia les banques d'expression génique de cellules souches embryonnaires en comparaison à des cellules somatiques et obtient ainsi 24 gènes candidats enrichis dans les cellules pluripotentes. La transfection de chaque gène indépendamment dans des fibroblastes de souris n'a cependant pas permis d'induire la pluripotence. C'est par contre en surexprimant les 24 gènes en même temps que des clones avec des propriétés de cellules ES émergèrent. Afin d'identifier quels marqueurs étaient requis pour l'induction, Dr. Yamanaka étudia l'effet d'ôter chaque marqueur du pool indépendamment et en déduit que les gènes POU5F1 (codant pour la protéine OCT3/4), KLF4, SOX2, et c-MYC étaient les facteurs clés de la reprogrammation. Ainsi, seul la combinaison de ces 4 facteurs permettra de générer des cellules souches pluripotentes alors appelées « iPS » [112] (Figure 8). Par la suite, Dr. Yamanaka publiera en 2007 l'efficacité de sa méthode à partir de fibroblastes humains [113]. Cette découverte ouvrira la porte à de nombreuses applications telles que la

thérapie cellulaire ou la modélisation de maladies *in vitro*. Seulement un an après la découverte du Dr. Yamanaka, Dr. George Daley publiera les premières iPS issues de patients souffrant notamment de la maladie d'Huntington et de Parkinson. Depuis, le nombre de modèles de pathologies utilisant des iPS n'a cessé de croître [114-116]. En 2012, les Docteurs Yamanaka et Gurdon obtiendront le prix Nobel de médecine pour leurs travaux.

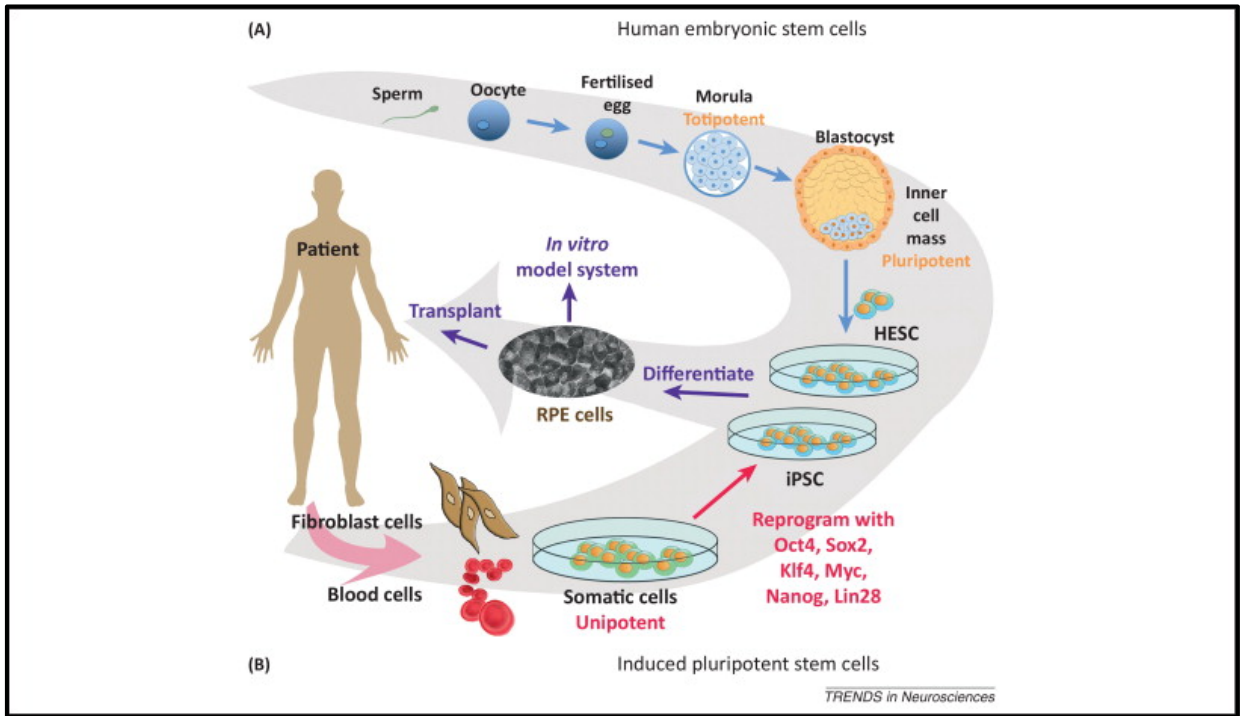

Figure 8 : Schéma décrivant l'origine et l'utilisation des cellules souches pluripotentes humaines [117].

1.2.2 La différenciation des cellules ES et iPS en neurones corticaux et organoïdes

À l'issue de la première semaine de l'embryogénèse, le blastocyste s'implante dans l'utérus et commence une phase de différenciation de sa masse interne. C'est à ce stade que sont formés les feuillets du mésoderme, de l'endoderme et de l'ectoderme qui seront à l'origine, à titre d'exemple, de cellules cardiaques, hépatiques et neuronales respectivement. La plaque neurale se forme 19 jours après la fertilisation à partir du feuillet de l'ectoderme. De la zone postérieure à antérieure, la plaque neurale se divise respectivement en 3 parties principales : le cerveau postérieur (ou rhombencéphale), le cerveau moyen (ou mésencéphale) et le cerveau antérieur (ou prosencéphale). Rapidement, la plaque neurale se replie pour former le tube neural (Figure 9). Ce sont les cellules qui tapissent le tube neural qui seront responsables de la neurogénèse et de la migration des cellules dans des couches spécifiques du cerveau. Ainsi se forme la corticogénèse afin de diviser un répertoire complexe de neurones dans des couches corticales. Tous ces processus de différenciation de la plaque neurale sont régis par des protéines de signalisation à des proportions bien définies. Par défaut, le feuillet de l'ectoderme est engagé vers la voie de différenciation en fibroblastes grâce au Bone Morphogenic Protein 4 (BMP4), une protéine de la famille des Transforming Growth Factor béta (TGFβ). Le BMP4 est produit en grande quantité par le notochord, situé juste en dessous du tube neural. Pour contrer la différenciation en fibroblastes, le tube neural sécrète des polypeptides comme la noggin et la chordin. Ces peptides sont capables de se lier directement au BMP4 afin d'en inhiber son action et ainsi permettre la neurogénèse. Par défaut, et en absence de BMP4, les cellules se

différencient en neurones corticaux et c'est cette même stratégie qui est employée pour différencier des cellules ES ou iPS en neurones corticaux [118-120].

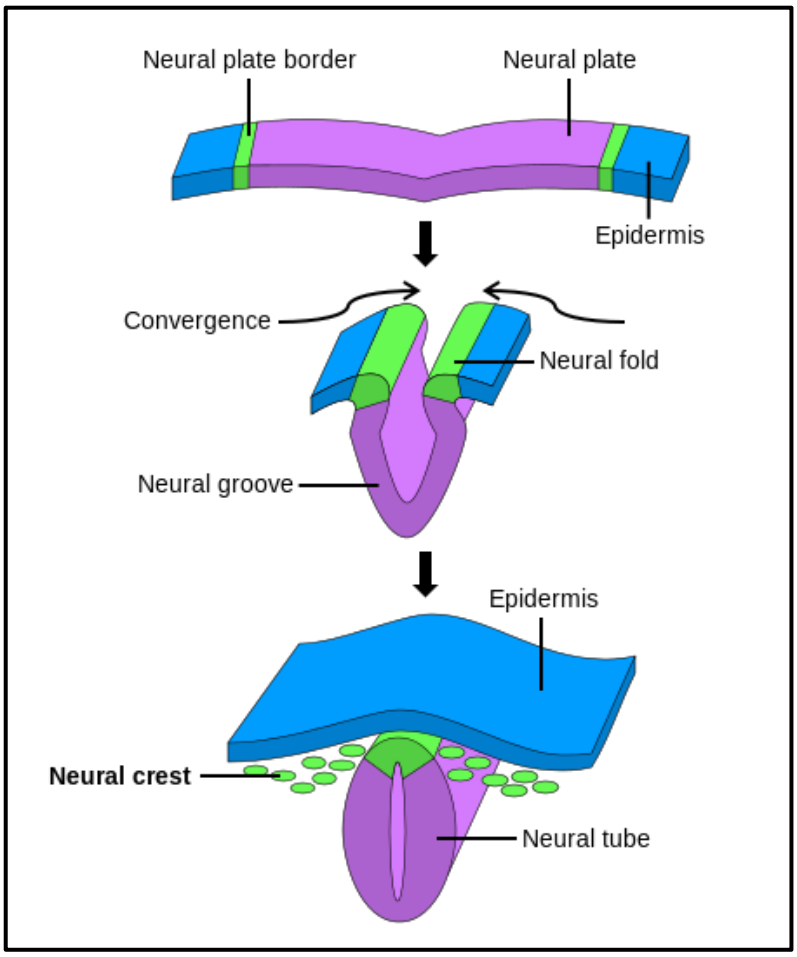

Figure 9 : Schéma montrant la formation du tube neural à partir de la plaque neurale. Image libre de droit.

Les neurones corticaux sont les neurones peuplant le cortex cérébral qui ont été décrit en détail par le neuropathologiste Espagnol Santiago Cajal en 1889. Il en existe plusieurs types avec des fonctions bien distinctes. Les interneurones et les neurones pyramidaux sont les principaux neurones du cortex et sont par conséquent largement affectés dans la MA. Les

interneurones sont multipolaires mais présentent une grande diversité au niveau de leurs morphologies. Par exemple, les neurones granulaires sont des interneurones minoritaires dans le cortex qui présentent une grande arborisation de leurs dendrites. À l'inverse, les neurones pyramidaux se caractérisent par un soma – hors axone et dendrite – de forme triangulaire.

Les interneurones et les neurones pyramidaux peuvent être soit excitateurs soit inhibiteurs. Les neurones inhibiteurs produisent un potentiel d'action négatif au moyen de la production de neurotransmetteurs tels que la glycine ou le GABA. Les neurones produisant les neurotransmetteurs GABA sont alors appelés GABAergiques. Lorsque le GABA se fixe aux récepteurs GABA des neurones, cela a pour conséquence d'ouvrir un canal au chlore et de charger négativement la membrane des neurones. À l'inverse, les neurones dits Glutamatergiques produisent du glutamate se fixant aux récepteurs NMDA ou AMPA des neurones. Cela conduit à l'ouverture de pores faisant passer du sodium, du potassium et du calcium et ainsi induit un potentiel d'action positif. Les neurones Glutamatergiques sont donc considérés comme excitateurs. Ce sont ces derniers qui sont impliqués dans la plasticité neuronale ainsi que dans la mémoire. D'autres neurotransmetteurs tels que l'acéthylcholine, la dopamine et la sérotonine sont quant à eux produits par d'autres types de neurones appelés respectivement cholinergiques, dopaminergiques et sérotoninergiques [120].

Dès les premières isolations de cellules ES, de nombreux laboratoires ont établi puis amélioré des protocoles de différenciation en neurones mais c'est seulement depuis l'avènement des cellules iPS que le nombre de protocoles publiés a augmenté exponentiellement. Dans la plupart des cas, la différenciation commence par une phase d'induction ectodermale via l'inhibition du BMP4 ou du TGFβ pendant 2 à 3 semaines. C'est à la fin de cette induction que les progéniteurs neuronaux peuvent être passés et que la différenciation terminale peut

commencer. Cette dernière nécessite 3 à 4 semaines pour obtenir des neurones post-mitotiques matures capables de répondre à un stimuli. Par défaut, les progéniteurs neuronaux produisent des neurones corticaux majoritairement GABAergiques et Glutamatergiques [121-125].

En suivant la même logique de différenciation mais en agrégeant les cellules dès le départ, cela permet de former des tissus cérébraux organisés de 4-5 mm de diamètre. Ces organoïdes cérébraux sont ensuite cultivés en bioréacteurs et permettent de se rapprocher encore plus de la complexité du cerveau humain et ainsi de modéliser des maladies [126-128].

1.2.3 Les modèles iPS de la MA

Il aura fallu 4 ans après la découverte de la reprogrammation par le Dr. Yamanaka pour voir publier les premières cellules iPS issues de patients Alzheimer. Dans cette étude japonaise, les auteurs ont dérivé 4 lignées d'iPS porteuses de mutations connues dans *PSEN1* ou *PSEN2* qu'ils ont par la suite différencié en neurones. Les auteurs ont pu mettre en évidence une sécrétion accrue en Aβ42 dans les neurones fMA en comparaison à des lignées contrôles. Ils ont aussi pu noter une faible augmentation de la sécrétion en Aβ40 et une réponse des cellules aux inhibiteurs des gamma-sécrétases [129]. Bien que les modèles iPS de la fMA se multiplieront par la suite, il faudra attendre 2012 pour voir les première lignées sMA pour lesquelles les patients ont développé une forme tardive de la MA en absence d'historique familial. Parmi les 12 lignées d'iPS sMA générées depuis 2012 et caractérisées, seulement 9 possèdent les marqueurs pathologiques de la MA incluant la sécrétion d'Aβ42 et la présence d'une hyperphosphorylation de Tau [116, 130-134].

Il existe également des modèles d'organoïdes cérébraux basés sur la différenciation de cellules iPS provenant de patients Alzheimer. C'est le cas principalement pour des patients ayant la forme familiale de la MA [135]. Enfin, un groupe de chercheurs belges a pu également greffer des neurones issus d'iPS de la fMA dans le cerveau de souris immunodéficientes afin d'obtenir un modèle murin plus adapté et étudier la progression de la maladie. Ainsi, les souris greffées développent les principaux marqueurs de la pathologie incluant la présence de plaques amyloïdes et l'accumulation de Tau hyperphosphorylé au niveau des neurones entourant ces plaques. Cependant, les fibrilles de Tau aussi appelés « Tau tangles » n'ont pu être observés dans ces souris et aucune transmission de la maladie vers les cellules hôtes n'a été noté [136].

SECTION 3: Modifications épigénétiques et le rôle des polycombs

1.3.1 L'épigénome et sa modulation

1.3.1.1 La chromatine et sa régulation

La chromatine se définit par l'ensemble des facteurs enrobant l'ADN génomique. L'ADN s'enroule sur une longueur de 147 bases autour d'un octamère de 4 histones (H2A, H2B, H3 et H4). Chaque histone comporte un fragment N-terminal qui s'écarte de la structure nucléosomique et qui est propice à diverses modifications post-traductionnelles. Ce sont ces modifications qui vont en partie dicter la façon dont le génome sera condensé [137-141]. Pour la plupart, ces modifications sont soit des phosphorylations, des méthylations ou des acétylations. L'ajout de ces groupements au fragment N-terminal des histones se fait principalement par l'action d'enzymes telles que les déméthylases et les histone déacétylasses (HDAC) pour enlever des groupements ou les méthyltransférases et les acétyltransférases pour ajouter des groupements [142]. Ces modifications alors appelées « épigénétiques » permettent à l'ADN d'avoir une conformation, soit relaxée à certains locus pour favoriser la transcription soit, condensée pour au contraire inhiber la transcription de certains gènes. Les modifications de la chromatine sont aussi utilisées par la cellule pour répliquer son ADN ou le réparer. En effet, il y a souvent besoin que l'ADN soit plus accessible pour permettre à des complexes d'agir. Les modifications d'histones les plus étudiées, car ayant un impact important sur la chromatine, sont la triple méthylation sur la lysine 4 de l'histone H3 (H3K4me3), la triple méthylation sur la lysine 27 de l'histone H3 (H3K27me3), la triple méthylation sur la lysine 9 de l'histone H3 (H3K9me3), l'acétylation sur la lysine 9 de l'histone H3 (H3K9ac) et

l'ubiquitination de H2A ($H2A_{ub}$). Les marques H3K4me3 et H3K9ac sont considérées comme activatrices car elles se retrouvent généralement au niveau des promoteurs et permettent l'activation de la transcription. Ces marques constituent la chromatine ouverte aussi appelée euchromatine. La marque H3K27me3 se retrouve également au niveau des promoteurs mais va quant à elle réprimer la transcription des gènes et constituer l'hétérochromatine facultative. Enfin, H3K9me3 est une marque répressive enrichie principalement dans des régions pauvres en gènes comme les régions télomériques ou péri-centromériques qui constituent l'hétérochromatine constitutive [143, 144].

L'épigénome comprend l'ensemble des modifications épigénétiques régissant la maintenance du génome. Par conséquent, l'épigénétique ne s'arrête pas à la modification des histones. En effet, la méthylation directe de l'ADN au niveau du promoteur des gènes est un mécanisme de régulation transcriptionnelle très important. La méthylation de l'ADN se fait au niveau des bases cytosine lorsqu'elle précède une guanine. Ces patrons appelés CpG sont répétés au niveau des promoteurs et leur méthylation inhibe la transcription des gènes. Ces cytosines méthylées peuvent également être greffées à un groupement hydroxyle pour former des 5-hydroxymethylcytosines pouvant par la suite être oxydées en 5-formylcytosine [145]. Enfin, les longs ARN non codants (lncARN) constituent une partie intégrante de l'épigénome. Les lncRNA peuvent réguler la transcription des gènes spécifiques en se liant à des facteurs de transcription ou directement à l'ARN polymérase II. Les lncRNA permettent aussi de réguler l'épissage alternatif des gènes [146].

1.3.1.2 Les protéines de groupes polycombs (PcG)

Les protéines membres des PcG correspondent à une famille de protéines capables de modifier la chromatine dans le but d'inhiber l'expression de certains gènes. Ces protéines sont importantes pour le développement embryonnaire normal via la répression des gènes HOX [147, 148]. Cette fonction des PcG fut décrite pour la première fois chez la Drosophile en 1978 [149]. Depuis leur découverte, les PcG ont été intensivement étudiés pour leur implication dans la différenciation, l'identité cellulaire et les pathologies tel que le cancer [150, 151]. La plupart des protéines PcG constituent des complexes répressifs (PRC) multimériques capables de se lier à l'ADN à des régions spécifiques et remodeler la chromatine localement. Le complexe PRC1 comprend une protéine PcG, une protéine polyhomeotique, une protéine avec un domaine RING et un posterior sex comb. PRC1 est responsable de l'ubiquitination de H2A à la lysine 119 par le biais de BMI1 qui se lie à l'ADN et RING1 qui catalyse la réaction d'ubiquitination [152]. Le complexe PRC2 cible quant à lui des gènes différents de ceux reconnus par le PRC1. PRC2 se compose de trois protéines que sont un enhancer de zeste (EZH1/2), un suppresseur de zeste 12 (SUZ12) et un extra sex comb (ESC). SUZ12 se lie au promoteur d'un répertoire de gènes et EZH1/2 est responsable de le tri-méthylation de H3K27 grâce à son domaine methyltransférase [148]. Les marques $H2A_{ub}$ et H3K27me3 ont pour conséquence de condenser la chromatine et réprimer l'expression des gènes.

1.3.1.3 La protéine PcG BMI1

BMI1 (B lymphoma Mo-MLV insertion region 1 homolog) est une protéine membre du PRC1 responsable de la répression de gènes impliqués notamment dans le développement du cerveau [153]. Cette protéine de 37 kDa comprend 326 acides aminés hautement conservés chez

les mammifères [154]. Elle est encodée par un gène se situant sur le chromosome 10 contenant 10 exons. En amont de *BMI1*, se trouve un autre gène appelé COpper Metabolism gene MURR1 Domain 3 (*COMMD3*) pouvant être transcrit en fusion (Figure 10). Bien que cette fusion fût détectée dans des bases de données de séquençage de l'ARN, aucune publication à ce jour porte sur la fonction de *COMMD3-BMI1*.

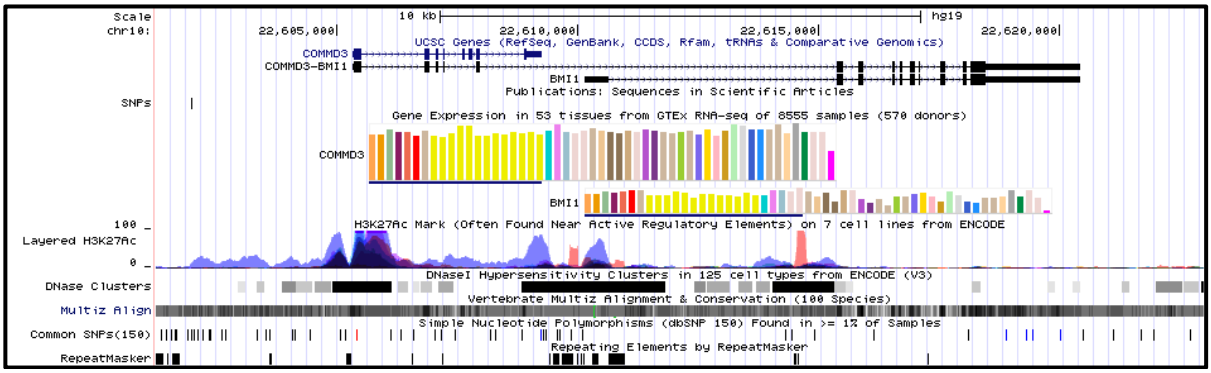

Figure 10 : Carte physique de *BMI1* et ses annotations incluant le profil d'expression dans tous les tissus du corps, les régions ouvertes, le niveau de conservation de la séquence entre les espèces et la présence de séquences répétitrices. UCSC.

La protéine BMI1 fut découverte pour la première fois en 1991 pour son implication dans le lymphome en coopération avec MYC [155-157]. En 1999, des auteurs démontrent aussi que BMI1 permet de bloquer la senescence grâce à la répression du locus INK4A/ARF [158]. Bien qu'exprimé dans la plupart des tissus, BMI1 est plus particulièrement enrichis dans les cellules souches hématopoïétiques ainsi que les cellules souches neurales [159]. Il est par ailleurs surexprimé dans le cancer du poumon, le cancer colorectal, le médulloblastome, le glioblastome et le neuroblastome [154, 160-162]. Le fait de surexprimer BMI1 dans des cellules normales ne

permet pas de transformer ou immortaliser la cellule mais lui confère une durée de vie plus importante [158]. En inhibant l'expression du locus INK4A/ARF, BMI1 empêche $p19^{ARF}$ de séquestrer mouse double minute 2 (MDM2), un inhibiteur de p53, et favorise la prolifération et l'auto-renouvèlement des cellules. À l'inverse, la perte de BMI1 induit la senescence des cellules par la voie $p16^{INK4A}$ et p53 [11]. Le laboratoire de Dr. Bernier a également démontré que BMI1 confère une radio résistance aux cellules souches cancéreuses du glioblastome par le biais du recrutement de la machinerie de réparation de l'ADN [163](Figure 11).

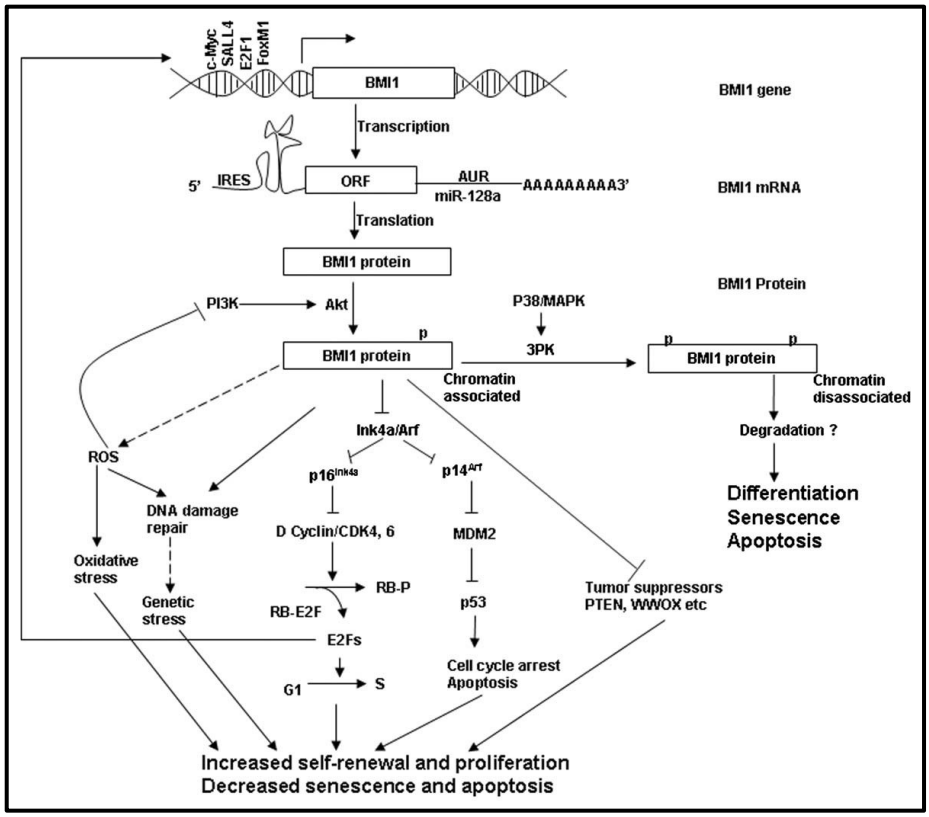

Figure 11 : Schéma montrant les voies moléculaires dans lesquelles BMI1 est impliqué [11].

SECTION 4: Hypothèses de travail et objectifs

1.4.1 La problématique de la MA sporadique

Comme nous avons pu le voir dans la section 1, l'origine de la sMA reste à élucider. L'hypothèse prédominante consiste à penser que l'apparition de la sMA en fonction de l'âge serait due à la pénétrance d'une combinaison de polymorphismes et de variants alléliques. Il est vrai que des variants alléliques tel que *APOE* et *SORL1* confère une forte susceptibilité de développer la maladie mais le lien mécanistique entre ces variants et tout le spectre de la maladie reste à démontrer. De plus, il est à noter que près de la moitié des patients de la sMA ne possède aucune copie de *APOE*ε4. À l'inverse, de nombreuses personnes avec une ou deux copies de *APOE*ε4 ne développeront jamais la maladie. De plus, la majeure partie de la recherche sur la sMA repose davantage sur les conséquences de la maladie avec l'étude des mécanismes de sécrétions et métabolisation de l'amyloïde ainsi que l'hyperphosphorylation de Tau mais peu d'études se concentre sur l'origine de ces marques pathologiques.

Par conséquent, il y a un besoin urgent d'identifier les mécanismes à l'origine de la maladie afin de développer des thérapies innovantes.

1.4.2 Les hypothèses de travail et les objectifs

Avant le début de mon doctorat, le Dr. Jida El Hajjar a pu démontrer que des souris hétérozygotes pour *Bmi1* (*Bmi1*$^{+/-}$) développaient, avec l'âge, une neurodégénérescence ressemblant à la MA. En effet, les souris *Bmi1*$^{+/-}$ âgées de 15 à 20 mois présentent une alopécie, une taille réduite, une altération de la mémoire ainsi que les marqueurs clés de l'Alzheimer

incluant la présence de dépôts amyloïdes et de Tau hyperphosphorylé dans le cerveau, en comparaison à des souris contrôle du même âge. De plus le croisement des souris *Bmi1*$^{+/-}$ avec des souris transgéniques *APP*^{swe} a montré que les souris double-transgéniques ont une espérance de vie moindre que les souris simple-transgéniques. La pathologie de l'Alzheimer fut également plus forte chez les souris double-transgéniques. Par ailleurs, il a été démontré par le laboratoire mais aussi par d'autres groupes que l'expression de *BMI1* diminue en fonction de l'âge dans la plupart des tissus incluant le cerveau.

Tous ces résultats préliminaires suggèrent fortement que BMI1 pourrait avoir un lien avec l'initiation et/ou la progression de la maladie. L'hypothèse de départ de cette étude fut que l'expression de *BMI1* serait affectée dans la MA et que cet évènement serait à l'origine de la maladie. Si la perte de BMI1 est bien un élément causal de la maladie, cela nous permettrait d'entrevoir une solution thérapeutique en réintroduisant BMI1.

Mon travail s'est divisé en plusieurs phases afin de valider ou invalider cette hypothèse :

- *Étudier les niveaux d'expressions de BMI1 dans le cerveau des patients Alzheimer*

Afin d'établir un lien entre BMI1 et la MA, nous avons tout d'abord étudié si l'expression de BMI1 était affectée dans le cerveau des patients atteints par la maladie d'Alzheimer. Dans cette première étape, une attention toute particulière a été portée sur le sélection des échantillons à analyser. En effet, la classification entre des individus souffrant de la MA et des individus sains âgés est parfois hasardeuse. Nous avons par conséquent sélectionné uniquement des cas typiques de l'Alzheimer n'ayant aucun historique familial pour cette maladie et présentant toutes les marques pathologiques. La même attention a été portée pour sélectionner les personnes saines. Des échantillons de cerveaux (cortex et hippocampe) furent analysés en Polymerase Chain

Reaction quantitative (qPCR) et en western-blot. De plus, une banque de donnée de séquençage des ARN (ARNseq) comprenant plus de 100 échantillons caractérisés avec détails fut interrogée pour l'expression de *BMI1*. J'ai par ailleurs effectué la même analyse sur d'autres échantillons provenant de patients souffrant de démence pour vérifier la spécificité de mes observations.

- *Générer des cellules iPS de patients Alzheimer et les différencier en neurones corticaux et organoïdes*

Pour disposer d'un modèle naturel d'étude de la MA, j'ai entrepris de reprogrammer des fibroblastes de la peau de patients sMA et d'individus sains du même âge en cellules iPS que j'ai par la suite caractérisé et différencié en neurones et organoïdes corticaux. Cette étape m'a permis de valider mes techniques d'analyses du phénotype Alzheimer mais aussi de comparer les niveaux de BMI1 entre les neurones contrôle et sMA.

- *Induire la perte de BMI1 dans des neurones corticaux humains*

Dans le but de déterminer si la perte de BMI1 pouvait initier ou promouvoir la pathologie d'Alzheimer, j'ai développé deux modèles. J'ai tout d'abord travaillé à adapter un protocole de différenciation de cellules ES humaines en neurones corticaux pour infecter des progéniteurs neuronaux avec un lentivirus permettant l'expression d'un ARN court double brins (shARN) dirigé contre BMI1. Dans un second modèle, j'ai réalisé une invalidation génétique par CRISPR/Cas9 en surexprimant la protéine Cas9 dans des neurones post-mitotiques puis en transfectant des ARN guides (sgRNA) synthétique dirigés contre *BMI1*. Ces deux modèles furent utilisés pour voir l'effet de la perte de BMI1 dans des neurones corticaux humains sur la sécrétion et déposition de l'amyloïde, l'hyperphosphorylation de Tau, l'apoptose et la perte

synaptique. Pour étudier cette dernière, des cultures à très haute densité, en trois-dimensions et plus matures ont été utilisées.

- *Disséquer le mécanisme moléculaire liant BMI1 à la pathologie d'Alzheimer*

Pour finir, j'ai réalisé des expériences pour établir le lien moléculaire entre BMI1 et tous les paramètres de la MA rencontré dans les deux modèles d'inactivation de BMI1 développés précédemment. Pour cela, j'ai d'une part regardé si BMI1 se liait au promoteur de gènes impliqués dans l'Alzheimer pour en réprimer l'expression et d'autre part j'ai réalisé un criblage de molécules dans des neurones ayant une perte de BMI1 pour savoir quelles voies de signalisations sont importantes dans l'établissement de la maladie.

Mes travaux ont donné lieu à la production de deux articles en premier auteur qui vous sont présentés ci-après. Par ailleurs, une troisième publication en lien avec cette étude est présente en annexe 1. L'annexe 2 comporte quant à elle une publication en tant que premier auteur qui n'est pas en lien avec cette étude mais qui fait partie intégrante de ma formation au doctorat.

CHAPITRE 2:

MODELING LATE-ONSET SPORADIC ALZHEIMER'S DISEASE THROUGH BMI1 DEFICIENCY

Ce chapitre vous présente le premier article de ma thèse paru le 29 Mai 2018 dans le journal Cell Reports. Il constitue l'essentiel de mes travaux et porte sur la modélisation de la maladie d'Alzheimer au moyen de l'inactivation de BMI1.

Modeling late-onset sporadic Alzheimer's disease through BMI1 deficiency

Anthony Flamier[1], Jida El Hajjar[1], James Adjaye [2], Karl J. Fernandes [3, 4], Mohamed Abdouh[1], and Gilbert Bernier[1, 4, *]

[1] Stem Cell and Developmental Biology Laboratory, Hôpital Maisonneuve-Rosemont, 5415 Boul. l'Assomption, Montreal, Canada, H1T 2M4.

[2] Max Planck Institute for Molecular Genetics, 14195, Berlin, Germany

[3] Research Center of the University of Montreal Hospital (CRCHUM), Montreal, QC H2X 0A9, Canada

[4] Department of Neurosciences, University of Montreal, Montreal, Canada

*Corresponding author and lead contact:

Tel: 514-252-3400 ext. 4648

Fax: 514-253-7626

E-mail: gbernier.hmr@ssss.gouv.qc.ca

Content:
7 Figures, 7 Supplementary Figures and 2 Supplementary Tables
Word count: 3 869 (w/o figure legends)

ABSTRACT

Late-onset sporadic Alzheimer's disease (AD) is the most prevalent form of dementia, but its origin remains poorly understood. The Bmi1/Ring1 protein complex maintains transcriptional repression of developmental genes through histone H2A mono-ubiquitination and *Bmi1* deficiency in mice results in growth retardation, progeria and neurodegeneration. Here, we demonstrate that BMI1 is silenced in AD brains, but not in those from early-onset familial AD, frontotemporal dementia or Lewy body dementia. BMI1 expression was also reduced in cortical neurons from AD patient-derived induced pluripotent stem cells but not in neurons over-expressing mutant *APP* and *PSEN1*. *BMI1* knockout in human post-mitotic neurons resulted in amyloid beta peptide secretion and deposition, p-Tau accumulation as well as neurodegeneration. Mechanistically, BMI1 was required to repress *MAPT* transcription and prevent GSK3beta and p53 stabilization, which otherwise resulted in neurodegeneration. Restoration of BMI1 activity through genetic or pharmaceutical approaches could represent a novel therapeutic strategy against AD.

INTRODUCTION

Late-onset sporadic Alzheimer's disease (AD) is the most common form of dementia, with advanced age as the greatest risk factor to develop AD [164]. While AD has no clearly defined etiology, carrying the *E4* variant of *Apolipoprotein* (*APOE4*) is the most important genetic risk factor [165]. In contrast, familial AD (FAD) is a rare autosomal dominant disorder occurring between the ages of 30-60 years and linked to mutations in *Amyloid Beta Precursor Protein* (*APP*), *PRESENILIN 1 (PSEN1) or PRESENILIN 2 (PSEN2)* [166]. AD and FAD are characterized by progressive memory and behavioral impairment owing to degeneration of limbic and cortical areas of the brain. Pathological hallmarks are the presence of extra-cellular amyloid plaques, intra-neuronal phospho-Tau (p-Tau) tangles, neuronal cell death and synaptic atrophy [166]. Because the probability to develop AD increases dramatically with age, ageing-associated alterations of the brain's epigenome may play a role in disease progression or origin [167]. Aged brains of primates are vulnerable to amyloid beta (Aβ42) toxicity, while those of young animals are not, indicative of fundamental alteration of the brain's epigenome and/or physiology with age [168]. Specific genes are also silenced in the ageing human brain through accumulation of oxidative DNA damage at their promoters [28], raising the possibility that epigenetic gene silencing could trigger AD.

Bmi1 is a component of the Polycomb Repressive Complex 1 (PRC1), which promotes chromatin compaction and gene silencing through its E3-mono-ubiquitin ligase activity mediated by Ring1a/b on histone H2A at lysine 119 ($H2A^{ub}$) [169, 170]. *Bmi1*-deficient cells undergo rapid senescence owing in part to up-regulation of the *Ink4a/Arf* (*Cdkn2a*) locus, encoding for the $p16^{Ink4a}$ and $p19^{Arf}$ ($p14^{ARF}$ in human) tumor suppressors [158, 171]. *Bmi1*-null

mice present post-natal growth defects, reduced lifespan and cerebellar degeneration [172]. While historically having been studied for its cell proliferation-promoting activities [173], Bmi1 is also widely expressed in post-mitotic cortical neurons where it prevents accumulation of oxidative damage [174].

Recently, induced pluripotent stem cells (iPSCs) have been derived from aged-match controls and sporadic AD patients, with some of those showing AD-like pathology upon neuronal differentiation [113, 131, 133, 134]. Other models, such as those over-expressing mutant *APP* and *PSEN1* in human neurons could recapitulate FAD in three dimension cultures [175]. Here we report that BMI1 expression is specifically reduced in AD brains and in iPSC-derived AD neurons. In contrast, BMI1 expression was unaffected in FAD, FTD and LBD brains, and in disease-affected 3xTG mice or human cortical neurons over-expressing mutant *APP* and *PSEN1*. *BMI1* inactivation in human neurons could reproduce AD pathological hallmarks in two- and three-dimensional cultures. Modeling AD through *BMI1* deficiency in cultured human neurons thus represents a novel platform to study neurodegeneration mechanisms and test therapeutic compounds against AD.

BMI1 expression is reduced in AD brains

To investigate a possible implication of *BMI1* in AD, we interrogated public RNA-seq datasets from age-matched normal and AD cortices. This first broad analysis did not reveal statistical difference between normal and AD brains for *BMI1* expression. A closer look at the pathological features of the samples however revealed several errors in classification. We thus only selected AD brain samples (n = 50) showing a classical AD neuropathology i.e. p-Tau accumulation, high concentration of p-Tau/mg of tissue, secretion of Aβ42 and presence of extracellular amyloid plaques. Only age-matched controls (n = 50) not presenting AD-related pathological features were selected (Fig. 1A). Upon comparative analysis of these samples, we found that reads number for *BMI1* were significantly lower in AD when compared to controls (Fig. 1B-C), while reads number for the *COMMD3* or *COMMD3-BMI1* isoforms were not significantly different (Fig. 1B-C). In contrast to AD, reads number for *BMI1* were not significantly different in vascular dementia and mixed dementia samples (Fig. S1A). Reduced *REST*, *BRCA1* and *LRP6* mRNA and/or protein levels were reported in AD brains [176-178]. However, reads number for these transcripts were not different between control and AD brains (Fig. S1B). Interestingly, *BMI1* reduction in human cortices, as measured by RNA-seq, strongly correlated with p-Tau accumulation (Fig. 1D). *BMI1* reduction in AD was furthermore confirmed by real time RT-PCR using frozen brain samples (hippocampus) and distinct primer-pairs covering the *BMI1* cDNA (Fig. 1E and Fig. S1C-D).

Using a specific antibody (Fig. S1E) and immuno-histochemistry, we observed robust nuclear expression of BMI1 in NeuN-positive pyramidal neurons in control samples (Fig. 1F). In contrast, BMI1 expression was reduced in AD pyramidal neurons (Fig. 1F). Lipofuscin accumulation was observed in both control and AD neurons (Fig. 1F-blue arrows). Using

immuno-blot analysis, it was found that BMI1 levels were significantly reduced in the AD hippocampus (n = 5, median age of 82 years) when compared to controls (n = 3, median age of 87 years) (Figs. 1G and S1F, and Table S1). In contrast, BMI1 transcript and protein levels were unaffected in the FAD hippocampus (n = 4, median age of 61 years) when compared to controls (n = 3, median age of 59 years) (Fig. 1G and I, Table S1 and data not shown).

AD pathology ultimately spreads to all cortical areas [164]. Using frontal cortex extracts and a second specific antibody (Fig. S1G), we observed that BMI1 expression was significantly reduced in AD cortices (n = 5, median age of 87 years) when compared to age-match controls (n = 5, median age of 87 years) (Fig. 1H-I and Table S1). Histone H2A is the main target of BMI1/RING1a/b biochemical activity [169, 170]. $H2A^{ub}$ levels were significantly reduced in AD but not in old controls or in FAD (Figs. 1G-H and S1H). Notably, BMI1 protein levels were not significantly altered in the frontal cortex of patients with frontotemporal dementia (FTD), Lewy body dementia (LBD), Pick's disease, progressive supranuclear palsy (PSP) or Korsakoff syndrome (Figs. 1I and S1I). Using a third specific BMI1 antibody (Fig. S1J), we found that chromatin-bound BMI1 and $H2A^{ub}$ were enriched at the *INK4A/ARF* locus in the non-demented old cortex but depleted in the AD cortex (Fig. 1J). This revealed that *BMI1* expression is preferentially reduced in AD brains.

BMI1 expression is reduced in iPSC-derived AD neurons

Using a protocol of neural induction "by default" [125], we differentiated iPSCs derived from control and sporadic AD patients into cortical neurons (Fig. S2A). As expected, neurons from the published AD line (sAD1) presented intra-neuronal accumulation of p-Tau and amyloid (Fig. 2A) [134]. Using MAP2 labeling, we observed that sAD1 neurons had shorter dendrites,

covering a smaller surface area and with less branching and strength than control neurons (Fig. 2A-B). sAD1 neurons also displayed a greater percentage of apoptotic nuclei (Fig. 2C) and a ~3-fold increase in Aβ42 secretion when compared to control neurons (Fig. 2D) [134]. Neurons from 2 additional independent AD lines (sAD3 and sAD4) also showed high levels of secreted Aβ42 (Fig. 2E). Notably, single cell and whole cell extract analyses revealed reduced *BMI1* mRNA and protein levels in iPSC-derived neurons originating for 4 unrelated AD patients (Figs. 2F-H and S2B) [131]. Reduced BMI1 level in the nucleus of sAD neurons was not a consequence of BMI1 protein sequestration into insoluble p-Tau aggregates present in the neuronal soma, axon or dendrites (Fig. S2C-D). To test if reduced BMI1 expression in AD neurons could result from Aβ42 toxicity, we over-expressed mutant *APP* and *PSEN1* in human neurons [175]. Despite massive Aβ42 secretion by *APP/PSEN1* neurons (Fig. 2I), BMI1 and $H2A^{ub}$ levels remained unaltered (Figs. 2J and S2E). Bmi1 expression was also unaltered in the hippocampus, cortex or dentate gyrus of 6 month-old $APP^{swe}/MAPT^{P301L}/PSEN1^{M146V}$ (3xTG) mice, which present amyloid plaques and neurodegeneration at this age and are considered as a model of FAD (Figs. 2K and S2F) [179].

BMI1 inactivation in human neurons induces a gene-expression signature related to AD

To test if BMI1 deficiency could result in AD-like pathology, we knockdown BMI1 in cortical neurons produced from the differentiation of the human embryonic stem cell line HUES9. This cell line is homozygous for the *APOE3* allele. After 24 days of neural induction, progenitors were dissociated and infected with a lentivirus expressing a small hairpin RNA (shRNA) with a scramble sequence (shCTL + Hygro-/GFP) or an shRNA directed against BMI1 (shBMI1 + Hygro/GFP), prior to differentiation in post-mitotic neurons (Fig. S3A-B) [162]. Presence of the

BMI1 protein was confirmed in neural progenitors at the time of viral infection (Fig. S3C). Two weeks later, the expression of BMI1 and $H2A^{ub}$ was notably reduced in shBMI1 neurons (Fig. S3A-B). The majority of differentiated cells were positive for the anterior neural/cortical marker FOXG1, the pan-neural markers β-III-tubulin, MAP2 and NeuN, and the glutamatergic, GABAergic and cholinergic markers vGLUT1, GABA and ChAT respectively (Fig. 3A). Morphometric analyses using the PMI index revealed that ~60% of βIII-tubulin neurons were cortical pyramidal neurons (Fig. 3B) [125, 180]. Gene expression profile analysis further confirmed efficient neuronal differentiation (Fig. 3C). Axonal swellings are present at the earliest stages of AD [181]. Notably, dystrophic neurites and axonal swelling could be readily observed 7-15 days after BMI1-knockdown (Figs. 3D-F and S3D). GABA-positive and vGLUT-positive neurons having dystrophic neurites and axonal swellings together with disrupted βIII-tubulin labeling along axonal segments were also observed (Fig. 3D-F). Since BMI1 operates as a transcriptional repressor, we extracted most up-regulated genes in shBMI1 neurons when compared to controls. Unbiased gene ontology analysis (P-value<0,01) revealed that these were predominantly associated with AD-associated signaling pathways, namely Cadherin, WNT and AD-presenilin [182-184] (Fig. 3G). Of the top 14 most up-regulated genes in shBMI1 neurons, only few showed BMI1 enrichment at their promoter when using BMI1 ChIP-seq analysis performed on neuronal progenitors. Notably however, many of the up-regulated genes encoded chaperones preventing protein misfolding, suggesting a cellular response to proteotoxic stress [185] (Table S2). This suggested that BMI1 inactivation in human neurons resulted in the apparition of pathology possibly related to AD.

BMI1 inactivation in human neurons recapitulates AD pathological hallmarks

AD-associated p-Tau can sequester normal Tau and lead to tangle formation and microtubule disassembly [186]. Using PHF1, we observed p-Tau immuno-reactivity in shBMI1 neurons in both axonal (labeled with NF-H) and MAP2-positive dendritic compartments (Fig. 4A-C and not shown). Consistently, axonal segments where vGLUT1 or □III-tubulin distribution was perturbed also presented focal accumulations of p-Tau (Fig. 4B). Diffuse PHF1 immuno-reactivity was also observed within axonal swellings (Fig. 4B-inset). In contrast, PHF1 weakly decorated the axons of some control neurons (Fig. 4A-B). Notably, the severe Tau pathology and reduced $H2A^{ub}$ level were both rescued by ectopic expression of an shRNA-resistant BMI1 construct introduced 15 days after BMI1 knockdown, thus excluding off-target effects (Fig. S4A-B). p-Tau accumulation was also observed using another antibody (Fig. S4C). Using distinct antibodies, including NU1, which recognizes oligomeric amyloid [133, 187], we observed robust beta-amyloid immuno-reactivity in the soma and neurites of BMI1-deficient neurons when compared to controls (Figs. 4D-E). Amyloid immuno-reactivity in BMI1-deficient neurons was reduced upon exposure to BACE inhibitor (BSI) (Fig. S4D). Amyloid accumulation was however not detected in non-neuronal cells deficient for BMI1 (Fig. S4E). Presence of the soluble Aβ42 peptide was detected using ELISA in the control neuronal culture media, but the relative amyloid concentration was significantly higher in BMI1-deficient cultures (Fig. 4F). The frequency of apoptotic nuclei was also higher in shBMI1 neurons, altogether revealing ongoing degeneration (Fig. 4G). To distinguish between developmental and neuronal maintenance functions of BMI1, we inactivated BMI1 in 15 day-old post-mitotic Ki67-, Nestin- and PCNA-negative neurons using polymeric delivery (Fig. S5A-D). This resulted in the accumulation of p-Tau and beta-amyloid and in neurodegeneration (Fig. S5E-F).

It was shown that neuronal cultures over-expressing FAD genes and grown in 3D could generate amyloid plaques and Tau tangles [175]. By adapting this method to our model system (Fig. S5G), we found that BMI1 knockdown resulted in the formation of large extra-cellular amyloid accumulations of up to 60μm, as revealed using amyloid antibodies or the auto-fluorescent compound K114, which binds amyloid fibrils and plaques (Fig. 5A). These conditions also resulted in the formation of diffuse extra-cellular p-Tau deposits (Fig. 5Bi) and of large p-Tau accumulations in the neuronal soma (Fig. 5B-C). The presence of p-Tau aggregates was observed in degenerating ChAT-positive cholinergic neurons, a neuronal cell type severely affected in AD (Fig. 5B) [188]. BMI1-deficient cultures were also characterized by the accumulation of amyloid species of ~37kDa, ~14kDa and ~4kDa as revealed by immuno-blot using whole cellular extracts (Fig. 5D). We also found that in contrast to control cultures, which underwent pre- (synaptophysin) and post- (PSD-95) synaptic maturation, BMI1 deficient neuronal cultures failed to express significant amounts of synaptophysin and PSD-95 (Fig. 5E).

To further validate our findings, we used a genetic approach, the Clustered Regularly Interspaced Short Palindromic Repeats (CRISPR)/CRISPR-associated (Cas) system (CRISPR/Cas), to introduce a bi-allelic null deletion at the *BMI1* locus [189]. A plasmid encoding for the Cas9 nuclease together with a control guide RNA (sgRNA-Ctrl) or a guide RNA targeting *BMI1* exon 1 (sgRNA-BMI1) were transfected in 30 day-old human post-mitotic neurons using a polymeric delivery agent (Fig. 6A). 10 days later, neurons were analyzed by genomic PCR. This revealed the presence of a ~400bp deletion in exon I of *BMI1* ($BMI1^{KO}$) only in neurons exposed to sgRNA-BMI1 (Fig. 6B). Notably, loss of BMI1 activity was observed in greater than 90% of cells in $BMI1^{KO}$ cultures, as revealed using antibodies against BMI1 and $H2A^{ub}$ (Fig. 6C-D). In contrast to other methods, this approach did not require viral

infection, drug-selection and/or cell sorting [190]. Notably, *BMI1*^{KO} neuronal cultures were characterized by the presence of piknotic nuclei and the accumulation of p-Tau and beta-amyloid (Fig. 6E-F). p-Tau immuno-reactivity was furthermore visualized at the single cell level in H2A^{ub}-low (*BMI1*^{KO}) neurons, but not in H2A^{ub}-high (wild type) neurons, suggesting a cell autonomous effect (Fig. 6E). To test the role of BMI1 in synaptic maintenance, *BMI1* knockout was induced in 60 days old neurons, which were analyzed 7 days later. While immuno-reactivity for PSD-95 and synaptophysin was observed in control neurons, it was strongly reduced in *BMI1*^{KO} neurons (Fig. 6G-H), revealing that BMI1 is required for the maintenance of synaptic integrity. Secretion of Aβ42 was also highly increased in the *BMI1*^{KO} media were compared to the control media (Fig. 6I).

BMI1 deficiency leads to activation of a *MAPT*, GSK3b and p53 triad

To get insight into the disease mechanism, we performed immuno-blot analyses using human neuronal culture extracts. BMI1 inactivation resulted in elevated APP and BACE1 levels when compared to controls, while BMI1 over-expression resulted in the opposite trend (Fig. 7A and S6A). Notably, accumulation of amyloid species of ~60kDa, ~37kDa and ~14kDa were uniquely observed in the BMI1-deficient cultures (Fig. 7A). Likewise, we found a significant increase in Tau, p-Tau, GSK3β, p-GSK3β (Ser9), p-p53 (Ser15) and □-Actin levels in BMI1-deficient neurons (Figs. 7A and S6A). Conversely, BMI1 over-expression in naive neurons could reduce baseline levels of Tau, p-Tau, GSK3β, p-GSK3β, p-p53 and β-Actin (Fig. 7A and S6A). Notably, the elevation in monomeric β-Actin levels correlated with F-Actin bundling in BMI1 knockdown neurons, as visualized using phalloidin staining (Fig. 7B). F-Actin bundling is present in AD and tauopathies and is largely dependent on cross-linking activities of Tau with

F-Actin and Tubulin dimers [191]. Considering the above findings, we analyzed the expression of known AD-related genes using real time RT-PCR. *CDKN2A(p16^{Ink4a})* and *CDKN1A(p21^{Cip1})* were used as canonical target genes repressed by BMI1 [162, 174]. Of the many tested, only *MAPT* (encoding for Tau) and *LRP2* were increased upon BMI1 deficiency (Fig. S6B). Despite elevation in monomeric β-Actin, *ACTB* gene expression was unaffected (not shown). The reduced *APP* expression observed in BMI1 knockdown neurons was also present in AD brains (Fig. S6C). Since *MAPT* duplication is possibly pathogenic [192], we investigated negative regulation of *MAPT* by BMI1. Upon BMI1 over-expression in naive neurons, *MAPT* expression was significantly reduced (Fig. S6D). Furthermore, BMI1 and H2A^{ub} were enriched at the chromatin on several portions of the *MAPT* locus -including the promoter region- in both cultured neurons and frozen human brain samples (Fig. S6E-G), suggesting transcriptional repression of *MAPT* by BMI1.

BMI1/RING1 can modulate the DNA damage response and promote p53 degradation through transcription-dependent and -independent mechanisms [163, 171, 193, 194]. GSK3β can phosphorylate Tau at Ser396/404, and GSK3β expression and activity are regulated by translational and post-translational mechanisms [195]. Considering this, we surmised that transcription-independent mechanisms could also explain some of the observed pathologies. We tested chemical inhibitors of DNA damage response proteins, p53 or GSK3β for their ability to rescue or not the BMI1-deficient phenotype. Caffein (a non-specific DDR inhibitor), DNA-PKi (NU7026) or p53i (Pifithrin) could all improve amyloid and p-Tau immuno-reactivity, but not apoptosis (not shown). In contrast, ATM/ATRi (CGK733) or ATMi (KU55933) primarily rescued apoptosis, while GSK3βi (CHIR99021) could improve all 3 pathological parameters. Notably, co-treatment of BMI1-deficient neurons with CHIR99021 and Pifithrin rescued

amyloid and p-Tau pathology as well as F-Actin bundling (Fig. 7B). We next introduced a GSK3β-expressing plasmid in naive neurons and exposed them or not to the MDM2 inhibitor Nutlin, which can promote p53 stabilization (Fig. 7C) [196]. While Nutlin or GSK3β alone resulted in modest p-Tau and amyloid immuno-reactivity, the addition of both could largely mimic the BMI1-deficient phenotype (Fig. 7D).

These above observations revealed that p53 stabilization could aggravate GSK3β-mediated pathology, but the underlying mechanism remained unclear. Defective proteostasis can promote neurodegeneration [197, 198] and levels of polyubiquitin at lysine 48 (polyUb-K48), which marks proteins for proteosomal degradation [199] are increased in AD neurons [200]. Heat shock factor 1 (HSF1), the master regulator of proteostasis, can prevent protein misfolding and amyloid fibrills accumulation in tumor cells, and *HSF1* is down-regulated following p53-induced senescence [201, 202]. Notably, we found that *HSF1* expression was reduced and that levels of polyubiquitin-bound proteins and of the multiubiquitin chain 4 (Ub4) were increased in BMI1 knockdown neurons (Fig. S7A-B). When primary human cells were treated with the proteasome inhibitor MG132 and/or with Nutlin [201], we found that Nutlin could induce accumulation of polyUb-K48 chains and of p53, but to a lesser extent than MG132 (Fig. S7C). When MG132 and Nutlin were combined, this resulted in an additive effect on K48-polyUb chains and p53 accumulation (Fig. S7C). This suggested that p53 stabilization and/or MDM2 inhibition can perturb proteostasis.

Several pharmaceutical inhibitors targeting the amyloid cascade have been developed in order to treat AD. We thus analyzed the capacity of BSI, γ-secretase inhibitor (GSI) and γ-secretase modulator (GSM) to rescue the BMI1-deficient AD phenotype [175]. BSI could reduce apoptosis and amyloid immuno-reactivity, but only partially that of p-Tau and F-Actin

(Fig. 7E). On the other hand, GSI and GSM did not improve most pathological parameters (Fig. 7E). While GSI reduced p-Tau intensity, the re-localization of p-Tau to the neuronal soma suggested tangle formation (Fig. 7E). Furthermore, amyloid immuno-reactivity reached saturation levels upon GSI treatment (Fig. 7E) [203]. Taken as a whole, these results revealed that BMI1 deficiency in human neurons results in activation of a *MAPT*, GSK3β and p53 pathological triad that cannot be blocked using amyloid cascade inhibitors (see model in Fig. S7D).

DISCUSSION

We have found that BMI1 brain expression is preferentially reduced in AD but not in FTD and LBD, which are also characterized by severe cortical neurodegeneration, suggesting that reduced BMI1 levels in AD cannot be simply attributed to neuronal loss. Hence, BMI1 gene expression was reduced even when normalized to that of neural-specific genes such as *FOXG1* or *NEUROD1*. BMI1 expression was also reduced in AD pyramidal neurons *in situ* and in cultured AD neurons produced from the differentiation of patient's iPSCs. BMI1 expression was unaffected in FAD brains, in human neurons over-expressing mutant *APP/PSEN1* and in brain extracts from 3xTG mice, suggesting that amyloid-related toxicity cannot explain BMI1 reduction in sporadic AD. BMI1 knockdown or knockout in human post-mitotic neurons could induce pathologies characteristic of AD, altogether distinguishing BMI1 developmental role from neuronal maintenance function.

Our molecular analyses revealed that BMI1 could repress *MAPT* transcription, suggesting that loss of BMI1 can result in a tauopathy independently of the APP/amyloid pathway. Hence, BSI prevented apoptosis and C99/amyloid accumulation in BMI1-deficient neurons, but only partially rescued p-Tau and F-Actin levels, suggesting the presence of two parallels disease-mediating pathways (see model in Fig. S7D). However, these pathways can be interconnected in particular contexts since inhibition of γ-secretase activity, which results in C99 accumulation, can promote Tau accumulation by a yet undefined mechanism [203]. In contrast with BSI, GSI or GSM, treatment of BMI1-deficient neurons with the GSK3β/p53 inhibitors could largely rescue the AD phenotype. Furthermore, combining GSK3β over-expression and p53 stabilization could mimic the AD neuronal phenotype, supporting the notion

that the *MAPT*, GSK3β and p53 triad is downstream of BMI1 in the pathological cascade (Fig. S7D).

BMI1 is a proto-oncogene overexpressed in many cancers, and BMI1 inactivation generally induces cellular senescence [173]. We speculate that abnormal BMI1 down-regulation in the ageing human brain may be in response to an oncogenic insult, thus providing at first protection against cancer [204]. BMI1 down-regulation could be also exacerbated by genetic, epigenetic and/or environmental factors in some individuals until its levels reach a pathological threshold. It is also noteworthy that across GWAS studies, no SNP on *BMI1* were reported to be associated with AD. Since BMI1 expression in non-demented elderly brains (median age of 87 years) was in general robust, it appears that BMI1 down-regulation during ageing is very modest in normal physiological conditions. Thus, brain ageing alone is not sufficient to trigger *BMI1* down-regulation. Further work will be required to decipher by which mechanism *BMI1* is down-regulated and weather this anomaly occurs before or at the time of AD onset. Restoration of *BMI1* activity could represent a novel therapeutic modality for AD.

METHODS SUMMARY

Post-mortem frozen human samples were provided by the Douglas Hospital and Banner Brain Banks and used according to the Maisonneuve-Rosemont Hospital Ethic Committee. Human embryonic stem cells were used in accordance with Canadian Institute Health Research (CIHR) guidelines and approved by the "Comité de Surveillance de la Recherche sur les Cellules Souches" (CSRCS) of the CIHR and Maisonneuve-Rosemont Hospital Ethic Committee. The complete method is available in Supplementary Informations.

Polymeric delivery of plasmids in cortical neurons

HA-GSK3beta in the pcDNA3 plasmid was obtained from Addgene (Cat#14753). A construct for the overexpression of a shResistant BMI1 were generated by permutation of 21 nucleotides from *BMI1* cDNA sequence (Target of the BMI1 shRNA) while keeping the amino acid sequence (WT sequence: CCTAATACTTTCCAGATTGAT; Permutated sequence: CCCAACACATTTCAAATAGAC). This modified cDNA sequence was then inserted into pcDNA3.1 backbone (Genescript). To investigate BMI1 expression in response to amyloid over-production, CTL neurons were tranfected by a IRES polycistronic vector overexpressing a double mutant human APP gene (K670N/M671L (Swedish) and V717I (London)) and PSEN1 with ΔE9 mutation (courtesy of Dr. Doo Yeon Kim). Neurons were transfected using Mirus TransIT-X2 (Cat#MIR6003) according to manufacturer instructions.

BMI1 inactivation in cortical neurons by CRISPR/Cas9

BMI1 inactivation using CRISPR/Cas9 were carried out by the polymeric delivery of a Cas9-expressing plasmid (Dharmacon #CAS10140), a synthetic guide RNA (sgRNA) Scramble (Dharmacon #U-007501) or complementary to *BMI1* (Target: AACGTGTATTGTTCGTTACC) and a synthetic trans-activating crRNA (Dharmacon #U-002005) using Mirus TransIT-X2 (Cat#MIR6003) according to manufacturer instructions.

Statistical analysis

Statistical analysis was performed using Graphpad software (Prism 6) excepted for DNA microarray analysis. Statistical differences were analyzed using Student's *t*-test for unpaired samples. In all cases, the criterion for significance (*P* value) was set as mentioned in the figures. When comparisons were made using independent samples of equal size and variance following a normal distribution, significance was assessed using an unpaired two-sided Student's t-test. Where several groups were compared, significance was assessed by ANOVA and adjusted for multiple comparisons using the Bonferroni correction. DNA microarray data analysis was performed using FlexArray software (version 1.6.2). Data were pre-processed using lumi package including a probe-intensity normalization, quality control and probe-gene mapping. Differential expression was assayed using log2 Fold Change statistical algorithm or one-way ANOVA with a *P*-value cutoff at 0.05. For gene ontology, a FDR cutoff of 0.01 was applied.

AUTHOR CONTRIBUTIONS

Conceived and designed: GB, AF

Performed the experiments: JEH, AF, MA

Analyzed the data: GB, AF, MA, JEH, KF

Wrote the paper: GB, AF

ACCESSION NUMBERS

Transcriptomic analysis: GSE113232

BMI1 ChIP-seq: GSE33912

ACKNOWLEDGMENT

This work was supported by grants from the Canadian Institute of Health Research and National Science and Engineering Research Council of Canada. A.F. and J.E.H. were supported by fellowships from the Molecular Biology Program of Université de Montréal. We acknowledge the Allen brain institute for providing the RNA-seq data through the aging, dementia and TBI study.

DECLARATION OF INTERESTS

G.B. and A.F. are founders of StemAxon™ and members of its scientific advisory board.

Flamier *et al.* 2018

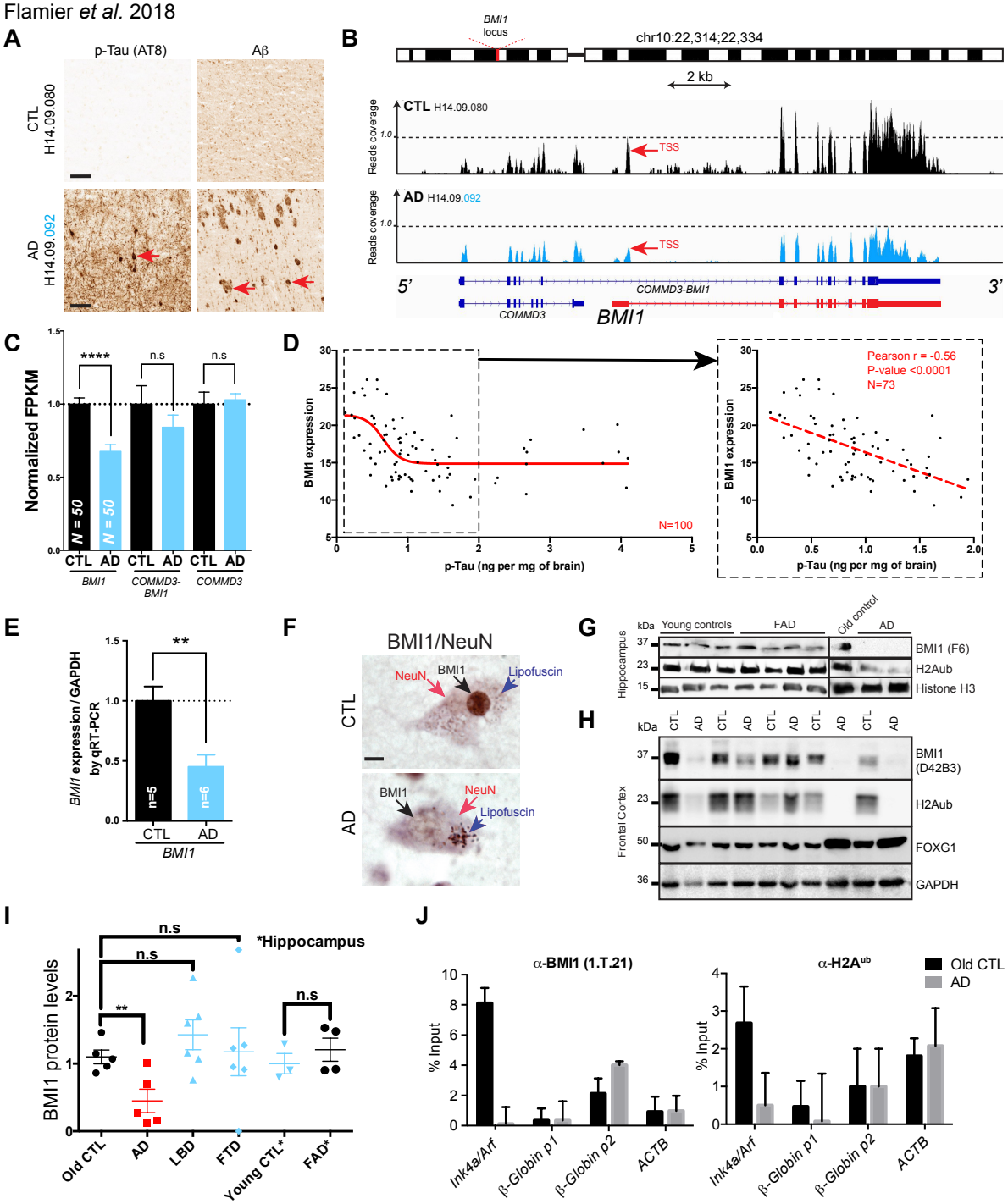

Figure 1

Figure 1. *BMI1* expression is reduced in AD brains but not in other dementias. See also Figure S1 and Table S1.

(A-D) RNA-seq analysis obtained through the Allen aging, dementia and TBI study.

(A) IHC representative images showing p-Tau (AT8) accumulation and presence of amyloid plaques on AD patient's brains selected for the RNA-seq study. Red arrow in p-Tau staining indicates a neuronal Tau tangle. Red arrows indicate a diffuse extracellular amyloid deposition and a dense amyloid plaque. Scale bar: 40μm.

(B) Normalized RNA-seq reads coverage throughout BMI locus in the cortex of a CTL and an AD patient characterized in A. Note the reduction of BMI1 specifically in the AD sample while the closest gene, *COMMD3* and the fusion *COMMD3-BMI1* are not affected as exemplified by red arrows.

(C) *BMI1, COMMD3* and *COMMD3-BMI1* normalized FPKM in the cortex of CTL (n=50) and AD patients (n=50). (****) $P<0.0001$; by Student's unpaired t-test.

(D) Correlations between *BMI1* levels in human cortices by RNA-seq and the quantity of phosphorylated Tau per mg of brain.

(E) *BMI1* gene expression levels in qPCR normalized to *GAPDH* in the hippocampus of CTL (n=5) and AD patients (n=6) from two independent sources (Douglas hospital and Banner health institute). (**) $P<0.01$; by Student's unpaired t-test.

(F) Immunostaining for BMI1 (black arrows) and NeuN (red arrows) on frontal cortex sections from age-matched control and AD patient. Note lipofuscin deposition (blue arrows). Scale bar: 8μm.

(G) Immunoblot on hippocampal extracts from young control (n=3), FAD (n=4) and AD (n=2) patients using clone F6 against BMI1.

(H) Immunoblot on frontal cortex from control (n=5) and AD (n=5) patients using clone D42B3 against BMI1.

(I) Quantification of normalized BMI1 protein levels in control, AD, fronto-temporal dementia (FTD), dementia with Lewy body (DLB), Pick's disease (PSP), Korsakoff's syndrome (KS) and FAD. All values are mean ± SEM. (**) $P<0.01$; by one-way ANOVA.

(J) ChIP-qPCR on control (#428; 89y) and AD (#1127: 88y) frontal cortex samples using IgG, $H2A^{ub}$ and Bmi1 clone 1.T.21 (ab14389) antibodies. N = 4 technical replicates. All values are mean ± SEM.

Flamier *et al.* 2018

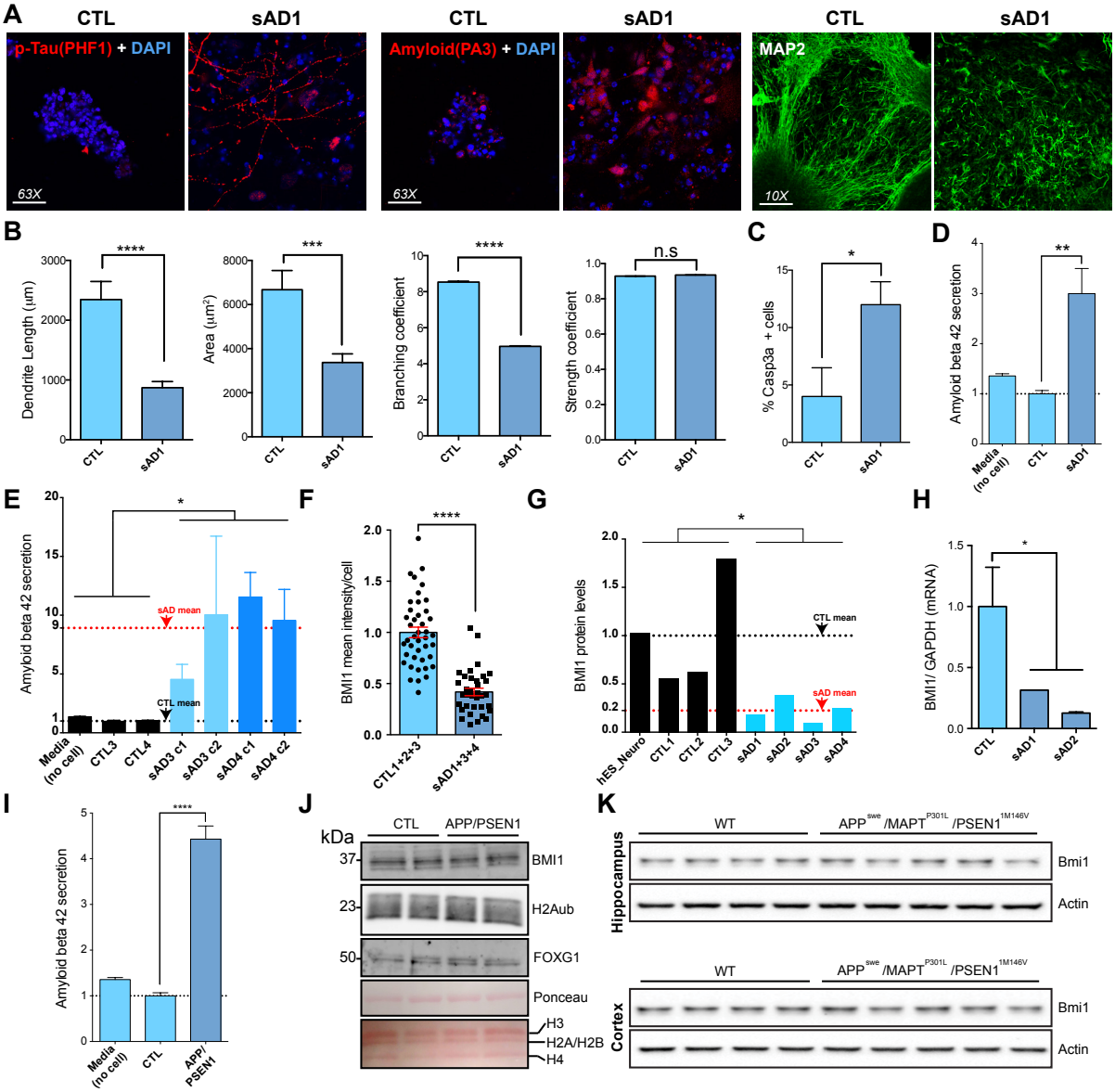

Figure 2

Figure 2. *BMI1* expression is reduced in sporadic AD models but not in FAD models. See also Figure S2.

(A) Cortical neurons obtained from control (CTL) and sporadic AD (sAD1) iPSCs and stained for p-Tau (PHF1), beta-amyloid (PA3) and MAP2. Note the accumulation of p-Tau and amyloid as well as the dendritic atrophy in sAD1 neurons. Scale bar: 40μm in p-Tau and beta-amyloid stainings. Scale bar: 100μm in MAP2 staining.

(B) Morphometric analysis of the dendrite's length, area, branching and strength in CTL (n = 99 dendrites from 4 independent differentiations) and sAD1 (n = 43 dendrites from 4 independent differentiations) neurons by using IMARIS platform. All values are mean ± SEM. (***) P< 0.001; (****) P< 0.0001 by Student's unpaired t-test.

(C) Quantification of activated caspase-3 positive cells in CTL (n = 4 from 2 independent differentiations) and sAD1 (n = 4 from 2 independent differentiations) neuronal populations. All values are mean ± SEM. (*) $P<0.05$ by Student's unpaired t-test.

(D) Secreted Aβ42 levels in CTL (n = 8; 4 biological replicates in 2 technical replicates) and sAD1 (n = 8; 4 biological replicates in 2 technical replicates) neurons by ELISA. Media not conditioned is used as negative control. All values are mean ± SEM. (**) $P<0.01$ by Student's unpaired t-test.

(E) Secreted Aβ42 levels in CTL3 (n = 4 in 2 technical replicates), CTL4 (n = 4 in 2 technical replicates), sAD3 (n = 4 in 2 technical replicates for each clone c1 and c2) and sAD4 (n = 4 in 2 technical replicates for each clone c1 and c2) neurons by ELISA. Media not conditioned is used as negative control. All values are mean ± SEM. (*) $P<0.05$ by Student's unpaired t-test.

(F) Quantification of BMI1 fluorescence intensity in neurons from 3 different CTL iPSC lines (n = 4 from 2 independent experiments with 2 independent clones for CTL2 and CTL3) and 3

different sAD iPSC lines (n = 4 from 2 independent experiments with 2 independent clones for sAD3 and sAD4). All values are mean ± SEM. (****) *P*<0.0001 by Student's unpaired t-test.

(G) Quantification of BMI1 protein levels in CTL (n=4 independent cell lines from 4 individuals including 1 hESC line) and sAD (n=6 independent cell lines from 4 individuals) neurons. FOXG1 is used as loading control. All values are mean ± SEM. (*) P<0.05 by Student's unpaired t-test.

(H) *BMI1* gene expression levels in qPCR normalized to *GAPDH* on CTL (n = 2 independent cell lines from 2 individuals) and sAD (n = 2 independent cell lines from 2 individuals) neurons. All values are mean ± SEM. (*) *P*<0.05 by One-way ANOVA.

(I) Extracellular Aβ42 levels in CTL (n = 8; 4 biological replicates in 2 technical replicates) and *APP/PSEN1* (n = 8; 4 biological replicates in 2 technical replicates) neurons by ELISA. Media not conditioned was used as negative control. All values are mean ± SEM. (****) *P*<0.0001 by Student's unpaired t-test.

(J) Immunoblot on CTL neurons transfected with GFP-expressing plasmid (n = 2 independent differentiations) and CTL neurons transfected with the *APP/PSEN1*-expressing plasmid (n = 2 independent experiments) for BMI1, H2Aub and FOXG1.

(K) Immunoblot of 6 month-old WT and 3xTG mice (APP^{swe}/$MAPT^{P301L}$/$PSEN1^{M146V}$) using hippocampus (top) and cortical (bottom) extracts (n = 4 WT; n = 5 3xTG).

Flamier *et al.* 2018

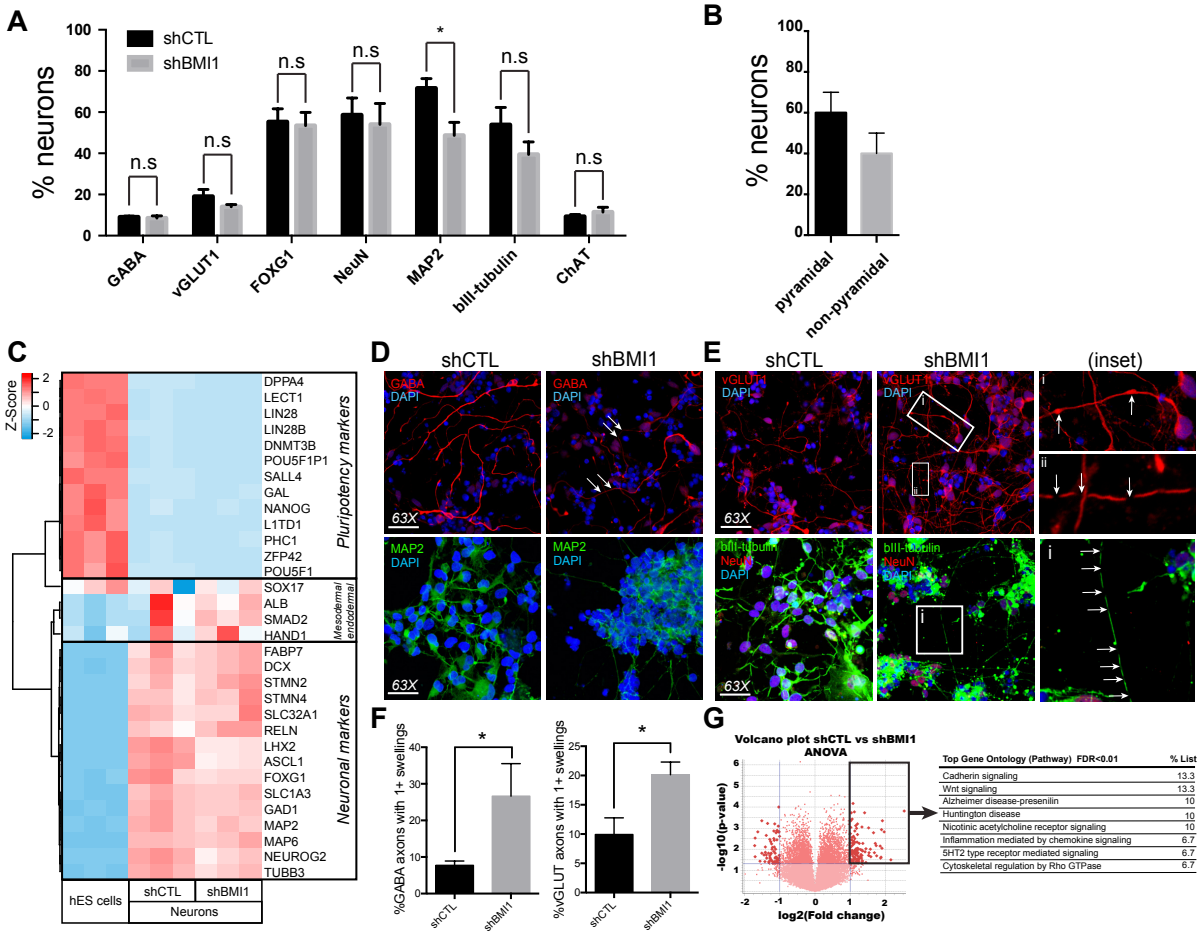

Figure 3

Figure 3. BMI1 deficiency in neurons induces a gene-expression signature related to AD. See also Figure S3 and Table S2.

(A) Quantification of GABA-, vGLUT1-, FOXG1-, NEUN-, MAP2-, bIII-tubulin- and ChAT-positive neurons in shCTL (n = 4) and shBMI1 (n = 4) cultures. All values are mean ± SEM. (*) $P<0.05$; by Student's unpaired t-test.

(B) Proportion of pyramidal neurons in the cultures (day 38).

(C) Normalized gene expression heatmap of hESC (n = 3 independent samples), shCTL neurons (n = 3 independent differentiations) and shBMI1 neurons (n = 3 independent differentiations) for neuronal, Meso/endodermal and pluripotency markers. Top: color code legend for expression level expressed as z-score.

(D) Expression of the neuronal markers GABA and MAP2 in shCTL and shBMI1 neurons (day 14). White arrows: distal axonal atrophy. Scale bar 40μm.

(E) Expression of the neuronal markers vGLUT1, bIII-tubulin and NeuN in shCTL and shBMI1 neurons (day 14). White arrows: axonal swelling and signal breaks along axonal segment. Scale bar: 40μm.

(F) Quantification of the percentage GABA positive (left) or vGLUT positive (right) axons containing 1 or more swellings in shCTL neurons (n=3 independent differentiations) and shBMI1 neurons (n = 3 independent differentiations) cultures. All values are mean ± SEM. (*) $P<0.05$; by Student's unpaired t-test.

(G) Left: volcano plot from ANOVA statistical analysis of shBMI1 versus shCTL neurons. Top right corner shows the significantly up-regulated genes in shBMI1 neurons. Right: gene ontology (PANTHER) analysis of up-regulated genes with FDR<0.01. See TableS2 for additional information on the significantly up-regulated genes in shBMI1 neurons.

Flamier *et al.* 2018

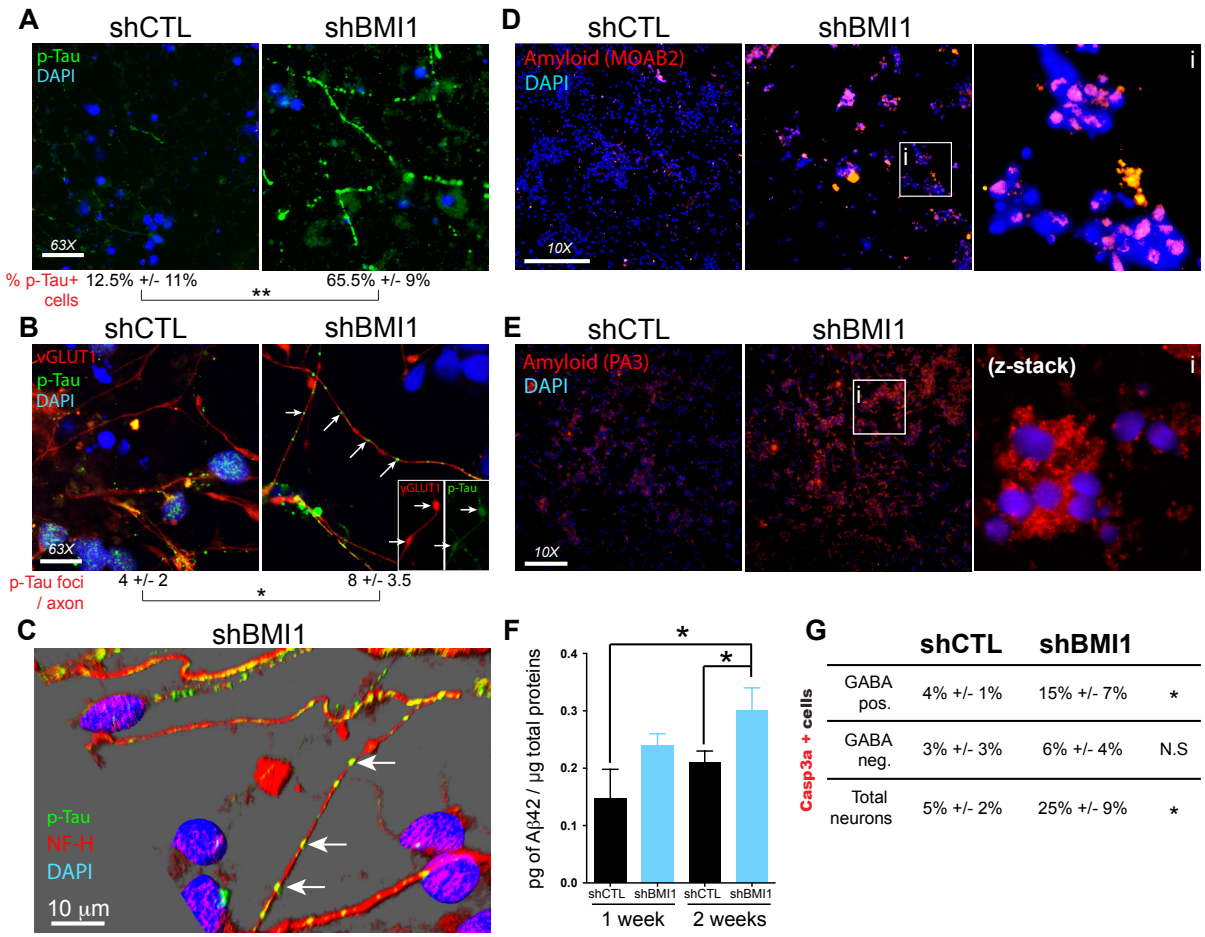

Figure 4

Figure 4. BMI1 deficiency in neurons results in p-Tau and amyloid accumulation. See also Figure S4 and S5.

(A) p-Tau (PHF1) accumulation in shBMI1 neurons but not in shCTL neurons (day 14). Scale bar: 40μm. Bottom: quantification of the percentage of p-Tau (PHF1) positive axons from shCTL (n = 3 independent differentiations) and shBMI1 (n = 3 independent differentiations) cultures. All values are mean ± SEM. (*) $P<0.05$; by Student's unpaired t-test.

(B) p-Tau (PHF1) accumulation in broken axonal segments of glutamatergic shBMI1 neurons (arrows), and co-localization of p-Tau with vGLUT1 in axonal swellings (arrows in the inset). Scale bar: 40μm. Bottom: quantification of the number of p-Tau (PHF1) foci per axons from shCTL (n = 3 independent differentiations) and shBMI1 (n = 3 independent differentiations) cultures. All values are mean ± SEM. (*) $P<0.05$; by Student's unpaired t-test.

(C) Axonal accumulation of p-Tau (PHF1) in shBMI1 neurons was revealed using the NF-H antibody (three-dimensional z-stacks reconstruction).

(D) Amyloid accumulation in shBMI1 neurons as compared to shCTL neurons using the MOAB2 antibody. Scale bars: 40μm.

(E) Amyloid accumulation in shBMI1 neurons as compared to shCTL neurons using the PA3 antibody. Scale bars: 40μm.

(F) Extracellular Aβ42 levels in shCTL (n = 3) and shBMI1 (n = 3) neurons by ELISA. All values are mean ± SEM. (**) $P<0.01$ by Student's unpaired t-test.

(G) Quantification of activated caspase-3 positive cells in GABA+, GABA- and total neuronal populations for shCTL and shBMI1 cultures. For total neuronal populations, only cells with a neuronal morphology in phalloidin staining were used. All values are mean ± SEM. (*) $P<0.05$ by Student's unpaired t-test.

Flamier *et al.* 2018

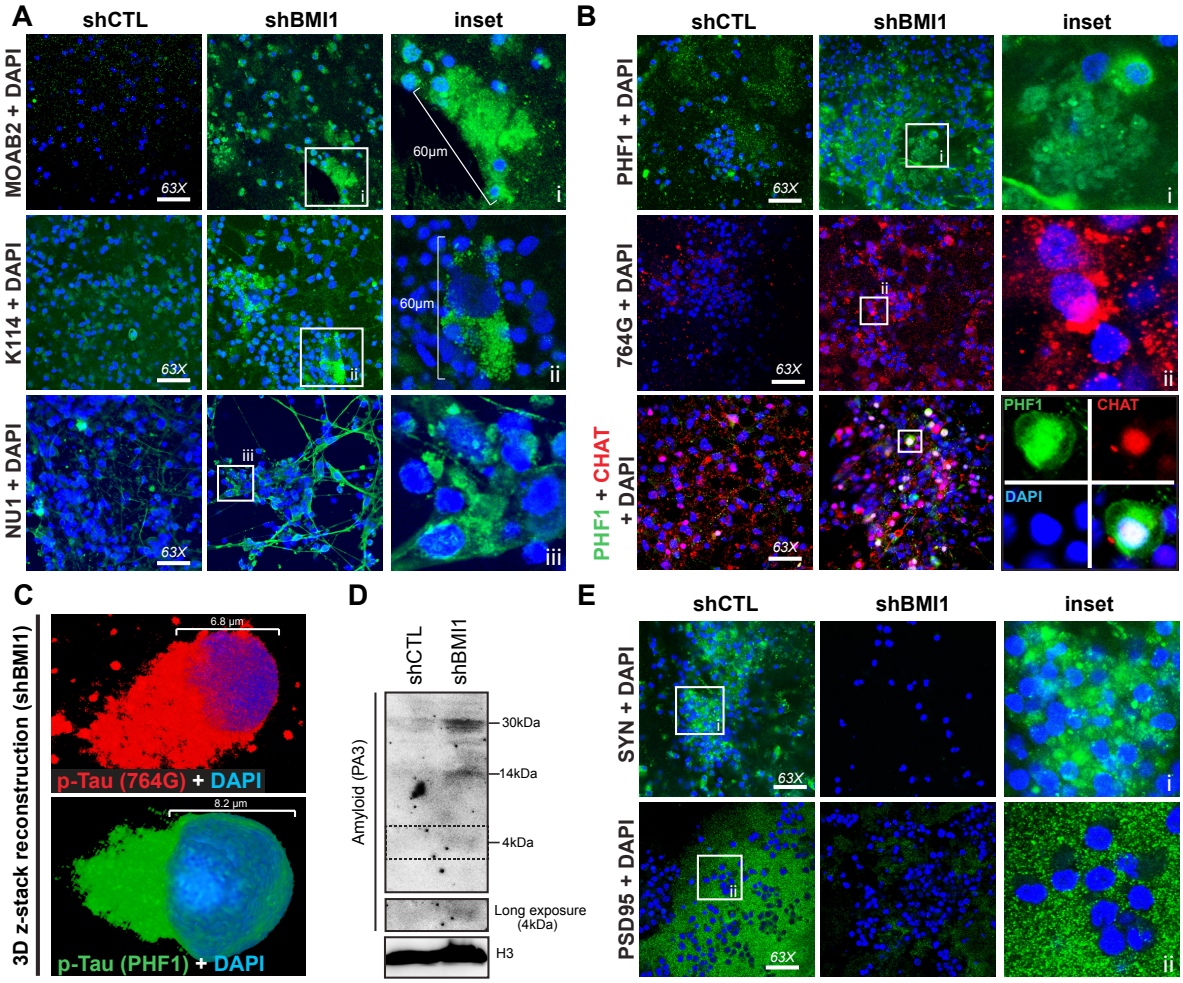

Figure 5

Figure 5. BMI1 deficiency results in the formation of p-Tau tangles and amyloid plaques. See also Figure S5.

(A) Amyloid plaques formation in shBMI1 neurons using MOAB2 or the auto-fluorescent compound K114. Deposition of oligomeric amyloid in the cytoplasm of BMI1 knockdown neurons as detected using the NU1 antibody. Scale bar: 40μm.

(B) Accumulation of p-Tau (PHF1 and 764G) as diffuse extra-cellular aggregates (i) or tangles (ii) in shBMI1 neurons in contrast to shCTL neurons. Co-staining with cholinergic neurons marker ChAT reveals degenerating ChAT-positive shBMI1 neurons with large p-Tau tangles. Scale bar: 40μm.

(C) Three-dimensional z-stacks reconstruction of p-Tau tangles located in the neuronal soma.

(D) Accumulation of aggregated amyloid (30kDa), C99 fragment (14kDa) and Aβ42 peptide (4kDa) in shBMI1 neurons lysates.

(E) Reduced immunoreactivity for synaptic markers synaptophysin (SYN) and PSD95 in shBMI1 neurons. Scale bar: 40μm.

Flamier *et al.* 2018

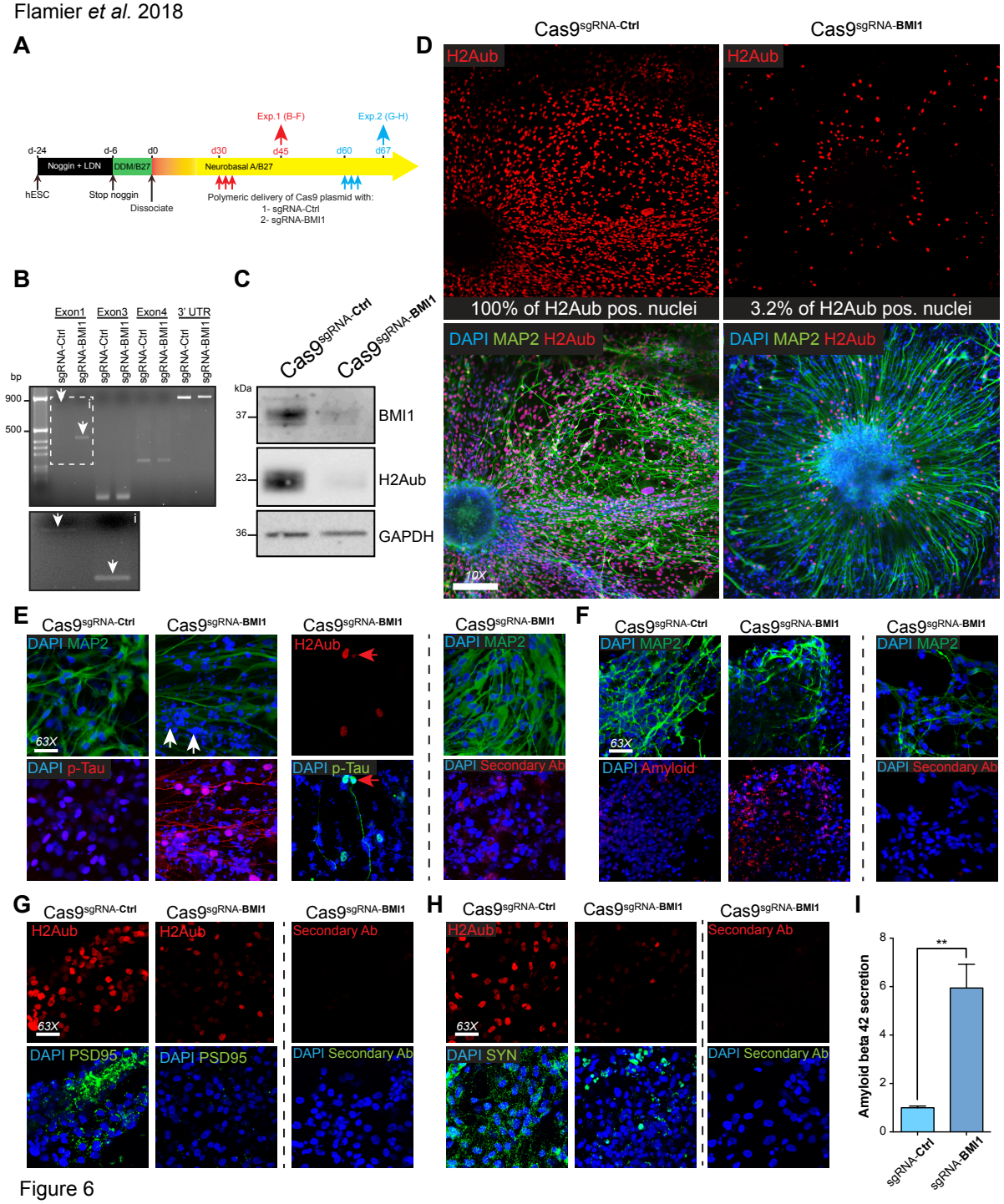

Figure 6

Figure 6. BMI1 knockout in human neurons results in AD pathologies.

(A) Experimental procedure for BMI1 inactivation in post-mitotic neurons. For panels B-F, cortical neurons were transfected three times with a plasmid for the overexpression of Caspase 9 nuclease, a synthetic guide RNA (sgRNA) Scramble or complementary to *BMI1* (Exon1) and a synthetic trans-activating crRNA after 1 month of maturation. Transfected neurons were analyzed after 2 weeks in culture. For panels G-H, cortical neurons were transfected three times after 2 months of maturation and analyzed after a week in culture.

(B) Genomic PCR on wild-type (sgRNA-Ctrl) and BMI1 *null* (sgRNA-BMI1) neurons at 4 different localizations of BMI1 locus. Note the deletion on Exon1 (white arrows) but not in Exon3, Exon4 or 3' end of the gene. Inset shows a magnification of the bands observed for exon1.

(C) Immunoblot on sgRNA-Ctrl and sgRNA-BMI1 neurons for BMI1 and H2Aub.

(D) Immunofluorescence on sgRNA-Ctrl and sgRNA-BMI1 neurons for MAP2 and H2Aub. Note the reduction of H2Aub positive nuclei in sgRNA-BMI1 neurons. Scale bar: 100μm.

(E) p-Tau (PHF1) accumulation in sgRNA-BMI1 but not sgRNA-Ctrl neurons. Note the presence of piknotic nuclei in sgRNA-BMI1 (white arrows) and the accumulation of p-Tau specifically in neurons KO for BMI1 (red arrow). sgRNA-BMI1 neurons stained using the secondary antibody only was used to assay for possible non-specific background fluorescence.

(F) Amyloid (D9A3A) accumulation in sgRNA-BMI1 but not sgRNA-Ctrl neurons. sgRNA-BMI1 neurons stained using the secondary antibody only was used to assay for possible non-specific background fluorescence.

(G) Reduced immunoreactivity for post-synaptic marker PSD95 in sgRNA-BMI1 but not sgRNA-Ctrl neurons. sgRNA-BMI1 neurons stained using the secondary antibody only was used to assay for possible non-specific background fluorescence.

(H) Reduced immunoreactivity for pre-synaptic marker Synaptophysin (SYN) in sgRNA-BMI1 but not sgRNA-Ctrl neurons. sgRNA-BMI1 neurons stained using the secondary antibody only was used to assay for possible non-specific background fluorescence.

(E-H) Scale bar: 40μm.

(I) Extracellular Aβ42 levels in sgRNA-Ctrl (n = 8; 4 biological replicates in 2 technical replicates) and sgRNA-BMI1 (n = 8; 4 biological replicates in 2 technical replicates) neurons by ELISA. All values are mean ± SEM. (**) $P<0.01$ by Student's unpaired t-test.

Flamier *et al.* 2018

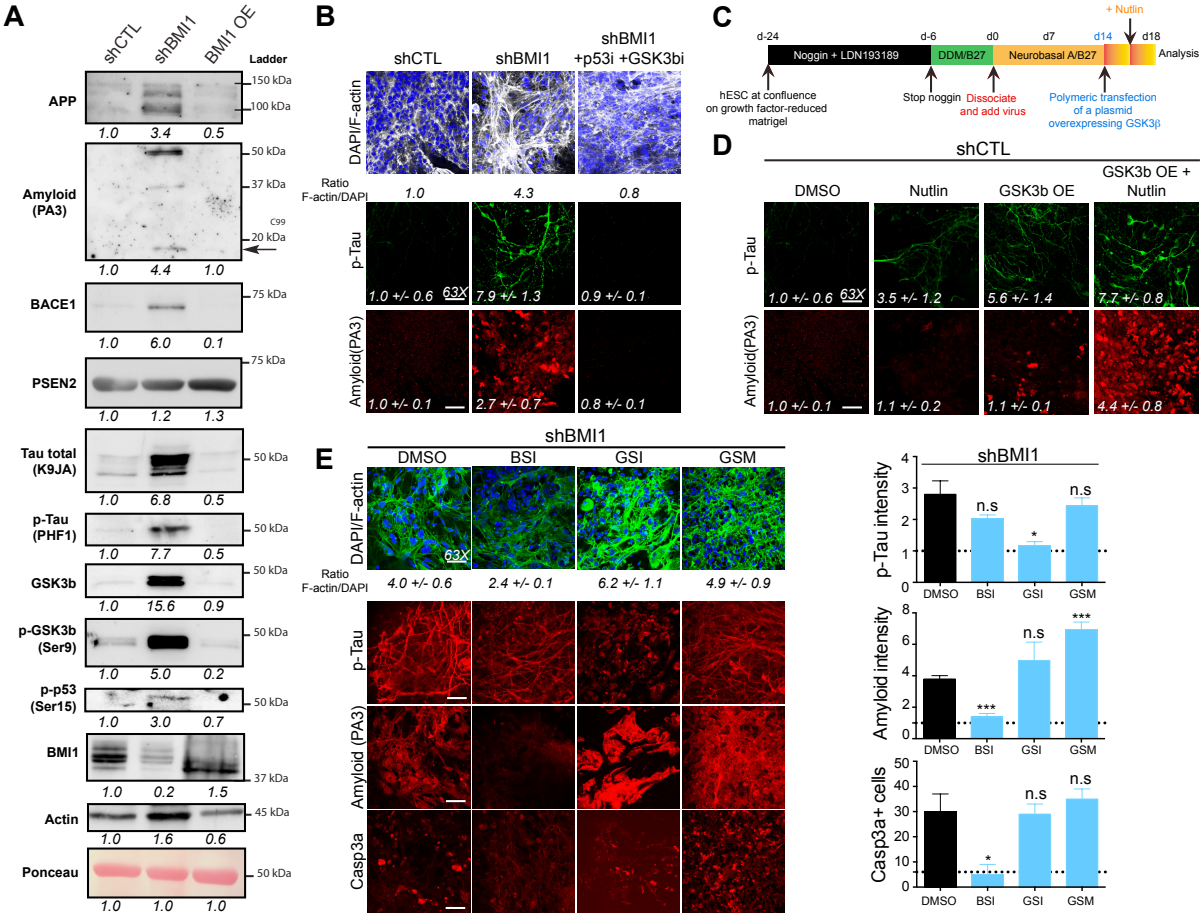

Figure 7

Figure 7. BMI1 deficiency activates the *MAPT*, GSK3b and p53 pathological triad. See also Figure S6 and S7.

(A) Immunoblots for AD-related proteins in shCTL, shBMI1 and BMI1 overexpressing (BMI1 OE) neurons. Protein expression ratios were established using Ponceau staining and where expression in shCTL neurons was set as 1.

(B) Confocal analysis of F-Actin (phalloidin), amyloid (PA3) and p-Tau (PHF1) in shCTL neurons and shBMI1 neurons treated with vehicle control, p53 and GSK3b inhibitors. Quantification was established using shCTL neurons set as 1. N = 3 independent differentiations for each group. All values are mean ± SEM. Scale bar: 40μm.

(C) Experimental scheme showing how control neurons over-expressing GSK3β (GSK3β OE) were treated with Nutlin or vehicle control.

(D) Confocal analysis of amyloid (PA3) and p-Tau (PHF1) in control and shCTL neurons over-expressing GSK3β (GSK3β OE) treated with Nutlin or vehicle control. Scale bar: 40μm. Quantification of pictures was established using shCTL (DMSO) neurons set as 1. N = 3 independent differentiations for each group. All values are mean ± SEM. Scale bar: 40μm.

(E) Confocal analysis of F-Actin (phalloidin), amyloid (PA3), p-Tau (PHF1) and activated caspase-3 (Casp3a) in shBMI1 neurons treated with DMSO, β-secretase inhibitor (BSI), γ-secretase inhibitor (GSI) or γ-secretase modulator (GSM). Quantification was established using shCTL neurons set as 1. All values are mean ± SEM. Scale bar: 40μm.

REFERENCES

Abdouh, M., Facchino, S., Chatoo, W., Balasingam, V., Ferreira, J., and Bernier, G. (2009). BMI1 sustains human glioblastoma multiforme stem cell renewal. J. Neurosci. *29*, 8884-8896.

Alonso, A.C., Grundke-Iqbal, I., and Iqbal, K. (1996). Alzheimer's disease hyperphosphorylated tau sequesters normal tau into tangles of filaments and disassembles microtubules. Nat. Med. *2*, 783-787.

Anckar, J., and Sistonen, L. (2011). Regulation of HSF1 function in the heat stress response: implications in aging and disease. Annu. Rev. Biochem. *80*, 1089-1115.

Ando, K., Uemura, K., Kuzuya, A., Maesako, M., Asada-Utsugi, M., Kubota, M., Aoyagi, N., Yoshioka, K., Okawa, K., Inoue, H., Kawamata, J., Shimohama, S., Arai, T., Takahashi, R., and Kinoshita, A. (2011). N-cadherin regulates p38 MAPK signaling via association with JNK-associated leucine zipper protein: implications for neurodegeneration in Alzheimer disease. J. Biol. Chem. *286*, 7619-7628.

Baskin, D.S., Browning, J.L., Pirozzolo, F.J., Korporaal, S., Baskin, J.A., and Appel, S.H. (1999). Brain choline acetyltransferase and mental function in Alzheimer disease. Arch. Neurol. *56*, 1121-1123.

Bihaqi, S.W., Schumacher, A., Maloney, B., Lahiri, D.K., and Zawia, N.H. (2012). Do epigenetic pathways initiate late onset Alzheimer disease (LOAD): towards a new paradigm. Curr Alzheimer Res *9*, 574-588.

Blennow, K., de Leon, M.J., and Zetterberg, H. (2006). Alzheimer's disease. Lancet *368*, 387-403.

Buchwald, G., van der Stoop, P., Weichenrieder, O., Perrakis, A., van Lohuizen, M., and Sixma, T.K. (2006). Structure and E3-ligase activity of the Ring-Ring complex of polycomb proteins Bmi1 and Ring1b. EMBO J. *25*, 2465-2474.

Calao, M., Sekyere, E.O., Cui, H.J., Cheung, B.B., Thomas, W.D., Keating, J., Chen, J.B., Raif, A., Jankowski, K., Davies, N.P., Bekkum, M.V., Chen, B., Tan, O., Ellis, T., Norris, M.D., Haber, M., Kim, E.S., Shohet, J.M., Trahair, T.N., Liu, T.*, et al.* (2013). Direct effects of Bmi1 on p53 protein stability inactivates oncoprotein stress responses in embryonal cancer precursor cells at tumor initiation. Oncogene *32*, 3616-3626.

Campisi, J. (2012). Aging, cellular senescence, and cancer. Annu. Rev. Physiol. *75*, 685-705.

Chatoo, W., Abdouh, M., David, J., Champagne, M.P., Ferreira, J., Rodier, F., and Bernier, G. (2009). The polycomb group gene Bmi1 regulates antioxidant defenses in neurons by repressing p53 pro-oxidant activity. J. Neurosci. *29*, 529-542.

Choi, S.H., Kim, Y.H., Hebisch, M., Sliwinski, C., Lee, S., D'Avanzo, C., Chen, H., Hooli, B., Asselin, C., Muffat, J., Klee, J.B., Zhang, C., Wainger, B.J., Peitz, M., Kovacs, D.M., Woolf, C.J., Wagner, S.L., Tanzi, R.E., and Kim, D.Y. (2014). A three-dimensional human neural cell culture model of Alzheimer's disease. Nature *515*, 274-278.

Culmsee, C., and Mattson, M.P. (2005). p53 in neuronal apoptosis. Biochem. Biophys. Res. Commun. *331*, 761-777.

Dammer, E.B., Na, C.H., Xu, P., Seyfried, N.T., Duong, D.M., Cheng, D., Gearing, M., Rees, H., Lah, J.J., Levey, A.I., Rush, J., and Peng, J. (2011). Polyubiquitin linkage profiles in three models of proteolytic stress suggest the etiology of Alzheimer disease. J. Biol. Chem. *286*, 10457-10465.

Elie, A., Prezel, E., Guerin, C., Denarier, E., Ramirez-Rios, S., Serre, L., Andrieux, A., Fourest-Lieuvin, A., Blanchoin, L., and Arnal, I. (2015). Tau co-organizes dynamic microtubule and actin networks. Sci Rep *5*, 9964.

Espuny-Camacho, I., Michelsen, K.A., Gall, D., Linaro, D., Hasche, A., Bonnefont, J., Bali, C., Orduz, D., Bilheu, A., Herpoel, A., Lambert, N., Gaspard, N., Peron, S., Schiffmann, S.N., Giugliano, M., Gaillard, A., and Vanderhaeghen, P. (2013). Pyramidal neurons derived from human pluripotent stem cells integrate efficiently into mouse brain circuits in vivo. Neuron *77*, 440-456.

Facchino, S., Abdouh, M., Chatoo, W., and Bernier, G. (2010). BMI1 confers radioresistance to normal and cancerous neural stem cells through recruitment of the DNA damage response machinery. J. Neurosci. *30*, 10096-10111.

Fraser, P.E., Yu, G., Levesque, L., Nishimura, M., Yang, D.S., Mount, H.T., Westaway, D., and St George-Hyslop, P.H. (2001). Presenilin function: connections to Alzheimer's disease and signal transduction. Biochem. Soc. Symp., 89-100.

Geula, C., Wu, C.K., Saroff, D., Lorenzo, A., Yuan, M., and Yankner, B.A. (1998). Aging renders the brain vulnerable to amyloid beta-protein neurotoxicity. Nat. Med. *4*, 827-831.

Hamilton, L.K., Dufresne, M., Joppe, S.E., Petryszyn, S., Aumont, A., Calon, F., Barnabe-Heider, F., Furtos, A., Parent, M., Chaurand, P., and Fernandes, K.J. (2015). Aberrant Lipid Metabolism in the Forebrain Niche Suppresses Adult Neural Stem Cell Proliferation in an Animal Model of Alzheimer's Disease. Cell Stem Cell *17*, 397-411.

Hand, R., Bortone, D., Mattar, P., Nguyen, L., Heng, J.I., Guerrier, S., Boutt, E., Peters, E., Barnes, A.P., Parras, C., Schuurmans, C., Guillemot, F., and Polleux, F. (2005). Phosphorylation of neurogenin2 specifies the migration properties and the dendritic morphology of pyramidal neurons in the neocortex. Neuron *48*, 45-62.

Hossini, A.M., Megges, M., Prigione, A., Lichtner, B., Toliat, M.R., Wruck, W., Schroter, F., Nuernberg, P., Kroll, H., Makrantonaki, E., Zouboulis, C.C., and Adjaye, J. (2015). Induced

pluripotent stem cell-derived neuronal cells from a sporadic Alzheimer's disease donor as a model for investigating AD-associated gene regulatory networks. BMC Genomics *16*, 84.

Ismail, I.H., Andrin, C., McDonald, D., and Hendzel, M.J. (2010). BMI1-mediated histone ubiquitylation promotes DNA double-strand break repair. J. Cell Biol. *191*, 45-60.

Israel, M.A., Yuan, S.H., Bardy, C., Reyna, S.M., Mu, Y., Herrera, C., Hefferan, M.P., Van Gorp, S., Nazor, K.L., Boscolo, F.S., Carson, C.T., Laurent, L.C., Marsala, M., Gage, F.H., Remes, A.M., Koo, E.H., and Goldstein, L.S. (2012). Probing sporadic and familial Alzheimer's disease using induced pluripotent stem cells. Nature *482*, 216-220.

Jackson, G.R., Wiedau-Pazos, M., Sang, T.K., Wagle, N., Brown, C.A., Massachi, S., and Geschwind, D.H. (2002). Human wild-type tau interacts with wingless pathway components and produces neurofibrillary pathology in Drosophila. Neuron *34*, 509-519.

Jacobs, J.J., Kieboom, K., Marino, S., DePinho, R.A., and van Lohuizen, M. (1999). The oncogene and Polycomb-group gene bmi-1 regulates cell proliferation and senescence through the ink4a locus. Nature *397*, 164-168.

Kanekiyo, T., Xu, H., and Bu, G. (2014). ApoE and Abeta in Alzheimer's disease: accidental encounters or partners? Neuron *81*, 740-754.

Kim, G., Meriin, A.B., Gabai, V.L., Christians, E., Benjamin, I., Wilson, A., Wolozin, B., and Sherman, M.Y. (2012). The heat shock transcription factor Hsf1 is downregulated in DNA damage-associated senescence, contributing to the maintenance of senescence phenotype. Aging Cell *11*, 617-627.

Kim, Y.E., Hipp, M.S., Bracher, A., Hayer-Hartl, M., and Hartl, F.U. (2013). Molecular chaperone functions in protein folding and proteostasis. Annu. Rev. Biochem. *82*, 323-355.

Kondo, T., Asai, M., Tsukita, K., Kutoku, Y., Ohsawa, Y., Sunada, Y., Imamura, K., Egawa, N., Yahata, N., Okita, K., Takahashi, K., Asaka, I., Aoi, T., Watanabe, A., Watanabe, K., Kadoya, C., Nakano, R., Watanabe, D., Maruyama, K., Hori, O.*, et al.* (2013). Modeling Alzheimer's disease with iPSCs reveals stress phenotypes associated with intracellular Abeta and differential drug responsiveness. Cell Stem Cell *12*, 487-496.

Lambert, M.P., Velasco, P.T., Chang, L., Viola, K.L., Fernandez, S., Lacor, P.N., Khuon, D., Gong, Y., Bigio, E.H., Shaw, P., De Felice, F.G., Krafft, G.A., and Klein, W.L. (2007). Monoclonal antibodies that target pathological assemblies of Abeta. J. Neurochem. *100*, 23-35.

Li, Z., Cao, R., Wang, M., Myers, M.P., Zhang, Y., and Xu, R.M. (2006). Structure of a Bmi-1-Ring1B polycomb group ubiquitin ligase complex. J. Biol. Chem. *281*, 20643-20649.

Liu, C.C., Tsai, C.W., Deak, F., Rogers, J., Penuliar, M., Sung, Y.M., Maher, J.N., Fu, Y., Li, X., Xu, H., Estus, S., Hoe, H.S., Fryer, J.D., Kanekiyo, T., and Bu, G. (2014). Deficiency in

LRP6-mediated Wnt signaling contributes to synaptic abnormalities and amyloid pathology in Alzheimer's disease. Neuron *84*, 63-77.

Lu, T., Aron, L., Zullo, J., Pan, Y., Kim, H., Chen, Y., Yang, T.H., Kim, H.M., Drake, D., Liu, X.S., Bennett, D.A., Colaiacovo, M.P., and Yankner, B.A. (2014). REST and stress resistance in ageing and Alzheimer's disease. Nature *507*, 448-454.

Lu, T., Pan, Y., Kao, S.Y., Li, C., Kohane, I., Chan, J., and Yankner, B.A. (2004). Gene regulation and DNA damage in the ageing human brain. Nature *429*, 883-891.

Mali, P., Esvelt, K.M., and Church, G.M. (2013). Cas9 as a versatile tool for engineering biology. Nat Methods *10*, 957-963.

Mano, T., Nagata, K., Nonaka, T., Tarutani, A., Imamura, T., Hashimoto, T., Bannai, T., Koshi-Mano, K., Tsuchida, T., Ohtomo, R., Takahashi-Fujigasaki, J., Yamashita, S., Ohyagi, Y., Yamasaki, R., Tsuji, S., Tamaoka, A., Ikeuchi, T., Saido, T.C., Iwatsubo, T., Ushijima, T.*, et al.* (2017). Neuron-specific methylome analysis reveals epigenetic regulation and tau-related dysfunction of BRCA1 in Alzheimer's disease. Proc. Natl. Acad. Sci. U. S. A. *114*, E9645-E9654.

Medina, M., and Avila, J. (2014). New insights into the role of glycogen synthase kinase-3 in Alzheimer's disease. Expert Opin Ther Targets *18*, 69-77.

Moore, S., Evans, L.D., Andersson, T., Portelius, E., Smith, J., Dias, T.B., Saurat, N., McGlade, A., Kirwan, P., Blennow, K., Hardy, J., Zetterberg, H., and Livesey, F.J. (2015). APP metabolism regulates tau proteostasis in human cerebral cortex neurons. Cell Rep *11*, 689-696.

Pickart, C.M., and Eddins, M.J. (2004). Ubiquitin: structures, functions, mechanisms. Biochim. Biophys. Acta *1695*, 55-72.

Rovelet-Lecrux, A., Hannequin, D., Guillin, O., Legallic, S., Jurici, S., Wallon, D., Frebourg, T., and Campion, D. (2010). Frontotemporal dementia phenotype associated with MAPT gene duplication. J Alzheimers Dis *21*, 897-902.

Rubio, A., Luoni, M., Giannelli, S.G., Radice, I., Iannielli, A., Cancellieri, C., Di Berardino, C., Regalia, G., Lazzari, G., Menegon, A., Taverna, S., and Broccoli, V. (2016). Rapid and efficient CRISPR/Cas9 gene inactivation in human neurons during human pluripotent stem cell differentiation and direct reprogramming. Sci Rep *6*, 37540.

Savva, G.M., Wharton, S.B., Ince, P.G., Forster, G., Matthews, F.E., and Brayne, C. (2009). Age, neuropathology, and dementia. N. Engl. J. Med. *360*, 2302-2309.

Sherr, C.J. (2001). The INK4a/ARF network in tumour suppression. Nat Rev Mol Cell Biol *2*, 731-737.

Smith, H.L., Li, W., and Cheetham, M.E. (2015). Molecular chaperones and neuronal proteostasis. Semin. Cell Dev. Biol. *40*, 142-152.

Stokin, G.B., Lillo, C., Falzone, T.L., Brusch, R.G., Rockenstein, E., Mount, S.L., Raman, R., Davies, P., Masliah, E., Williams, D.S., and Goldstein, L.S. (2005). Axonopathy and transport deficits early in the pathogenesis of Alzheimer's disease. Science *307*, 1282-1288.

Takahashi, K., Tanabe, K., Ohnuki, M., Narita, M., Ichisaka, T., Tomoda, K., and Yamanaka, S. (2007). Induction of pluripotent stem cells from adult human fibroblasts by defined factors. Cell *131*, 861-872.

Tang, Z., Dai, S., He, Y., Doty, R.A., Shultz, L.D., Sampson, S.B., and Dai, C. (2015). MEK guards proteome stability and inhibits tumor-suppressive amyloidogenesis via HSF1. Cell *160*, 729-744.

Valk-Lingbeek, M.E., Bruggeman, S.W., and Van Lohuizen, M. (2004). Stem cells and cancer; the polycomb connection. Cell *118*, 409-418.

van der Lugt, N.M., Domen, J., Linders, K., van Roon, M., Robanus-Maandag, E., te Riele, H., van der Valk, M., Deschamps, J., Sofroniew, M., van Lohuizen, M., and et al. (1994). Posterior transformation, neurological abnormalities, and severe hematopoietic defects in mice with a targeted deletion of the bmi-1 proto-oncogene. Genes Dev. *8*, 757-769.

MATERIALS AND METHODS

Primers list:

Gene	Forward	Reverse
Gene expression		
ACTB	CATGTACGTTGCTATCCAGGC	CTCCTTAATGTCACGCACGAT
BMI1 p1	TCATCCTTCTGCTGATGCTG	CCGATCCAATCTGTTCTGGT
BMI1 p2	AATCCCCACCTGATGTGTGT	GCTGGTCTCCAGGTAACGAA
BMI1 p3	ATCCCCACTTAATGTGTGTCCT	CTTGCTGGTCTCCAAGTAACG
BMI1 p4	GGAGACCAGCAAGTATTGTCCTATTTG	CATTGCTGCTGGGCATCGTAAG
FOXG1	GAGCGACGACGTGTTCATC	GCCGTTGTAACTCAAAGTGCTG
GAPDH	TCACCAGGGCTGCTTTTAAC	ATCCACAGTCTTCTGGGTGG
MAPT	CCAAGTGTGGCTCATTAGGCA	CCAATCTTCGACTGGACTCTGT
NEUROD1	GGATGACGATCAAAAGCCCAA	GCGTCTTAGAATAGCAAGGCA
P16	CAACGCCCCGAACTCTTTC	GCAGAAGAGCTGCTACGTGAAC
P21	TGTCTTGCACTCTGGTGTCTG	ATCTGCGCTTGGAGTGATAGA
Chromatin Immunoprecipitation (ChIP)		
ACTB	CCTCAATCTCGCTCTCGCTC	CTCTAAGGCTGCTCAATGTC
Ink4a/Arf	GGATGGTGGTGTTAAAGAGGAGT	GTTTTATGACCAAGACGAAGGACT
MAPT_p1	CCCGTGTCCAAGTTCACCG	GAGCCTCGCAGTACCCAG
MAPT_p2	GGTACTCACTAGGGCCAAGC	TGGTGGAGAGCATGCAGTTT
MAPT_p3	CTGACAGTCACCCCAACTCC	AACCTGCTGTGTGACTCTGG
MAPT_p4	GTGTGGACGCCTAACACAGA	CTGTGGGACACCAACTCTCC
Genomic PCR		
BMI1_Ex1	TAGTATGAGAGGCAGAGATCGGG	GTCGTTCAGCAGAAAATGAATGC
BMI1_Ex3	ATTGTTCGTTACCTGGAGACCA	TGGTCTTGTGAACTTGGACATCA
BMI1_Ex4	ACATTTTTAGTTCTTGCCATCTGAA	AGCTGCATAAAAATCCCTTCTTCT
BMI1_3'UTR	ATCTGTATGCCTAAAAGCGGGT	TTAAAGAAAGCAGAAGTAACAGCA

Compounds list:

Compound	Company	Name	Cat#	Working concentration
BSI	SCB	BSI-IV	sc-222304	1 μM
GSI	Sigma	DAPT	D5942	0.5 μM
GSK3Bi	Cayman chem	CHIR99021	13122	1 μM
GSM	Millipore	GSM XXII	565791	30 μM
K114	Sigma	K114	K1015	30 nM
LDN	Sigma	LDN193189	SML0559	0.5 μM
Nutlin	Cayman chem	Nutlin	10004372	1 μM
p53i	Cayman chem	pifithrin	13326	20 μM
ROCKi	Cayman chem	Y-27632	10005583	10 μM

Antibodies list:

Name Reactivity (h:Human; ms:Mouse)	Source	Cat#	Dilution IF/IHC	Dilution WB
Amyloid – Aβ42 h and ms	Abcam	ab2539	1/400	
Amyloid – Aβ42 (D9A3A) h	Cell Signaling	14974	1/1600	
Amyloid – Aβ42 (MOAB2) h and ms	Novus	NBP2-13075	1/400	1/1000
Amyloid – oligomeric (NU1) h and ms	William Klein, Northwestern University		1/50	
Amyloid (PA3) h	Thermo	PA3-16761 (discontinued)	1/400	1/500
BACE1	Thermo	PA1-757		1/1000
beta-Actin	Genetex	GTX109639		1/5000

BIII-Tubulin	Abcam	ab78078	1/400	
BMI1 (ChIP grade)	Abcam	ab14389		
BMI1 (D42B3)	Cell Signaling	5856		1/500
BMI1 (F6)	Millipore	05-637	1/250	1/1000
Caspase3 activated	Cell Signaling	9661	1/400	
ChAT	Thermo	PA5-26597	1/50	
FOXG1	Abcam	ab18259	1/400	
GABARG1	Abcam	ab55051	1/1000	
GAPDH (D-6)	SCB	sc-166545		1/250
GSK3beta	Cell Signaling	9315		1/1000
H2Aub (D27C4)	Cell Signaling	8240	1/1600	1/2000
H2Aub (E6C5)	Millipore	05-678		1/1000
Histone H3 (C-16)	SCB	sc-8654		1/250
MAP2	Abcam	ab5392	1/10000	
Nestin (C-20)	SCB	sc-21247		1/250
NeuN	Abcam	ab104225	1/500	
p-GSK3beta	Thermo	MA5-14873		1/1000
p-p53 (Ser15)	Cell Signaling	9284		1/1000
p-Tau (PHF1)	Peter Davies, Albert Einstein College of Medicine		1/50	1/250

p-Tau (S422)	Invitrogen	44-764G		1/1000
p53	SCB	sc-6243		1/250
PCNA (C-20)	SCB	sc-9857		1/250
PSD95	Thermo	MA1-046	1/200	
PSEN2	Thermo	MA1-754		1/1000
Synaptophysin	Abcam	ab8049	1/400	
Tau total (K9JA)	DAKO	A0024		1/500
vGluT1	Abcam	ab72321	1/400	

Human samples

Paraffin-embedded human brains were obtained from the department of pathology of Maisonneuve-Rosemont Hospital. All other human brain samples were obtained from the Douglas Health institute and the Banner Sun Health institute. All samples were confirmed by patient history and brain pathology analysis as non-demented controls (n=18 samples), classical AD (n=20 samples), FAD (n=4 samples), FTD (n=3 samples), and DLB (n=6 samples) cases (see Table S1). Patients with vascular dementia or mixed AD pathologies were excluded from the study.

Differentiation of human embryonic stem cells into cortical neurons

The differentiation protocol was based on a previous study [125]. However, the Noggin agonist LDN193189 was used to reduce recombinant Noggin concentration. The H9 (WiCell), HUES9 (Harvard Stem Cell Institute), sAD1 (Coriell Institute #GM24666) and sAD2 (courtesy of Dr. Adjaye) cell lines were dissociated using Accutase (Innovative Cell Technology #AT-104) and platted on growth factor reduced matrigel (Corning #356231) in PeproGrow hES cell media (PeproTech #BM-hESC) supplemented with ROCK inhibitor (Y-27632;10µM, Cayman

Chemical #10005583). Upon 70% of confluency, the media was changed to DDM supplemented with B27 (1X final), Noggin (10 ng/ml, PeproTech #120-10C) and LDN193189 (0.5µM; Sigma #SML0559). The medium was changed every day. After 16 days of differentiation, the medium was changed to DDM/B27 and replenished every day. At day 24, neural progenitors were manually detached from the plate and mixed with lentiviral supernatant for 30 min at 37C. Infected neural progenitors were subsequently mixed in DDM/B27 supplemented with ROCK inhibitor (Y-27632; 10µM) and platted on growth factor reduced matrigel coated plates or chamber slides (LabTek #154534). Five days after the dissociation/infection, half of the medium was changed for Neurobasal A media supplemented with B27 (1X final) and changed again every three days.

For 3D cultures, neural progenitors at day 24 were mixed with ice-cold growth factor reduced Matrigel (1:20 dilution) and plated onto 8-well chamber slides. After 30 min of incubation at 37C, fresh Neurobasal A/B27 were added.

When indicated, cells were treated with BSI-IV at 1µM (Santa-Cruz Biotechnology; sc-222304) 2 days prior analysis.

Lentiviral constructs and production

For BMI1 overexpression, human BMI1 (2436 to +2175; GeneBank Accession # NM_005180) cDNA was cloned by PCR using human retina cDNA, and cloned into the CMV-GFP:EF1a for lentiviral production. The double- stranded short-hairpin RNA (shRNA) sequences were cloned down- stream of the H1P promoter of the H1P-UbqC-HygroEGFP plasmid using Age1, SmaI, and XbaI cloning sites (Ivanova et al., 2006). The shRNA-expressing lentiviral plasmids were cotransfected with plasmids pCMVdR8.9 and pHCMV-G into 293FT packaging cells using

Lipo- fectamine (Invitrogen) according to the manufacturer's instructions. Viral containing media were collected and filtered. For viral transduction, lentiviral vectors were added to dissociated neural progenitors and incubated 30 min at 37C before platting. Hygromycin selection (150 g/ml) was added 72 h later. Five days after transduction, 40-50% of the cells were expressing shRNA sequences. After 2 weeks of constant hygromycin selection, >90% of the cells were expressing shRNA sequences.

Chromatin ImmunoPrecipitation

Chromatin was prepared on 100.000 neurons after 6 weeks of differentiation. For brain samples, around 5 mm^3 of frozen brain tissue were chopped into small pieces prior to cross-linking. Chromatin was subsequently sheared 10 sec at 30% of amplitude and immunoprecipitated using 1µg of primary antibody (α-BMI1, α-$H2A^{ub}$ or α-IgG) following manufacturer instructions (ChIP kit, Abcam #ab500). Primers used are listed in Supplementary Materials.

Drug screening assay

Drugs used for the screening assay were reconstituted in DMSO. Cells were treated 48 hours prior analysis. Drugs used are listed in Supplementary Materials.

ELISA

ELISA assays (Invitrogen #PP0812) were done on cellular supernatant and cell extracts. Cell supernatants were sonicated before the assay. Extracts were processed according to manufacturer's instructions.

Immunofluorescence microscopy

All secondary antibodies were tested alone or in combination to assay for possible non-specific background fluorescence. Cells were fixed with 4% PFA for 15 min and permeabilized with Triton X-100 for 10 min. Unspecific antigen blocking was performed using 1% BSA in PBST for 30 min. Cells were incubated with the primary antibody overnight at 4C in a humidified chamber (see dilutions in Table). After incubation with the secondary antibody, slides were counter stained with DAPI. Pictures were taken using a confocal microscopy system (Olympus). For Figure S2D, formic acid at 70% was added for 10 min after fixation.

Quantification of immunofluorescence images

For Figure 3F, low magnification images of GABA and vGLUT stainings were used for the quantifications. Individual axons were traced using ImageJ v2.0.0 and scored manually for the presence of axonal swellings. For Figure 2B, IMARIS station v8.4.1 (Bitplane) was used with the filament module for dendritic tracing. A scholl regression coefficient at 1μm was set.

Transcriptome analysis

Total RNA from three independent biological samples (three distinct differentiations) was extracted using standard procedure (Trizol method). RNA samples were subjected to a secondary purification on columns and assayed for RNA integrity. cDNA were prepared according to manufacturer's instructions (Illumina) and hybridized onto Illumina HumanHT-12 expression Beadchip version 4 (BD-103-0204). Data were first normalized using lumi algorithm (BeadArray specific method) followed by ANOVA and Fold Change statistical tests. FlexArray software was used for data mining. Gene Ontology was performed using PANTHER [205-207].

Heatmap of gene expression was generated using Heatmapper Expression module. Average linkage method was used for clustering. Distance computing between row genes was done by Pearson method.

RNA-seq data were obtained through the Allen brain institute under the aging, dementia and TBI study.

Western Blot

Cell extracts were homogenized in the Complete Mini Protease inhibitor cocktail solution (Roche Diagnostics), followed by sonication. Protein material was quantified using the Bradford reagent. Proteins were resolved in 1x Laemelli reducing buffer by SDS-PAGE electrophoresis and transferred to a Nitrocellulose blotting membrane (Bio-Rad). Subsequently, membranes were blocked for 1h in 5% non-fat milk-1X TBS solution and incubated overnight with primary antibodies. Membranes were then washed 3 times in 1X TBS; 0.05% Tween solution and incubated for 1h with corresponding horseradish peroxidase-conjugated secondary antibodies. Membranes were developed using the Immobilon Western (Millipore). Blots were quantified using the Image quant program. Antibodies used are listed in Supplementary Materials.

Real-time RT-PCR

Mouse cortices were diced and RNA was isolated using TRIzol reagent (Invitrogen). Reverse transcription (RT) was performed using 1 μg of total RNA and the MML-V reverse transcriptase (Invitrogen). Real-time PCR was carried in triplicates using Platinum SYBRGreen Supermix (Invitrogen) and Real-time PCR apparatus (ABI prism 7002). Primer sets used are listed in Supplementary Materials.

REFERENCES

[1] Espuny-Camacho, I., Michelsen, K. A., Gall, D., Linaro, D., Hasche, A., Bonnefont, J., Bali, C., Orduz, D., Bilheu, A., Herpoel, A., Lambert, N., Gaspard, N., Peron, S., Schiffmann, S. N., Giugliano, M., Gaillard, A. & Vanderhaeghen, P. Pyramidal neurons derived from human pluripotent stem cells integrate efficiently into mouse brain circuits in vivo. *Neuron* **77**, 440-456, (2013).

[2] Mi, H., Muruganujan, A., Casagrande, J. T. & Thomas, P. D. Large-scale gene function analysis with the PANTHER classification system. *Nat Protoc* **8**, 1551-1566, (2013).

[3] Mi, H., Muruganujan, A. & Thomas, P. D. PANTHER in 2013: modeling the evolution of gene function, and other gene attributes, in the context of phylogenetic trees. *Nucleic Acids Res* **41**, D377-386, (2013).

[4] Mi, H. & Thomas, P. PANTHER pathway: an ontology-based pathway database coupled with data analysis tools. *Methods Mol. Biol.* **563**, 123-140, (2009).

Flamier *et al.* 2018

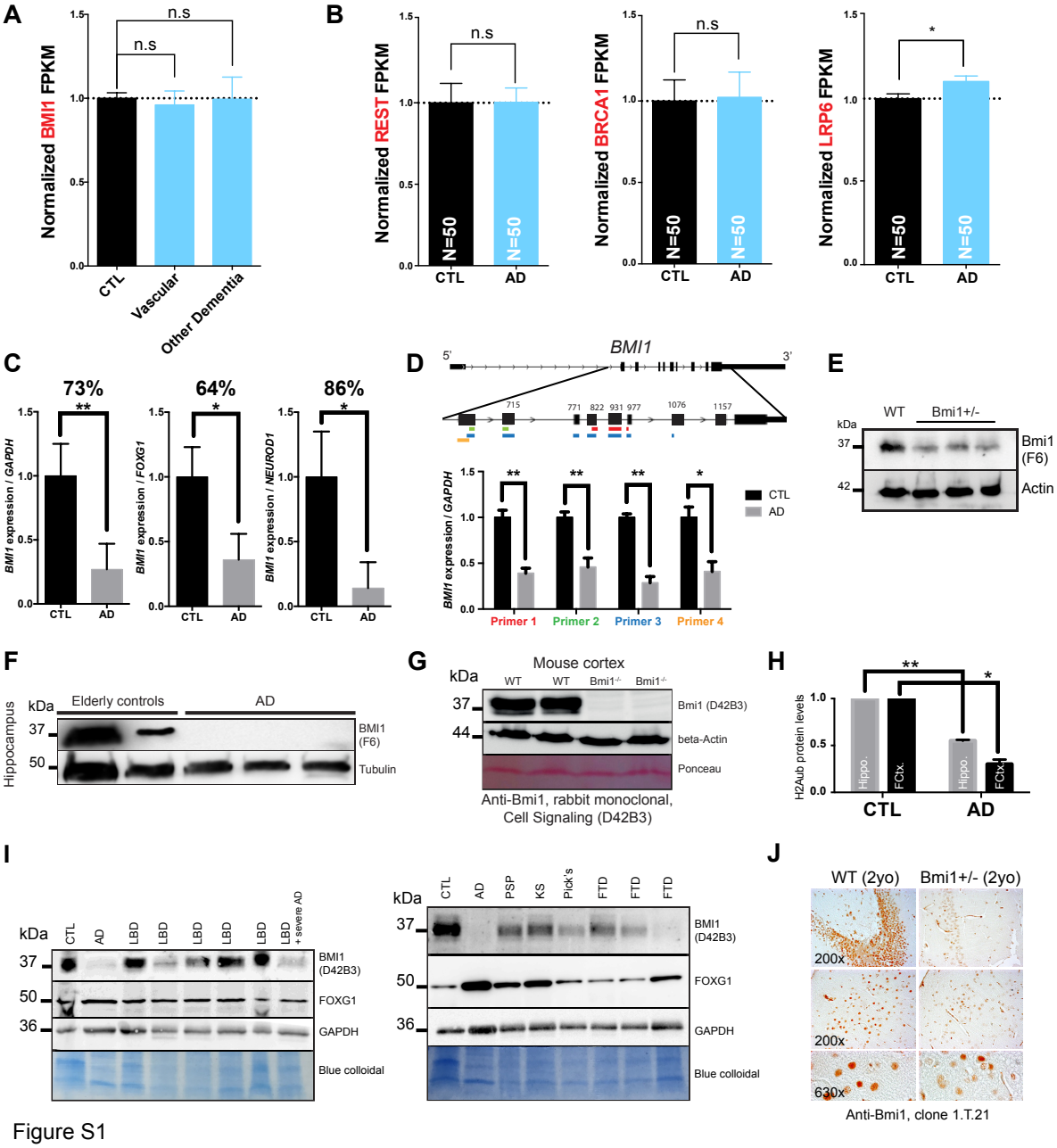

Figure S1

Figure S1. BMI1 brain expression is reduced in AD but not in elderly controls or other related dementias. Related to Figure 1.

(A) *BMI1* normalized FPKM in the cortex of CTL individuals (n=50), vascular dementia patients (n=4) and patients with other dementia (n=16). All values are mean ± SEM; by Student's unpaired t-test.

(B) *REST, BRCA1* and *LRP6* normalized FPKM in the cortex of CTL (n=50) and AD patients (n=50). All values are mean ± SEM. (*) $P<0.05$; by Student's unpaired t-test.

(C) *BMI1* gene expression levels in qPCR normalized to *GAPDH, FOXG1* and *NEUROD1* in the hippocampus of CTL (n=2) and AD patients (n=3). Top: percentage of *BMI1* reduction in AD versus CTL brains. All values are mean ± SEM. (*) $P<0.05$; (**) $P<0.01$; by Student's unpaired t-test.

(D) *BMI1* gene expression levels in qPCR normalized to *GAPDH* using 4 non-overlapping primer pairs in the hippocampus of CTL (n=2) and AD patients (n=3). All values are mean ± SEM. (*) $P<0.05$; (**) $P<0.01$; by Student's unpaired t-test.

(E) Bmi1 protein levels in 15-month old WT and $Bmi1^{+/-}$ mice using clone F6 BMI1 antibody.

(F) Immunoblot on hippocampal extracts from control (n=2) and AD (n=3) patients.

(G) Immunoblot on WT and Bmi1 cortical extracts using Cell signaling BMI1 antibody clone D42B3.

(H) Quantification of H2Aub protein levels in hippocampal (Hippo) and frontal cortex (Fctx) extracts from control and AD patients. Hippocampus: 3 old controls and 5 AD brains. Frontal cortex: 6 old controls and 6 AD brains. All values are mean ± SEM. (*) $P<0.05$; (**) $P<0.01$; (***) $P<0.001$ by Student's unpaired t-test.

(I) Immunoblot on frontal cortex from control, AD, fronto-temporal dementia (FTD), Pick's disease (PSP), Korsakoff's syndrome (KS) and dementia with Lewy body (DLB) patients using clone D42B3 BMI1 antibody.

(J) IHC on mouse cortical sections showing reduced Bmi1 immuno-labeling in neurons of *Bmi1*$^{+/-}$ mice clone 1.T.21 BMI1 antibody (ab14389).

Flamier *et al.* 2018

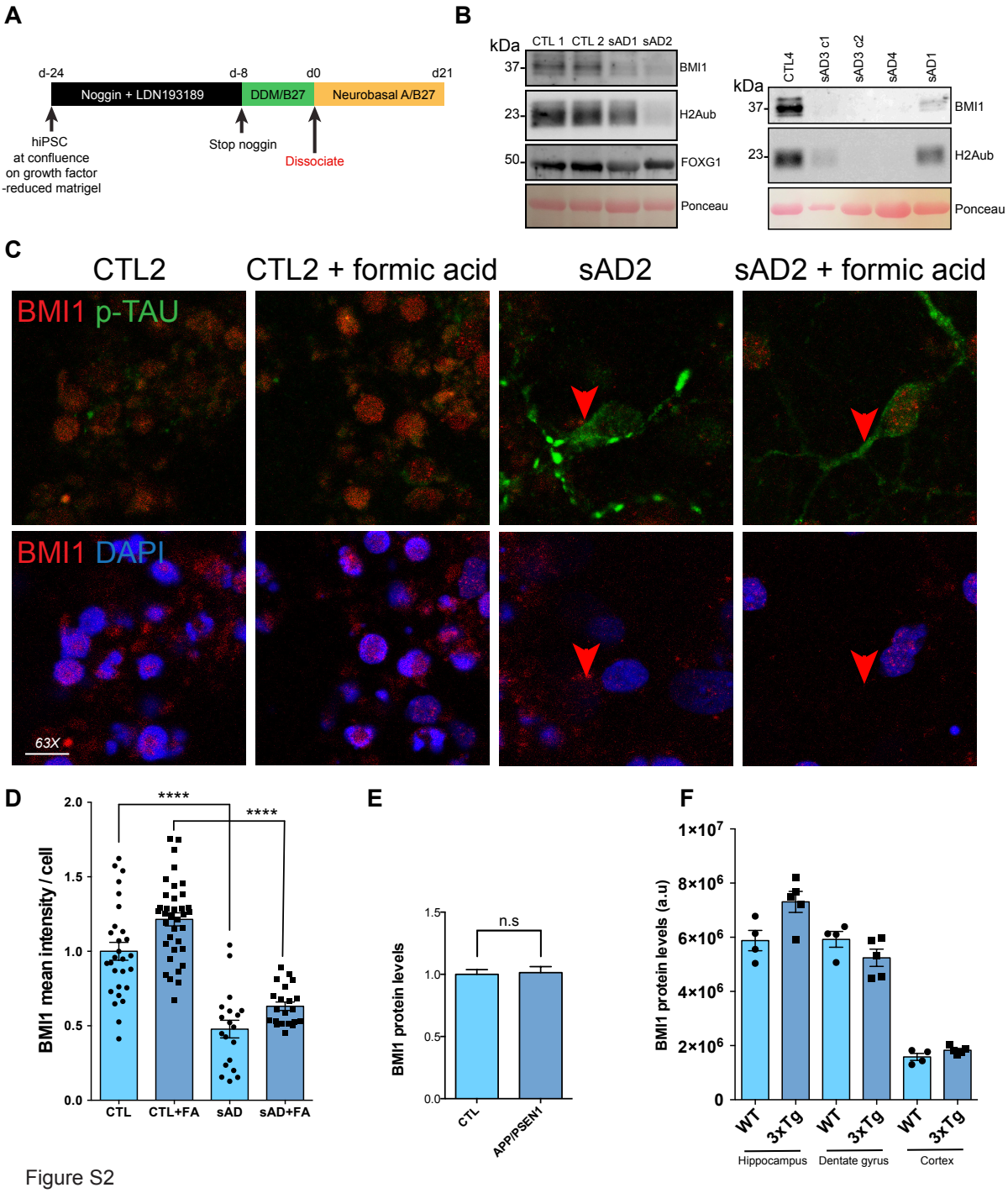

Figure S2

Figure S2. *BMI1* expression is reduced in sporadic AD models but not in FAD models. Related to Figure 2.

(A) Protocol for the differentiation of hiPS cells into cortical neurons.

(B) Left: immunoblot on CTL (n = 2 independent cell lines from 2 individuals) and sAD1 and sAD2 (n = 2 independent cell lines from 2 individuals) neurons. Right: immunoblot on CTL and sAD (n=4 independent cell lines from 3 individuals) neurons. Note the reduced BMI1 and $H2A^{ub}$ levels.

(C) Representative images of CTL2 and sAD2 neurons treated or not with formic acid (FA) and immunostained for BMI1 and p-Tau (PHF1).

(D) Quantification of BMI1 fluorescence intensity in neurons from CTL2 and sAD2 neurons treated or not with formic acid (FA). n = 4 from 2 independent experiments. All values are mean ± SEM. (****) $P<0.0001$ by Student's unpaired t-test.

(E) Quantification of BMI1 protein levels in CTL neurons transfected with GFP-expressing plasmid (n=2 independent differentiations) and CTL neurons transfected with APP/PSEN1-expressing plasmid (n=2 independent differentiations). FOXG1 is used as loading control. All values are mean ± SEM.

(F) Quantification of BMI1 protein levels in the hippocampus, dentate gyrus and cortex of WT (n=4) and triple transgenic mice APP^{swe}/$MAPT^{P301L}$/$PSEN1^{M146V}$ (n=5) at 6 months.

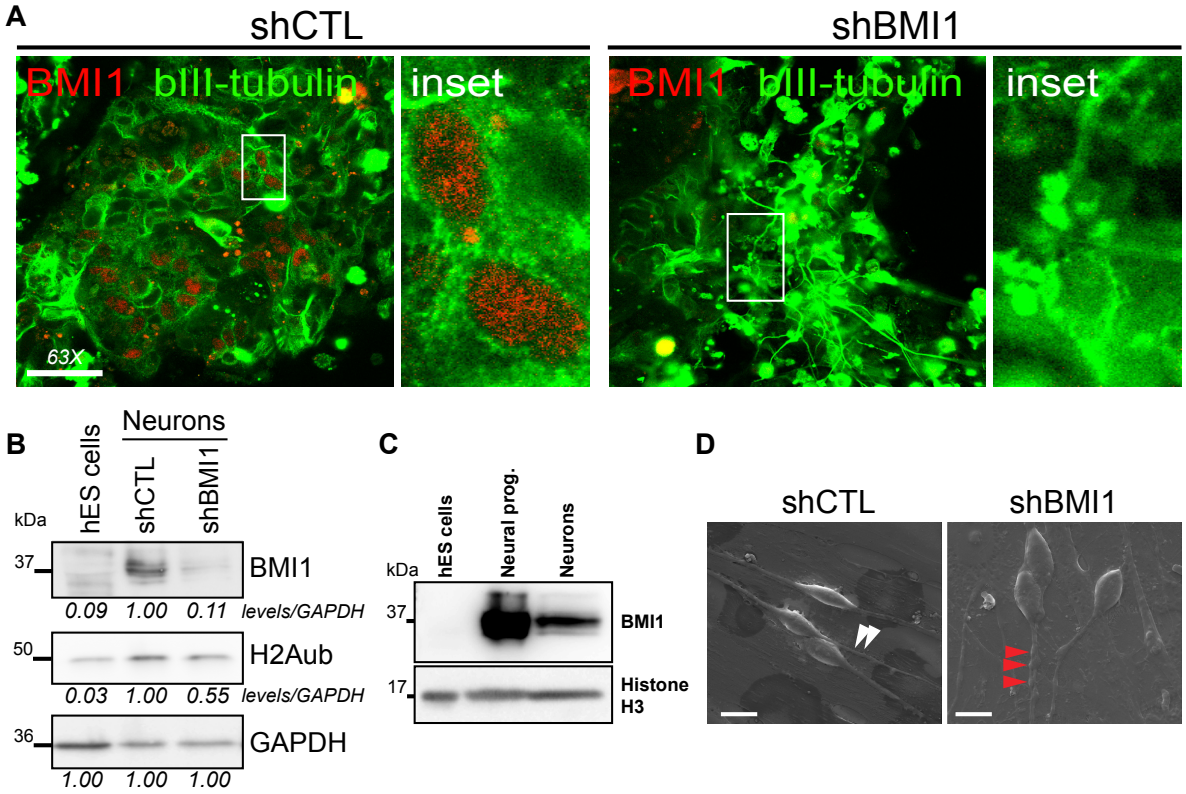
A
shCTL
shBMI1
BMI1 bIII-tubulin
inset
63X
B
hES cells
Neurons
shCTL
shBMI1
kDa
37
BMI1
0.09 1.00 0.11 levels/GAPDH
50
H2Aub
0.03 1.00 0.55 levels/GAPDH
36
GAPDH
1.00 1.00 1.00
C
hES cells
Neural prog.
Neurons
kDa
37
BMI1
17
Histone H3
D
shCTL
shBMI1

Figure S3

Figure S3. BMI1 is reduced upon knockdown in human cortical neurons. Related to Figure 3.

(A) Confocal immunofluorescence of BMI1 and bIII-tubulin of differentiated neurons infected with the shScramble (shCTL) or shBMI1 (shBMI1) viruses 7 days prior to analysis. Scale bar 40μm.

(B) Reduced levels of BMI1 and H2Aub in shBMI1 neurons compared to shCTL neurons by immunoblot.

(C) BMI1 expression in control neural progenitors (24 div) and neurons (40 div) by immunoblot.

(D) Scanning electron microscopy images of shCTL and shBMI1 neurons. White arrowheads: axon of shCTL neurons. Red arrowheads: axonal swellings in shBMI1 neurons.

Flamier *et al.* 2017

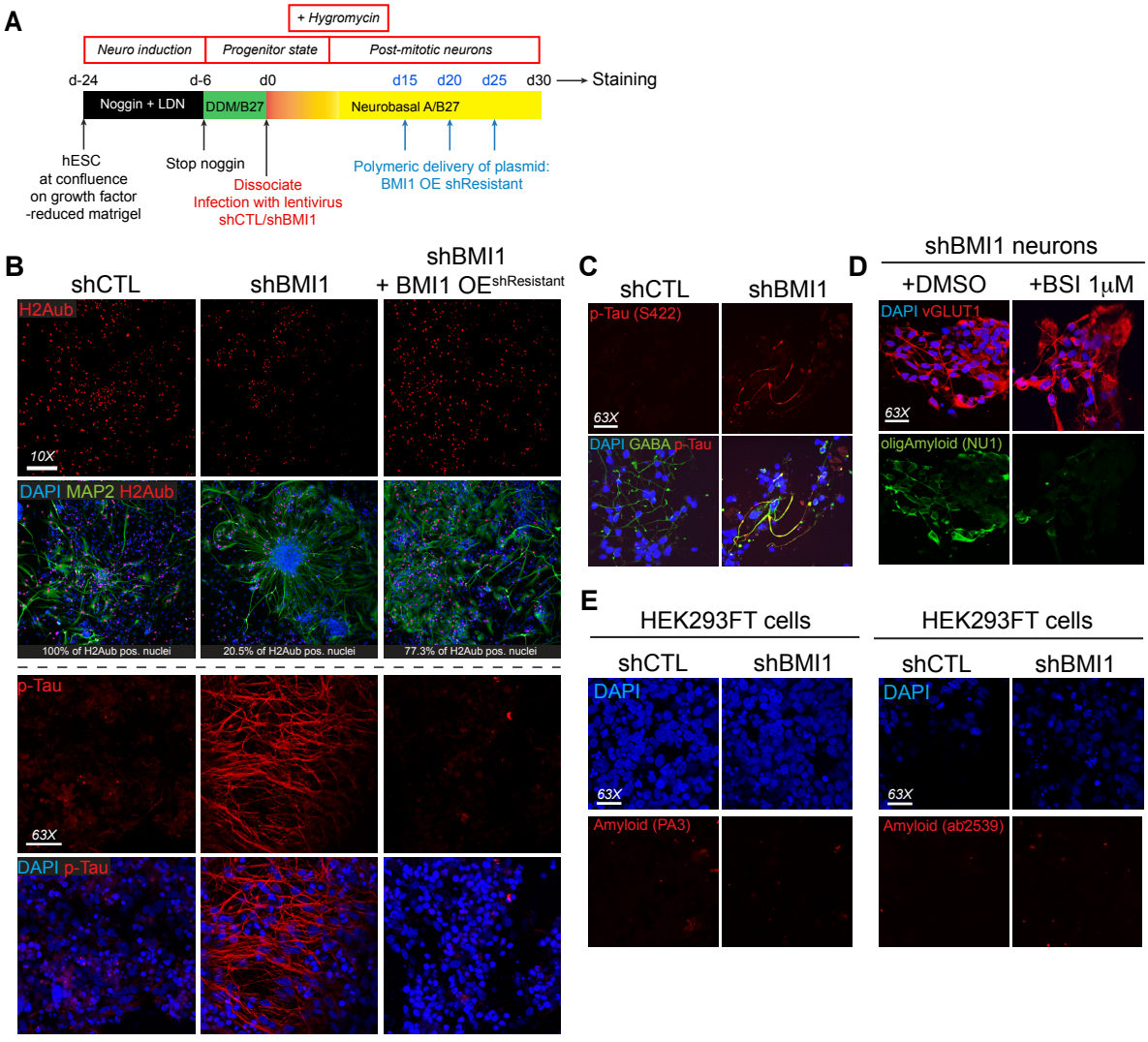

Figure S4

Figure S4. BMI1 deficiency in cortical neurons results in p-Tau and amyloid accumulation. Related to Figure 4.

(A) Protocol for the differentiation of hES cells into shCTL and shBMI1 cortical neurons followed by the overexpression of a shResistant BMI1.

(B) Immunofluorescence on shCTL and shBMI1 cortical neurons overexpressing or not a shResistant isoform of BMI1. Top: rescue of H2A ubiquitination upon BMI1 overexpression, scale bar: 100μm. Bottom: rescue of p-Tau (PHF1) accumulation in shBMI1 neurons upon BMI1 overexpression, scale bar: 40μm.

(C) Immunofluorescence on shCTL and shBMI1 HEK293FT cells for beta-amyloid (PA3 and abcam ab2539). The same exposition time as in shBMI1 neurons were applied.

(D) p-Tau (S422) accumulation in shBMI1 GABA+ neurons but not in shCTL neurons (day 14).

(E) Immunofluorescence performed on shBMI1 neurons exposed or not to BSI. Note the reduction in oligomeric amyloid (NU1) signal intensity in shBMI1 neurons treated with BSI.

(C-E) Scale bars: 40μm.

Flamier *et al.* 2017

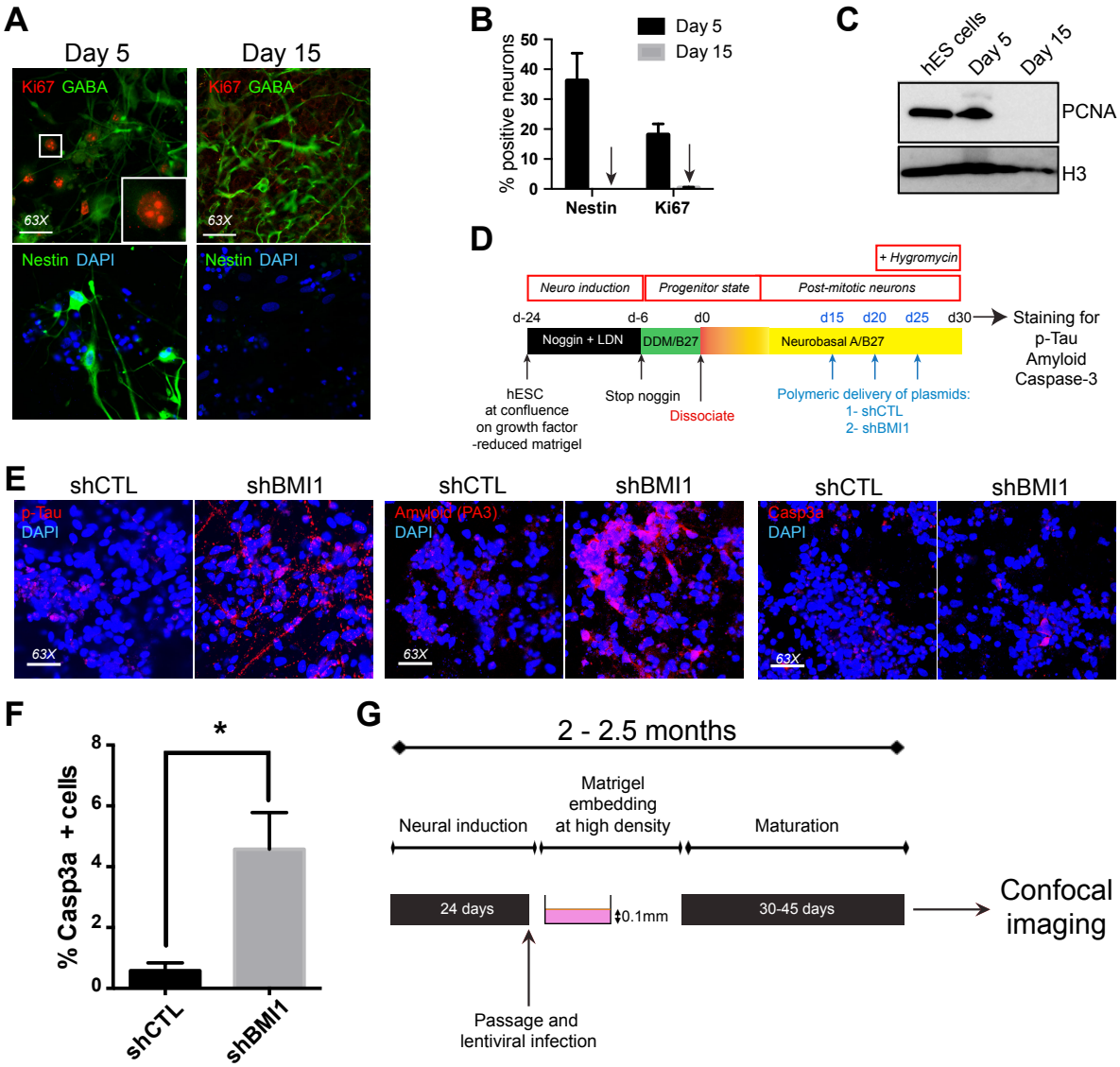

Figure S5

Figure S5. BMI1 deficiency in post-mitotic cortical neurons results in p-Tau and amyloid accumulation. Related to Figure 4 and 5.

(A) Confocal analyses of proliferation marker Ki67, neural stem cell marker Nestin and GABAergic neuronal marker GABA in cortical neurons at day 5 and 15 of differentiation.

(B) Percentage of neurons positive for Nestin or Ki67 at 5 (n=4) and 15 (n=4) days of neural differentiation. All values are mean ± SEM.

(C) Loss of proliferation marker PCNA at day 15 of differentiation by western-blot.

(D) Protocol for the differentiation of hES cells into cortical neurons and BMI1 knockdown using polymeric delivery of plasmids expressing shCTL and shBMI1 shRNA.

(E) p-Tau (PHF1) and amyloid (PA3) accumulation in shBMI1 neurons but not in shCTL neurons after 30 days of differentiation (3 plasmid deliveries). Confocal immunofluorescence for the apoptosis marker activated caspase-3 Scale bar: 40μm.

(F) Quantification of activated caspase-3 positive cells in shCTL and shBMI1 cultures. N=3 independent differentiations with 2 fields quantified for each. All values are mean ± SEM. (*) $P<0.05$ by Student's unpaired t-test.

(G) Experimental scheme for the long-term culture of cortical neurons in 3D.

Flamier *et al.* 2018

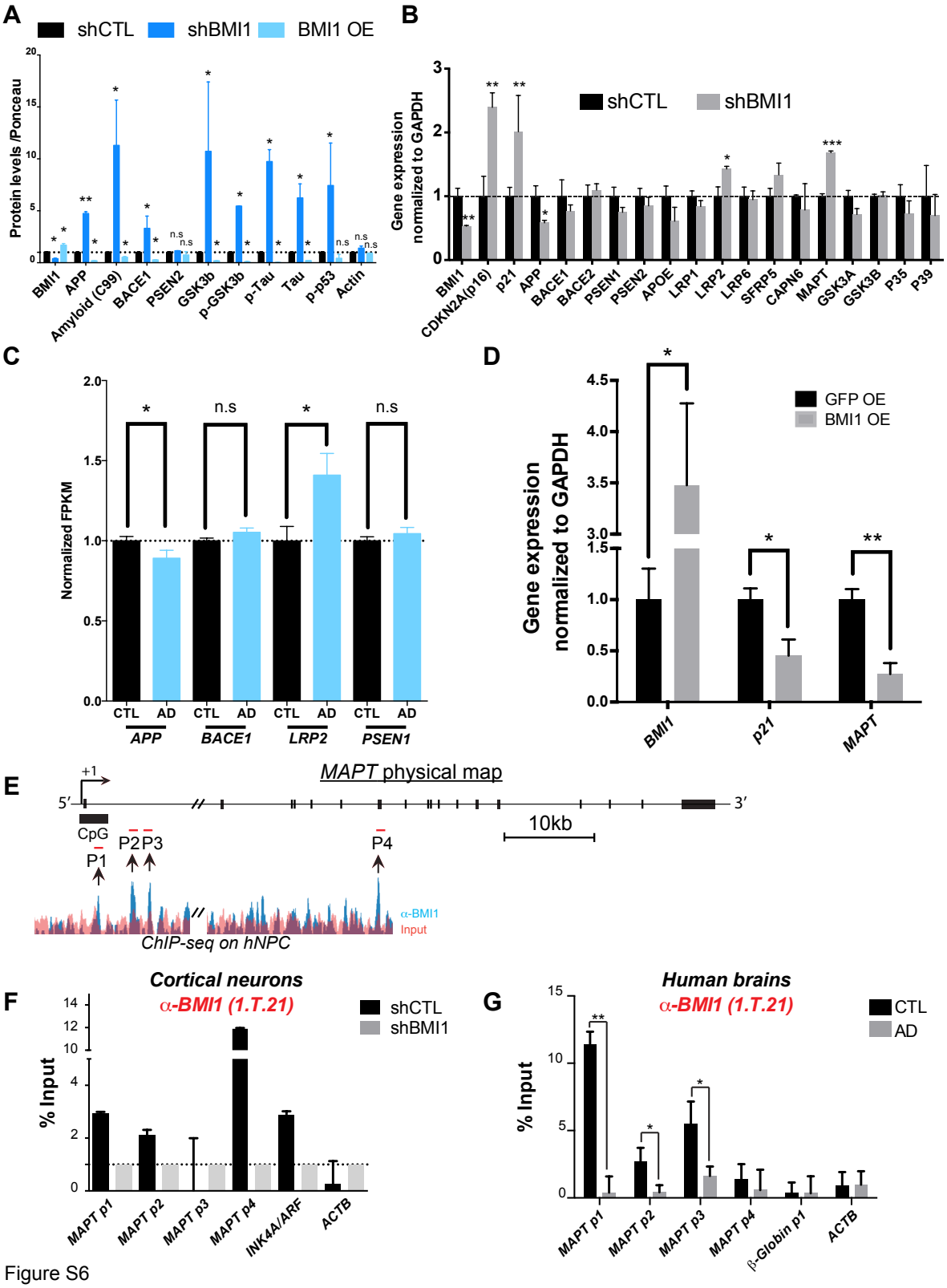

Figure S6

Figure S6. BMI1 inhibits *MAPT* transcription. Related to Figure 7.

(A) Quantification of protein levels in shCTL, shBMI1 and BMI1 OE neurons (n=3 independent differentiations). Ponceau is used as loading control. All values are fold of shCTL neurons and mean ± SEM. (*) P<0.05; (**) P<0.01 by Student's unpaired t-test.

(B) AD-related mRNA levels in human cortical neurons by qPCR (shCTL, n=3; shBMI1, n=3). *BMI1*, *CDKN2A* and *p21* (*CDKN1A*) were used as internal controls. All results were normalized to *GAPDH* expression. All values are mean ± SEM. (**) P<0.01; (***) P<0.001 by Student's unpaired t-test.

(C) *APP, BACE1, LRP2* and *PSEN1* normalized FPKM in the cortex of CTL (n=50) and AD patients (n=50). (*) *P*<0.05; by Student's unpaired t-test.

(D) MAPT mRNA levels in GFP over-expressing (GFP OE, n=3) and BMI1 over-expressing (BMI1 OE, n=4) neurons by qPCR. *BMI1* and *p21* (*CDKN1A*) were used as internal controls. All results were normalized to *GAPDH* expression. All values are mean ± SEM. (*) P<0.05; (**) P<0.01 by Student's unpaired t-test.

(E) Physical map of the *MAPT* locus and localization of primers (P1-4) used for qPCR.

(F) ChIP-qPCR on neurons using BMI1 clone 1.T.21 (ab14389) and IgG antibodies in shCTL and shBMI1 neurons. BMI1 is highly enriched at the *INK4A/ARF* locus in control neurons. BMI1 is also enriched at multiple genomic regions of the *MAPT* locus but not at the β-*ACTIN* (*ACTB*) locus. Results are expressed as proportion of the input. N=3 independent chromatin immunoprecipitation from 2 differentiations. All values are mean ± SEM.

(G) ChIP-qPCR on control (#428; 89y) and AD (#1127: 88y) frontal cortex samples using IgG, $H2A^{ub}$ and Bmi1 clone 1.T.21 (ab14389) antibodies. N=4 technical replicates.

All values are mean ± SEM. (*) P<0.05; (**) P<0.01 by Student's unpaired t-test.

Flamier *et al.* 2018

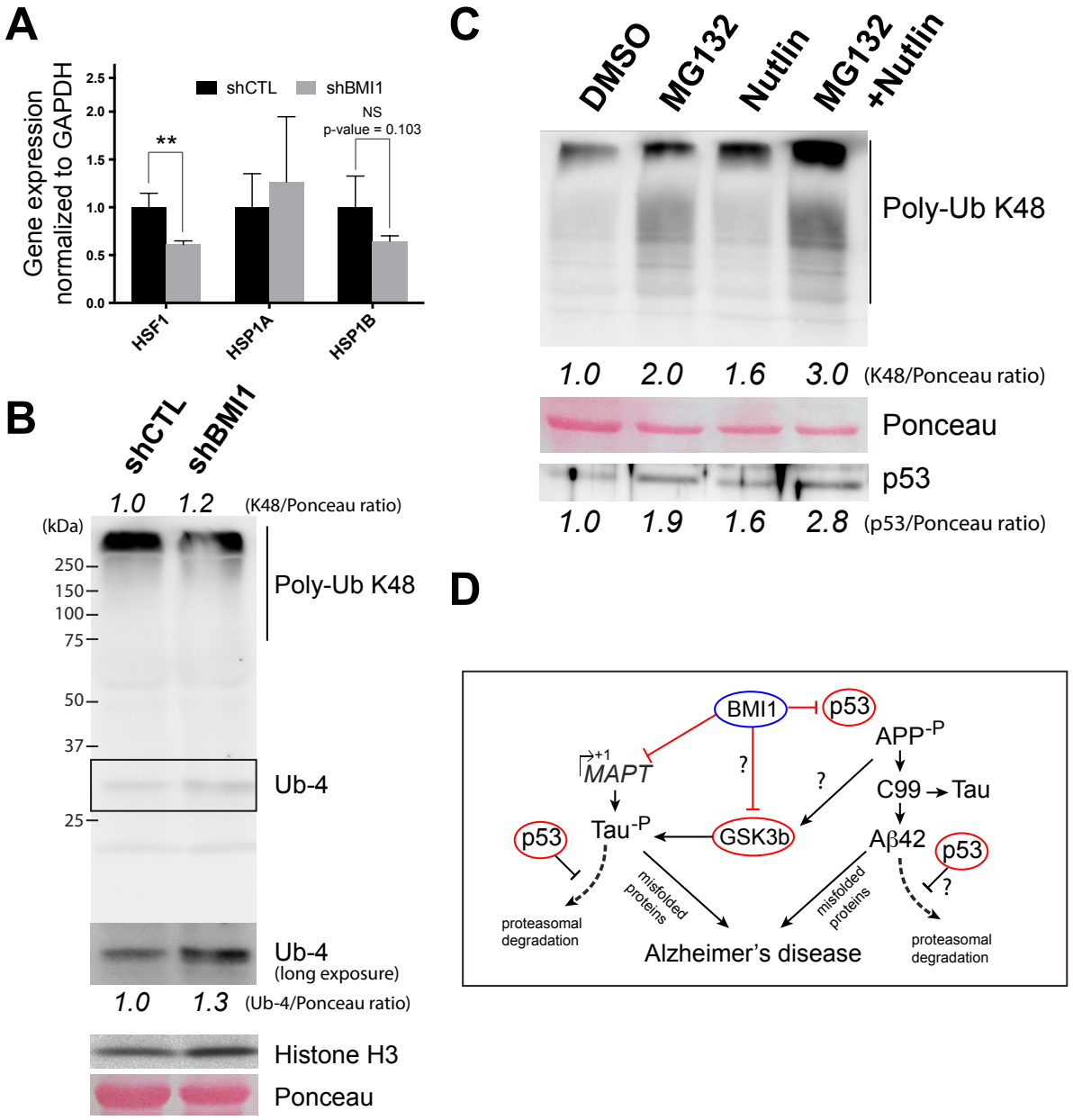

Figure S7

Figure S7. p53 stabilization can disturb proteostasis. Related to Figure 7.

(A) *HSF1, HSP1A* and *HSP1B* mRNA levels in human cortical neurons by qPCR (shCTL, n=3; shBMI1, n=3). All values are mean ± SEM. (**) P<0.01 by Student's unpaired t-test.

(B) Immunoblots using extracts from shCTL and shBMI cortical neurons. Protein expression ratios were established using histone H3, and where expression in shCTL neurons was set as 1. Multi-ubiquitin chain 4: Ub4.

(C) Immunoblot with extracts from primary human dermal fibroblasts untreated (DMSO), or treated with chemical inhibitors. Protein expression ratios were established using Ponceau staining, and where expression in shCTL neurons was set as 1.

(D) Proposed model linking BMI1 deficiency to AD. In healthy neurons, BMI1 represses *MAPT* transcription and prevents GSK3β and p53 stabilization (red bars). Upon BMI1 deficiency, Tau expression increases, and GSK3β phosphorylates Tau and other possible substrates such as APP, leading to over-production of p-Tau, C99 and Aβ42 (black bars and arrows). Activation and/or stabilization of p53 can inhibit proteasome activity, which exacerbates the disease by leading to accumulation of toxic misfolded proteins.

Table S1. List of all human brain samples used in the study.

IHC samples

Phenotype	ID	Brain region	Sex	Age
Elderly Ctrl	12c00024	Frontal cortex	M	90
Elderly Ctrl	10c00052	Frontal cortex	M	72
Elderly Ctrl	10c00020	Frontal cortex	M	82
AD	10c00088	Frontal cortex	M	75
AD	10c00042	Frontal cortex	M	89
AD	10c00030	Frontal cortex	M	81

Western-blot samples (I)

Phenotype	ID	Brain region	Sex	Age
Young Ctrl	1388	Hippocampus	M	57
Young Ctrl	1705	Hippocampus	M	61
Young Ctrl	1722	Hippocampus	M	59
FAD	1214	Hippocampus	M	64
FAD	410	Hippocampus	M	63
FAD	1201	Hippocampus	M	63
FAD	1147	Hippocampus	F	55
Elderly Ctrl	626	Hippocampus	F	87
Elderly Ctrl	1582	Hippocampus	M	85
Elderly Ctrl	1585	Hippocampus	M	88
AD	1427	Hippocampus	F	82
AD	1129	Hippocampus	M	88
AD	1065	Hippocampus	M	76
AD	588	Hippocampus	M	82
AD	450	Hippocampus	F	83
Elderly Ctrl	428	Frontal cortex	M	89
Elderly Ctrl	488	Frontal cortex	F	86
Elderly Ctrl	616	Frontal cortex	F	86
Elderly Ctrl	727	Frontal cortex	M	87
Elderly Ctrl	881	Frontal cortex	M	85
Elderly Ctrl	1487	Frontal cortex	F	91
AD	999	Frontal cortex	F	87
AD	1018	Frontal cortex	M	88
AD	1073	Frontal cortex	M	85
AD	1127	Frontal cortex	M	88
AD	1157	Frontal cortex	F	85
AD	1599	Frontal cortex	F	90

Western-blot samples (II)

Phenotype	ID	Brain region	Sex	Age
FTD	1015	Frontal cortex	F	74
FTD	1367	Frontal cortex	M	55
FTD	1040	Frontal cortex	F	88
Pick's	1390	Frontal cortex	M	67
PSP	1285	Frontal cortex	F	72
KS	1384	Frontal cortex	M	86
LBD	948	Frontal cortex	M	79
LBD	1012	Frontal cortex	M	69
LBD	975	Frontal cortex	F	77
LBD	977	Frontal cortex	F	81
LBD+SYN	1171	Frontal cortex	F	78
LBD+SYN	1158	Frontal cortex	M	70

qRT-PCR samples

Phenotype	ID	Brain region	Sex	Age
Elderly Ctrl	1495	Hippocampus	F	79
Elderly Ctrl	533	Hippocampus	F	76
Elderly Ctrl	0728	Hippocampus	M	86
Elderly Ctrl	0737	Hippocampus	M	89
Elderly Ctrl	0855	Hippocampus	M	71
AD	1578	Hippocampus	F	80
AD	1034	Hippocampus	F	77
AD	1366	Hippocampus	M	79
AD	0334	Hippocampus	F	88
AD	1354	Hippocampus	F	85
AD	1519	Hippocampus	F	83

Young Ctrl : Young control ; n=3 ; Median age= 59
Elderly Ctrl : Elderly control ; n=15 ; Median age= 84.1
FAD : Familial Alzheimer's Disease ; n=4 ; Median age= 61.3
AD : Alzheimer's disease (Late-onset) ; n=20 ; Median age= 83.6
FTD : Fronto-Temporal DJNeuroementia ; n=3 ; Median age= 72.3
LBD : Dementia with Lewy Bodies ; n=4 ; Median age= 76.5
LBD+SYN : Dementia with Lewy Bodies and synuclein ; n=2 ; Median age= 74
PSP : Progressive Spastic Paraparesis ; n=1 ; Median age= 72
Pick's : Pick's disease ; n=1 ; Median age= 67
KS : Korsakoff's disease ; n=1 ; Median age= 86

Gene Symbol	Gene name	Fold Change (shCTL vs shBMI1)	p-value	Fold Change (BMI1 ChIP-seq) Promoter	Function
SNORA35	Small nucleolar RNA, H/ACA box 35	5,81	0,0002	--	rRNA modification guidance
TTR	Transthyretin	4,47	0,0321	--	Carrier protein, mutations lead to amyloid deposition
HTR2C	Serotonin receptor 2C	3,77	0,0005	20,8	Serotonin receptor activity
TNMD	Tenomodulin	3,69	0,0237	--	Inhibits tube formation of endothelial cells
TEKT1	Tektin 1	3,61	0,0072	1,6	Interacts with Tubulins to form microtubules
UBR1	Ubiquitin protein ligase E3 component n-recognin 1	3,39	0,0210	--	Proteasomal degradation
TNNC1	Troponin C	3,28	0,0053	--	Muscle contraction, can interact with Actin/Myosin and UBE2C
KCTD8	Potassium channel tetramerization domain containing 8	3,23	0,0145	8,8	GPCR signalling pathway, can interact with HSP90
KISS1	KiSS-1 metastasis-suppressor	2,73	0,0096	--	Cytoskeletal reorganization, overexpressed in AD, can interact with Aβ42
CRYAB	αB-crystallin	2,70	0,0136	--	Prevents protein misfolding
ANKRD52	Ankyrin repeat domain 52	2,66	0,0002	--	Can interact with Aβ
RYR3	Ryanodine Receptors 3	2,52	0,0108	--	Calcium release from intracellular, abnormal expression in AD
GPR37	G protein-coupled receptor 37	2,45	0,0217	--	Can interact with HSPA1A, prevents protein misfolding
DNAJA4	DnaJ (Hsp40) homolog, subfamily A, member 4	2,39	0,0273	--	Prevents protein misfolding

Table S2. Function of the top 14 genes upregulated in shBMI1 neurons. Related to Figure 3

CHAPITRE 3:

AMYLOID AND TAU PATHOLOGY IN IPSC-DERIVED SPORADIC ALZHEIMER'S DISEASE NEURONS AND BRAIN ORGANOIDS

Ce chapitre vous présente le deuxième article en lien avec ma thèse et prêt à être soumis pour publication. Il fait suite à l'article précédent et porte sur la reprogrammation de cellules de la peau de patients Alzheimer en cellules souches pluripotentes ainsi que leur différenciation en neurones corticaux.

Amyloid and Tau pathology in iPSC-derived sporadic Alzheimer's disease neurons and brain organoids

Anthony Flamier[1], Roy Hanna[1], Andrea Barabino[1] and Gilbert Bernier[1, 2*]

[1] Stem Cell and Developmental Biology Laboratory, Hôpital Maisonneuve-Rosemont, 5415 Boul. l'Assomption, Montréal, Canada, H1T 2M4

[2] Department of Neurosciences, University of Montreal, Montreal, Canada

[†]These authors contributed equally to this work

*Corresponding author

Tel: 514-252-3400 ext. 4648

E-mail: gbernier.hmr@ssss.gouv.qc.ca

Key words: Alzheimer's disease, iPSC, neuron, amyloid, Tau, brain organoid

Running title: *Amyloid and Tau pathology in AD neurons*

Content:

4 Figures

3 supplementary Figures

SUMMARY

Sporadic Alzheimer's disease (AD) is the most common form of dementia, but its etiology remains uncertain. Because of this, experimental models that faithfully recapitulate the pathology observed in the patient's neurons *in situ* are rare. Herein, we describe the generation of induced pluripotent stem cells (iPSCs) from 2 unrelated elderly controls and 2 unrelated AD patients. Cortical neurons produced from the differentiation of the AD iPSC lines presented elevated secretion of amyloid-beta 42 (Aβ42) as well as intra-neuronal accumulation of Aβ42 and p-Tau. AD neurons also displayed dendritic atrophy, an important pathological characteristic of AD. Brain organoids produced from the differentiation of AD iPSCs also displayed neuronal pathologies, the most remarkable being the accumulation of fiber-like amyloid aggregates. We conclude that neurons produced from patient's iPSCs can recapitulate most AD neuronal pathologies, thus representing an interesting tool to study the disease's mechanisms and test new therapeutics.

INTRODUCTION

Sporadic Alzheimer's disease (AD) is the most common dementia with an estimated prevalence of 5.2 million Americans in 2014 [55]. The brain changes in AD begin 20 or more years before symptoms appear [208]. 11% of people aged 65 and older have AD. This number grows to 32% for the people aged 85 and more. The greatest risk factor to develop AD is thus advanced age [164]. Furthermore, carriers of the E4 allele of *APOLIPOPROTEIN* have increased risk to develop AD [165]. Familial AD (FAD) occurs between the ages of 30-50 year, is autosomal dominant and linked to mutation in *AMYLOID PRECURSOR PROTEIN* (*APP)*, *PRESENILIN 1* (*PSEN1)* or *PRESENILIN 2* (*PSEN2)* [166]. AD and FAD are characterized by progressive memory and behavioral impairment owing to degeneration of limbic and cortical areas of the brain. Pathological hallmarks of the disease are the presence of amyloid plaques, neurofibrillary phospho-Tau tangles and synaptic dysfunction [166]. In contrast with FAD, for which numerous experimental models exist, faithful experimental models of AD are very rare because the disease's origin remains uncertain.

The induced pluripotent stem cell (iPSC) technology allows the reprogrammation of somatic cells from the donor into embryonic stem cell-like cells capable of self-renewal and differentiation into cell progenies from the 3 primordial germ layers [113]. Upon directed differentiation into a specific cell type, iPSCs have enabled modeling of several human neurological diseases [209]. In the recent years, multiple iPSC lines have been produced from AD and FAD patients. While FAD iPSC lines consistently display amyloid-beta 42 (Aβ42) and Tau pathologies upon neuronal differentiation [129], few AD iPSC lines were reported to do so [133, 134].

Herein, we report on the generation of iPSCs from 2 non-demented controls and 2 AD patients. Upon differentiation of the iPSCs into cortical neurons or brain organoids, AD neurons presented most classical pathological hallmarks of the disease. These new AD iPSC lines thus represent a tool for AD modeling and better understanding of the disease underlying mechanisms.

RESULTS

Dermal fibroblasts from 2 elderly non-demented controls and 2 elderly sporadic AD patients were reprogrammed into iPSCs using 3 plasmid vectors expressing the Yamanaka factors (OCT3/4, SOX2, KLF4, L-MYC and LIN28A) and a small hairpin RNA against p53 (Fig. 1A) [210]. The obtained clones (6 clones/cell line) from the 4 cell lines presented the typical morphology of iPSC colonies (on both feeder cells and matrigel) and displayed a large nuclear/cytoplasmic ratio (Fig. 1B) [113]. We next selected 1 clone/line based on the morphology and growth, Selected clones were positive for Nanog and Tra1-60, as revealed using imuno-fluorescence (Fig. 1C). G-banding analysis revealed the presence of a normal karyotype (Fig. 1D). Polymerase Chain Reaction (PCR) analysis on genomic DNA from the iPSC clones confirmed the absence of plasmid vector integration (Fig. 1E). The iPSCs showed comparable expression levels with the H9 human embryonic stem cell line for *POU5F1* (encoding for OCT3/4) and *NANOG*, but lower levels for *ZFP42* (REX01) (Fig. 1F) [211]. All four iPSC lines were able to generate teratomas upon sub-cutaneous injections, with tumors showing cell differentiation into the mesoderm, endoderm and ectoderm lineages (Fig. 1G and not shown) [113].

Neuropathology in AD is first observed in the hippocampus and limbic system but ultimately spreads to all cortical areas. To obtain cortical neurons from pluripotent stem cells, we tested a method of neural induction “by default” using the H9 cell line (Fig. S1A) [125]. After 67 days in the neuronal differentiation media, cultures were processed for RNA-seq analysis. When compared to any other tissues, differentiated cells were closer to brain tissues, and even more closer to pre-frontal and frontal cortex areas of the brain than to cerebellum or

temporal lobe (Fig. S1B). Consistently, most neuronal sub-types present in the human cortex were represented, including GABAergic, glutamatergic, Cajal-Retzius, upper layers and deep layers neurons, confirming the efficiency of the method (Fig. S1C). The 2 controls (CTL1 and CTL2) and 2 AD (sAD1 and sAD2) iPSC lines were thus differentiated accordingly. Consistently, ~80% of the cells after 54 days *in vitro* were positive for □III-tubulin, a marker of newly differentiated neurons, and ~60% of the cells were also positive for MAP2, a dendritic marker (Fig. 2A-B). The neurons also expressed markers of telencephalic origin, including FOXP2, FOXG1, GABA and ChAT (Fig. 2A-B) [125]. The number of neurons/field was not significantly different between the control and AD cell lines (Fig. 2A-B).

Differentiated neurons were next analyzed for the presence of pathological markers that are characteristics of AD i.e. p-Tau and Aβ42. By immuno-fluorescence using PHF1, which recognizes phosphorylated Tau at Ser396 and Ser404, we observed strong immuno-reactivity in sAD1 neurons, and lower but consistent immuno-reactivity in sAD2 neurons (Figs. 3A and S2A) [212, 213]. PHF1 immuno-reactivity was present in axons and dendrites (not shown). Using specific antibodies, we also observed Aβ42 immuno-reactivity in both sAD1 and sAD2 neurons (Figs. 3A and S2B and not shown) [214]. By immuno-blot, we found that when compared to controls, total APP levels were much higher in sAD1 neurons, while levels of the C88/C99 fragment were much higher in sAD2 neurons (Fig. 3B) [215]. These marked pathological differences were also observed when comparing BACE1, GSK3β, p-GSK3β (Ser9) and total Tau levels (Fig. 3B). More particularly, GSK3β, p-GSK3β and Tau levels were extremely high in sAD1 neurons, while barely different from that of control neurons in sAD2 neurons (Fig. 3B). To test for Aβ42 secretion, we used ELISA. When compared to media from control neurons, Aβ42 levels were 4-5 times higher in sAD1 neurons and more than 10 times higher in the sAD2

neurons (Fig. 3C). Morphometric analyses further revealed that sAD1 and sAD2 neurons had reduced mean dendritic volume, area and diameter, altogether suggesting dendritic atrophy (Fig. 3D) [216]. While classical neuronal cell death was not prominent in sAD2 neurons, apoptotic nuclei were very abundant in sAD1 neurons as measured using activated caspase-3 immuno-labeling (Fig. 3E).

Human iPSCs can be differentiated into mini-brain organoids and these have been used to produce models of normal human brain development and of diseases such as microcephaly [126]. Applying this method for all iPSC lines, we have generated floating brain organoids that were maintained for a period of 90 days (Fig. 4A). Brain organoids measuring ~2 mm in diameter were harvested to perform immuno-fluorescence analyses on frozen sections. Brain organoids frequently showed an internal cavity and expressed the neuronal markers □III-tubulin and MAP2 (Fig. 4B and not shown). Brain organoids from the sAD2 cell line were highly immmuno-reactive for Aβ42 (Figs. 4B). The specificity for amyloid immuno-reactivity in sAD2 organoids was confirmed using 3 distinct Aβ42 antibodies (Fig. 4C). By confocal microscopy, we observed intra-cellular and extra-cellular accumulation of Aβ42-positive fiber-like structures (Fig. 4C). Classical amyloid plaques of ~60 μm in diameter were however not observed. Both sAD1 and sAD2 organoids also showed p-Tau accumulation, with the Tau pathology being more severe in the sAD1 organoids (Fig. S3). High-resolution microscopy analyses furthermore revealed the presence of p-Tau deposits resembling p-Tau tangles and that were more prominent in sAD1 neurons (Fig. S3). We concluded that brain organoids produced from AD iPSCs can help recapitulate some of the neuronal pathologies observed in AD brains.

DISCUSSION

We reported on the generation of iPSCs from elderly controls and AD patients that could be differentiated into cortical neurons and brain organoids. In contrast to control neurons, AD neurons from both patients displayed intra-neuronal accumulation of p-Tau and amyloid and produced high levels of the secreted Aβ42 peptide. AD brain organoids also showed accumulation of fiber-like amyloid deposits and p-Tau tangles. These results suggest that the two patient-derived iPSC lines can recapitulate several of AD neuropathological hallmarks upon neuronal differentiation.

The origin of AD still remains elusive, with aging being the number one risk factor. While the disease is largely assumed to be restricted to the brain, it is intriguing that dermal fibroblasts can carry the disease imprint after reprogrammation into iPSCs and upon neuronal differentiation. When compared, the 2 AD lines presented similar but yet distinct pathological phenotypes. Both the amyloid and Tau pathologies were severe in sAD1 neurons, while the amyloid pathology was predominant in sAD2 neurons. In sAD2 neurons, increased BACE1 levels also correlated with abundance of the C88/99 fragment and with elevated secretion of the Aβ42 peptide.

Most cellular and animal models of AD are based on the over-expression of mutant human APP, PSEN1 and/or PSEN2 genes [129, 175, 217-221]. These models may recapitulate FAD but should not be considered as models of AD, since these genes are not known to be specifically duplicated or mutated in AD [222]. Likewise, mutations or duplications of *MAPT* have been associated with frontotemporal dementia linked to Chromosome 17 (FTD-17), not with AD [192, 223, 224]. In contrast to these FAD and FTD-17 models, iPSC-derived AD

neurons are not genetically modified and intrinsically carry the disease's imprint [131, 133, 134]. We conclude that despite the fact that they cannot reflect the complexity present in a living organism, AD neurons produced from some iPSC lines are able to recapitulate pathologies observed in the patient's neurons *in situ* and thus represent a unique and valuable tool to study AD.

AUTHOR CONTRIBUTIONS

Conceived and designed, GB, AF

Performed the experiments, AF, AB, RH

Analyzed the data, GB, AF

Wrote the paper, GB, AF

ACKNOWLEDGMENT

This work was supported by grants from the Canadian Institute of Health Research (CIHR) and National Science and Engineering Research Council of Canada (NSERC). We thank Dr. Patrick Nkanza for the histological analysis of the teratomas. AF, RH and AB were supported by fellowships from the Molecular Biology Program of Université de Montréal.

METHODS SUMMARY

Human embryonic stem cells were used in accordance with Canadian Institute Health Research (CIHR) guidelines and approved by the "Comité de Surveillance de la Recherche sur les Cellules Souches" (CSRCS) of the CIHR and Maisonneuve-Rosemont Hospital Ethic Committee. The complete method is available in Supplementary Informations.

REFERENCES

Anfossi, M., Vuono, R., Maletta, R., Virdee, K., Mirabelli, M., Colao, R., Puccio, G., Bernardi, L., Frangipane, F., Gallo, M.*, et al.* (2011). Compound heterozygosity of 2 novel MAPT mutations in frontotemporal dementia. Neurobiol. Aging *32*, 757 e751-757 e711.

Blennow, K., de Leon, M.J., and Zetterberg, H. (2006). Alzheimer's disease. Lancet *368*, 387-403.

Buee, L., Bussiere, T., Buee-Scherrer, V., Delacourte, A., and Hof, P.R. (2000). Tau protein isoforms, phosphorylation and role in neurodegenerative disorders. Brain Res. Brain Res. Rev. *33*, 95-130.

Chapman, P.F., White, G.L., Jones, M.W., Cooper-Blacketer, D., Marshall, V.J., Irizarry, M., Younkin, L., Good, M.A., Bliss, T.V., Hyman, B.T.*, et al.* (1999). Impaired synaptic plasticity and learning in aged amyloid precursor protein transgenic mice. Nat. Neurosci. *2*, 271-276.

Choi, S.H., Kim, Y.H., Hebisch, M., Sliwinski, C., Lee, S., D'Avanzo, C., Chen, H., Hooli, B., Asselin, C., Muffat, J.*, et al.* (2014). A three-dimensional human neural cell culture model of Alzheimer's disease. Nature *515*, 274-278.

Cuyvers, E., and Sleegers, K. (2016). Genetic variations underlying Alzheimer's disease: evidence from genome-wide association studies and beyond. Lancet Neurol *15*, 857-868.

Espuny-Camacho, I., Michelsen, K.A., Gall, D., Linaro, D., Hasche, A., Bonnefont, J., Bali, C., Orduz, D., Bilheu, A., Herpoel, A.*, et al.* (2013). Pyramidal neurons derived from human pluripotent stem cells integrate efficiently into mouse brain circuits in vivo. Neuron *77*, 440-456.

Galvan, V., Gorostiza, O.F., Banwait, S., Ataie, M., Logvinova, A.V., Sitaraman, S., Carlson, E., Sagi, S.A., Chevallier, N., Jin, K.*, et al.* (2006). Reversal of Alzheimer's-like pathology and behavior in human APP transgenic mice by mutation of Asp664. Proc. Natl. Acad. Sci. U. S. A. *103*, 7130-7135.

Hebert, L.E., Weuve, J., Scherr, P.A., and Evans, D.A. (2013). Alzheimer disease in the United States (2010-2050) estimated using the 2010 census. Neurology *80*, 1778-1783.

Hooli, B.V., Kovacs-Vajna, Z.M., Mullin, K., Blumenthal, M.A., Mattheisen, M., Zhang, C., Lange, C., Mohapatra, G., Bertram, L., and Tanzi, R.E. (2014). Rare autosomal copy number variations in early-onset familial Alzheimer's disease. Mol. Psychiatry *19*, 676-681.

Hossini, A.M., Megges, M., Prigione, A., Lichtner, B., Toliat, M.R., Wruck, W., Schroter, F., Nuernberg, P., Kroll, H., Makrantonaki, E.*, et al.* (2015). Induced pluripotent stem cell-derived neuronal cells from a sporadic Alzheimer's disease donor as a model for investigating AD-associated gene regulatory networks. BMC Genomics *16*, 84.

Ishida, C., Kobayashi, K., Kitamura, T., Ujike, H., Iwasa, K., and Yamada, M. (2015). Frontotemporal dementia with parkinsonism linked to chromosome 17 with the MAPT R406W mutation presenting with a broad distribution of abundant senile plaques. Neuropathology *35*, 75-82.

Israel, M.A., Yuan, S.H., Bardy, C., Reyna, S.M., Mu, Y., Herrera, C., Hefferan, M.P., Van Gorp, S., Nazor, K.L., Boscolo, F.S.*, et al.* (2012). Probing sporadic and familial Alzheimer's disease using induced pluripotent stem cells. Nature *482*, 216-220.

Ittner, L.M., Ke, Y.D., Delerue, F., Bi, M., Gladbach, A., van Eersel, J., Wolfing, H., Chieng, B.C., Christie, M.J., Napier, I.A.*, et al.* (2010). Dendritic function of tau mediates amyloid-beta toxicity in Alzheimer's disease mouse models. Cell *142*, 387-397.

Kanekiyo, T., Xu, H., and Bu, G. (2014). ApoE and Abeta in Alzheimer's disease: accidental encounters or partners? Neuron *81*, 740-754.

Kondo, T., Asai, M., Tsukita, K., Kutoku, Y., Ohsawa, Y., Sunada, Y., Imamura, K., Egawa, N., Yahata, N., Okita, K.*, et al.* (2013). Modeling Alzheimer's disease with iPSCs reveals stress phenotypes associated with intracellular Abeta and differential drug responsiveness. Cell Stem Cell *12*, 487-496.

Lancaster, M.A., Renner, M., Martin, C.A., Wenzel, D., Bicknell, L.S., Hurles, M.E., Homfray, T., Penninger, J.M., Jackson, A.P., and Knoblich, J.A. (2013). Cerebral organoids model human brain development and microcephaly. Nature *501*, 373-379.

Lauritzen, I., Pardossi-Piquard, R., Bauer, C., Brigham, E., Abraham, J.D., Ranaldi, S., Fraser, P., St-George-Hyslop, P., Le Thuc, O., Espin, V.*, et al.* (2012). The beta-secretase-derived C-terminal fragment of betaAPP, C99, but not Abeta, is a key contributor to early intraneuronal lesions in triple-transgenic mouse hippocampus. J. Neurosci. *32*, 16243-16255a.

Leissring, M.A., Farris, W., Chang, A.Y., Walsh, D.M., Wu, X., Sun, X., Frosch, M.P., and Selkoe, D.J. (2003). Enhanced proteolysis of beta-amyloid in APP transgenic mice prevents plaque formation, secondary pathology, and premature death. Neuron *40*, 1087-1093.

Lujan, E., Zunder, E.R., Ng, Y.H., Goronzy, I.N., Nolan, G.P., and Wernig, M. (2015). Early reprogramming regulators identified by prospective isolation and mass cytometry. Nature *521*, 352-356.

Mendieta, J., Fuertes, M.A., Kunjishapatham, R., Santa-Maria, I., Moreno, F.J., Alonso, C., Gago, F., Munoz, V., Avila, J., and Hernandez, F. (2005). Phosphorylation modulates the alpha-helical structure and polymerization of a peptide from the third tau microtubule-binding repeat. Biochim. Biophys. Acta *1721*, 16-26.

Okita, K., Matsumura, Y., Sato, Y., Okada, A., Morizane, A., Okamoto, S., Hong, H., Nakagawa, M., Tanabe, K., Tezuka, K.*, et al.* (2011). A more efficient method to generate integration-free human iPS cells. Nat Methods *8*, 409-412.

Qiang, L., Fujita, R., and Abeliovich, A. (2013). Remodeling neurodegeneration: somatic cell reprogramming-based models of adult neurological disorders. Neuron *78*, 957-969.

Rovelet-Lecrux, A., Hannequin, D., Guillin, O., Legallic, S., Jurici, S., Wallon, D., Frebourg, T., and Campion, D. (2010). Frontotemporal dementia phenotype associated with MAPT gene duplication. J Alzheimers Dis *21*, 897-902.

Savva, G.M., Wharton, S.B., Ince, P.G., Forster, G., Matthews, F.E., and Brayne, C. (2009). Age, neuropathology, and dementia. N. Engl. J. Med. *360*, 2302-2309.

Takahashi, K., Tanabe, K., Ohnuki, M., Narita, M., Ichisaka, T., Tomoda, K., and Yamanaka, S. (2007). Induction of pluripotent stem cells from adult human fibroblasts by defined factors. Cell *131*, 861-872.

Tomiyama, T., Matsuyama, S., Iso, H., Umeda, T., Takuma, H., Ohnishi, K., Ishibashi, K., Teraoka, R., Sakama, N., Yamashita, T.*, et al.* (2010). A mouse model of amyloid beta oligomers: their contribution to synaptic alteration, abnormal tau phosphorylation, glial activation, and neuronal loss in vivo. J. Neurosci. *30*, 4845-4856.

Villemagne, V.L., Burnham, S., Bourgeat, P., Brown, B., Ellis, K.A., Salvado, O., Szoeke, C., Macaulay, S.L., Martins, R., Maruff, P.*, et al.* (2013). Amyloid beta deposition, neurodegeneration, and cognitive decline in sporadic Alzheimer's disease: a prospective cohort study. Lancet Neurol *12*, 357-367.

Yagi, T., Ito, D., Okada, Y., Akamatsu, W., Nihei, Y., Yoshizaki, T., Yamanaka, S., Okano, H., and Suzuki, N. (2011). Modeling familial Alzheimer's disease with induced pluripotent stem cells. Hum. Mol. Genet. *20*, 4530-4539.

Youmans, K.L., Tai, L.M., Kanekiyo, T., Stine, W.B., Jr., Michon, S.C., Nwabuisi-Heath, E., Manelli, A.M., Fu, Y., Riordan, S., Eimer, W.A.*, et al.* (2012). Intraneuronal Abeta detection in 5xFAD mice by a new Abeta-specific antibody. Mol Neurodegener *7*, 8.

Flamier *et al.* 2018

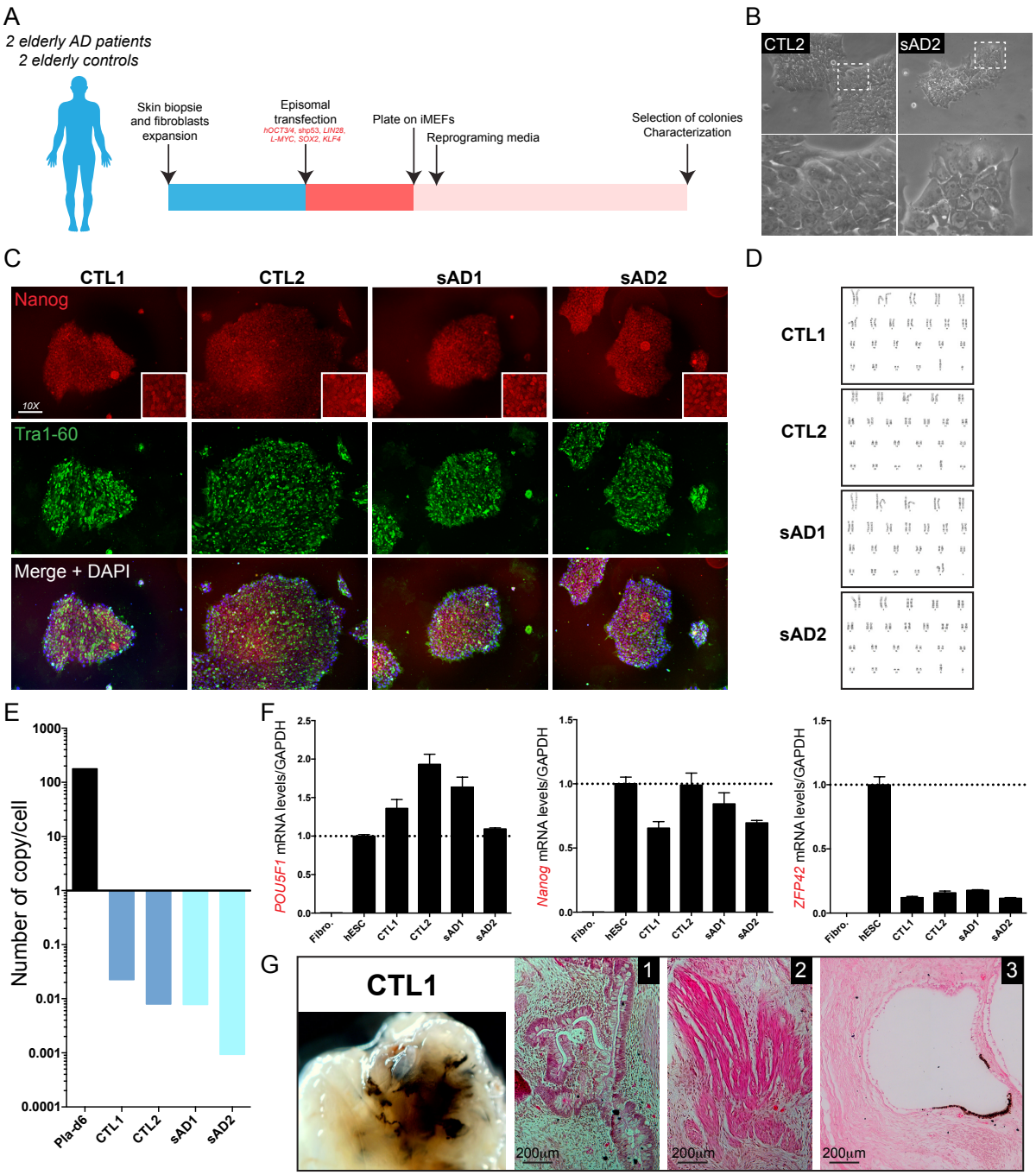

Figure 1

Figure 1. Generation of iPSCs from control and AD patient's fibroblasts

(A) Schematic overview for the reprogramming of dermal fibroblasts into induced pluripotent stem cells (iPSC).

(B) Phase contrast representative images of one control iPSC line (CTL2) and one sporadic AD iPSC line (sAD2) adapted to Matrigel culture conditions. The insets exemplify the high nuclear/cytoplasm ratio, characteristic of pluripotency.

(C) Immuno-fluorescence on CTL1, CTL2, sAD1 and sAD2 iPSC line colonies for pluripotency markers Nanog and Tra1-60. Note the nuclear localization of Nanog in the insets. Scale bar: 40μm.

(D) Karyotyping analyses on CTL1, CTL2, sAD1 and sAD2 iPSC lines by G-banding.

(E) Quantification of episomal integrations on CTL1, CTL2, sAD1 and sAD2 iPSC lines by quantitative genomic PCR. Fibroblasts after 6 days of reprogramming were used as positive control (Pla-d6).

(F) *POU5F1* (OCT3/4), *NANOG* and *ZFP42* (REX1) gene expression levels in qPCR normalized to GAPDH on CTL1, CTL2, sAD1 and sAD2 iPSC lines. Dermal fibroblasts (Fibro.) and human embryonic stem cell line H9 (hESC) were used as negative and positive controls respectively. N=3 for each line. All values are mean ± SEM.

(G) Teratoma formation after injection of CTL1 iPSC line under the skin of NOD/SCID mice. Hematoxylin and Eosin histology shows the formation of glandular epithelium (1), skeletal muscle (2) and retinal pigment epithelium (3).

Flamier *et al.* 2018

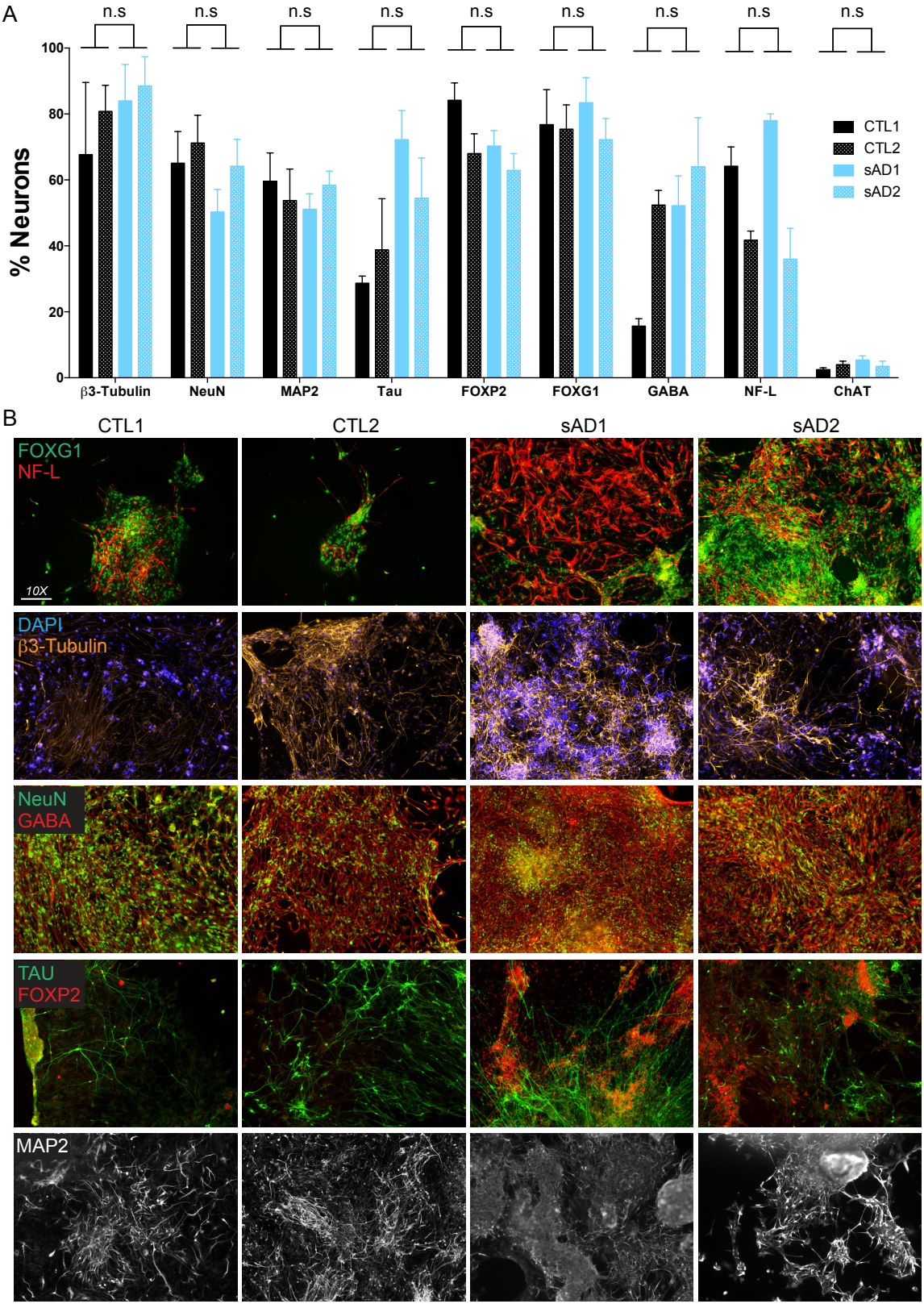

Figure 2

Figure 2. Differentiation of iPSCs into cortical neurons

(A) Differentiated neuronal cultures were labeled with antibodies against βIII-tubulin, NeuN, MAP2, Tau (total), FOXP2, FOXG1, GABA, NF-L, and ChAT. No significant difference in the number of positive neurons for each marker was found between CTL1, CTL2, sAD1 and sAD2 cultures (n = 4 biological replicates/cell line). All values are mean ± SEM. Analyzed by Student's unpaired t-test.

(B) Representative images of immuno-labeled cultures after 2 months of differentiation. Scale bar: 100μm.

Flamier *et al.* 2018

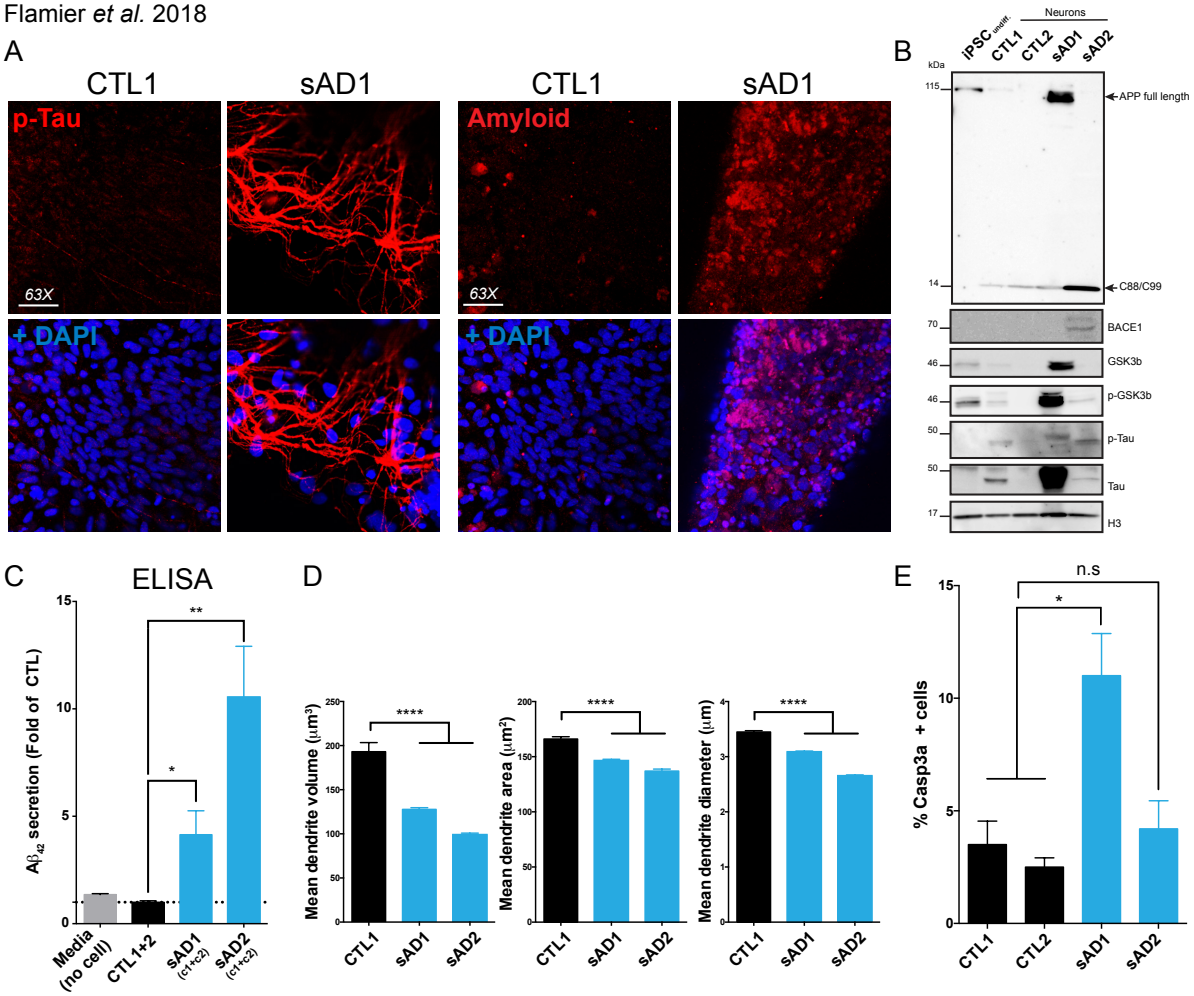

Figure 3

Figure 3. p-Tau accumulation and Amyloid-beta 42 secretion in AD neurons

(A) p-Tau (PHF1) and Amyloid (B-4) accumulation in sAD neurons but not in CTL neurons (21 days of maturation).

(B) Immunoblot on CTL1, CTL2, sAD1 and sAD2 neuronal cultures for APP, BACE1, GSK3beta, p-GSK3beta (Ser9), phospho-Tau (PH13) and Tau (K9JA). H3 was used as loading control. Undifferentiated iPSC was used as negative control.

(C) Extracellular Aβ42 levels in CTL1+2 (n = 16; 2 lines; 4 biological replicates in 2 technical replicates), sAD1 (n = 16; 2 clones; 4 biological replicates in 2 technical replicates) and sAD2 (n = 16; 2 clones; 4 biological replicates in 2 technical replicates) neurons by ELISA. Media not conditioned is used as negative control. All values are mean ± SEM.

(D) Morphometric analysis of the dendrite's volume, area and diameter in CTL1 (N>150 dendrites from 4 independent differentiations), sAD1 (N>150 dendrites from 4 independent differentiations) and sAD2 (N>150 dendrites from 4 independent differentiations) neurons by using IMARIS platform. All values are mean ± SEM. (****) P< 0.0001 by Student's unpaired t-test.

(E) Quantification of the number of Caspase 3 activated positive neurons in CTL1, CTL2, sAD1 and sAD2 neuronal cultures (n = 4 for each culture). All values are mean ± SEM. (*) P< 0.05 by Student's unpaired t-test.

Flamier *et al.* 2018

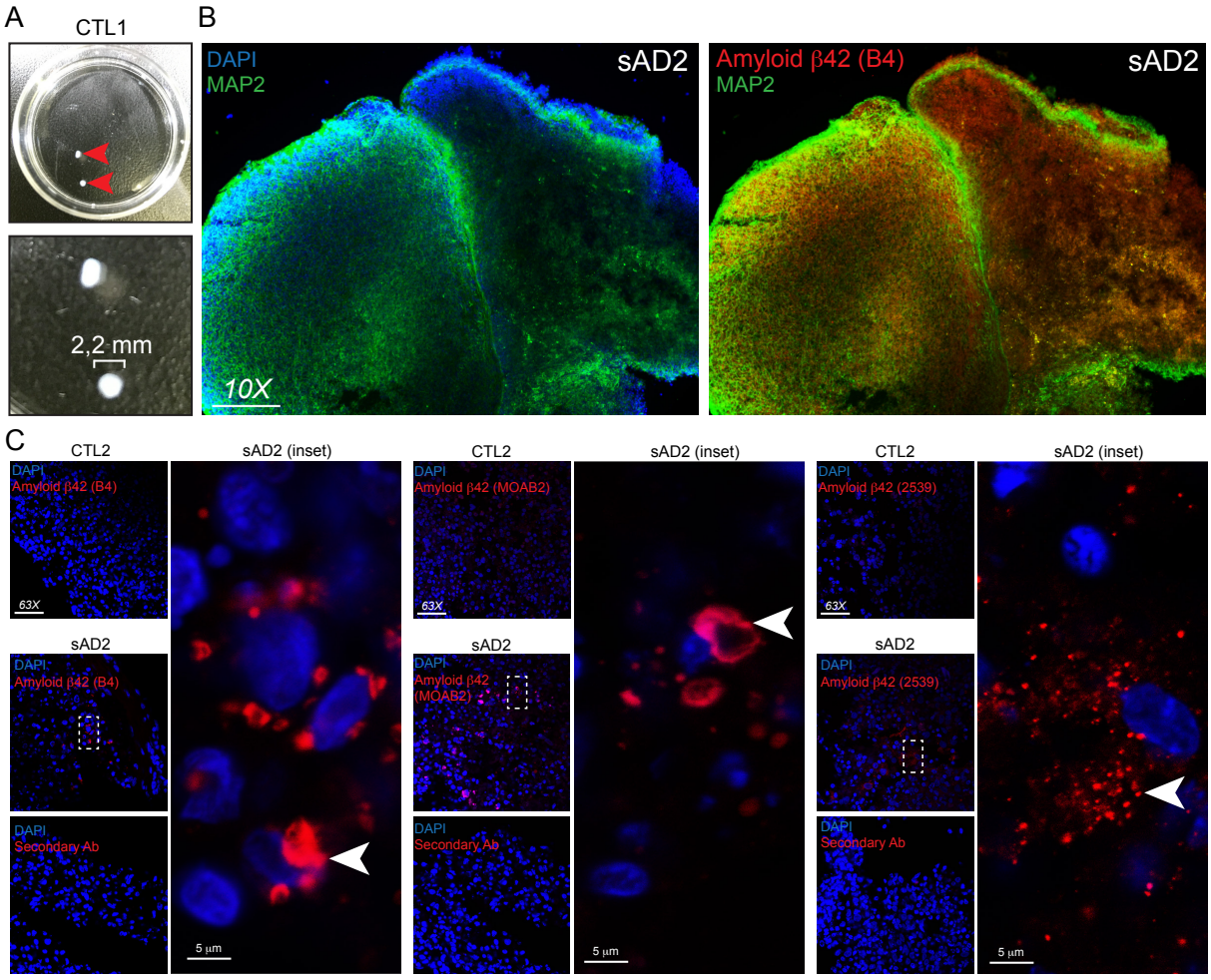

Figure 4

Figure 4. Accumulation of fiber-like amyloid structures on AD brain organoids

(A) Images of brain organoids formed using CTL1 iPSC lines after 3 months of maturation.

(B) Dendritic staining (MAP2) and Amyloid staining in sAD2 brain organoids cryosectioned after 3 months of maturation. Scale bar: 100 μm.

(C) Extra-cellular Amyloid-beta 42 accumulation in sAD2 brain organoids but not in CTL1 brain organoids after 4 months of differentiation using 3 independent antibodies (B4, MOAB2 and ab2539). The white arrow shows extra-cellular deposits. sAD2 brain organoids stained only with the secondary antibody was used to assay for possible non-specific background fluorescence. Scale bar: 40μm.

SUPPLEMENTARY MATERIALS AND METHODS

Generation of human induced pluripotent stem cells

Dermal fibroblasts of a 82 years old male and a 92 years old female with no cognitive impairments were used as controls (CTL1 and CTL2, respectively). Dermal fibroblasts were taken from a 72 years old male (sAD1) affected by AD and with no familial history of AD. Dermal fibroblasts were taken from a 90 years old male (sAD2) clinically affected by AD. The presence of p-Tau tangles and amyloid plaques was confirmed in post-mortem studies. This patient had a dementia since the age of 87 years old and had no familial history of AD. The reprogramming of dermal fibroblasts was based on a previous method [210]. Briefly, dermal fibroblasts were expanded (using DMEM/F12 + 10% FBS media) and transfected by 3 plasmids for the expression of Yamanaka reprogramming factors (pCXLE-hSK, pCXLE-hOCT3/4-shp53-F and pCXLE-hUL). After 7 days, transfected cells were transferred onto irradiated Mouse Embryonic Fibroblasts (MEF) and further cultured in ReproTeSR media (StemCell Technologies). After 25-30 days of transfection, iPSC clones were manually picked, expanded and characterized.

Differentiation of human pluripotent stem cells into cortical neurons

The differentiation protocol was based on a previous study. However, the Noggin agonist LDN193189 was used to reduce recombinant Noggin concentration. The CTL1, CTL2, sAD1 and sAD2 cell lines were dissociated using Accutase (Innovative Cell Technology #AT-104) and platted on growth factor reduced matrigel (Corning #356231) in PeproGrow hES cell media (PeproTech #BM-hESC) supplemented with ROCK inhibitor (Y-27632;10µM, Cayman

Chemical #10005583). Upon 70% of confluency, the media was changed to DDM supplemented with B27 (1X final), Noggin (10 ng/ml, PeproTech #120-10C) and LDN193189 (0.5µM; Sigma #SML0559). The medium was changed every day. After 16 days of differentiation, the medium was changed to DDM/B27 and replenished every day. At day 24, neural progenitors were manually detached from the plate and platted on growth factor reduced matrigel coated plates or chamber slides (LabTek #154534). Five days after the dissociation/infection, half of the medium was changed for Neurobasal A media supplemented with B27 (1X final) and changed again every three days.

ELISA

ELISA assays (Invitrogen #PP0812) were done on cellular supernatants. Cell supernatants were sonicated before the assay. Extracts were processed according to manufacturer's instructions. Cellular extracts were used to normalize to the total quantity of proteins.

Immunofluorescence microscopy

All secondary antibodies were tested alone or in combination to assay for possible non-specific background fluorescence. Cells were fixed with 4% PFA for 15 min and permeabilized with Triton X-100 for 10 min. Unspecific antigen blocking was performed using 1% BSA in PBST for 30 min. Cells were incubated with the primary antibody overnight at 4C in a humidified chamber. After incubation with the secondary antibody, slides were counter stained with DAPI. Pictures were taken using a confocal microscopy system (Olympus). For figures 4 and 5, brain organoids were fixed overnight with 4% PFA, dehydrated using sucrose gradient baths and cryo-sectioned (20µm) prior to permeabilization. For Figure 4, formic acid at 70% was added for 10

min after fixation.

Antibodies list:

Name Reactivity (h:Human; ms:Mouse)	Source	Cat#	Dilution IF/IHC	Dilution WB
Amyloid – Aβ42 h and ms	Abcam	ab2539	1/400	
Amyloid – Aβ42 (MOAB2) h and ms	Novus	NBP2-13075	1/400	
Amyloid – Aβ42 (B4) h	SCB	sc-28365	1/400	1/500
BACE1	Thermo	PA1-757		1/1000
BIII-Tubulin	Abcam	ab78078	1/400	
Caspase3 activated	Cell Signaling	9661	1/400	
ChAT	Thermo	PA5-26597	1/50	
FOXG1	Abcam	ab18259	1/400	
GABARG1	Abcam	ab55051	1/1000	
GSK3beta	Cell Signaling	9315		1/1000
Histone H3 (C-16)	SCB	sc-8654		1/250
MAP2	Abcam	ab5392	1/10000	
NeuN	Abcam	ab104225	1/500	

p-GSK3beta	Thermo	MA5-14873		1/1000
p-Tau (PHF1)	Peter Davies, Albert Einstein College of Medicine		1/50	1/250
Tau total (K9JA)	DAKO	A0024		1/500
NF-L	SCB	sc-20012	1/200	
FOXP2	SCB	sc-517261	1/200	
Nanog	Abcam	ab21624	1/400	
Tra1-60	Abcam	ab16288	1/400	

Quantification of immunofluorescence images

For Figure 3D, low magnification images of MAP2 staining was used for the quantifications. IMARIS station v8.4.1 (Bitplane) was used with the filament module for dendritic tracing. A scholl regression coefficient at 1μm was set.

Western Blot

Cell extracts were homogenized in the Complete Mini Protease inhibitor cocktail solution (Roche Diagnostics), followed by sonication. Protein material was quantified using the Bradford reagent. Proteins were resolved in 1x Laemelli reducing buffer by SDS-PAGE electrophoresis and transferred to a Nitrocellulose blotting membrane (Bio-Rad). Subsequently, membranes

were blocked for 1h in 5% non-fat milk-1X TBS solution and incubated overnight with primary antibodies. Membranes were then washed 3 times in 1X TBS; 0.05% Tween solution and incubated for 1h with corresponding horseradish peroxidase-conjugated secondary antibodies. Membranes were developed using the Immobilon Western (Millipore). Blots were quantified using the Image quant program.

Real-time RT-PCR

RNA was isolated using TRIzol reagent (Invitrogen). Reverse transcription (RT) was performed using 1 μg of total RNA and the MML-V reverse transcriptase (Invitrogen). Real-time PCR was carried in triplicates using Platinum SYBRGreen Supermix (Invitrogen) and Real-time PCR apparatus (ABI prism 7002). Primers used were:

ZFP42_F	AGAAACGGGCAAAGACAAGAC
ZFP42_R	GCTGACAGGTTCTATTTCCGC
NANOG_F	AAGGTCCCGGTCAAGAAACAG
NANOG_R	CTTCTGCGTCACACCATTGC
POU5F1_F	CTTGAATCCCGAATGGAAAGGG
POU5F1_R	GTGTATATCCCAGGGTGATCCTC

Detection of potential plasmid integration

Genomic DNA was extracted using DNA/RNAeasy kit from Qiagen from each iPSC line and then subjected to real-time PCR as previously described [210]. Fibroblasts transfected with the 3 plasmids and collected at day 6 were used as positive control.

Teratoma formation

$2x10^5$ iPS cells from each line were collected and re-suspended into DMEM/F12/1%Matrigel supplemented with ROCK inhibitor (Y-27632;10µM, Cayman Chemical #10005583). Each line was injected into 2 flanks of NOD/SCID mice. When the tumor was greater than 0,5 cm the teratoma was extracted and included into paraffin blocks for histology.

Statistical analysis

Statistical analysis was performed using Graphpad software (Prism 6). Statistical differences were analyzed using Student's *t*-test for unpaired samples. In all cases, the criterion for significance (*P* value) was set as mentioned in the figures. When comparisons were made using independent samples of equal size and variance following a normal distribution, significance was assessed using an unpaired two-sided Student's t-test. Where several groups were compared, significance was assessed by ANOVA and adjusted for multiple comparisons using the Bonferroni correction.

METHOD REFERENCES

Okita, K., Matsumura, Y., Sato, Y., Okada, A., Morizane, A., Okamoto, S., Hong, H., Nakagawa, M., Tanabe, K., Tezuka, K.*, et al.* (2011). A more efficient method to generate integration-free human iPS cells. Nat Methods *8*, 409-412.

Flamier *et al.* 2018

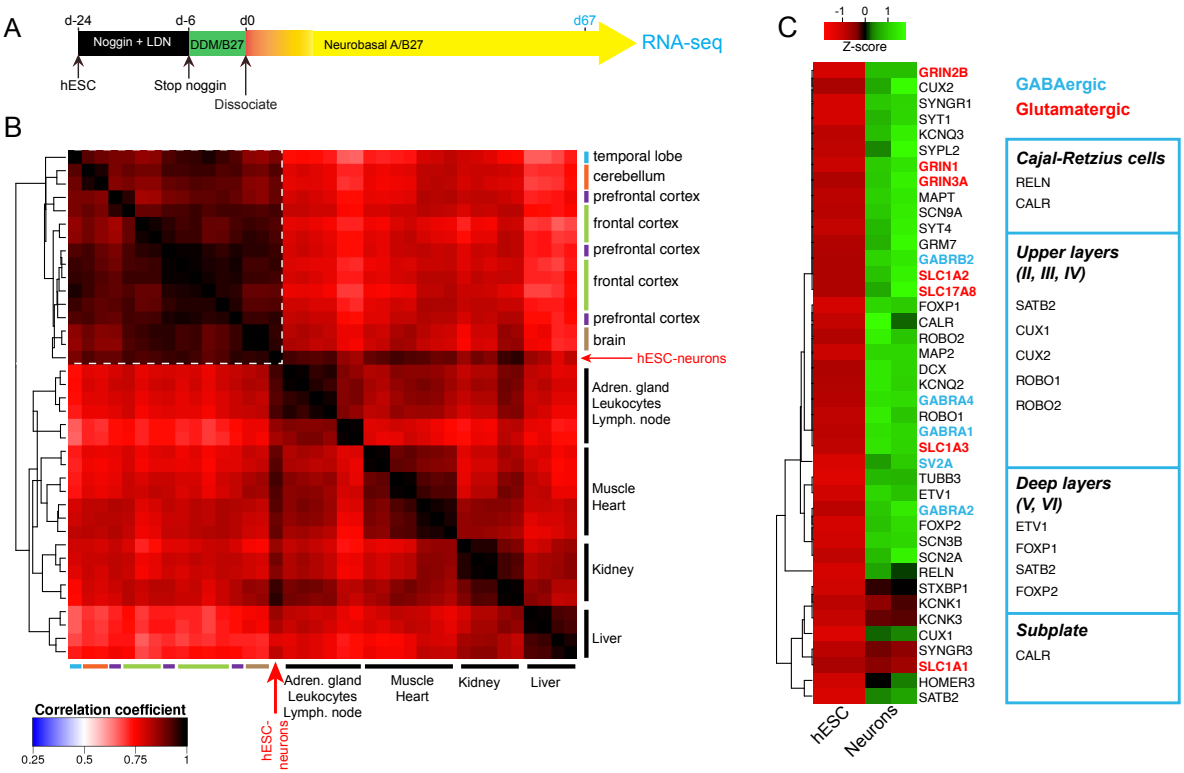

Figure S1

Figure S1. Differentiation of hESCs into cortical neurons

(A) Schematic representation of the neural differentiation protocol.

(B) Whole transcriptome correlation plot between hESC-derived neurons and a collection of 52 RNA-seq data from human body tissues (GTEx project).

(C) Comparative analysis of gene expression between undifferentiated hESC and hESC-derived neurons for multiple cortical neuron markers.

Flamier *et al.* 2018

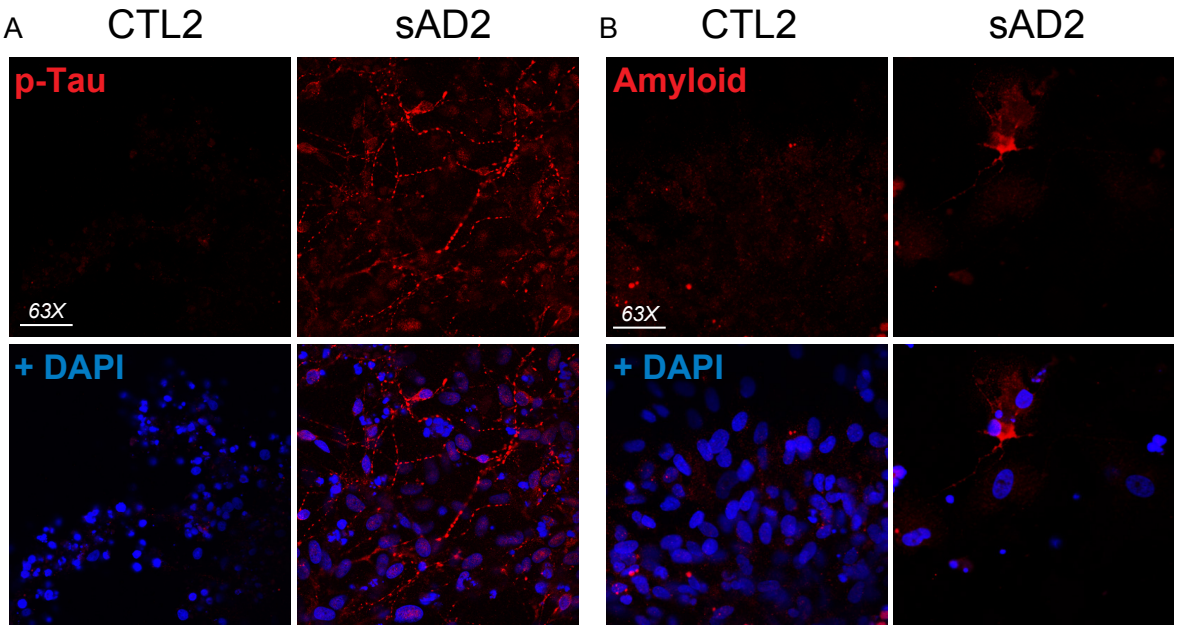

Figure S2

Figure S2. p-Tau accumulation and Amyloid-beta 42 secretion in sAD2 neurons

(A) p-Tau (PHF1) accumulation in sAD neurons but not in CTL2 neurons. Neurons were labeled after 21 days of maturation. Scale bar: 40μm.

(B) Amyloid (B-4) accumulation in sAD neurons but not in CTL2 neurons. Neurons were labeled after 21 days of maturation. Scale bar: 40μm.

Flamier *et al.* 2018

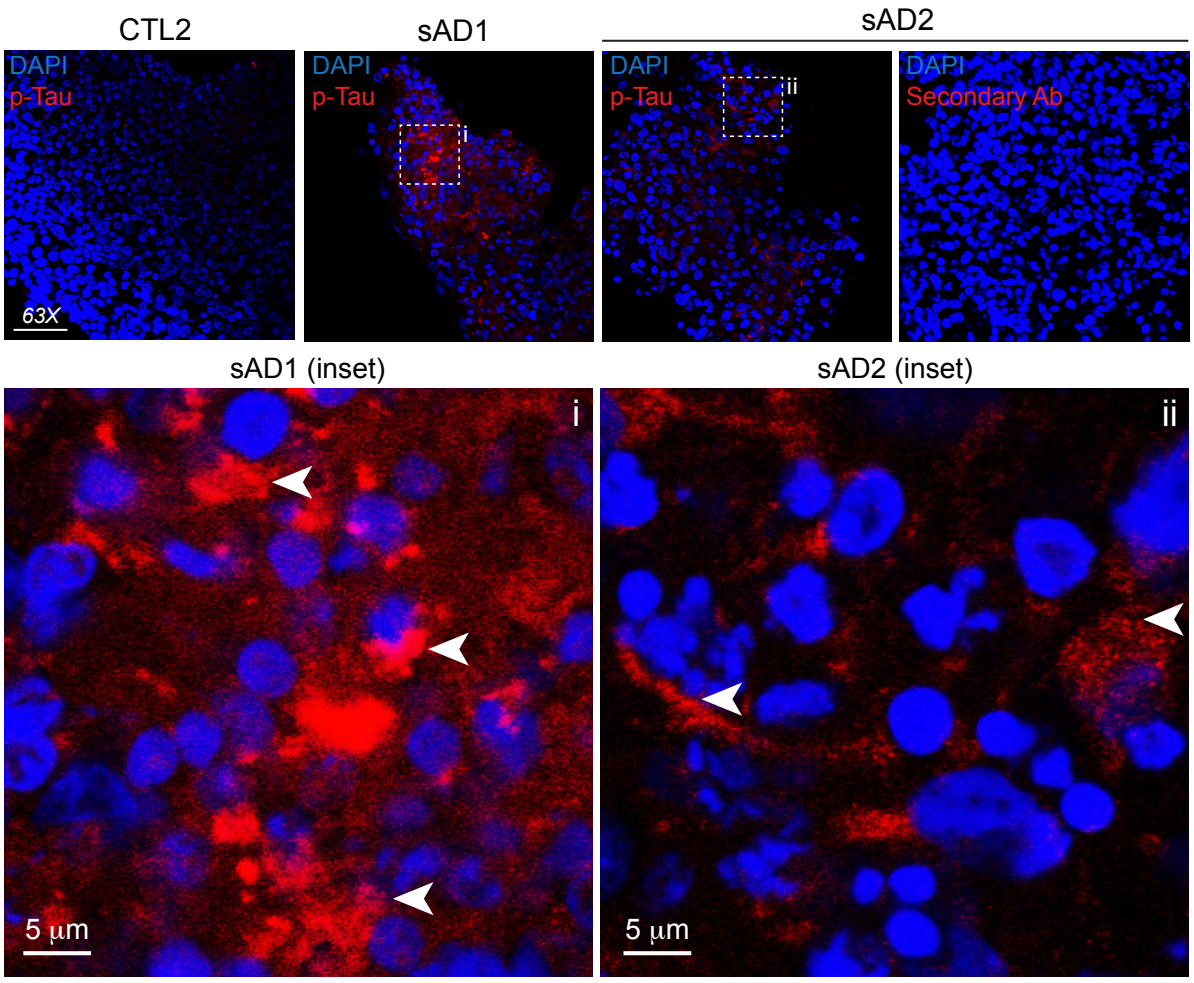

Figure S3

Figure S3. p-Tau accumulation in AD organoids

p-Tau accumulation in sAD1 and sAD2 brain organoids, but not in CTL2 brain organoids after 4 months of differentiation. Sections from the sAD2 brain organoids were labeled only with the secondary antibody to test for possible non-specific fluorescence. The white arrows in the high magnification images indicate p-Tau deposits resembling Tau tangles. Scale bar: 40μm.

CHAPITRE 4: Discussion et perspectives

Ce dernier chapitre propose une discussion sur mes travaux et ouvre la voie vers les perspectives thérapeutiques liées à mon projet. Il décrit entre autre par quels mécanismes BMI1 pourrait être réprimé dans la MA et comment on peut tirer parti de cette découverte en clinique.

SECTION 1: Fonction moléculaire de BMI1 dans la MA

Comme on peut le voir dans la Figure 7E du chapitre 2, le traitement des neurones corticaux shBMI1 aux inhibiteurs des β- et γ-sécrétases ne permet pas de limiter la tauopathie. Ces résultats indiquent que la tauopathie peut être dissociée de l'amyloïdopathie et que, par conséquent, BMI1 régule ces deux aspects de la pathologie de façon indépendante.

4.1.1 BMI1 et la tauopathie

Dans la figure 7A du chapitre 2, nous pouvons voir que la perte de BMI1 dans les neurones corticaux entraine une accumulation de protéines impliquées dans l'Alzheimer. Parmi celles-ci, la protéine Tau totale, la forme hyperphosphorylée de Tau ainsi que la GSK3β, une kinase pouvant phosphoryler Tau, sont particulièrement augmentées [225]. Cependant, lorsqu'on regarde le niveau d'ARN messagers de ces marqueurs pathologiques, nous pouvons voir que l'expression de la *GSK3B* est inchangée dans les neurones shBMI1 alors que les niveaux de *MAPT* y sont doublés. Cette observation nous a amené à penser que BMI1 serait capable de se lier directement au niveau de *MAPT* pour le réprimer. Ceci fut confirmé par des expériences d'immunoprécipitation de la chromatine sur des neurones shCTL et shBMI1 mais aussi sur des échantillons de cerveaux sains et affectés de la MA. Nous savons donc que la perte de BMI1 entraine une dérepression directe du gène MAPT ce qui provoque une surproduction de Tau. En parallèle, la GSK3β est stabilisée par un mécanisme encore inconnu ce qui permet une phosphorylation accrue de Tau. C'est l'accumulation de ces deux protéines qui permet d'induire la tauopathie [226, 227].

Le lien potentiel entre BMI1 et la GSK3β n'a que très peu été étudié. En 2009, une étude a rapporté des résultats contradictoires à nos observations mais dans un modèle de cancer. Dans

cette étude, la diminution de BMI1 au moyen d'un shARN dans des cellules primaires de glioblastome entraine une diminution de la GSK3β. Sans établir le lien moléculaire entre la GSK3β et BMI1, les auteurs proposent que ces deux protéines soient liées et orchestrent la différenciation des cellules souches cancéreuses [228]. Il semblerait donc que l'effet de la perte de BMI1 sur la GSK3β soit dépendante du contexte cellulaire. Cette différence pourrait s'expliquer par un défaut de localisation cellulaire de la GSK3β. En effet, la localisation de la GSK3β est régulée par la voie Phosphatidylinositol 3-kinase (PI3K)/protéine kinase B (AKT1) qui phosphoryle directement la GSK3β pour en inhiber sa fonction enzymatique [229, 230]. La GSK3β phosphorylée et donc inactive est alors relocalisée dans le noyau. Ce phénomène est retrouvé dans la plupart des cancers [229, 231, 232]. À l'inverse, la GSK3β dans les neurones sains ont une localisation cytoplasmique [233]. Par ailleurs, il a pu être démontré dans de nombreuses études que la perte de BMI1 entraine de façon mécanique une baisse de la voie de signalisation PI3K/AKT [234, 235].

Ainsi, je propose que la perte de BMI1 dans les neurones corticaux humains puisse provoquer une réduction de la signalisation PI3K/AKT. AKT étant moins présente pour phosphoryler et inactiver la GSK3β, cette dernière reste localisée dans le cytoplasme et se lie à la protéine Tau pour la phosphoryler. Pour vérifier cette hypothèse, il faudrait tout d'abord analyser le niveau des formes natives et phosphorylées d'AKT dans des neurones shBMI1. Si AKT est diminué dans ce modèle, il faudrait par la suite stabiliser AKT dans ces neurones et regarder l'effet sur la phosphorylation de la GSK3β et l'hyperphosphorylation de Tau.

4.1.2 BMI1 et l'amyloïdopathie

Plusieurs phénomènes peuvent expliquer l'apparition d'une amyloïdopathie après la perte de BMI1. Tout d'abords, nous savons que la diminution de BMI1 entraine une augmentation de $p19^{ARF}$ ce qui a pour conséquence d'inhiber MDM2, le principal inhibiteur de p53 [163, 171, 193, 194]. Nous avons par ailleurs pu démontrer dans le chapitre 2 que la stabilisation de p53 induisait un défaut de la capacité du protéasome à dégrader les protéines poly-ubiquitynées. Cette perte de fonction peut entrainer une accumulation d'amyloïde fibrillaire et promouvoir une neurodégénérescence [197, 198].

En parallèle à cela, il est à noter que le niveau d'ARN messagers de *APP* est réduit dans les neurones shBMI1 alors que le niveau de la protéine est augmenté. Il semblerait donc que APP non clivé soit stabilisé dans les neurones shBMI1 ce qui peut entrainer une amyloïdopathie comme chez les patients présentant une duplication de *APP*. Il n'est d'ailleurs pas impossible que la GSK3β soit capable de phosphoryler APP pour en assurer sa stabilisation. Pour vérifier cela il faudrait déterminer si le niveau d'APP total revient à la normale lorsque les neurones shBMI1 sont traités avec un inhibiteur de la GSK3β.

4.1.3 L'initiation et la progression de la pathologie après la perte de BMI1

Afin d'étudier les évènements moléculaires induis à la suite d'une perte de BMI1 dans des neurones corticaux, il faudrait disséquer d'avantage l'effet de la stabilisation et de l'inhibition de la GSK3β et p53 dans les neurones corticaux. Bien que les voies de la tauopathie

et de l'amyloidopathie semblent avoir des origines différentes, je pense également qu'il y a beaucoup d'interactions entre les deux pathologies. D'une part, le défaut de protéasome provoqué par la présence accrue de p53 a un impact probable sur l'accumulation des formes insolubles de Tau dans la cellule. D'autre part, il est connu qu'Aβ est un inhibiteur de la voie de signalisation PI3K/AKT ce qui induit une accumulation de la GSK3β dans sa forme active [236-238]. Enfin, certaines études semblent montrer que le fragment C99 de l'amyloïde puisse stabiliser Tau par un mécanisme encore inconnu [203].

Nous pouvons voir dans la figure 7 du chapitre 2 que l'effet de la stabilisation ou inhibition de la GSK3β sur l'hyperphosphorylation de Tau et l'amyloïde est bien plus prononcé que lors de la stabilisation ou inhibition de p53. Ces résultats m'amènent à penser que la stabilisation de la GSK3b est un élément pionnier dans le développement de l'Alzheimer à la suite d'une perte de BMI1. C'est seulement en concomitance avec la stabilisation de p53 que l'amyloïdopathie se développerait. Il faudrait par ailleurs étayer cela en faisant une cinétique d'inhibition de BMI1 dans des neurones sains pour voir quel élément apparaît en premier. La courbe de corrélation entre la quantité de phospho-Tau dans le cerveau et les niveaux de BMI1 me conforte dans cette hypothèse (Chapitre 2 Figure 1D).

Pour finir, il serait intéressant d'inactiver par CRISPR/Cas9 *MAPT* ou *APP* dans des neurones issus d'iPS Alzheimer afin de dissocier pleinement les deux pathologies. Si les neurones Alzheimer inactivés pour *APP* développent une tauopathie, cela indiquerait que l'amyloïde n'est pas à l'apex de la tauopathie. À l'inverse, si les neurones Alzheimer inactivés pour *MAPT* développent une amyloïdopathie, cela indiquerait que la présence de phospho-Tau n'est pas le régulateur clé de l'amyloïdopathie. Cette expérience déterminerait également si les deux voies majeures de la pathologie d'Alzheimer que sont la tauopathie et l'amyloïdopathie

sont complètement indépendantes. Si c'est bien le cas, cela conforterait la présence de BMI1 à l'apex de ces deux voies moléculaires.

4.1.4 BMI1 et l'hétérochromatine

Nous avons publié en 2016 que BMI1 était requis pour la formation de l'hétérochromatine constitutive (Annexe I) [239]. Il a par ailleurs été démontré une perte de l'hétérochromatine constitutive dans les maladies neurodégénératives, notamment dans la MA. Selon une étude publiée en 2014, il est proposé que la phosphorylation aberrante de Tau induit une déformation des mitochondries ce qui mène à la production de ROS. Cela serait la production de ces ROS qui seraient à l'origine de dommages à l'ADN et de la perte de l'hétérochromatine constitutive dans l'Alzheimer [240, 241]. Une autre étude publiée en 2016 reposant sur l'inactivation de *MAPT* dans des neurones primaires de souris propose au contraire que Tau aurait pour fonction dans le noyau de se lier aux régions de l'hétérochromatine constitutive pour la réguler. Lorsque Tau devient hyperphosphorylé comme dans la MA, la protéine serait séquestrée dans le soma des neurones et ne pourrait pas exercer sa fonction de maintien de l'hétérochromatine constitutive [242].

À la vue des résultats présentés en chapitre 2 et en annexe 1, je pense que la diminution de BMI1 dans la MA pourrait expliquer le phénotype d'hétérochromatine observé chez les patients et ce en amont de Tau. Pour vérifier cela, il faudrait inhiber Tau dans les neurones shBMI1 ou les neurones issus d'iPS Alzheimer en les traitant avec un inhibiteur de la GSK3β ou au moyen d'un shARN dirigé contre *MAPT*. La prédiction serait que la perte de l'hétérochromatine constitutive persiste dans ces cellules même en absence de tauopathie.

4.1.5 La fusion COMMD3-BMI1

Pour finir, je pense qu'il serait intéressant d'investiguer d'avantage le lien entre la protéine de fusion COMMD3-BMI1 et la pathogenèse de l'Alzheimer. La fonction des protéines de la famille des COMMD a très peu été décrite dans la littérature. Il a cependant été démontré que le domaine COMM permettait aux protéines de se lier au promoteur des gènes répondant à la voie de signalisation Nuclear Factor-κB (NF-κB). Il est ainsi proposé que les protéines COMMD puissent se lier à NF-κB et induire son ubiquitination par un mécanisme encore inconnu ce qui a pour effet d'inhiber l'activité de NF-κB sur ses gènes cibles [243-251]. L'hypothèse la plus probable serait que COMMD3-BMI1 puisse se lier à NF-κB qui est par la suite ubiquitiné grâce au recrutement de RING1B sur BMI1. La modulation de cette fusion pourrait expliquer en partie l'inflammation retrouvée dans l'Alzheimer via la voie de signalisation NF-κB [252].

Bien que cette fusion n'ait jamais été décrite dans la littérature, notre étude tant à prouver que cette fusion existe à des niveaux similaires à ceux de BMI1. En effet, l'utilisation de certains anticorps contre BMI1 en immunoblot ont permis de détecter une bande supplémentaire au poids moléculaire attendu de COMMD3-BMI1. De plus, les analyses de séquençage de l'ARN ont permis de détecter des transcripts correspondant à cette fusion.

SECTION 2: La perte de BMI1 dans l'Alzheimer

4.2.1 Mécanismes de répression

Comme nous avons pu le voir au travers des deux articles, l'expression de *BMI1* est affectée dans la majorité des patients atteints de la MA non familiale. Une des perspectives les plus intéressantes serait de déterminer par quels mécanismes BMI1 est réprimé. Nous savons qu'une répression se fait directement au moment de la transcription du gène car les niveaux d'ARN messagers sont réduits dans le cerveau des patients Alzheimer. Cependant, cela n'exclut pas que la protéine soit aussi dégradée. En effet, lorsqu'on regarde les niveaux d'expression de BMI1 dans les neurones corticaux issus d'iPS de patients Alzheimer, nous pouvons voir que la diminution de BMI1 est moins forte pour certaines lignées même si la protéine n'est plus présente.

Il y a différents mécanismes pouvant être responsables de la répression de BMI1 :

- *La méthylation du promoteur de BMI1*

La première hypothèse consiste à penser que le promoteur de *BMI1* soit hyperméthylé avec l'âge ce qui a pour conséquence de réprimer la transcription. Pour déterminer si cette hypothèse est valide, il faudrait analyser le niveau de méthylation du promoteur de *BMI1* dans le cerveau des patients Alzheimer. De nombreuses études ont investigué le méthylome dans le cerveau des patients Alzheimer mais aucune n'a rapporté une région différentiellement méthylée au niveau du promoteur de *BMI1*. Cependant, ces études reposent souvent sur l'utilisation de puces à oligonucléotides ciblant des ilots CpG et n'offre par conséquent pas une bonne couverture du génome. C'est d'autant plus vrai que le promoteur de BMI1 est enrichi en séquences répétitrices

pour lesquelles il est difficile de concevoir des sondes spécifiques. De plus, les analyses sont faites sur des extraits de cerveaux entiers et nous savons que la perte de BMI1 se retrouve principalement dans les neurones. Par conséquent, il est possible que le promoteur de *BMI1* soit en fait hyperméthylé dans l'Alzheimer en comparaison à des cerveaux âgés sains mais que les technologies utilisées à l'heure actuelle ne permettent pas de l'affirmer [253-257]. Pour explorer cette hypothèse, je proposerais d'une part de trier des échantillons de cortex au Fluorescent Activated Cell Sorting (FACS) pour les cellules positives pour NeuN, un marquer nucléaire des neurones, puis d'étudier la méthylation du promoteur de *BMI1* par pyro-séquencage. Cette technique permet d'avoir une résolution à la base nucléique près. En parallèle, je propose de faire la même analyse par pyro-séquencage sur des neurones issus d'iPS Alzheimer.

Par ailleurs, en analysant de nouveau des résultats de méthylome sur des cerveaux de patients à différents stades de Braak, j'ai pu voir une augmentation de la méthylation à une région proche du promoteur de *BMI1* en fonction de score de Braak [256]. Cette région serait donc une bonne candidate pour investiguer la méthylation (Figure 12).

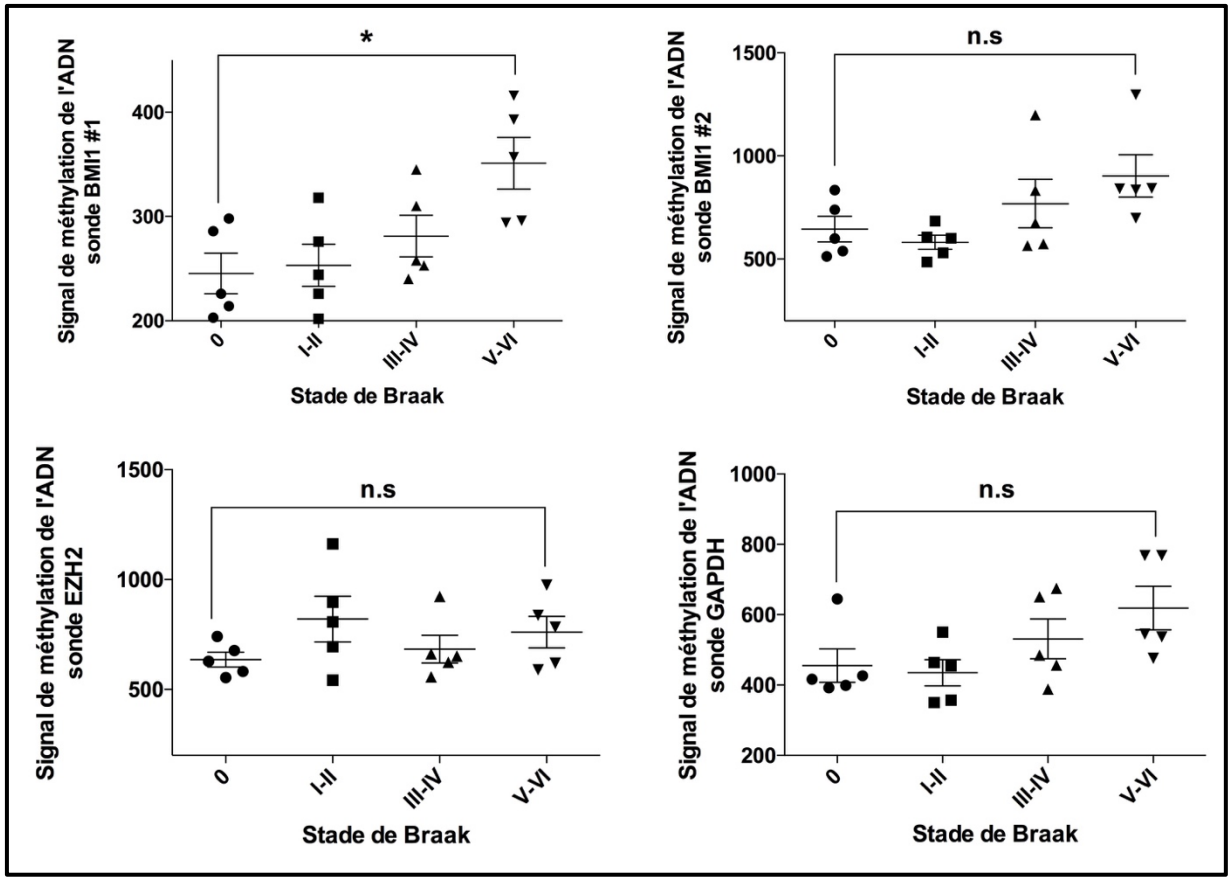

Figure 12 : Signal de méthylation de l'ADN dans le cerveau d'individus à différents stades de braak pour 4 sondes spécifiques de *BMI1*, *EZH2* et *GAPDH*. [256]

Notez la différence méthylation de *BMI1* dans les stades de Braak élevés. *EZH2*, un gène codant pour une autre protéine de polycomb et *GAPDH* sont utilisés comme contrôle négatif.

- *La modification d'histones*

Autre que la méthylation de l'ADN, la modification des histones au promoteur de *BMI1* n'est pas à exclure. De fait, il est connu que la chromatine est globalement affectée dans la MA. Cependant, il est plus souvent observé une perte d'hétérochromatine dans le cerveau des patients ce qui a pour conséquence d'induire la transcription de gènes normalement réprimés et provoquer un « bruit transcriptionnel » [240, 242, 258]. Dans le cas du promoteur de *BMI1*, on s'attendrait à retrouver un enrichissement de marques d'histones associées à la répression des gènes. La meilleure candidate serait la marque H3K27me3 car elle est caractéristique de l'hétérochromatine facultative. Pour étudier cela, il faudrait immunoprécipiter la chromatine de neurones Alzheimer avec un anticorps reconnaissant la marque H3K27me3 et analyser l'enrichissement de cette marque au niveau du promoteur de *BMI1* par PCR quantitative.

- *Action d'un micro ARN*

Les micro ARN sont des éléments régulateurs de l'expression très importants pour la cellule. D'une longueur d'environ 20 nucléotides, ils reconnaissent des ARN messagers complémentaires ce qui a pour conséquence de recruter un complexe de dégradation des ARN. Des micro ARN comme le miR-603 ont pu être associés à la MA et participe directement à la pathologie. Ce dernier est capable par exemple de se lier à l'ARN messager de low-density Lipoprotein Receptor-related Protein 1 (*LRP1*) pour induire sa dégradation. La perte de LRP1 provoque un défaut de métabolisation de l'amyloïde [259-264]. Les micro ARN miR-200, miR-141 et miR-300 sont connus pour se lier spécifiquement à l'ARN messager de BMI1 et ont un rôle important dans la régulation de la senescence, l'oncogenèse et la différenciation des progéniteurs cardiaques [265-268]. En particulier, le miR-141 a été retrouvé differentiellement

exprimé dans le sang des patients Alzheimer [269]. Il serait intéressant dans un premier temps de quantifier l'expression de miR-141 dans le cerveau des patients Alzheimer. Si l'expression de miR-141 est affectée, il faudrait transfecter des neurones issus d'iPS Alzheimer avec un anti-miR-141 pour voir si les niveaux de BMI1 sont rétablis et si cela permet de renverser la pathologie.

- *Répression par des lncARN*

Depuis l'avènement des techniques de séquençage de l'ARN, le répertoire des lncARN ne cesse de croître et leurs fonctions sont de plus en plus étudiées. Les lncARN sont d'une longueur supérieure à 200 nucléotides, contiennent parfois plusieurs exons et ne sont pas traduits en protéines. Ces ARN non codant peuvent moduler l'expression des gènes via leurs interactions avec les ARN messagers, micro ARN, remodeleurs de la chromatine ou activateurs de la transcription [270-275]. Plusieurs lncARN ont été identifiés dans la MA [276]. Il y a notamment le lncARN anti sens BACE1-AS qui, comme son nom l'indique, agit directement sur l'expression de *BACE1* [277]. Il serait intéressant dans un premier temps d'analyser des banques de données de séquençage de l'ARN de patients Alzheimer et d'individus sains pour détecter la présence de lncARN ayant une homologie de séquence *BMI1*. Ainsi, des lncARN candidats pourraient par la suite être validés dans les modèles iPS.

- *La répression indirecte*

Il est également possible que la répression de BMI1 se fasse de manière indirecte via la stabilisation ou l'inhibition d'un activateur ou répresseur transcriptionnel. Pour investiguer cela, il faudrait soit immunoprécipiter les protéines liées au promoteur de BMI1 et les identifier par

des techniques de protéomiques soit identifier les motifs de séquences nucléotidiques au niveau de *BMI1* pouvant être reconnus par des activateurs transcriptionnels. Il est également à noter que le gène contenant le plus de sites de liaison pour BMI1 est le gène BMI1 lui-même [278]. On peut donc imaginer que BMI1 participe à la répression de son propre promoteur.

- *L'épissage alternatif*

Environ 10 isoformes de BMI1 ont pu être identifiées après analyse de séquençages d'ARN. La fonction de chacune de ces isoformes reste à évaluer. Il n'est pas à exclure qu'il y ait un débalancement dans la proportion de ces isoformes ce qui induit une perte de stabilité de l'ARN ou un défaut dans la traduction de la protéine.

- *Les polymorphismes*

Il n'y a à ce jour aucun polymorphisme au niveau du promoteur ou des exons de *BMI1* qui soit associé à la MA. Cependant, il est possible que des erreurs de classification des cas d'Alzheimer masquent la présence de polymorphismes pouvant influencer l'expression de *BMI1*.

Il est intéressant de noter que lors de la reprogrammation de cellules somatiques en cellules iPS, l'épigénome est partiellement effacé. Si l'on en croit ces observations, il serait attendu que la répression de *BMI1* dans les neurones issus d'iPS Alzheimer ne soit pas due à des anomalies épigénétiques. Cependant, il n'est pas clair que l'ensemble des marques épigénétiques soient véritablement effacées lors de la reprogrammation.

Par ailleurs, toutes ces possibilités de répression de *BMI1* ne sont pas mutuellement exclusives. En effet, il est possible que plusieurs de ces mécanismes soient à l'origine de la perte

de BMI1 dans la MA. De plus, nous pouvons penser que les mécanismes à l'œuvre puissent être différents selon les patients.

4.2.2 Origines de la perte de BMI1

Il est bien établi par des études épidémiologiques que le style de vie et la qualité de vie prédispose du développement de la MA. Comme nous avons pu le voir, le corps humain est agressé au cours du vieillissement par des stresses oxydatifs ou chimiques. Ces stresses sont majoritairement liés à ce que nous consommons et à notre environnement. La santé cognitive tout au long de la vie joue aussi un rôle important dans le développement de la pathologie. La première hypothèse qui pourrait expliquer la perte progressive de BMI1 en fonction de l'âge et la perte drastique chez les patients atteints de la MA, serait que tous ces stresses entrainent la perte de marques épigénétiques qui, ultimement, affectent l'expression de *BMI1*.

Nous pouvons également imaginer que chaque individu nait avec un pool de BMI1 qui, avec le temps, diminue pour atteindre un seuil critique pour l'initiation de la maladie. De nombreuses études ont également évoqué l'ambivalence entre la MA et le développement de cancers. Ainsi, il est établi qu'une personne ayant un cancer est protégée naturellement contre la MA. À l'inverse les patients Alzheimer sont moins propices à développer des cancers. Cette observation est pertinente dans le cadre de l'étude de BMI1 dans l'Alzheimer car BMI1 est surexprimé dans la plupart des cancers et agit en tant que proto-oncogène en coopération avec l'oncogène c-Myc. Cela amène donc à penser que la diminution de BMI1 avec l'âge serait une réponse physiologique contre oncogenèse jusqu'à ce que le manque de BMI1 devienne pathologique.

4.2.3 La perte de BMI1 comme outil diagnostic

Une des premières applications que l'on peut imaginer à travers cette découverte consiste à utiliser la perte de BMI1 dans l'Alzheimer comme outil diagnostic afin de pouvoir traiter les patients avant l'apparition des symptômes. Cependant, nous ne savons pas à ce jour si la perte dramatique de BMI1 chez les patients Alzheimer est systémique. Si la perte de BMI1 est spécifique aux neurones corticaux, il serait alors impossible d'utiliser l'expression de *BMI1* comme outil diagnostic car la reprogrammation en iPS et leurs différenciations en neurones corticaux demeure trop couteuse et lente. La première étape pour envisager la création d'un outil de diagnostic serait d'examiner les niveaux d'expression de *BMI1* dans les fibroblastes ayant servis à l'obtention des lignées iPS sAD1 et sAD2. Si la perte de BMI1 est observée dans ces fibroblastes Alzheimer de la même manière que dans les neurones, cela indiquerait que cette perte est probablement systémique mais qu'elle a un impact uniquement dans le cerveau. Pour que l'expression de *BMI1* soit véritablement utilisée en tant que diagnostic, il faudrait qu'une perte de BMI1 soit également observée dans le sang des patients Alzheimer et non dans les patients atteints de la fMA ou d'autres démences. Plusieurs études ont comparé le profil transcriptionnel du sang de patients Alzheimer à celui d'individus sains. Cependant, ces études reposent sur l'utilisation de puces à ARN qui ne permettent pas une détection fidèle des niveaux de BMI1 à cause de la complexité de ce gène notamment avec la présence du transcrit de fusion *COMMD3-BMI1* [279-281]. La seule manière de détecter BMI1 avec cette technologie serait d'avoir une sonde spécifique de la portion 5' UTR de *BMI1* qui n'est pas retrouvé dans la fusion. Il existe une seule étude à ce jour ayant étudié par séquençage de l'ARN le sang de 48 patients

Alzheimer et 22 patients contrôles. Cependant, cette étude s'est uniquement focalisé sur l'expression des micro ARN et non des ARN codants pour des protéines [282]. Il serait donc intéressant d'analyser de nouveau ces données pour voir si la perte de BMI1 est significative dans le sang des patients Alzheimer. Nous pouvons par ailleurs avoir un indice que c'est bien le cas. En effet, Dr. Wiltfang a rapporté en 2006 que le nombre de cellules positives pour CD34, un marqueur de surface des cellules souches hématopoïétiques, diminue significativement chez les patients atteints de l'Alzheimer [283]. Cette observation est intéressante sachant que *BMI1* est très fortement exprimé dans les cellules souches hématopoïétiques et est requis pour leur maintenance. Cela tend à penser que BMI1 serait aussi diminué dans les cellules souches hématopoïétiques ce qui entrainerait leur déclin progressif.

SECTION 3: Perspectives de traitements de la MA

4.3.1 Les molécules pharmaceutiques

La première solution thérapeutique serait de cribler des molécules capables de stabiliser l'ARN messager ou la protéine BMI1. Pour cela, il faudrait greffer un rapporteur fluorescent au début ou la fin de *BMI1* endogène dans des cellules iPS de patients Alzheimer, les différencier en neurones corticaux et réaliser un criblage à haut débit. Les molécules candidates peuvent par la suite être validées pour leur effet sur la pathologie et leur capacité à croiser la barrière hémato-encéphalique. Il est important de réaliser le criblage sur des neurones Alzheimer car il faut s'assurer qu'un niveau résiduel de BMI1 persiste afin de le stabiliser. Une autre option serait d'utiliser d'autres molécules n'agissant pas nécessairement sur l'expression de BMI1 mais étant capables d'agir plus loin dans la cascade moléculaire. Comme démontré dans l'article du chapitre 1 (Figure 7), la combinaison d'un inhibiteur de p53 et d'un inhibiteur de la GSK3β permet de renverser la plupart des paramètres pathologiques. La combinaison des deux est primordiale car, comme démontré dans une étude clinique de phase 2 en 2015 portant sur 306 patients de l'Alzheimer, la simple inhibition de la GSK3β ne permet pas de renverser la maladie ou même de ralentir sa progression. C'est l'effet synergétique de ces deux inhibitions qui permet d'agir à la fois sur la tauopathie et l'amyloïdopathie.

4.3.2 La thérapie génique

Une autre stratégie consiste à injecter des virus adéno-associés (AAV) de façon intranasale ou intraveineuse. Les AAV sont de petits virus à ADN non pathogéniques capables de délivrer une portion d'ADN ne s'intégrant pas dans le génome. Ces virus infectant les cellules

humaines sont modifiés afin qu'ils ne puissent pas se répliquer. Les AAV sont très utilisés dans le cadre des protocoles de thérapie génique afin d'introduire une séquence d'ADN restant extra-chromosomique et capable d'être transcrit par la cellule. Cela permet ainsi d'introduire de façon sécuritaire un gène étant défectueux dans la cellule hôte. L'utilisation des AAV est particulièrement intéressante dans le traitement de la MA car les AAV sont aussi efficaces sur les cellules en division que sur les cellules quiescentes, ils sont capables de traverser la barrière hémato-encéphalique et sont utilisables directement en clinique. Des AAV porteurs du gène BMI1 sous le contrôle d'un promoteur neuronal permettrait d'entrevoir un traitement efficace pour la MA. Notamment, cette méthode serait aussi efficace pour des patients n'exprimant plus aucun transcrit de *BMI1*. Le point négatif de cette méthode repose sur le fait que les AAV, dans le cerveau, infectent préférentiellement les astrocytes et non les neurones. *BMI1* n'étant pas exprimé dans les astrocytes, cela peut entrainer, au-delà d'une efficacité moindre, un effet secondaire sévère si un promoteur qui ne soit pas strictement spécifique aux neurones est choisi. Pour parer aux problèmes d'efficacités, l'injection intranasale permettrait aux AAV d'intégrer plus facilement le cerveau et ainsi infecter plus de cellules dont les neurones. Par ailleurs, l'excès de virus dans le cerveau peut provoquer une réaction immunitaire et une neuroinflammation.

4.3.3 Le traitement d'autres démences

BMI1 étant à l'apex des cascades moléculaires à l'origine de l'amyloïdopathie et la tauopathie, il est envisageable que les traitements stabilisant BMI1 puissent fonctionner également dans d'autres démences ayant une composante de Tau ou de l'amyloïde. C'est le cas par exemple des patients atteints de DFT avec une mutation dans *MAPT* ou ceux atteints de

Paralysie Supranucléaire Progressive (PSP) avec une tauopathie proche de celle de la MA. Enfin, nous savons que l'expression de *BMI1* n'est pas affectée dans le cerveau des patients ayant la fMA ni dans les démences vasculaires. Cependant, ces deux pathologies possèdent une forte amyloïdopathie. Il serait intéressant de voir l'effet d'une surexpression de BMI1 dans ces démences.

4.3.4 Problématique des traitements proposés

Les problèmes que l'on pourrait entrevoir par rapport au traitement rétablissant des niveaux physiologiques de BMI1 résident sur le fait que BMI1 ait été étudié depuis de nombreuses années dans le cadre du cancer. Des essais cliniques portant sur l'utilisation d'inhibiteurs de BMI1 sont d'ailleurs à l'œuvre pour traiter le cancer du côlon. Le fait d'exprimer de façon ectopique un proto-oncogène tel que *BMI1* pourrait être un obstacle au développement de ces thérapies pour l'Alzheimer. Cependant, il faut considérer que la surexpression seule de BMI1 ne permet pas de transformer une cellule somatique ou une cellule souche en cellule cancéreuse.

Par ailleurs, BMI1 a une fonction importante pour le maintien des cellules souches hématopoïétiques et nous ne savons pas si les niveaux de BMI1 sont diminués dans les cellules souches hématopoïétiques des patients Alzheimer. Si la perte de BMI1 n'est pas systémique, l'utilisation d'une molécule pharmaceutique stabilisant BMI1 pourrait entrainer une polycythémie caractérisée par une augmentation du nombre de cellules sanguines.

SECTION 4: Conclusion

En conclusion, nous avons pu voir au travers des deux articles présentés que l'expression de BMI1 était réduite dans le cerveau des patients Alzheimer mais aussi dans les neurones issus d'iPS de patients Alzheimer. De plus, cette répression ne fut pas observée dans le cerveau des patients atteints de la fMA ou d'autres démences telles que la DFT ou la PSP. Les résultats indiquent que la perte de BMI1 semble être à l'origine de la MA et que BMI1 est par conséquent à l'apex de toutes les voies pathogéniques de l'Alzheimer incluant la tauopathie et l'amyloïdopathie. Bien que le mécanisme moléculaire doive encore être disséqué en profondeur, nous avons établi que BMI1 est un répresseur transcriptionnel de *MAPT* capable également d'inhiber la GSK3β et prévenir l'accumulation d'Aβ (Figure 13). Nous avons également pu voir que des neurones issus de cellules iPS de patients Alzheimer présentent la plupart des marqueurs pathologiques. Cependant, il serait intéressant de déterminer si les neurones issus de ces cellules iPS ont des propriétés électrophysiologiques altérées. Ces travaux sont à mettre en perspective avec ceux de Dr. Yankner qui montra en 2014 de façon similaire que la protéine repressor element 1-silencing transcription (REST) était diminuée dans l'Alzheimer, les DFT ainsi que les démences à corps de Lewy. REST est un répresseur transcriptionnel de gènes impliqués dans l'Alzheimer et protège contre le stress oxydatif et la toxicité de l'amyloïde [177]. Cependant, nous avons déterminé dans cette étude que le niveau d'ARN messager de REST était inchangé dans le cerveau des patients Alzheimer (Chapitre 2 Figure S1B). De plus, l'inhibition de REST dans les neurones ne permet pas de récapituler toute la pathologie de l'Alzheimer comme c'est le cas pour BMI1 [177]. Par conséquent, la perte de REST ne peut expliquer l'origine de la MA

mais représente une bonne opportunité pour le développement d'un traitement contre les maladies neurodégénératives.

Cette étude montre pour la première fois un lien entre la MA et la fonction de BMI1. Je pense que le développement de thérapies visant à rétablir un niveau physiologique de BMI1 constituerait le premier traitement capable de ralentir ou arrêter la progression de la MA

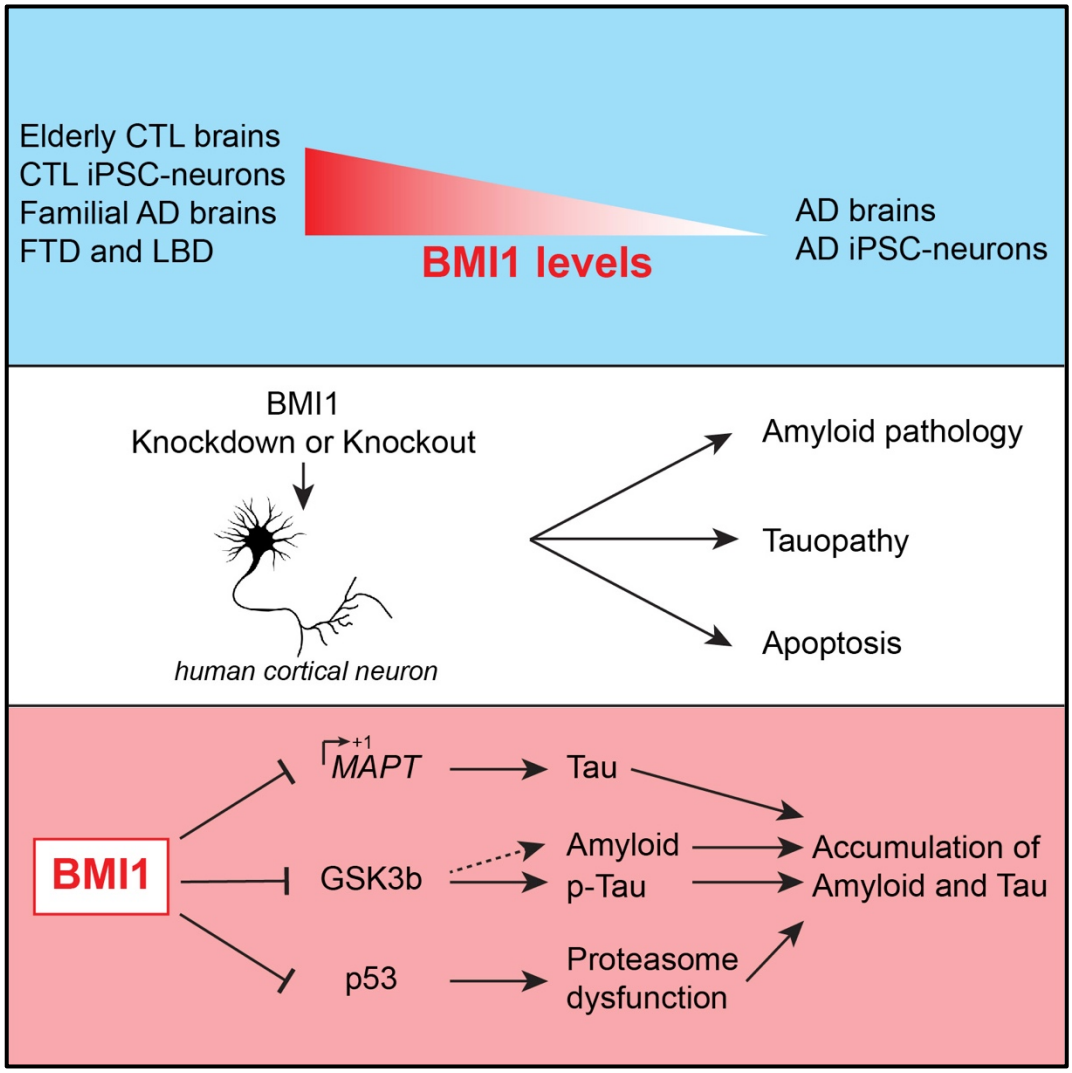

Figure 13 : Résumé des résultats exposés dans la thèse. Flamier et al. *Cell Reports* 2018

Références

1. Kirkwood, T.B., *Evolution of ageing.* Mech Ageing Dev, 2002. **123**(7): p. 737-45.
2. Fjell, A.M., et al., *One-year brain atrophy evident in healthy aging.* J Neurosci, 2009. **29**(48): p. 15223-31.
3. Ruan, L., X. Zhang, and R. Li, *Recent insights into the cellular and molecular determinants of aging.* J Cell Sci, 2018. **131**(3).
4. Zeng, X.S., et al., *Cellular and Molecular Basis of Neurodegeneration in Parkinson Disease.* Front Aging Neurosci, 2018. **10**: p. 109.
5. Gordon, P.H., H. Mitsumoto, and A.P. Hays, *Amyotrophic lateral sclerosis.* Sci Aging Knowledge Environ, 2003. **2003**(35): p. dn2.
6. Poddar, J., et al., *Biochemical deficits and cognitive decline in brain aging: Intervention by dietary supplements.* J Chem Neuroanat, 2018.
7. Kim, K. and H.K. Choe, *Role of hypothalamus in aging and its underlying cellular mechanisms.* Mech Ageing Dev, 2018.
8. Paraskevoudi, N., F. Balci, and A. Vatakis, *"Walking" through the sensory, cognitive, and temporal degradations of healthy aging.* Ann N Y Acad Sci, 2018.
9. LaPak, K.M. and C.E. Burd, *The molecular balancing act of p16(INK4a) in cancer and aging.* Mol Cancer Res, 2014. **12**(2): p. 167-83.
10. Zindy, F., et al., *Expression of the p16INK4a tumor suppressor versus other INK4 family members during mouse development and aging.* Oncogene, 1997. **15**(2): p. 203-11.

11. Cao, L., et al., *BMI1 as a novel target for drug discovery in cancer.* J Cell Biochem, 2011. **112**(10): p. 2729-41.

12. Matheu, A., et al., *Increased gene dosage of Ink4a/Arf results in cancer resistance and normal aging.* Genes Dev, 2004. **18**(22): p. 2736-46.

13. Ressler, S., et al., *p16INK4A is a robust in vivo biomarker of cellular aging in human skin.* Aging Cell, 2006. **5**(5): p. 379-89.

14. Chkhotua, A.B., et al., *Increased expression of p16(INK4a) and p27(Kip1) cyclin-dependent kinase inhibitor genes in aging human kidney and chronic allograft nephropathy.* Am J Kidney Dis, 2003. **41**(6): p. 1303-13.

15. Krishnamurthy, J., et al., *Ink4a/Arf expression is a biomarker of aging.* J Clin Invest, 2004. **114**(9): p. 1299-307.

16. Zukowski, P., M. Maciejczyk, and D. Waszkiel, *Sources of free radicals and oxidative stress in the oral cavity.* Arch Oral Biol, 2018. **92**: p. 8-17.

17. Sies, H., *Oxidative stress: a concept in redox biology and medicine.* Redox Biol, 2015. **4**: p. 180-3.

18. Liguori, I., et al., *Oxidative stress, aging, and diseases.* Clin Interv Aging, 2018. **13**: p. 757-772.

19. Dunaway, S., et al., *Natural Antioxidants: Multiple Mechanisms to Protect Skin From Solar Radiation.* Front Pharmacol, 2018. **9**: p. 392.

20. Cobley, J.N., M.L. Fiorello, and D.M. Bailey, *13 reasons why the brain is susceptible to oxidative stress.* Redox Biol, 2018. **15**: p. 490-503.

21. Hussain, M.S. and V. Tripathi, *Smoking under hypoxic conditions: a potent environmental risk factor for inflammatory and autoimmune diseases.* Mil Med Res, 2018. **5**(1): p. 11.

22. Simioni, C., et al., *Oxidative stress: role of physical exercise and antioxidant nutraceuticals in adulthood and aging.* Oncotarget, 2018. **9**(24): p. 17181-17198.

23. Yin, H. and N.A. Porter, *New insights regarding the autoxidation of polyunsaturated fatty acids.* Antioxid Redox Signal, 2005. **7**(1-2): p. 170-84.

24. Evans, M.D., M. Dizdaroglu, and M.S. Cooke, *Oxidative DNA damage and disease: induction, repair and significance.* Mutat Res, 2004. **567**(1): p. 1-61.

25. Harman, D., *Aging: a theory based on free radical and radiation chemistry.* J Gerontol, 1956. **11**(3): p. 298-300.

26. Halliwell, B., *Role of free radicals in the neurodegenerative diseases: therapeutic implications for antioxidant treatment.* Drugs Aging, 2001. **18**(9): p. 685-716.

27. Halliwell, B., *Oxidative stress and neurodegeneration: where are we now?* J Neurochem, 2006. **97**(6): p. 1634-58.

28. Lu, T., et al., *Gene regulation and DNA damage in the ageing human brain.* Nature, 2004. **429**(6994): p. 883-91.

29. Hou, Y., et al., *Genome instability in Alzheimer disease.* Mech Ageing Dev, 2017. **161**(Pt A): p. 83-94.

30. Merlo, D., et al., *DNA Double Strand Breaks: A Common Theme in Neurodegenerative Diseases.* Curr Alzheimer Res, 2016. **13**(11): p. 1208-1218.

31. Khan, M.M., et al., *DNA damage and neurodegenerative phenotypes in aged Ciz1 null mice.* Neurobiol Aging, 2018. **62**: p. 180-190.

32. Birnbaum, J.H., et al., *Oxidative stress and altered mitochondrial protein expression in the absence of amyloid-beta and tau pathology in iPSC-derived neurons from sporadic Alzheimer's disease patients.* Stem Cell Res, 2018. **27**: p. 121-130.

33. Jackson, S.P. and J. Bartek, *The DNA-damage response in human biology and disease.* Nature, 2009. **461**(7267): p. 1071-8.

34. Mecocci, P., et al., *Oxidative damage to mitochondrial DNA shows marked age-dependent increases in human brain.* Ann Neurol, 1993. **34**(4): p. 609-16.

35. Swain, U. and K. Subba Rao, *Study of DNA damage via the comet assay and base excision repair activities in rat brain neurons and astrocytes during aging.* Mech Ageing Dev, 2011. **132**(8-9): p. 374-81.

36. Sen, T., et al., *Gene-specific oxidative lesions in aged rat brain detected by polymerase chain reaction inhibition assay.* Free Radic Res, 2007. **41**(3): p. 288-94.

37. Mandavilli, B.S. and K.S. Rao, *Accumulation of DNA damage in aging neurons occurs through a mechanism other than apoptosis.* J Neurochem, 1996. **67**(4): p. 1559-65.

38. Rutten, B.P., et al., *The aging brain: accumulation of DNA damage or neuron loss?* Neurobiol Aging, 2007. **28**(1): p. 91-8.

39. Braak, H. and E. Braak, *Neuropathological stageing of Alzheimer-related changes.* Acta Neuropathol, 1991. **82**(4): p. 239-59.

40. Hunting, P., *Alois Alzheimer (1864-1915).* J Med Biogr, 2015. **23**(4): p. 238-9.

41. Tejada-Vera, B., *Mortality from Alzheimer's disease in the United States: data for 2000 and 2010.* NCHS Data Brief, 2013(116): p. 1-8.

42. Arrighi, H.M., et al., *Lethality of Alzheimer disease and its impact on nursing home placement.* Alzheimer Dis Assoc Disord, 2010. **24**(1): p. 90-5.

43. Goldman, J.S., et al., *Genetic counseling and testing for Alzheimer disease: joint practice guidelines of the American College of Medical Genetics and the National Society of Genetic Counselors.* Genet Med, 2011. **13**(6): p. 597-605.

44. Bekris, L.M., et al., *Genetics of Alzheimer disease.* J Geriatr Psychiatry Neurol, 2010. **23**(4): p. 213-27.

45. Marioni, R.E., et al., *GWAS on family history of Alzheimer's disease.* Transl Psychiatry, 2018. **8**(1): p. 99.

46. Tanzi, R.E., *The genetics of Alzheimer disease.* Cold Spring Harb Perspect Med, 2012. **2**(10).

47. Minino, A.M., et al., *Deaths: final data for 2000.* Natl Vital Stat Rep, 2002. **50**(15): p. 1-119.

48. Murphy, S.L., et al., *Deaths: Final Data for 2015.* Natl Vital Stat Rep, 2017. **66**(6): p. 1-75.

49. Baumgart, M., et al., *Summary of the evidence on modifiable risk factors for cognitive decline and dementia: A population-based perspective.* Alzheimers Dement, 2015. **11**(6): p. 718-26.

50. Evans, D.A., et al., *Incidence of Alzheimer disease in a biracial urban community: relation to apolipoprotein E allele status.* Arch Neurol, 2003. **60**(2): p. 185-9.

51. Kukull, W.A., et al., *Dementia and Alzheimer disease incidence: a prospective cohort study.* Arch Neurol, 2002. **59**(11): p. 1737-46.

52. Sando, S.B., et al., *Risk-reducing effect of education in Alzheimer's disease.* Int J Geriatr Psychiatry, 2008. **23**(11): p. 1156-62.

53. Stern, Y., *What is cognitive reserve? Theory and research application of the reserve concept.* J Int Neuropsychol Soc, 2002. **8**(3): p. 448-60.

54. Stern, Y., *Cognitive reserve in ageing and Alzheimer's disease.* Lancet Neurol, 2012. **11**(11): p. 1006-12.

55. Hebert, L.E., et al., *Alzheimer disease in the United States (2010-2050) estimated using the 2010 census.* Neurology, 2013. **80**(19): p. 1778-83.

56. Chene, G., et al., *Gender and incidence of dementia in the Framingham Heart Study from mid-adult life.* Alzheimers Dement, 2015. **11**(3): p. 310-320.

57. Rocca, W.A., et al., *Sex and gender differences in the causes of dementia: a narrative review.* Maturitas, 2014. **79**(2): p. 196-201.

58. Reisberg, B., et al., *Behavioral symptoms in Alzheimer's disease: phenomenology and treatment.* J Clin Psychiatry, 1987. **48 Suppl**: p. 9-15.

59. Fillenbaum, G.G., et al., *Consortium to Establish a Registry for Alzheimer's Disease (CERAD): the first twenty years.* Alzheimers Dement, 2008. **4**(2): p. 96-109.

60. Davis, P.C., et al., *The Consortium to Establish a Registry for Alzheimer's Disease (CERAD). Part III. Reliability of a standardized MRI evaluation of Alzheimer's disease.* Neurology, 1992. **42**(9): p. 1676-80.

61. Mirra, S.S., et al., *The Consortium to Establish a Registry for Alzheimer's Disease (CERAD). Part II. Standardization of the neuropathologic assessment of Alzheimer's disease.* Neurology, 1991. **41**(4): p. 479-86.

62. Morris, J.C., et al., *The Consortium to Establish a Registry for Alzheimer's Disease (CERAD). Part I. Clinical and neuropsychological assessment of Alzheimer's disease.* Neurology, 1989. **39**(9): p. 1159-65.

63. Annaert, W., et al., *Presenilin function in APP processing.* Ann N Y Acad Sci, 2000. **920**: p. 158-64.

64. De Strooper, B. and W. Annaert, *Proteolytic processing and cell biological functions of the amyloid precursor protein.* J Cell Sci, 2000. **113 (Pt 11)**: p. 1857-70.

65. Reinhard, C., S.S. Hebert, and B. De Strooper, *The amyloid-beta precursor protein: integrating structure with biological function.* EMBO J, 2005. **24**(23): p. 3996-4006.

66. Zhao, J., et al., *G Protein-Coupled Receptors (GPCRs) in Alzheimer's Disease: A Focus on BACE1 Related GPCRs.* Front Aging Neurosci, 2016. **8**: p. 58.

67. Iqbal, K., et al., *Tau in Alzheimer disease and related tauopathies.* Curr Alzheimer Res, 2010. **7**(8): p. 656-64.

68. Hara, M., et al., *Isoform transition from four-repeat to three-repeat tau underlies dendrosomatic and regional progression of neurofibrillary pathology.* Acta Neuropathol, 2013. **125**(4): p. 565-79.

69. Le, M.N., et al., *Multiple mechanisms of extracellular tau spreading in a non-transgenic tauopathy model.* Am J Neurodegener Dis, 2012. **1**(3): p. 316-33.

70. Seppala, T.T., et al., *CSF biomarkers for Alzheimer disease correlate with cortical brain biopsy findings.* Neurology, 2012. **78**(20): p. 1568-75.

71. Buerger, K., et al., *CSF phosphorylated tau protein correlates with neocortical neurofibrillary pathology in Alzheimer's disease.* Brain, 2006. **129**(Pt 11): p. 3035-41.

72. Olsson, B., et al., *CSF and blood biomarkers for the diagnosis of Alzheimer's disease: a systematic review and meta-analysis.* Lancet Neurol, 2016. **15**(7): p. 673-684.

73. Cai, Z., M.D. Hussain, and L.J. Yan, *Microglia, neuroinflammation, and beta-amyloid protein in Alzheimer's disease.* Int J Neurosci, 2014. **124**(5): p. 307-21.

74. Voyle, N., et al., *Blood Protein Markers of Neocortical Amyloid-beta Burden: A Candidate Study Using SOMAscan Technology.* J Alzheimers Dis, 2015. **46**(4): p. 947-61.

75. Westwood, S., et al., *Blood-Based Biomarker Candidates of Cerebral Amyloid Using PiB PET in Non-Demented Elderly.* J Alzheimers Dis, 2016. **52**(2): p. 561-72.

76. Burnham, S.C., et al., *Predicting Alzheimer disease from a blood-based biomarker profile: A 54-month follow-up.* Neurology, 2016. **87**(11): p. 1093-101.

77. Wakselman, S., et al., *Developmental neuronal death in hippocampus requires the microglial CD11b integrin and DAP12 immunoreceptor.* J Neurosci, 2008. **28**(32): p. 8138-43.

78. Holtzman, D.M., J. Herz, and G. Bu, *Apolipoprotein E and apolipoprotein E receptors: normal biology and roles in Alzheimer disease.* Cold Spring Harb Perspect Med, 2012. **2**(3): p. a006312.

79. Raber, J., Y. Huang, and J.W. Ashford, *ApoE genotype accounts for the vast majority of AD risk and AD pathology.* Neurobiol Aging, 2004. **25**(5): p. 641-50.

80. Loy, C.T., et al., *Genetics of dementia.* Lancet, 2014. **383**(9919): p. 828-40.

81. Mayeux, R., et al., *Utility of the apolipoprotein E genotype in the diagnosis of Alzheimer's disease. Alzheimer's Disease Centers Consortium on Apolipoprotein E and Alzheimer's Disease.* N Engl J Med, 1998. **338**(8): p. 506-11.

82. Ward, A., et al., *Prevalence of apolipoprotein E4 genotype and homozygotes (APOE e4/4) among patients diagnosed with Alzheimer's disease: a systematic review and meta-analysis.* Neuroepidemiology, 2012. **38**(1): p. 1-17.

83. Spinney, L., *Alzheimer's disease: The forgetting gene.* Nature, 2014. **510**(7503): p. 26-8.

84. Maple-Grodem, J., et al., *Alzheimer disease associated variants in SORL1 accelerate dementia development in Parkinson disease.* Neurosci Lett, 2018. **674**: p. 123-126.

85. Kukull, W.A., et al., *Apolipoprotein E in Alzheimer's disease risk and case detection: a case-control study.* J Clin Epidemiol, 1996. **49**(10): p. 1143-8.

86. Pesch, B., et al., *Cigarette smoking and lung cancer--relative risk estimates for the major histological types from a pooled analysis of case-control studies.* Int J Cancer, 2012. **131**(5): p. 1210-9.

87. Reilly, J.F., et al., *Amyloid deposition in the hippocampus and entorhinal cortex: quantitative analysis of a transgenic mouse model.* Proc Natl Acad Sci U S A, 2003. **100**(8): p. 4837-42.

88. Masliah, E., et al., *Comparison of neurodegenerative pathology in transgenic mice overexpressing V717F beta-amyloid precursor protein and Alzheimer's disease.* J Neurosci, 1996. **16**(18): p. 5795-811.

89. Games, D., et al., *Alzheimer-type neuropathology in transgenic mice overexpressing V717F beta-amyloid precursor protein.* Nature, 1995. **373**(6514): p. 523-7.

90. Guo, B. and Q. Zhou, *How efficient are rodent models for Alzheimer's disease drug discovery?* Expert Opin Drug Discov, 2018. **13**(2): p. 113-115.

91. Corcoran, K.A., et al., *Overexpression of hAPPswe impairs rewarded alternation and contextual fear conditioning in a transgenic mouse model of Alzheimer's disease.* Learn Mem, 2002. **9**(5): p. 243-52.

92. Hsiao, K., et al., *Correlative memory deficits, Abeta elevation, and amyloid plaques in transgenic mice.* Science, 1996. **274**(5284): p. 99-102.

93. Duff, K., et al., *Increased amyloid-beta42(43) in brains of mice expressing mutant presenilin 1.* Nature, 1996. **383**(6602): p. 710-3.

94. Oddo, S., et al., *Triple-transgenic model of Alzheimer's disease with plaques and tangles: intracellular Abeta and synaptic dysfunction.* Neuron, 2003. **39**(3): p. 409-21.

95. Treuting, P.M., et al., *Generation of genetically altered mouse models for aging studies.* Exp Mol Pathol, 2002. **72**(1): p. 49-55.

96. Takeda, T., et al., *A new murine model of accelerated senescence.* Mech Ageing Dev, 1981. **17**(2): p. 183-94.

97. Puzzo, D., et al., *Rodent models for Alzheimer's disease drug discovery.* Expert Opin Drug Discov, 2015. **10**(7): p. 703-11.

98. Puzzo, D., et al., *Picomolar amyloid-beta positively modulates synaptic plasticity and memory in hippocampus.* J Neurosci, 2008. **28**(53): p. 14537-45.

99. Balducci, C. and G. Forloni, *In vivo application of beta amyloid oligomers: a simple tool to evaluate mechanisms of action and new therapeutic approaches.* Curr Pharm Des, 2014. **20**(15): p. 2491-505.

100. Billings, L.M., et al., *Intraneuronal Abeta causes the onset of early Alzheimer's disease-related cognitive deficits in transgenic mice.* Neuron, 2005. **45**(5): p. 675-88.

101. Cramer, P.E., et al., *Aging African green monkeys manifest transcriptional, pathological, and cognitive hallmarks of human Alzheimer's disease.* Neurobiol Aging, 2018. **64**: p. 92-106.

102. Hu, W., et al., *Direct Conversion of Normal and Alzheimer's Disease Human Fibroblasts into Neuronal Cells by Small Molecules.* Cell Stem Cell, 2015. **17**(2): p. 204-12.

103. Evans, M.J. and M.H. Kaufman, *Establishment in culture of pluripotential cells from mouse embryos.* Nature, 1981. **292**(5819): p. 154-6.

104. Martin, G.R., *Isolation of a pluripotent cell line from early mouse embryos cultured in medium conditioned by teratocarcinoma stem cells.* Proc Natl Acad Sci U S A, 1981. **78**(12): p. 7634-8.

105. Thomson, J.A., et al., *Embryonic stem cell lines derived from human blastocysts.* Science, 1998. **282**(5391): p. 1145-7.

106. De Los Angeles, A., et al., *Hallmarks of pluripotency.* Nature, 2015. **525**(7570): p. 469-78.

107. Gurdon, J.B., *The developmental capacity of nuclei taken from intestinal epithelium cells of feeding tadpoles.* J Embryol Exp Morphol, 1962. **10**: p. 622-40.

108. Tada, M., et al., *Nuclear reprogramming of somatic cells by in vitro hybridization with ES cells.* Curr Biol, 2001. **11**(19): p. 1553-8.

109. Hochedlinger, K. and R. Jaenisch, *Monoclonal mice generated by nuclear transfer from mature B and T donor cells.* Nature, 2002. **415**(6875): p. 1035-8.

110. Byrne, J.A., et al., *Nuclei of adult mammalian somatic cells are directly reprogrammed to oct-4 stem cell gene expression by amphibian oocytes.* Curr Biol, 2003. **13**(14): p. 1206-13.

111. Cowan, C.A., et al., *Nuclear reprogramming of somatic cells after fusion with human embryonic stem cells.* Science, 2005. **309**(5739): p. 1369-73.

112. Takahashi, K. and S. Yamanaka, *Induction of pluripotent stem cells from mouse embryonic and adult fibroblast cultures by defined factors.* Cell, 2006. **126**(4): p. 663-76.

113. Takahashi, K., et al., *Induction of pluripotent stem cells from adult human fibroblasts by defined factors.* Cell, 2007. **131**(5): p. 861-72.

114. Park, I.H., et al., *Disease-specific induced pluripotent stem cells.* Cell, 2008. **134**(5): p. 877-86.

115. Dimos, J.T., et al., *Induced pluripotent stem cells generated from patients with ALS can be differentiated into motor neurons.* Science, 2008. **321**(5893): p. 1218-21.

116. Inoue, H., et al., *iPS cells: a game changer for future medicine.* EMBO J, 2014. **33**(5): p. 409-17.

117. Carr, A.J., et al., *Development of human embryonic stem cell therapies for age-related macular degeneration.* Trends Neurosci, 2013. **36**(7): p. 385-95.

118. Yoo, S. and S. Blackshaw, *Regulation and function of neurogenesis in the adult mammalian hypothalamus.* Prog Neurobiol, 2018.

119. Kempermann, G., et al., *Human Adult Neurogenesis: Evidence and Remaining Questions.* Cell Stem Cell, 2018.

120. Farhy-Tselnicker, I. and N.J. Allen, *Astrocytes, neurons, synapses: a tripartite view on cortical circuit development.* Neural Dev, 2018. **13**(1): p. 7.

121. Eiraku, M., et al., *Self-organized formation of polarized cortical tissues from ESCs and its active manipulation by extrinsic signals.* Cell Stem Cell, 2008. **3**(5): p. 519-32.

122. Li, X.J., et al., *Coordination of sonic hedgehog and Wnt signaling determines ventral and dorsal telencephalic neuron types from human embryonic stem cells.* Development, 2009. **136**(23): p. 4055-63.

123. Shi, Y., et al., *Human cerebral cortex development from pluripotent stem cells to functional excitatory synapses.* Nat Neurosci, 2012. **15**(3): p. 477-86, S1.

124. Zeng, H., et al., *Specification of region-specific neurons including forebrain glutamatergic neurons from human induced pluripotent stem cells.* PLoS One, 2010. **5**(7): p. e11853.

125. Espuny-Camacho, I., et al., *Pyramidal neurons derived from human pluripotent stem cells integrate efficiently into mouse brain circuits in vivo.* Neuron, 2013. **77**(3): p. 440-56.

126. Lancaster, M.A., et al., *Cerebral organoids model human brain development and microcephaly.* Nature, 2013. **501**(7467): p. 373-9.

127. Li, Y., et al., *Induction of Expansion and Folding in Human Cerebral Organoids.* Cell Stem Cell, 2017. **20**(3): p. 385-396 e3.

128. Lancaster, M.A., et al., *Guided self-organization and cortical plate formation in human brain organoids.* Nat Biotechnol, 2017. **35**(7): p. 659-666.

129. Yagi, T., et al., *Modeling familial Alzheimer's disease with induced pluripotent stem cells.* Hum Mol Genet, 2011. **20**(23): p. 4530-9.

130. Ochalek, A., et al., *Neurons derived from sporadic Alzheimer's disease iPSCs reveal elevated TAU hyperphosphorylation, increased amyloid levels, and GSK3B activation.* Alzheimers Res Ther, 2017. **9**(1): p. 90.

131. Hossini, A.M., et al., *Induced pluripotent stem cell-derived neuronal cells from a sporadic Alzheimer's disease donor as a model for investigating AD-associated gene regulatory networks.* BMC Genomics, 2015. **16**: p. 84.

132. Young, J.E., et al., *Elucidating molecular phenotypes caused by the SORL1 Alzheimer's disease genetic risk factor using human induced pluripotent stem cells.* Cell Stem Cell, 2015. **16**(4): p. 373-85.

133. Kondo, T., et al., *Modeling Alzheimer's disease with iPSCs reveals stress phenotypes associated with intracellular Abeta and differential drug responsiveness.* Cell Stem Cell, 2013. **12**(4): p. 487-96.

134. Israel, M.A., et al., *Probing sporadic and familial Alzheimer's disease using induced pluripotent stem cells.* Nature, 2012. **482**(7384): p. 216-20.

135. Raja, W.K., et al., *Self-Organizing 3D Human Neural Tissue Derived from Induced Pluripotent Stem Cells Recapitulate Alzheimer's Disease Phenotypes.* PLoS One, 2016. **11**(9): p. e0161969.

136. Espuny-Camacho, I., et al., *Hallmarks of Alzheimer's Disease in Stem-Cell-Derived Human Neurons Transplanted into Mouse Brain.* Neuron, 2017. **93**(5): p. 1066-1081 e8.

137. Ghirlando, R. and G. Felsenfeld, *Chromatin structure outside and inside the nucleus.* Biopolymers, 2013. **99**(4): p. 225-32.

138. Simpson, R.T., F. Thoma, and J.M. Brubaker, *Chromatin reconstituted from tandemly repeated cloned DNA fragments and core histones: a model system for study of higher order structure.* Cell, 1985. **42**(3): p. 799-808.

139. Simpson, R.T. and D.W. Stafford, *Structural features of a phased nucleosome core particle.* Proc Natl Acad Sci U S A, 1983. **80**(1): p. 51-5.

140. Luger, K., et al., *Crystal structure of the nucleosome core particle at 2.8 A resolution.* Nature, 1997. **389**(6648): p. 251-60.

141. Kornberg, R.D. and L. Stryer, *Statistical distributions of nucleosomes: nonrandom locations by a stochastic mechanism.* Nucleic Acids Res, 1988. **16**(14A): p. 6677-90.

142. Clapier, C.R. and B.R. Cairns, *The biology of chromatin remodeling complexes.* Annu Rev Biochem, 2009. **78**: p. 273-304.

143. Zhang, T., S. Cooper, and N. Brockdorff, *The interplay of histone modifications - writers that read.* EMBO Rep, 2015. **16**(11): p. 1467-81.

144. Huang, H., et al., *SnapShot: histone modifications.* Cell, 2014. **159**(2): p. 458-458 e1.

145. Moore, L.D., T. Le, and G. Fan, *DNA methylation and its basic function.* Neuropsychopharmacology, 2013. **38**(1): p. 23-38.

146. Wu, Z., et al., *Regulation of lncRNA expression.* Cell Mol Biol Lett, 2014. **19**(4): p. 561-75.

147. Aloia, L., B. Di Stefano, and L. Di Croce, *Polycomb complexes in stem cells and embryonic development.* Development, 2013. **140**(12): p. 2525-34.

148. Di Croce, L. and K. Helin, *Transcriptional regulation by Polycomb group proteins.* Nat Struct Mol Biol, 2013. **20**(10): p. 1147-55.

149. Lewis, E.B., *A gene complex controlling segmentation in Drosophila.* Nature, 1978. **276**(5688): p. 565-70.

150. Richter, G.H., et al., *EZH2 is a mediator of EWS/FLI1 driven tumor growth and metastasis blocking endothelial and neuro-ectodermal differentiation.* Proc Natl Acad Sci U S A, 2009. **106**(13): p. 5324-9.

151. Dovey, J.S., et al., *Bmi1 is critical for lung tumorigenesis and bronchioalveolar stem cell expansion.* Proc Natl Acad Sci U S A, 2008. **105**(33): p. 11857-62.

152. Shao, Z., et al., *Stabilization of chromatin structure by PRC1, a Polycomb complex.* Cell, 1999. **98**(1): p. 37-46.

153. Leung, C., et al., *Bmi1 is essential for cerebellar development and is overexpressed in human medulloblastomas.* Nature, 2004. **428**(6980): p. 337-41.

154. Park, I.K., S.J. Morrison, and M.F. Clarke, *Bmi1, stem cells, and senescence regulation.* J Clin Invest, 2004. **113**(2): p. 175-9.

155. Brunk, B.P., E.C. Martin, and P.N. Adler, *Drosophila genes Posterior Sex Combs and Suppressor two of zeste encode proteins with homology to the murine bmi-1 oncogene.* Nature, 1991. **353**(6342): p. 351-3.

156. van Lohuizen, M., et al., *Identification of cooperating oncogenes in E mu-myc transgenic mice by provirus tagging.* Cell, 1991. **65**(5): p. 737-52.

157. Haupt, Y., et al., *Novel zinc finger gene implicated as myc collaborator by retrovirally accelerated lymphomagenesis in E mu-myc transgenic mice.* Cell, 1991. **65**(5): p. 753-63.

158. Jacobs, J.J., et al., *The oncogene and Polycomb-group gene bmi-1 regulates cell proliferation and senescence through the ink4a locus.* Nature, 1999. **397**(6715): p. 164-8.

159. Molofsky, A.V., et al., *Bmi-1 dependence distinguishes neural stem cell self-renewal from progenitor proliferation.* Nature, 2003. **425**(6961): p. 962-7.

160. Zencak, D., et al., *Bmi1 loss produces an increase in astroglial cells and a decrease in neural stem cell population and proliferation.* J Neurosci, 2005. **25**(24): p. 5774-83.

161. Liu, S., et al., *miR-200c inhibits melanoma progression and drug resistance through down-regulation of BMI-1.* Am J Pathol, 2012. **181**(5): p. 1823-35.

162. Abdouh, M., et al., *BMI1 sustains human glioblastoma multiforme stem cell renewal.* J Neurosci, 2009. **29**(28): p. 8884-96.

163. Facchino, S., et al., *BMI1 confers radioresistance to normal and cancerous neural stem cells through recruitment of the DNA damage response machinery.* J Neurosci, 2010. **30**(30): p. 10096-111.

164. Savva, G.M., et al., *Age, neuropathology, and dementia.* N Engl J Med, 2009. **360**(22): p. 2302-9.

165. Kanekiyo, T., H. Xu, and G. Bu, *ApoE and Abeta in Alzheimer's disease: accidental encounters or partners?* Neuron, 2014. **81**(4): p. 740-54.

166. Blennow, K., M.J. de Leon, and H. Zetterberg, *Alzheimer's disease.* Lancet, 2006. **368**(9533): p. 387-403.

167. Bihaqi, S.W., et al., *Do epigenetic pathways initiate late onset Alzheimer disease (LOAD): towards a new paradigm.* Curr Alzheimer Res, 2012. **9**(5): p. 574-88.

168. Geula, C., et al., *Aging renders the brain vulnerable to amyloid beta-protein neurotoxicity.* Nat Med, 1998. **4**(7): p. 827-31.

169. Buchwald, G., et al., *Structure and E3-ligase activity of the Ring-Ring complex of polycomb proteins Bmi1 and Ring1b.* Embo J, 2006. **25**(11): p. 2465-74.

170. Li, Z., et al., *Structure of a Bmi-1-Ring1B polycomb group ubiquitin ligase complex.* J Biol Chem, 2006. **281**(29): p. 20643-9.

171. Sherr, C.J., *The INK4a/ARF network in tumour suppression.* Nat Rev Mol Cell Biol, 2001. **2**(10): p. 731-7.

172. van der Lugt, N.M., et al., *Posterior transformation, neurological abnormalities, and severe hematopoietic defects in mice with a targeted deletion of the bmi-1 proto-oncogene.* Genes Dev, 1994. **8**(7): p. 757-69.

173. Valk-Lingbeek, M.E., S.W. Bruggeman, and M. Van Lohuizen, *Stem cells and cancer; the polycomb connection.* Cell, 2004. **118**(4): p. 409-18.

174. Chatoo, W., et al., *The polycomb group gene Bmi1 regulates antioxidant defenses in neurons by repressing p53 pro-oxidant activity.* J Neurosci, 2009. **29**(2): p. 529-42.

175. Choi, S.H., et al., *A three-dimensional human neural cell culture model of Alzheimer's disease.* Nature, 2014. **515**(7526): p. 274-8.

176. Mano, T., et al., *Neuron-specific methylome analysis reveals epigenetic regulation and tau-related dysfunction of BRCA1 in Alzheimer's disease.* Proc Natl Acad Sci U S A, 2017. **114**(45): p. E9645-E9654.

177. Lu, T., et al., *REST and stress resistance in ageing and Alzheimer's disease.* Nature, 2014. **507**(7493): p. 448-54.

178. Liu, C.C., et al., *Deficiency in LRP6-mediated Wnt signaling contributes to synaptic abnormalities and amyloid pathology in Alzheimer's disease.* Neuron, 2014. **84**(1): p. 63-77.

179. Hamilton, L.K., et al., *Aberrant Lipid Metabolism in the Forebrain Niche Suppresses Adult Neural Stem Cell Proliferation in an Animal Model of Alzheimer's Disease.* Cell Stem Cell, 2015. **17**(4): p. 397-411.

180. Hand, R., et al., *Phosphorylation of neurogenin2 specifies the migration properties and the dendritic morphology of pyramidal neurons in the neocortex.* Neuron, 2005. **48**(1): p. 45-62.

181. Stokin, G.B., et al., *Axonopathy and transport deficits early in the pathogenesis of Alzheimer's disease.* Science, 2005. **307**(5713): p. 1282-8.

182. Jackson, G.R., et al., *Human wild-type tau interacts with wingless pathway components and produces neurofibrillary pathology in Drosophila.* Neuron, 2002. **34**(4): p. 509-19.

183. Ando, K., et al., *N-cadherin regulates p38 MAPK signaling via association with JNK-associated leucine zipper protein: implications for neurodegeneration in Alzheimer disease.* J Biol Chem, 2011. **286**(9): p. 7619-28.

184. Fraser, P.E., et al., *Presenilin function: connections to Alzheimer's disease and signal transduction.* Biochem Soc Symp, 2001(67): p. 89-100.

185. Kim, Y.E., et al., *Molecular chaperone functions in protein folding and proteostasis.* Annu Rev Biochem, 2013. **82**: p. 323-55.

186. Alonso, A.C., I. Grundke-Iqbal, and K. Iqbal, *Alzheimer's disease hyperphosphorylated tau sequesters normal tau into tangles of filaments and disassembles microtubules.* Nat Med, 1996. **2**(7): p. 783-7.

187. Lambert, M.P., et al., *Monoclonal antibodies that target pathological assemblies of Abeta.* J Neurochem, 2007. **100**(1): p. 23-35.

188. Baskin, D.S., et al., *Brain choline acetyltransferase and mental function in Alzheimer disease.* Arch Neurol, 1999. **56**(9): p. 1121-3.

189. Mali, P., K.M. Esvelt, and G.M. Church, *Cas9 as a versatile tool for engineering biology.* Nat Methods, 2013. **10**(10): p. 957-63.

190. Rubio, A., et al., *Rapid and efficient CRISPR/Cas9 gene inactivation in human neurons during human pluripotent stem cell differentiation and direct reprogramming.* Sci Rep, 2016. **6**: p. 37540.

191. Elie, A., et al., *Tau co-organizes dynamic microtubule and actin networks.* Sci Rep, 2015. **5**: p. 9964.

192. Rovelet-Lecrux, A., et al., *Frontotemporal dementia phenotype associated with MAPT gene duplication.* J Alzheimers Dis, 2010. **21**(3): p. 897-902.

193. Ismail, I.H., et al., *BMI1-mediated histone ubiquitylation promotes DNA double-strand break repair.* J Cell Biol, 2010. **191**(1): p. 45-60.

194. Calao, M., et al., *Direct effects of Bmi1 on p53 protein stability inactivates oncoprotein stress responses in embryonal cancer precursor cells at tumor initiation.* Oncogene, 2013. **32**(31): p. 3616-26.

195. Medina, M. and J. Avila, *New insights into the role of glycogen synthase kinase-3 in Alzheimer's disease.* Expert Opin Ther Targets, 2014. **18**(1): p. 69-77.

196. Culmsee, C. and M.P. Mattson, *p53 in neuronal apoptosis.* Biochem Biophys Res Commun, 2005. **331**(3): p. 761-77.

197. Anckar, J. and L. Sistonen, *Regulation of HSF1 function in the heat stress response: implications in aging and disease.* Annu Rev Biochem, 2011. **80**: p. 1089-115.

198. Smith, H.L., W. Li, and M.E. Cheetham, *Molecular chaperones and neuronal proteostasis.* Semin Cell Dev Biol, 2015. **40**: p. 142-52.

199. Pickart, C.M. and M.J. Eddins, *Ubiquitin: structures, functions, mechanisms.* Biochim Biophys Acta, 2004. **1695**(1-3): p. 55-72.

200. Dammer, E.B., et al., *Polyubiquitin linkage profiles in three models of proteolytic stress suggest the etiology of Alzheimer disease.* J Biol Chem, 2011. **286**(12): p. 10457-65.

201. Kim, G., et al., *The heat shock transcription factor Hsf1 is downregulated in DNA damage-associated senescence, contributing to the maintenance of senescence phenotype.* Aging Cell, 2012. **11**(4): p. 617-27.

202. Tang, Z., et al., *MEK guards proteome stability and inhibits tumor-suppressive amyloidogenesis via HSF1.* Cell, 2015. **160**(4): p. 729-44.

203. Moore, S., et al., *APP metabolism regulates tau proteostasis in human cerebral cortex neurons.* Cell Rep, 2015. **11**(5): p. 689-96.

204. Campisi, J., *Aging, cellular senescence, and cancer.* Annu Rev Physiol, 2012. **75**: p. 685-705.

205. Mi, H., et al., *Large-scale gene function analysis with the PANTHER classification system.* Nat Protoc, 2013. **8**(8): p. 1551-66.

206. Mi, H., A. Muruganujan, and P.D. Thomas, *PANTHER in 2013: modeling the evolution of gene function, and other gene attributes, in the context of phylogenetic trees.* Nucleic Acids Res, 2013. **41**(Database issue): p. D377-86.

207. Mi, H. and P. Thomas, *PANTHER pathway: an ontology-based pathway database coupled with data analysis tools.* Methods Mol Biol, 2009. **563**: p. 123-40.

208. Villemagne, V.L., et al., *Amyloid beta deposition, neurodegeneration, and cognitive decline in sporadic Alzheimer's disease: a prospective cohort study.* Lancet Neurol, 2013. **12**(4): p. 357-67.

209. Qiang, L., R. Fujita, and A. Abeliovich, *Remodeling neurodegeneration: somatic cell reprogramming-based models of adult neurological disorders.* Neuron, 2013. **78**(6): p. 957-69.

210. Okita, K., et al., *A more efficient method to generate integration-free human iPS cells.* Nat Methods, 2011. **8**(5): p. 409-12.

211. Lujan, E., et al., *Early reprogramming regulators identified by prospective isolation and mass cytometry.* Nature, 2015. **521**(7552): p. 352-6.

212. Mendieta, J., et al., *Phosphorylation modulates the alpha-helical structure and polymerization of a peptide from the third tau microtubule-binding repeat.* Biochim Biophys Acta, 2005. **1721**(1-3): p. 16-26.

213. Buee, L., et al., *Tau protein isoforms, phosphorylation and role in neurodegenerative disorders.* Brain Res Brain Res Rev, 2000. **33**(1): p. 95-130.

214. Youmans, K.L., et al., *Intraneuronal Abeta detection in 5xFAD mice by a new Abeta-specific antibody.* Mol Neurodegener, 2012. **7**: p. 8.

215. Lauritzen, I., et al., *The beta-secretase-derived C-terminal fragment of betaAPP, C99, but not Abeta, is a key contributor to early intraneuronal lesions in triple-transgenic mouse hippocampus.* J Neurosci, 2012. **32**(46): p. 16243-55a.

216. Ittner, L.M., et al., *Dendritic function of tau mediates amyloid-beta toxicity in Alzheimer's disease mouse models.* Cell, 2010. **142**(3): p. 387-97.

217. Chapman, P.F., et al., *Impaired synaptic plasticity and learning in aged amyloid precursor protein transgenic mice.* Nat Neurosci, 1999. **2**(3): p. 271-6.

218. Galvan, V., et al., *Reversal of Alzheimer's-like pathology and behavior in human APP transgenic mice by mutation of Asp664.* Proc Natl Acad Sci U S A, 2006. **103**(18): p. 7130-5.

219. Leissring, M.A., et al., *Enhanced proteolysis of beta-amyloid in APP transgenic mice prevents plaque formation, secondary pathology, and premature death.* Neuron, 2003. **40**: p. 1087-1093.

220. Tomiyama, T., et al., *A mouse model of amyloid beta oligomers: their contribution to synaptic alteration, abnormal tau phosphorylation, glial activation, and neuronal loss in vivo.* J Neurosci, 2010. **30**(14): p. 4845-56.

221. Hooli, B.V., et al., *Rare autosomal copy number variations in early-onset familial Alzheimer's disease.* Mol Psychiatry, 2014. **19**(6): p. 676-81.

222. Cuyvers, E. and K. Sleegers, *Genetic variations underlying Alzheimer's disease: evidence from genome-wide association studies and beyond.* Lancet Neurol, 2016. **15**(8): p. 857-68.

223. Anfossi, M., et al., *Compound heterozygosity of 2 novel MAPT mutations in frontotemporal dementia.* Neurobiol Aging, 2011. **32**(4): p. 757 e1-757 e11.

224. Ishida, C., et al., *Frontotemporal dementia with parkinsonism linked to chromosome 17 with the MAPT R406W mutation presenting with a broad distribution of abundant senile plaques.* Neuropathology, 2015. **35**(1): p. 75-82.

225. Hanger, D.P., et al., *Glycogen synthase kinase-3 induces Alzheimer's disease-like phosphorylation of tau: generation of paired helical filament epitopes and neuronal localisation of the kinase.* Neurosci Lett, 1992. **147**(1): p. 58-62.

226. Lucas, J.J., et al., *Decreased nuclear beta-catenin, tau hyperphosphorylation and neurodegeneration in GSK-3beta conditional transgenic mice.* EMBO J, 2001. **20**(1-2): p. 27-39.

227. Mudher, A., et al., *GSK-3beta inhibition reverses axonal transport defects and behavioural phenotypes in Drosophila.* Mol Psychiatry, 2004. **9**(5): p. 522-30.

228. Korur, S., et al., *GSK3beta regulates differentiation and growth arrest in glioblastoma.* PLoS One, 2009. **4**(10): p. e7443.

229. Liao, Y. and M.C. Hung, *Physiological regulation of Akt activity and stability.* Am J Transl Res, 2010. **2**(1): p. 19-42.

230. Hooper, C., R. Killick, and S. Lovestone, *The GSK3 hypothesis of Alzheimer's disease.* J Neurochem, 2008. **104**(6): p. 1433-9.

231. Sagredo, A.I., et al., *TRPM4 regulates Akt/GSK3-beta activity and enhances beta-catenin signaling and cell proliferation in prostate cancer cells.* Mol Oncol, 2018. **12**(2): p. 151-165.

232. Bechard, M. and S. Dalton, *Subcellular localization of glycogen synthase kinase 3beta controls embryonic stem cell self-renewal.* Mol Cell Biol, 2009. **29**(8): p. 2092-104.

233. Lee, H. and J.Y. Ro, *Differential expression of GSK3beta and pS9GSK3beta in normal human tissues: can pS9GSK3beta be an epithelial marker?* Int J Clin Exp Pathol, 2015. **8**(4): p. 4064-73.

234. Kitagishi, Y., et al., *Dietary regulation of PI3K/AKT/GSK-3beta pathway in Alzheimer's disease.* Alzheimers Res Ther, 2014. **6**(3): p. 35.

235. Wang, X., et al., *Bmi-1 regulates stem cell-like properties of gastric cancer cells via modulating miRNAs.* J Hematol Oncol, 2016. **9**(1): p. 90.

236. Lee, H.K., et al., *The insulin/Akt signaling pathway is targeted by intracellular beta-amyloid.* Mol Biol Cell, 2009. **20**(5): p. 1533-44.

237. Park, H.H., et al., *Novel vaccine peptide GV1001 effectively blocks beta-amyloid toxicity by mimicking the extra-telomeric functions of human telomerase reverse transcriptase.* Neurobiol Aging, 2014. **35**(6): p. 1255-74.

238. Choi, H., et al., *Coenzyme Q10 restores amyloid beta-inhibited proliferation of neural stem cells by activating the PI3K pathway.* Stem Cells Dev, 2013. **22**(15): p. 2112-20.

239. Abdouh, M., et al., *The Polycomb Repressive Complex 1 Protein BMI1 Is Required for Constitutive Heterochromatin Formation and Silencing in Mammalian Somatic Cells.* J Biol Chem, 2016. **291**(1): p. 182-97.

240. Frost, B., et al., *Tau promotes neurodegeneration through global chromatin relaxation.* Nat Neurosci, 2014. **17**(3): p. 357-66.

241. DuBoff, B., J. Gotz, and M.B. Feany, *Tau promotes neurodegeneration via DRP1 mislocalization in vivo.* Neuron, 2012. **75**(4): p. 618-32.

242. Mansuroglu, Z., et al., *Loss of Tau protein affects the structure, transcription and repair of neuronal pericentromeric heterochromatin.* Sci Rep, 2016. **6**: p. 33047.

243. Burstein, E., et al., *COMMD proteins, a novel family of structural and functional homologs of MURR1.* J Biol Chem, 2005. **280**(23): p. 22222-32.

244. de Bie, P., et al., *Characterization of COMMD protein-protein interactions in NF-kappaB signalling.* Biochem J, 2006. **398**(1): p. 63-71.

245. Narindrasorasak, S., et al., *Characterization and copper binding properties of human COMMD1 (MURR1).* Biochemistry, 2007. **46**(11): p. 3116-28.

246. Maine, G.N. and E. Burstein, *COMMD proteins and the control of the NF kappa B pathway.* Cell Cycle, 2007. **6**(6): p. 672-6.

247. Maine, G.N. and E. Burstein, *COMMD proteins: COMMing to the scene.* Cell Mol Life Sci, 2007. **64**(15): p. 1997-2005.

248. Bartuzi, P., M.H. Hofker, and B. van de Sluis, *Tuning NF-kappaB activity: a touch of COMMD proteins.* Biochim Biophys Acta, 2013. **1832**(12): p. 2315-21.

249. Riera-Romo, M., *COMMD1: A Multifunctional Regulatory Protein.* J Cell Biochem, 2018. **119**(1): p. 34-51.

250. Fedoseienko, A., et al., *COMMD Family Regulates Plasma LDL Levels and Attenuates Atherosclerosis Through Stabilizing the CCC Complex in Endosomal LDLR Trafficking.* Circ Res, 2018.

251. Jin, P., et al., *Genome-wide organization, evolutionary diversification of the COMMD family genes of amphioxus (Branchiostoma belcheri) with the possible role in innate immunity.* Fish Shellfish Immunol, 2018. **77**: p. 31-39.

252. Hong, J.T., *NF-kB as a mediator of brain inflammation in AD.* CNS Neurol Disord Drug Targets, 2017.

253. Watson, C.T., et al., *Genome-wide DNA methylation profiling in the superior temporal gyrus reveals epigenetic signatures associated with Alzheimer's disease.* Genome Med, 2016. **8**(1): p. 5.

254. Sanchez-Mut, J.V., et al., *Human DNA methylomes of neurodegenerative diseases show common epigenomic patterns.* Transl Psychiatry, 2016. **6**: p. e718.

255. Sanchez-Mut, J.V., et al., *DNA methylation map of mouse and human brain identifies target genes in Alzheimer's disease.* Brain, 2013. **136**(Pt 10): p. 3018-27.

256. Sanchez-Mut, J.V. and J. Graff, *Epigenetic Alterations in Alzheimer's Disease.* Front Behav Neurosci, 2015. **9**: p. 347.

257. Ziller, M.J., et al., *Charting a dynamic DNA methylation landscape of the human genome.* Nature, 2013. **500**(7463): p. 477-81.

258. Crapper, D.R., S. Quittkat, and U. de Boni, *Altered chromatin conformation in Alzheimer's disease.* Brain, 1979. **102**(3): p. 483-95.

259. Zhang, C., et al., *Primate-specific miR-603 is implicated in the risk and pathogenesis of Alzheimer's disease.* Aging (Albany NY), 2016. **8**(2): p. 272-90.

260. Nunez-Iglesias, J., et al., *Joint genome-wide profiling of miRNA and mRNA expression in Alzheimer's disease cortex reveals altered miRNA regulation.* PLoS One, 2010. **5**(2): p. e8898.

261. Lau, P., et al., *Alteration of the microRNA network during the progression of Alzheimer's disease.* EMBO Mol Med, 2013. **5**(10): p. 1613-34.

262. Santa-Maria, I., et al., *Dysregulation of microRNA-219 promotes neurodegeneration through post-transcriptional regulation of tau.* J Clin Invest, 2015. **125**(2): p. 681-6.

263. Nair, V.D. and Y. Ge, *Alterations of miRNAs reveal a dysregulated molecular regulatory network in Parkinson's disease striatum.* Neurosci Lett, 2016. **629**: p. 99-104.

264. Kayano, M., et al., *Plasma microRNA biomarker detection for mild cognitive impairment using differential correlation analysis.* Biomark Res, 2016. **4**: p. 22.

265. Dimri, M., et al., *microRNA-141 regulates BMI1 expression and induces senescence in human diploid fibroblasts.* Cell Cycle, 2013. **12**(22): p. 3537-46.

266. Liu, S., et al., *miR-200c/Bmi1 axis and epithelial-mesenchymal transition contribute to acquired resistance to BRAF inhibitor treatment.* Pigment Cell Melanoma Res, 2015. **28**(4): p. 431-41.

267. Dimri, M., M. Kang, and G.P. Dimri, *A miR-200c/141-BMI1 autoregulatory loop regulates oncogenic activity of BMI1 in cancer cells.* Oncotarget, 2016. **7**(24): p. 36220-36234.

268. Cruz, F.M., et al., *miR-300 mediates Bmi1 function and regulates differentiation in primitive cardiac progenitors.* Cell Death Dis, 2015. **6**: p. e1953.

269. Lugli, G., et al., *Plasma Exosomal miRNAs in Persons with and without Alzheimer Disease: Altered Expression and Prospects for Biomarkers.* PLoS One, 2015. **10**(10): p. e0139233.

270. Briggs, J.A., et al., *Mechanisms of Long Non-coding RNAs in Mammalian Nervous System Development, Plasticity, Disease, and Evolution.* Neuron, 2015. **88**(5): p. 861-877.

271. Gutschner, T. and S. Diederichs, *The hallmarks of cancer: a long non-coding RNA point of view.* RNA Biol, 2012. **9**(6): p. 703-19.

272. Qureshi, I.A., J.S. Mattick, and M.F. Mehler, *Long non-coding RNAs in nervous system function and disease.* Brain Res, 2010. **1338**: p. 20-35.

273. Esteller, M., *Non-coding RNAs in human disease.* Nat Rev Genet, 2011. **12**(12): p. 861-74.

274. Magistri, M., et al., *Transcriptomics Profiling of Alzheimer's Disease Reveal Neurovascular Defects, Altered Amyloid-beta Homeostasis, and Deregulated Expression of Long Noncoding RNAs.* J Alzheimers Dis, 2015. **48**(3): p. 647-65.

275. Gellert, P., et al., *Noncoder: a web interface for exon array-based detection of long non-coding RNAs.* Nucleic Acids Res, 2013. **41**(1): p. e20.

276. Zhou, X. and J. Xu, *Identification of Alzheimer's disease-associated long noncoding RNAs.* Neurobiol Aging, 2015. **36**(11): p. 2925-2931.

277. Faghihi, M.A., et al., *Expression of a noncoding RNA is elevated in Alzheimer's disease and drives rapid feed-forward regulation of beta-secretase.* Nat Med, 2008. **14**(7): p. 723-30.

278. Meng, S., et al., *Identification and characterization of Bmi-1-responding element within the human p16 promoter.* J Biol Chem, 2010. **285**(43): p. 33219-29.

279. Naughton, B.J., et al., *Blood genome-wide transcriptional profiles reflect broad molecular impairments and strong blood-brain links in Alzheimer's disease.* J Alzheimers Dis, 2015. **43**(1): p. 93-108.

280. Maes, O.C., et al., *Methodology for discovery of Alzheimer's disease blood-based biomarkers.* J Gerontol A Biol Sci Med Sci, 2009. **64**(6): p. 636-45.

281. Maes, O.C., et al., *Transcriptional profiling of Alzheimer blood mononuclear cells by microarray.* Neurobiol Aging, 2007. **28**(12): p. 1795-809.

282. Leidinger, P., et al., *A blood based 12-miRNA signature of Alzheimer disease patients.* Genome Biol, 2013. **14**(7): p. R78.

283. Maler, J.M., et al., *Decreased circulating CD34+ stem cells in early Alzheimer's disease: Evidence for a deficient hematopoietic brain support?* Mol Psychiatry, 2006. **11**(12): p. 1113-5.

<u>Annexe I:</u> The Polycomb Repressive Complex 1 Protein BMI1 Is Required for Constitutive Heterochromatin Formation and Silencing in Mammalian Somatic Cells

L'annexe 1 vous présente un article en lien avec mon projet de doctorat et paru le 14 Octobre 2015 dans *Journal of Biological Chemistry*. Dans cette étude, j'ai réalisé les analyses bio-informatiques et j'ai constitué la figure 3.

THE JOURNAL OF BIOLOGICAL CHEMISTRY VOL. 291, NO. 1, pp. 182–197, January 1, 2016

The Polycomb Repressive Complex 1 Protein BMI1 Is Required for Constitutive Heterochromatin Formation and Silencing in Mammalian Somatic Cells*[S]

Received for publication, April 29, 2015, and in revised form, October 13, 2015 Published, JBC Papers in Press, October 14, 2015, DOI 10.1074/jbc.M115.662403

Mohamed Abdouh[1], **Roy Hanna**[1], **Jida El Hajjar**[2], **Anthony Flamier**[2], **and Gilbert Bernier**[3]

From the Department of Neurosciences, University of Montreal, and The Stem Cell and Developmental Biology Laboratory, Hôpital Maisonneuve-Rosemont, 5415 Boul. l'Assomption, Montreal H1T 2M4, Canada

Background: BMI1 silences the expression of genes located at the facultative heterochromatin.
Results: BMI1 is abundant at repetitive genomic regions, including the pericentromeric heterochromatin (PCH), where it is required for compaction and silencing.
Conclusion: BMI1 is essential for PCH formation.
Significance: BMI1 function at PCH is important to understand how BMI1 regulates genomic stability.

The polycomb repressive complex 1 (PRC1), containing the core BMI1 and RING1A/B proteins, mono-ubiquitinylates histone H2A ($H2A^{ub}$) and is associated with silenced developmental genes at facultative heterochromatin. It is, however, assumed that the PRC1 is excluded from constitutive heterochromatin in somatic cells based on work performed on mouse embryonic stem cells and oocytes. We show here that BMI1 is required for constitutive heterochromatin formation and silencing in human and mouse somatic cells. BMI1 was highly enriched at intergenic and pericentric heterochromatin, co-immunoprecipitated with the architectural heterochromatin proteins HP1, DEK1, and ATRx, and was required for their localization. In contrast, BRCA1 localization was BMI1-independent and partially redundant with that of BMI1 for $H2A^{ub}$ deposition, constitutive heterochromatin formation, and silencing. These observations suggest a dynamic and developmentally regulated model of PRC1 occupancy at constitutive heterochromatin, and where BMI1 function in somatic cells is to stabilize the repetitive genome.

Chromosomes are structurally organized in distinct subcompartments as determined by the local DNA sequence and chromatin organization. Euchromatin defines "relaxed" chromatin regions containing actively transcribed genes. In contrast, heterochromatin defines "compacted" chromatin regions containing tissue-specific and developmental genes (the facultative heterochromatin) or gene-poor regions (the constitutive heterochromatin) (1). The constitutive heterochromatin is found at the center (centromere) and ends (telomeres) of chromosomes and is mostly constituted of repetitive DNA sequences (1). Numerous (about 10,000) repetitive A/T-rich DNA elements of 231 bp are also found in the pericentromeric heterochromatin (PCH)[4] of mouse chromosomes. Because constitutive heterochromatin regions contained repetitive DNA sequences, the maintenance of chromatin compaction is essential to preserve genomic stability (2). During mitosis, repetitive elements can recombine, resulting in non-homologous recombination between different chromosomes or different regions of paired chromosomes and thus chromosomes deletion, translocation, and fusion (3). Repetitive DNA sequences can be also transcribed, resulting in aberrant non-coding RNA. Stabilization of telomeres and centromers is also essential for chromosome end capping and kinetochore attachment during mitosis (4). Finally, about 40% of the mammalian genome is constituted of "parasitic" retro-element located in intergenic regions of chromosomes. Active repression of these elements is important to maintain genomic stability because some of these can self-replicate and randomly integrate the genome (5, 6).

Nucleosomes are the basic building unit of chromatin and are constituted of a 147-bp DNA wrapped against a histone octamer containing two molecules of each of the four histones H2A, H2B, H3, and H4 (the nucleosome core particle) (1). Addition of linker histones, such as histone H1, increases the amount of associated DNA by 20 bp to elicit higher levels of chromatin compaction and high order chromatin structure. The chromatin is also attached at multiple points to the nuclear envelope and spatial organization of the chromatin in the nucleus is important for the regulation of gene transcription (7, 8). Post-translational modifications of histones, such as methylation, acetylation, and ubiquitylation can modify chromatin compaction and stability. For example, silent or compact chromatin is associated with trimethylation of histone H3 at lysine 9 ($H3K9^{me3}$) or 27 ($H3K27^{me3}$), whereas open chromatin is associated with histone H3 trimethylation

* This work was supported in part by a grant from the Natural Science and Engineering Research Council of Canada. The authors declare that they have no conflict of interest regarding the content of this manuscript.
[S] This article contains supplemental "Experimental Procedures".
[1] Both authors contributed equally to this work.
[2] Supported by fellowships from the University of Montreal Molecular Biology Program.
[3] To whom correspondence should be addressed. Tel.: 514-252-3400 (ext. 4648); Fax: 514-253-7626; E-mail: gbernier.hmr@ssss.gouv.qc.ca.

[4] The abbreviations used are: PCH, pericentromeric heterochromatin; PcG, polycomb group; PRC, polycomb repressive complex; IP, immunoprecipitation; IF, immunofluorescence; qPCR, quantitative PCR; DKN, double knockdown; nt, nucleotide.

at lysine 4 ($H3K4^{me3}$) or acetylation at lysine 9 ($H3K9^{ac}$) (9). Acetylation brings in a negative charge, acting to neutralize the positive charge on histones and decreases the interaction of the N termini of histones with the negatively charged phosphate groups of DNA. In pathological conditions, histones hyper-acetylation can result in chromatin and chromosomes de-condensation (10).

A core of proteins is involved in establishment and maintenance of constitutive heterochromatin. Most of these proteins are conserved in *Drosophila* and were identified as modifiers of position effect variegation (1). In mammals, the buildup of these proteins to heterochromatic DNA follows a relatively well characterized sequence where zinc finger proteins recognize and bind repetitive DNA sequences. This is followed by enrichment for Histones H1 and H2a/z, accumulation of Hmga1/2, attachment of KAP1/Trim28 (a SUMO E3 ligase), and of the ATP-dependent chromatin remodeler ATRx, deacetylation of histones by HDAC2, and trimethylation of histone H3 at lysine 9 by SUV39h1 and SUV39h2. Association of SUMOylated HP1a and HP1b to a non-coding RNA results in increased binding affinity for $H3K9^{me3}$ and this is further enhanced and stabilized by the *suppressor of variegation* protein DEK1 (11, 12). The DEK1-HP1-SUV39 complex then propagates the $H3K9^{me3}$ marks on the chromatin, resulting in heterochromatin formation (13–17). Interestingly, ATRx localizes at both telomeric and PCH, and germline mutations in ATRx are associated with the α-thalassemia with mental retardation X-linked syndrome (18–20). Surprisingly, it was showed that the BRCA1 protein, which possesses histone H2A monoubiquitin ligase activity when in complex with BARD1, is also enriched at PCH and required for H2A ubiquitinylation, heterochromatin compaction, and silencing (21–23). This novel BRCA1 function was proposed to explain the severe genomic instability phenotype of BRCA1-deficient cells (22).

Polycomb group (PcG) proteins form large multimeric complexes involved in gene silencing through modifications of chromatin organization (24). They are classically subdivided into two groups, namely polycomb repressive complex 1 (PRC1) and PRC2 (25). Histone modifications induced by the PRC2 complex (which includes EZH2, EED, and SUV12) and the PRC1 complex (which includes BMI1, RING1A, and RING1B/RNF2) allows stable silencing of gene expression in euchromatin and facultative heterochromatin (26–28). Notably, previous recruitment models of PcG proteins through sequential histone modifications have been revised following that PRC1-variants could operate independently, and even upstream of PRC2 (29,30). The PRC2 contains histone H3 trimethylase activity at lysine 27 ($H3K27^{me3}$), whereas the PRC1 contains histone H2A monoubiquitin ligase activity at lysine 119 ($H2A^{ub}$) (26–28). A number of observations have implicated these proto-oncogenes in human cancers (31–36). At the opposite, *Bmi1*-deficient mice display neurological abnormalities, postnatal depletion of stem cells, increased reactive oxygen species, reduced lifespan, and premature aging phenotypes (37–40). Likewise, primary human and mouse cells deficient for BMI1 undergo rapid senescence, in part through activation of the tumor suppressor *INK4A* locus (39–41). BMI1 was also implicated in DNA damage response and repair, and maintenance of genomic stability (42–45).

Although PRC1 proteins have not been directly implicated in constitutive heterochromatin formation or maintenance, at least some line of evidences support this possibility: 1) immuno-gold localization of BMI1 by electron microscopy in U-2 OS cells revealed high enrichment in electron-dense heterochromatin; 2) BMI1 immunolocalization was found at PCH in transformed human cell lines (46–49). However, based on work performed on mouse embryonic stem cells and oocytes, it is generally assumed that PRC1 proteins are excluded from PCH in normal mammalian somatic cells (30, 50–52). In contrast with this model, we found that BMI1 is abundant at constitutive heterochromatin in mouse and human somatic cells, and required for heterochromatin formation/maintenance and silencing. In *Bmi1*-null mice, cortical neurons showed loss of heterochromatin compaction and activation of intergenic retro-elements and satellite repeats. Consistently, Bmi1 co-localized with $H3K9^{me3}$ and was highly enriched at PCH in mouse neurons. BMI1 was also enriched at constitutive heterochromatin, including PCH, in normal human neural precursors. Furthermore, BMI1 co-purified with architectural heterochromatin proteins and with histone $H3K9^{me3}$. BMI1 localization and $H2A^{ub}$ deposition at constitutive heterochromatin were *EZH2* and $H3K27^{me3}$ independent. In both transformed and normal primary somatic cells, BMI1 inactivation resulted in loss of heterochromatin and alteration in the architecture of the nuclear envelope. Notably, BRCA1 localization was unaffected upon BMI1 deficiency, and both proteins showed partial functional redundancy for H2A ubiquitinylation, heterochromatin formation, and silencing. These findings reveal an essential function for BMI1 in constitutive heterochromatin formation and silencing in mammalian somatic cells.

Experimental Procedures

Animals—Mice were used in accordance with the Animal Care Committee of the Maisonneuve-Rosemont Hospital Research Center (approval ID numbers 2009-40, 2009-42, and 2011-23).

Neuronal Cultures—Embryonic day 18.5 cortices were dissected in oxygenated Hanks' balanced salt solution. Following meninges removal, cortices were cut to ~1 mm^3 pieces, and incubated at 37 °C for 15 min in 2 ml of TrypleEx solution (Invitrogen). Afterward, enzymatic solution was discarded, and cortex pieces dissociated in Hanks' balanced salt solution with a 1-ml tip (10 times up and down). After dissociation, cells were plated at 1.5×10^5 cells/well on poly-L-lysine-coated 6-well plates or 8-well cultures slides (BD Biosciences). Cells were maintained in normal medium composed of Neurobasal-A medium (Invitrogen), Glutamax-I (Gibco), gentamycin (50 μg/ml; Gibco), B27 supplement (Gibco), NGF (50 ng/ml; Invitrogen), and BDNF (0.5 ng/ml; Invitrogen).

Chromatin Immunoprecipitation (ChIP) Assay—ChIP was performed using the ChIP Assay kit (Upstate). Cells were homogenized at room temperature according to the manufacturer's protocol and sonicated on ice for 10 s at 30% amplitude to shear the chromatin (Branson Digital Sonifier 450, Crystal Electronics, On. Canada). Sonicated materials were

immunoprecipitated using 2 μg of mouse anti-BMI1, mouse anti-H2AK119ub clone E6C5, mouse anti-RING1B, and mouse anti-HP1 (Millipore), rabbit anti-H3K9me3, and rabbit anti-H3K27me3 (Abcam), rabbit anti-BRCA1 (Santa Cruz Biotechnology), and rabbit anti-mouse IgG (Upstate) antibodies. Fragments were then amplified by real-time PCR in triplicates. Human primers sets used were as described in Ref. 22. ChIP-quantitative PCR (qPCR) data were analyzed according to the Percent Input method. First, the raw C_t of the diluted 1% input fraction is adjusted by subtracting 6.64 cycles (*i.e.* log2 of the dilution factor 100). Subsequently, the percent input of each immunoprecipitation (IP) fraction is calculated according to this equation: $100 \times 2^{(\text{Adjusted Input Ct} - \text{Ct(IP)})}$.

Real-time RT-PCR—Mouse cortices or human cells were diced and RNA was isolated using TRIzol reagent (Invitrogen). Reverse transcription (RT) was performed using 1 μg of total RNA and the Moloney murine leukemia virus reverse transcriptase (Invitrogen). Real-time PCR was carried in triplicates using Platinum SYBR Green Supermix (Invitrogen) and Real-time PCR apparatus (ABI Prism 7002).

Micrococcal Nuclease and DNase Assays—One million (10^6) cells were harvested at the log phase growth and used in either nuclease sensitivity assay. Cells were permeabilized (0.02% L-α-lysolecithin, 150 mM sucrose, 35 mM HEPES, 5 mM KH_2PO_4, 5 mM $MgCl_2$, 0.5 mM $CaCl_2$) on ice for 90 s, and than washed in ice-cold PBS. The cell pellet was resuspended in nuclease buffer (150 mM sucrose, 50 mM Tris-HCl (pH 7.5), 50 mM NaCl, 2 mM $CaCl_2$) on ice, and nucleases were added. Digestions were performed at 24 °C. Reactions were stopped by adding digestion stop buffer (20 mM Tris-Cl (pH 7.4), 0.2 M NaCl, 10 mM EDTA, 2% SDS) and 0.1 mg/ml of RNase A for 30 min at 37 °C. DNA was extracted by phenol/chloroform and visualized on 0.8% native agarose gel/ethidium bromide.

Plasmid Constructs and Viruses—Sequence-specific oligonucleotides stretch shRNA designed to target the BMI-1 ORF (accession number BC011652) were synthesized. Oligo#1 (nt 1061–1081) 5′-CCTAATACTTTCCAGATTGAT-3′, and oligoScramble (nt 573–591) 5′-GGTACTTCATTGATGCCAC-3′ were used in this study. These sequences are followed by the loop sequence (TTCAAGAGA) and finally the reverse complements of the targeting sequences. The double stranded shRNA sequences were cloned downstream of the H1P promoter of the H1P-UbqC-HygroEGFP plasmid using Age1, SmaI, and XbaI cloning sites. The shRNA-expressing lentiviral plasmids were cotransfected with plasmids pCMVdR8.9 and pHCMV-G into 293FT packaging cells using Lipofectamine (Invitrogen) according to the manufacturer's instructions. Viral containing media were collected, filtered, and concentrated by ultracentrifugation. Viral titers were measured by serial dilution on 293T cells followed by microscopic analysis 48 h later. For viral transduction, lentiviral vectors were added to dissociated cells prior to plating. Hygromycin selection (150 μg/ml) was added 48 h later. shBRCA1 constructs (MISSION shRNA) were from Sigma, and siRING1B (FlexiTube siRNA) from Qiagen. The RNAi-resistant BMI1-Myc construct ($BMI1^{myc-R}$) was generated by synthesis (GenScript) and where the nucleotide sequence of the human BMI1 cDNA (5′-CCTAATACTTTCCAGATTGAT-3′) was changed to (5-CC**C**AA**C**A-C**A**TT**T**CA**A**AT**A**GA**C**-3), thus preserving the original amino acid sequence of BMI1.

Proteomics—293T cells were transfected with the EFv-CMV-GFP (GFP-293T) or EFv-BMI1-Myc-CMV-GFP (Myc-293T) plasmids. Protein extracts were subjected to immunoprecipitation using an anti-Myc antibody. Immunoprecipitates were resolved by SDS-PAGE and LC-MS analysis was performed.

Fixation, Sectioning, and Immunolabeling—Tissues were fixed in 10% buffered formalin and embedded in paraffin according to standard protocols. 5 to 7-μm thick sections were mounted on Super-Frost glass slides (Fisher Scientific) and processed for immunohistochemistry staining. Formalin-fixed paraffin-embedded slices were analyzed by using the Vectastain® ABC kit (Vector) according to the manufacturer's instructions. Peroxidase substrate DAB (brown) was used (Sigma). Observations were made under a fluorescence microscope (Leica DMRE, Leica Microsystems) and images were captured with a digital camera (Retiga EX; QIMAGING; with OpenLab, version 3.1.1 software; Open-Lab, Canada). Antibodies used in this study were mouse anti-BMI1 and anti-HP1 (Millipore), and rabbit anti-H3K9Ac and anti-H3K9me3 (Abcam). Secondary antibodies used were FITC-conjugated donkey anti-mouse and rhodamine-conjugated donkey anti-rabbit (Chemicon).

Immunoprecipitation and Western Blot—For BMI1/Myc immunoprecipitation experiments, 293T cells were transfected with EFv-/CMV-GFP or EFv-$BMI1^{Myc}$/CMV-GFP plasmids using Lipofectamine according to the manufacturer's instructions. Whole cell extracts were collected in IP buffer (100 mM Tris-HCl, pH 7.5, 150 mM NaCl, 0.1% Tween 20, protease inhibitors Complete (Roche Applied Science)). Following the determination of protein concentration, lysates were subjected to immunoaffinity purification. Briefly, protein extracts (4 mg) were incubated with continuous rotation for 3 h at 4 °C with 50 μl of affinity matrix carrying mouse monoclonal anti-c-Myc IgG (clone 9E10; Covance). The matrix was washed four times with the wash buffer (50 mM Tris-HCl, pH 7.5, 150 mM NaCl, 0.1% Tween 20, protease inhibitors Complete). The bound proteins were eluted by treating the beads twice with 1 bead volume (50 μl) of c-Myc peptide solution (Covance) (400 μg/ml in 20 mM Tris-HCl, pH 7.5, 150 mM NaCl) for 15 min and used in Western blot experiments. Detection and identification of immunoprecipitated proteins were performed by Western blot and LC-MS/MS (liquid chromatography-tandem mass spectrometry). For LC-MS/MS analysis, proteins were revealed in silver-stained gels, according to standard protocol. Protein band cutting, trypsin-based in-gel protein digestions, and subsequent LCMS/MS procedures were performed in the Innovation Centre at Genome Quebec.

Primer Sequences—All primer sequences used in this study are shown in the supplemental Experimental Procedures.

Statistical Analysis—Statistical differences were analyzed using Student's *t* test for unpaired samples. Two-way analysis of variance test was used for multiple comparisons with one control group. In all cases, the criterion for significance (*p* value) was set as mentioned in the figures.

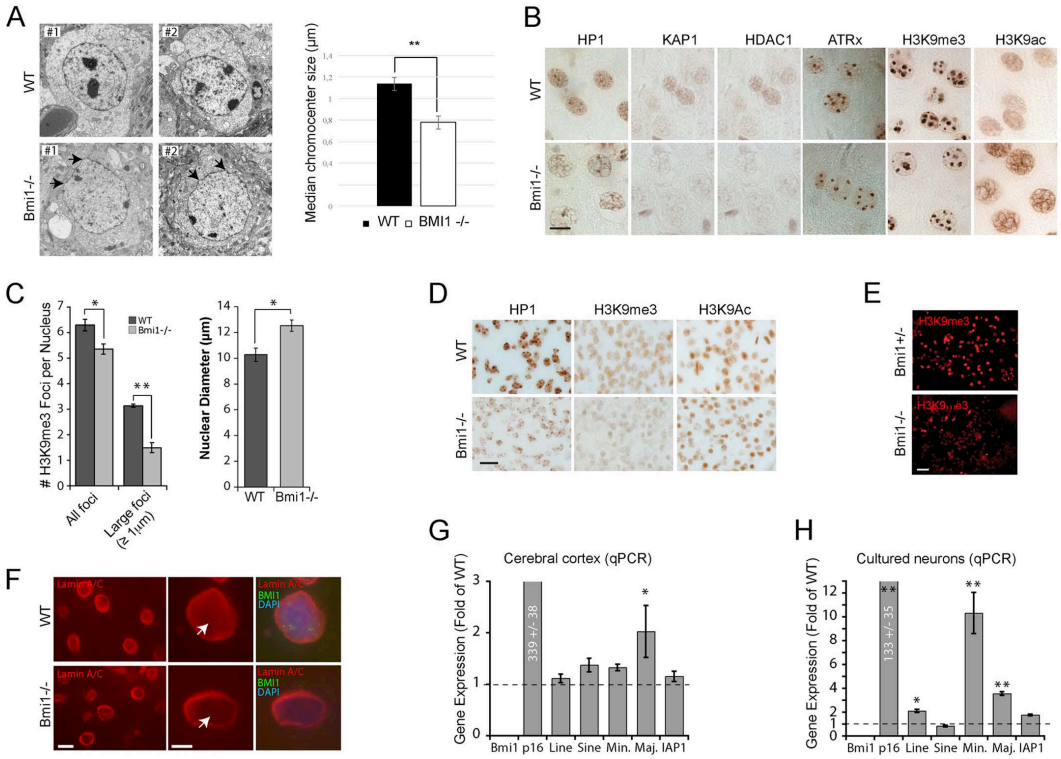

FIGURE 1. **Bmi1-deficient mouse cortical neurons present heterochromatin anomalies.** *A,* transmission electron microscopy analysis of cortical neurons in P30 WT and *Bmi1*$^{-/-}$ mice. Note the reduction in electron dense chromocenters and the anomalies in nuclear membrane architecture in *Bmi1*$^{-/-}$ neurons (*arrows*). *B,* paraffin-embedded brain sections from P30 WT and *Bmi1*$^{-/-}$ mice were analyzed by immunohistochemistry. Labeled cells are neurons located in the upper cortical layers of the cerebral cortex. *Scale bar,* 10 μm. *C,* quantification of the total number of H3K9^{me3}-positive chromocenter and number of large H3K9^{me3}-positive chromocenters. Note that the nuclear diameter of the neuron is increased in *Bmi1*$^{-/-}$ mice. Where $n = 3$ brains for each genotype. *, $p < 0.05$, **, $p < 0.01$. *D,* paraffin-embedded brain sections from e18.5 WT and *Bmi1*$^{-/-}$ embryos were analyzed as in *B*. *E* and *F,* cultured embryonic cortical neurons (*E*) and P30 cortical sections (*F*) were analyzed by immunofluorescence, revealing reduced H3K9^{me3} and Lamin A/C labeling (*arrows*) in *Bmi1*$^{-/-}$ neurons. *Scale bars*: 40 (*E*), 10 (*F*), and 5 μm (*F'*). *G,* whole cortices or (*H*) e18.5 neurons from WT and *Bmi1*$^{-/-}$ mice were analyzed by qPCR for satellite repeats and intergenic retroelements expression. *P16*^{Ink4a} was used as positive control. Note the up-regulation of minor and major satellite repeats in *Bmi1*$^{-/-}$ neurons. Where $n = 3$ independent samples for each genotype. *, $p < 0.05$; **, $p < 0.01$.

Results

Bmi1 Is Required for Constitutive Heterochromatin Formation and Silencing in Mouse Cortical Neurons—We performed transmission electron microscopy on cortical slices from WT and *Bmi1*$^{-/-}$ mice at postnatal day 30 (P30). Notably, electron-dense chromocenters were smaller and the nuclear envelope was generally irregular in *Bmi1*$^{-/-}$ neurons (Fig. 1*A*). By immunohistochemistry on cortical sections and using antibodies against H3K9^{me3} and H3K9^{ac}, a mark of open chromatin, we observed reduced H3K9^{me3} labeling in *Bmi1*$^{-/-}$ neurons together with increased H3K9^{ac} labeling (Fig. 1*B*). Immunoreactivity for HP1, KAP1, HDAC1, and ATRx was also reduced in *Bmi1*$^{-/-}$ neurons, suggesting heterochromatin anomalies (Fig. 1*B*). Quantitative analysis revealed that the number of H3K9^{me3}-positive chromocenters was reduced in *Bmi1*$^{-/-}$ neurons, whereas the nuclear diameter of the neuron was increased (Fig. 1*C*). Because postnatal neurodegeneration may account for the observed chromatin anomalies, we analyzed cortical sections from WT and *Bmi1*$^{-/-}$ embryos at e18.5. We found that H3K9^{me3} and HP1 staining were reduced in *Bmi1*$^{-/-}$ neurons, whereas that of H3K9^{ac} was unaffected, suggesting that histone hyperacetylation is secondary to defective heterochromatinization (Fig. 1*D*). Likewise, cultured cortical neurons from *Bmi1*$^{-/-}$ embryos showed reduced H3K9^{me3} labeling when compared with *Bmi1*$^{+/-}$ littermates (Fig. 1*E*). By immunofluorescence (IF) on P30 brain sections, we observed reduced immunolabeling for Lamin A/C at the neuron nuclei center of *Bmi1*$^{-/-}$ when compared with WT, suggesting anomalies in the nuclear envelope (Fig. 1*F*). Deficiency in constitutive heterochromatin formation can affect repeat-DNA sequences expression. By qRT-PCR analyses, we found increased expression of Major pericentromeric repeats in *Bmi1*$^{-/-}$ mouse cortices and of intergenic LINE elements and major and minor pericentromeric repeats in *Bmi1*$^{-/-}$ cultured e18.5 neurons, when compared with WT (Fig. 1, *G* and *H*). To test if Bmi1 was enriched at PCH in mouse neurons, we performed ChIP-qPCR

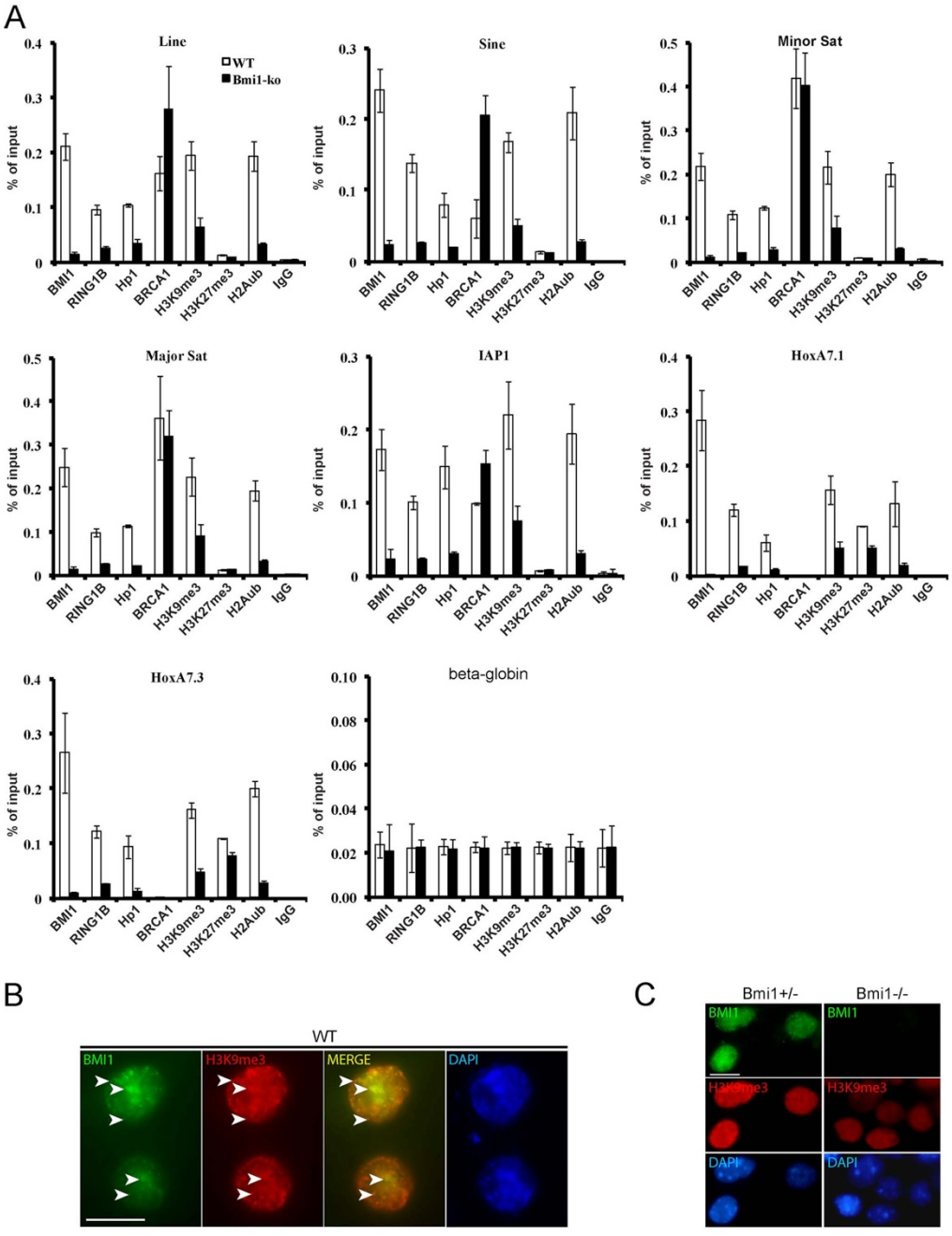

on cultured WT and *Bmi1*$^{-/-}$ e18.5 neurons after 7 days *in vitro*. We found that Bmi1 specifically accumulated at all repeat-DNA sequences and at the Bmi1-target gene *Hoxa7* (Fig. 2*A*). Notably, whereas enrichment for H3K27^{me3} was observed at *Hoxa7* in WT neurons (and slightly reduced in *Bmi1*$^{-/-}$ neurons), H3K27^{me3} enrichment at repeat-DNA was negligible in both conditions (Fig. 2*A*). *Bmi1* deficiency in mouse neurons also resulted in depletion of RING1B, HP1, H3K9^{me3}, and H2A^{ub} at repeat-DNA sequences, whereas accumulation of BRCA1 was unaffected or increased (Fig. 2*A*). Bmi1 co-localization with H3K9^{me3} in mouse cortical neurons was confirmed by IF on brain sections at P30 (Fig. 2*B*). Bmi1 antibody specificity was further validated by IF on cultured e18.5 cortical neurons (Fig. 2*C*). These results revealed that Bmi1 is required for heterochromatin formation and repeat-DNA silencing in mouse cortical neurons and enriched at PCH together with RING1B and BRCA1.

BMI1 Is Highly Enriched at Repetitive Sequences in Human Neural Precursors—To investigate BMI1 distribution on the chromatin genome-wide, we took advantage of publicly available BMI1 ChIP-Seq raw data on normal human neural precursors (53). Using MACS statistical peak calling, we identified 21,525 BMI1 binding sites. The majority of the peaks (56%) were located at intergenic regions, which are highly enriched for constitutive heterochromatin (Fig. 3*A*). As expected, we observed BMI1 enrichment at the canonical BMI1 targets *CDKN2A* (p16^{INK4A}) and *HOXC* locus (Fig. 3*E, top*). Among 9,471 gene-associated BMI1 peaks, 714 peaks were also enriched by at least 2-fold for either H3K9^{me3} or H3K27^{me3}. Notably, 565 were marked for both H3K9^{me3} and H3K27^{me3} (Fig. 3*B*). We further annotated BMI1 peaks surrounding DNA repetitive sequences using a repeat masker. Surprisingly, 81% of the total pool of BMI1 was located at repetitive sequences (Fig. 3*C*) with 985 peaks co-enriched with H3K9^{me3} and 1,067 peaks co-enriched with H3K27^{me3} (Fig. 3*D*). If considering repetitive sequences containing at least one BMI1 peak, LINE, SINE, and LTR were the most represented families of repeats. Among satellite repeats, BMI1 was mainly enriched at PCH regions (Fig. 3*F, inset*). A closer look at PCH regions on chromosome 9 revealed a "pocket-like" disposition of BMI1 peaks surrounding the H3K9^{me3} deposition (Fig. 3*E*). A similar pattern of BMI1 peak distribution was also found at PCH regions in human chromosomes 1–10. Notably, repetitive sequences containing 3 or more BMI1 peaks were largely represented (80%) in centromeric satellite repeats (Fig. 3*G*). In contrast, although 20% of LINE L1 repeats contained 3 or more BMI1 peaks, no other LINE subfamilies were highly enriched for BMI1 (Fig. 3*G*). We concluded that in human neural precursors, BMI1 is enriched at constitutive and facultative heterochromatin with prevalence for repetitive sequences.

BMI1 Co-purifies with Architectural Heterochromatin Proteins—To identify new BMI1 partner proteins, we infected 293T cells with a lentivirus expressing a Myc-tagged BMI1 fusion protein and GFP (EFv-BMI1^{Myc}/CMV-GFP) or a control virus only expressing GFP. After IP with an anti-Myc antibody, samples were separated on a one-dimensional gel and sequenced by LC-MS (Fig. 4*A*). We identified several unique peptides in BMI1^{Myc} samples corresponding to proteins involved in heterochromatin organization, including histone H1x, HP1a (also called CBX5), LAMIN A/C and LAMIN B, DEK (also called DEK1), and CENP-V (Fig. 4*A*) (7, 11, 54, 55). We also identified 2 members of the ISWI family, BAZ1a (also called ACF1) and BAZ1b, which can promote heterochromatin formation and transcription silencing by generating spaced nucleosome arrays (56). To validate some of these findings, we performed IP experiments on control and BMI1^{Myc} virus-infected cells. As expected, we observed that RING1B, but not EZH2, co-precipitated with BMI1 (Fig. 4*B*). Co-precipitation of ATRx, KAP1, DEK1, and HP1 with BMI1 was also observed, with a notable enrichment of ATRx when compared with input (Fig. 4*B*), and where the full-length (~280 kDa) and truncated (~180 kDa) ATRx isoforms were present, together with a lower molecular mass isoform of ~115 kDa. Notably, whereas co-precipitation with histones H3K9^{me3}, H3 (total), H1, and H2A^{ub} was robust, co-precipitation was not observed with histones H3K9^{me2}, H3K27^{me2}, and H3K27^{me3} (Fig. 4*B*). We use FPLC to separate protein complexes and found that BMI1 was present in one fraction of very large molecular weight and in several other fractions of lower molecular weight all also containing HP1 and ATRx (Fig. 4*C*). By IF studies, we confirmed that BMI1 largely co-localized with H3K9^{me3} in interphase nuclei (Fig. 4*D*).

BMI1 Is Required for Heterochromatin Compaction and Silencing—To evaluate BMI1 activity in heterochromatin silencing, we measured gene expression in loss- and gain-of-function experiments. Upon BMI1 deficiency, 293T cells showed reduced proliferation and underwent cell proliferation arrest after 3 passages (Fig. 5*A*). BMI1 overexpression had, however, no apparent adverse effect on cell proliferation (not shown). In BMI1 knockdown cells, expression of the canonical BMI1 target gene *p16*^{Ink4a} as well as that of *McBox* and *SATIII* was increased (Fig. 5*B*). Conversely, BMI1 overexpression resulted in transcriptional repression of *p16*^{Ink4a} and of all tested repeat-DNA sequences (Fig. 5*C*). By ChIP-qPCR experiments on shScramble and shBMI1-treated cells, we found that BMI1 and RING1B were highly enriched at repeat-DNA sequences and *HOXC13* in control cells (Fig. 5*D*). In shBMI1 cells, BMI1, RING1B, HP1, H3K9^{me3}, and H2A^{ub} were reduced at all chromatin regions tested (Fig. 5*D*). In contrast, BRCA1 enrichment at repeat-DNA sequences was independent of BMI1 function. Increased BRCA1 enrichment was even

FIGURE 2. **Bmi1 is required for H2Aub deposition and accumulates at repeat-DNA sequences in mouse cortical neurons.** *A*, WT and *Bmi1*$^{-/-}$ neurons were analyzed by ChIP for proteins enrichment at satellite repeats, intergenic retroelements, and *HoxA7* (positive control). Note the accumulation of Bmi1 and Ring1b at all repeat-DNA sequences, including major and minor satellite repeats. Although HP1 accumulation and H2A^{ub} and H3K9^{me3} deposition were reduced in *Bmi1*$^{-/-}$ neurons at all tested loci, BRCA1 accumulation was either unaffected (Minor and Major satellites) or increased (*Line*, *Sine*, and *IAP*). Note the near absence of BRCA1 accumulation at *HoxA7.1* and *HoxA7.3* in both WT and *Bmi1*$^{-/-}$ neurons. *B*, immunofluorescence analysis showing Bmi1 co-localization with H3K9^{me3} in WT mouse cortical neurons at P30 (*arrowheads*). *Scale bar*, 10 μm. *C*, immunofluorescence analysis showing loss of Bmi1 signal and reduced H3K9^{me3} labeling in cultured e18.5 *Bmi1*$^{-/-}$ mouse cortical neurons when compared with *Bmi1*$^{+/-}$ neurons. *Scale bar*, 10 μm.

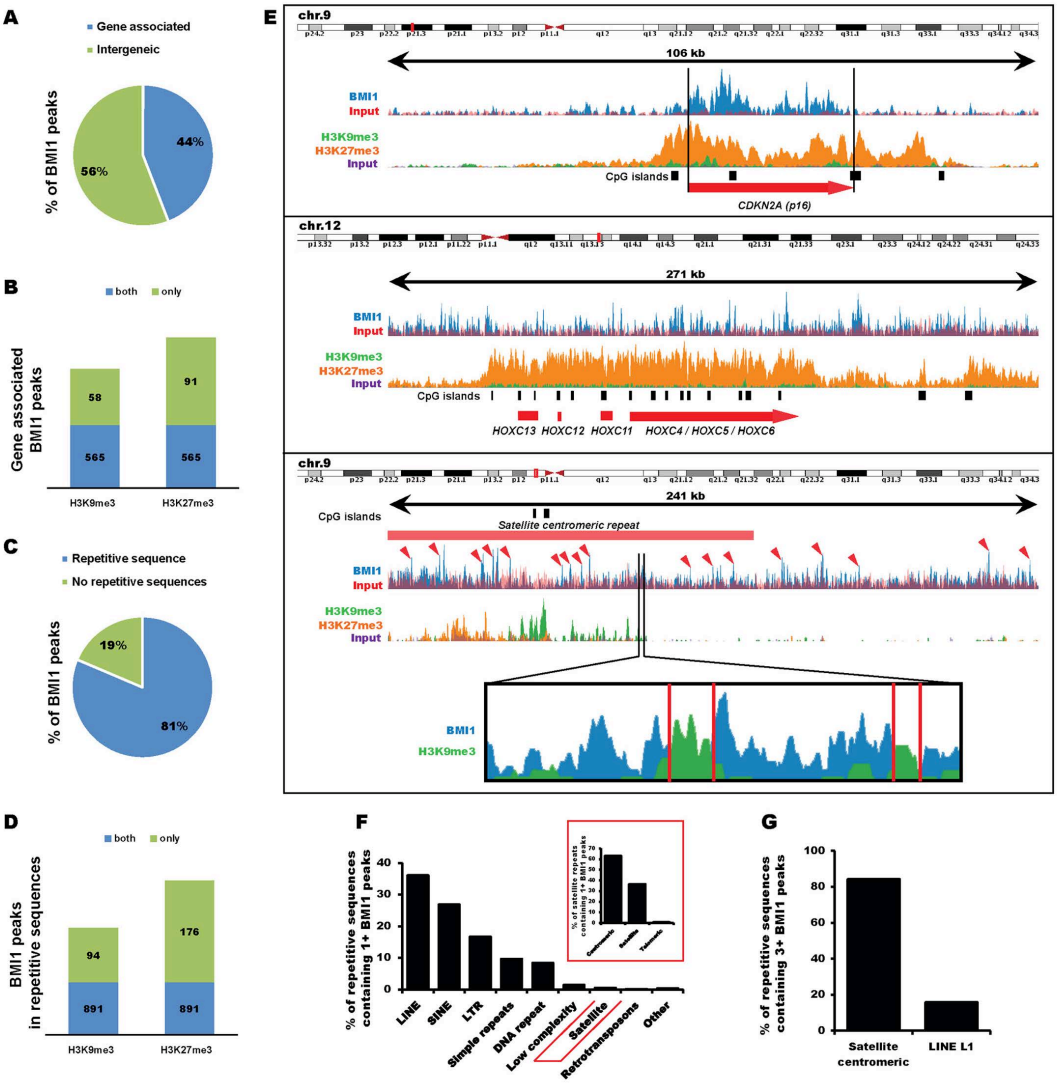

FIGURE 3. **BMI1 is enriched at repetitive sequences in human neural progenitor cells.** *A*, proportion of BMI1 peaks associated to a gene (surrounding or upstream 2 kb of a gene). Total number of peaks: 21,525. *B*, proportion of gene-associated BMI1 peaks co-enriched for H3K9^{me3} or H3K27^{me3}. *C*, proportion of BMI1 peaks surrounding a repetitive sequence. *D*, proportion of repeat-associated BMI1 peaks co-enriched for H3K9^{me3} or H3K27^{me3}. *E*, example of canonical BMI1 target genes (*CDKN2A* and *HOXC*) and the pericentromeric region of human chromosome 9. *Red arrowheads* indicate BMI1 peaks. *Top*: physical map on the chromosome. *F*, families of repeat containing at least one BMI1 peak. *G*, families of repeat containing three or more BMI1 peak. BMI1 peaks determined by MACS peak calling; p value <0.05. At least 2-fold enrichment for H3K9^{me3} and H3K27^{me3} were considered.

observed at *ALU* sequences upon BMI1 deficiency (Fig. 5*D*). We tested if RING1B knockdown mimicked the BMI1-deficient phenotype. Although RING1B accumulation at constitutive heterochromatin and *HOXC13* was highly reduced in siRING1B-treated cells (clone #4, 80% RING1B knockdown), H2A^{ub} reduction was only detected at *HOXC13* (data not shown). Notably, RING1B knockdown had no effect on BMI1, HP1, and H3K9^{me3} on all tested regions. No significant effect on repeat-DNA sequence expression was observed (data not shown), revealing that RING1B knockdown is not sufficient to reproduce the BMI1-deficient heterochromatin phenotype. BMI1 enrichment at repeat-DNA sequences was also EZH2 and H3K27^{me3} independent (data not shown). Nuclease hypersensitivity is a common phenotype of cells

A

Protein Name	NCBI Accession	Molecular Weight(Da)	Identification Probability	%Sequence Coverage	#Unique Peptides
Histone H1x	NP_006017	22,469.90	100%	17.40%	3
CBX5/HP1	CAG33699	22,207.60	99.80%	12.60%	2
LMNB2	NP_116126	67,671.70	100%	15.30%	8
LMNA (Lamin-A/C)	CAI15523	74,053.50	100%	12.30%	8
BAF (Barrier-to-autointegration factor)	NP001137457	10,040.70	100%	42.70%	3
DEK	NP_003463	42,657.90	100%	13.60%	4
BAZ1A/ACF1 (Bromodomain adjacent to zinc finger domain protein 1A)	AAH20636	178,689	99.80%	2.19%	2
NUP93 (nucleoporin)	NP_055484	93,367.10	99.80%	3.17%	2
KPNB1 (karyopherin (importin) beta 1)	NP_002256.2	97,167.40	100%	8.11%	5
KPNA2 (karyopherin alpha 2 (importin alpha 1))	NP_002257	57,844.50	99.80%	7.56%	2
B3KRS5/HDAC2		55,347.50	99.80%	5.94%	2
CENPV (Centromere protein V)	NP_859067	29,928.20	100%	18.20%	3
BAZ1B	AAH65029	170,889	100%	2.36%	3

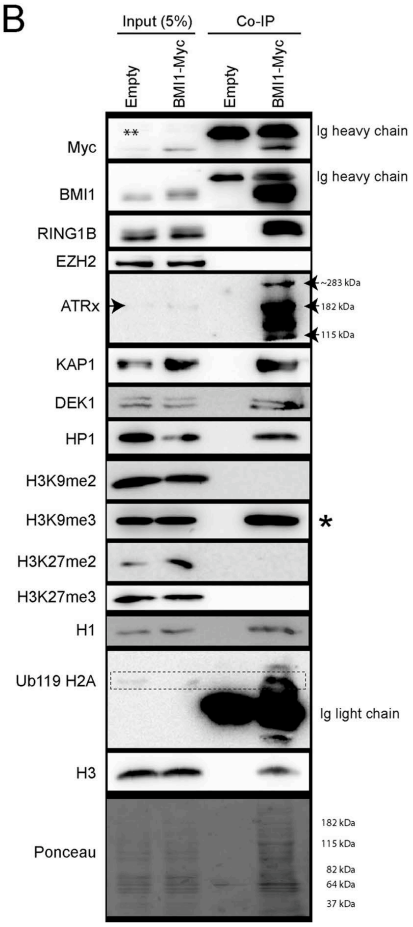

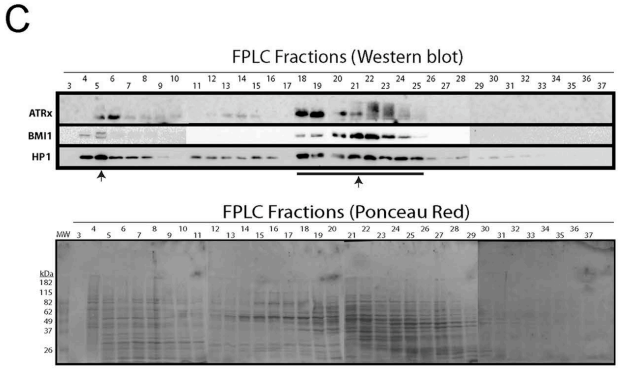

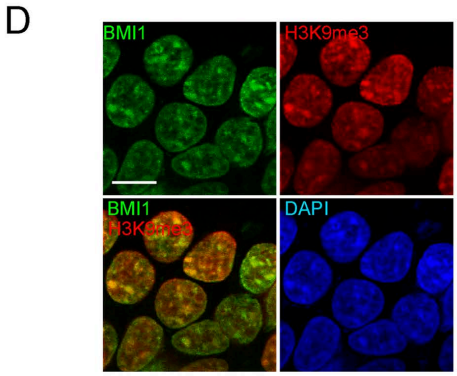

Overlapping	
Counted Cells	26
BMI1-H3K9me3 (Max.)	96%
BMI1-H3K9me3 (Min.)	42%
Average	79%
Std. Dev.	20%

FIGURE 4. **BMI1 co-purifies with architectural heterochromatin proteins.** *A* and *B*, 293T cells were infected with EFv/CMV-GFP or EFv-BMI1^{Myc}/CMV-GFP viruses. Protein extracts were subjected to IP using an anti-Myc antibody, and immunoprecipitates were resolved by SDS-PAGE and analyzed either by LC-MS/MS (*A*) or Western blot (*B*). *A*, note the co-purification of BMI1 with several heterochromatin proteins and Lamins. *B*, note the preferential co-purification of BMI1 with histone H3K9^{me3} (*) and ATRx. The ** symbol on the panel indicates an artifact coming from partial leakage of the second sample. *C*, native nuclear extracts were size fractionated by FPLC and analyzed by Western blot (*upper panel*) and Ponceau Red staining (*lower panel*). Note BMI1 co-fractionation with ATRx and HP1-containg protein complexes (*arrows*). *D*, 293T cells were labeled with BMI1 and H3K9^{me3} antibodies, counterstained with DAPI, and analyzed by confocal microscopy. Note the co-localization of BMI1 with H3K9^{me3}-positive chromatin domains. *Scale bar*, 10 μm. Quantitative confocal analysis was used to measure the proportion of overlapping signals.

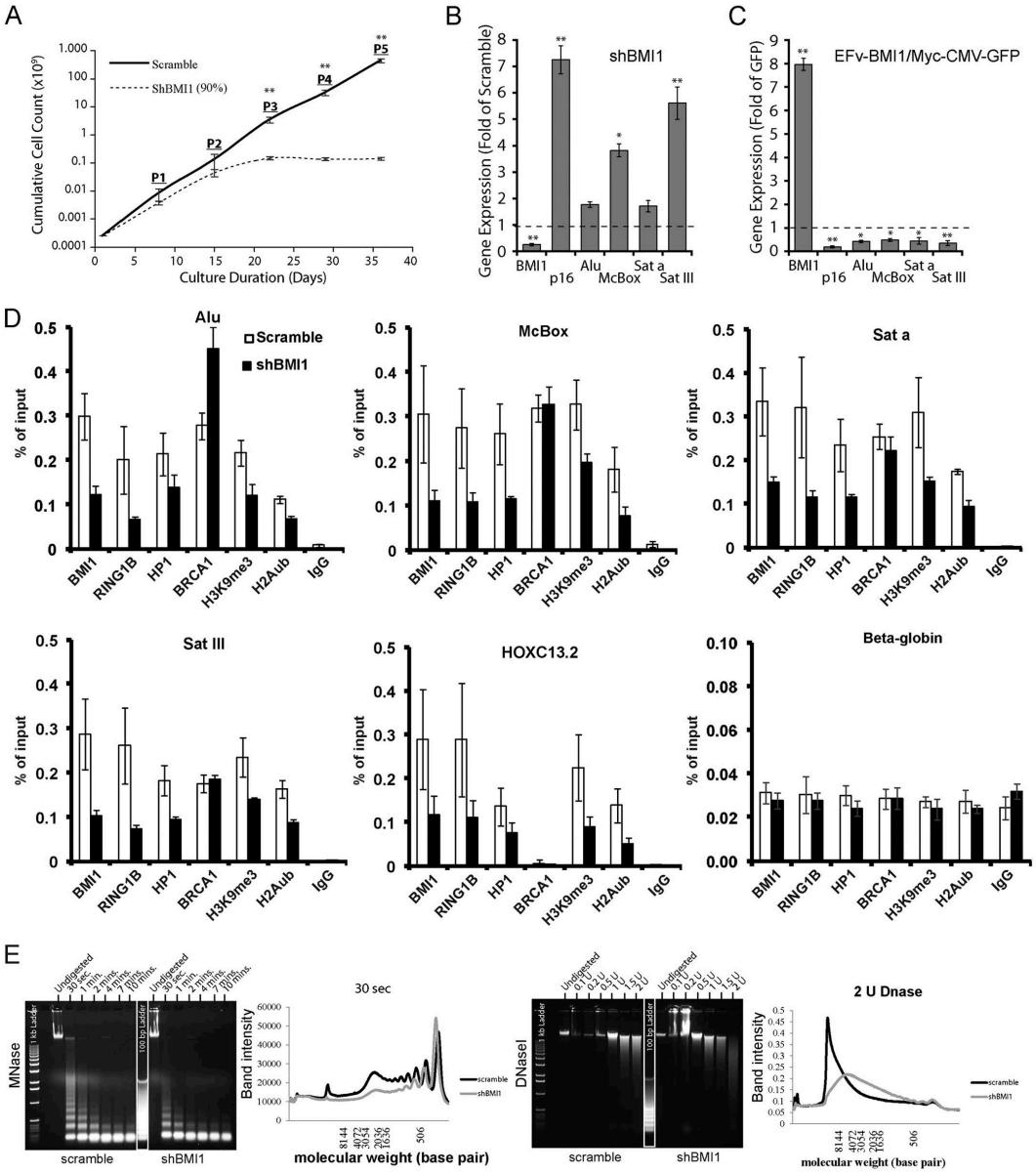

FIGURE 5. **BMI1 is required for heterochromatin compaction and silencing in human cells.** *A–C*, 293T cells were infected with shScramble or shBMI1 viruses (*A* and *B*), or with viruses expressing either GFP or the BMI1-myc fusion protein and GFP (*C*). *B* and *C*, gene expression was analyzed by qPCR, and where $n = 3$ independent cultures. *D*, 293T knockdown cells for BMI1 were analyzed by ChIP for protein enrichment at satellite repeats, intergenic retro-elements, and *HoxC13.2* (positive control). *E*, 293T cells were infected with shScramble or shBMI1 viruses and treated or not with MNase (0.4 units at 24 °C for different time periods) or DNase I at the indicated concentrations for 20 min at 24 °C. Note the nuclease hypersensitivity phenotype of BMI1 knockdown cells. *, $p < 0.05$; **, $p < 0.01$.

deficient in heterochromatin condensation (11, 57–59). We used native chromatin extracts isolated from control and shBMI1 293T cells in MNase and DNase I experiments and found that cells knocked down for BMI1 were hypersensitive to both nucleases (Fig. 5*E*), thus suggesting globally reduced chromatin compaction.

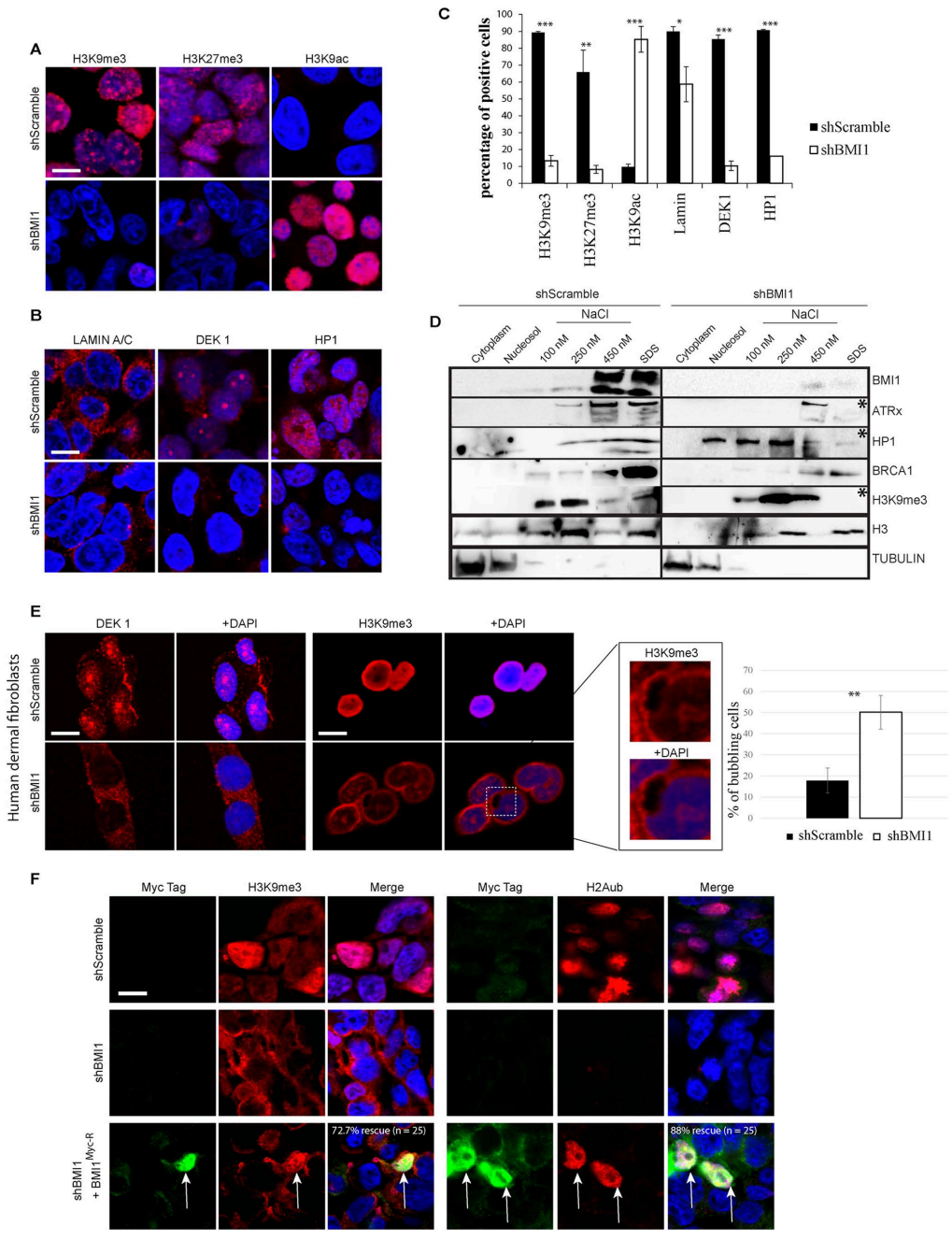

Severe Heterochromatin and Nuclear Envelope Alterations in Human Cells Deficient for BMI1—To further characterize the BMI1-deficient phenotype, we analyzed cells by confocal IF using heterochromatin and nuclear envelope markers. We found severe depletion of the H3K9^{me3} and H3K27^{me3} histone marks in BMI1-knockdown cells together with dramatic elevation of the H3K9ac mark (Fig. 6, *A* and *C*). Likewise, DEK1 and HP1 heterochromatic nuclear foci were lost upon BMI1 knockdown and positive cells for LAMIN A/C were significantly reduced (Fig. 6, *B* and *C*), suggesting perturbation of the nuclear envelope architecture.

To test whether this correlated with alterations in the subnuclear distribution of heterochromatin proteins, we performed cellular fractionation experiments and where the SDS-soluble fraction is thought to be highly enriched for constitutive heterochromatin proteins (11, 60). In control cells, BMI1 was detected in the 450 nM NaCl and SDS fractions (Fig. 6*D*). ATRx, HP1, BRCA1, and H3K9^{me3} were also highly enriched in the 100–450 nM NaCl- and SDS-soluble nuclear fractions. Modest HP1 distribution was also found in the nucleosol fraction (Fig. 6*D*). In shBMI1 cells, which underwent premature cell proliferation arrest (thus explaining the overall reduced total protein loading), ATRx, HP1, and H3K9^{me3} were highly reduced in the SDS fraction and displaced in the other fractions. In contrast, the distribution of BRCA1 in chromatin fractions and its overall expression were unaffected upon BMI1 knockdown (Fig. 6*D* and data not shown). To test BMI1 function in primary human cells, human dermal fibroblasts were infected with the lentiviruses and analyzed by IF. We observed that in contrast to control cells where robust H3K9^{me3} labeling was widespread throughout the interphase nucleus, H3K9^{me3} labeling in BMI1 knockdown cells was highly reduced and present at the nuclear periphery where it did not co-localize with DAPI (Fig. 6*E*). Notably, co-localization of H2A^{ub} and H3K9^{me3} with DAPI in shBMI1-infected cells could be rescued by an RNAi-resistant BMI1-Myc fusion protein (BMI1^{myc-R}), thus excluding possible off-target effects (Fig. 6*F*). Bubbling of the nuclear envelope and loss of DEK1 nuclear labeling were also observed (Fig. 6*E*), revealing BMI1 requirement for constitutive heterochromatin maintenance in both transformed and primary human cells.

BMI1 and BRCA1 Display Partial Functional Redundancy in Heterochromatin Compaction—Because BMI1/RING1A/RING1B and BRCA1/BARD1 display H2A monoubiquitinylation activities and that BRCA1 enrichment and distribution at heterochromatin is not affected upon BMI1 depletion, we tested whether BMI1 and BRCA1 displayed functional redundancy. For this, we first inactivated BRCA1 to test the impact on BMI1 localization. In control cells, both BRCA1 and BMI1 were enriched at repeat-DNA sequences (data not shown). In BRCA1 knockdown cells, BRCA1, HP1, H2A^{ub}, and H3K9^{me3} levels were reduced and transcription of repeat-DNA sequences was increased (data not shown), altogether confirming previous findings (22). Notably, however, BMI1 and RING1B were enriched at all tested regions upon BRCA1 knockdown (data not shown). Next, stably infected shBMI1 cells were transfected with an shBRCA1 plasmid, generating double knockdown (DKN) cells. Although H3K9^{me3} enrichment was reduced by 55–70% in DKN cells at all tested chromatin regions, enrichment for HP1 and H2A^{ub} was further reduced by 80–90% (Fig. 7*A*), suggesting additive effects in DKN cells when compared with single BRCA1 or BMI1 knockdown cells. To test whether BMI1 could compensate for BRCA1 deficiency, we overexpressed the BMI1^{Myc} construct. In control cells, BMI1 overexpression could not displace endogenous BRCA1 localization on the chromatin (Fig. 7*B*). However, chromatin accumulation of both endogenous and ectopic BMI1 proteins was highly increased at all tested regions following BRCA1 knockdown (Fig. 7*B*). A similar but less dramatic trend was also observed for RING1B. Most notably, whereas BMI1 overexpression could increase H2A^{ub} and H3K9^{me3} deposition as well as HP1 accumulation at all tested regions in control cells, it could also rescue the corresponding heterochromatin anomalies in shBRCA1 cells (Fig. 7*B*). BMI1 overexpression in shBRCA1 cells also resulted in normalization of *ALU*, *McBox*, *Sata*, and *SatIII* expression (Fig. 7*C*), altogether suggesting functional redundancy in constitutive heterochromatin compaction and silencing between BMI1 and BRCA1.

Discussion

We showed here that *Bmi1*-deficient mouse neurons and BMI1 knockdown human cells displayed severe anomalies at the constitutive heterochromatin. These anomalies were accompanied by transcriptional activation of repeat-DNA sequences and correlated with robust accumulation of BMI1 at constitutive heterochromatin. Genome-wide analysis of BMI1 distribution on the chromatin further revealed predominant enrichment at repetitive DNA sequences. BMI1 co-purified with architectural heterochromatin proteins, co-localized with H3K9^{me3}, and was required for HP1, DEK1, and ATRx localization at constitutive heterochromatin. In contrast, BRCA1 localization was BMI1-independent, and both proteins displayed partial functional redundancy for H2A^{ub} deposition, heterochromatin formation, and silencing.

The recruitment mechanisms of PcG proteins are complex and not fully understood. In mouse ES cells and oocytes, evidences suggest that recruitment of PcG proteins at PCH is prevented by a high level of DNA methylation (30, 52). Likewise, observations of Polycomb bodies at PCH in transformed human cells are thought to occur following loss of DNA methylation (30, 47, 52). Based on this, it was proposed that PcG

FIGURE 6. **BMI1 knockdown cells present heterochromatin and nuclear envelope alterations.** *A–C*, formaldehyde-fixed 293FT cells were immunolabeled and counterstained with DAPI. *Scale bar*, 10 μm. Positive cells were counted on 4 different images for a total of 200 cells per condition, and the percentage of positive cells was calculated accordingly. *t* test with two tails, where *, $p \leq 0.05$; **, ≤ 0.01; ***, ≤ 0.001. Note that the apparent localization of Lamin A/C in the cytosol is the result of Triton X-100 treatment. *D*, 293T cells were infected with shScramble or shBMI1 viruses and the compartments of the cell were fractionated. Note the reduction (*) of ATRx, HP1, and H3K9^{me3} in SDS fractions of shBMI1-treated cells. *E*, human dermal fibroblasts were infected with shScramble or shBMI1 viruses, immunolabeled, and counterstained with DAPI. Note the reduced DEK1 and H3K9^{me3} labeling, and H3K9^{me3} localization at the nuclear periphery, in BMI1-deficient cells. Bubbling of the nuclear envelope was also observed (*inset*); **, $p \leq 0.01$. *Scale bar*, 10 μm. *F*, human dermal fibroblasts were infected with shScramble or shBMI1 viruses, and next transfected with a plasmid encoding an RNAi-resistant BMI1 Myc-tagged construct. Note the rescue of H2Aub and H3K9me3 nuclear labeling in Myc-positive cells knockdown for BMI1 (*arrows*). *Scale bar*, 10 μm.

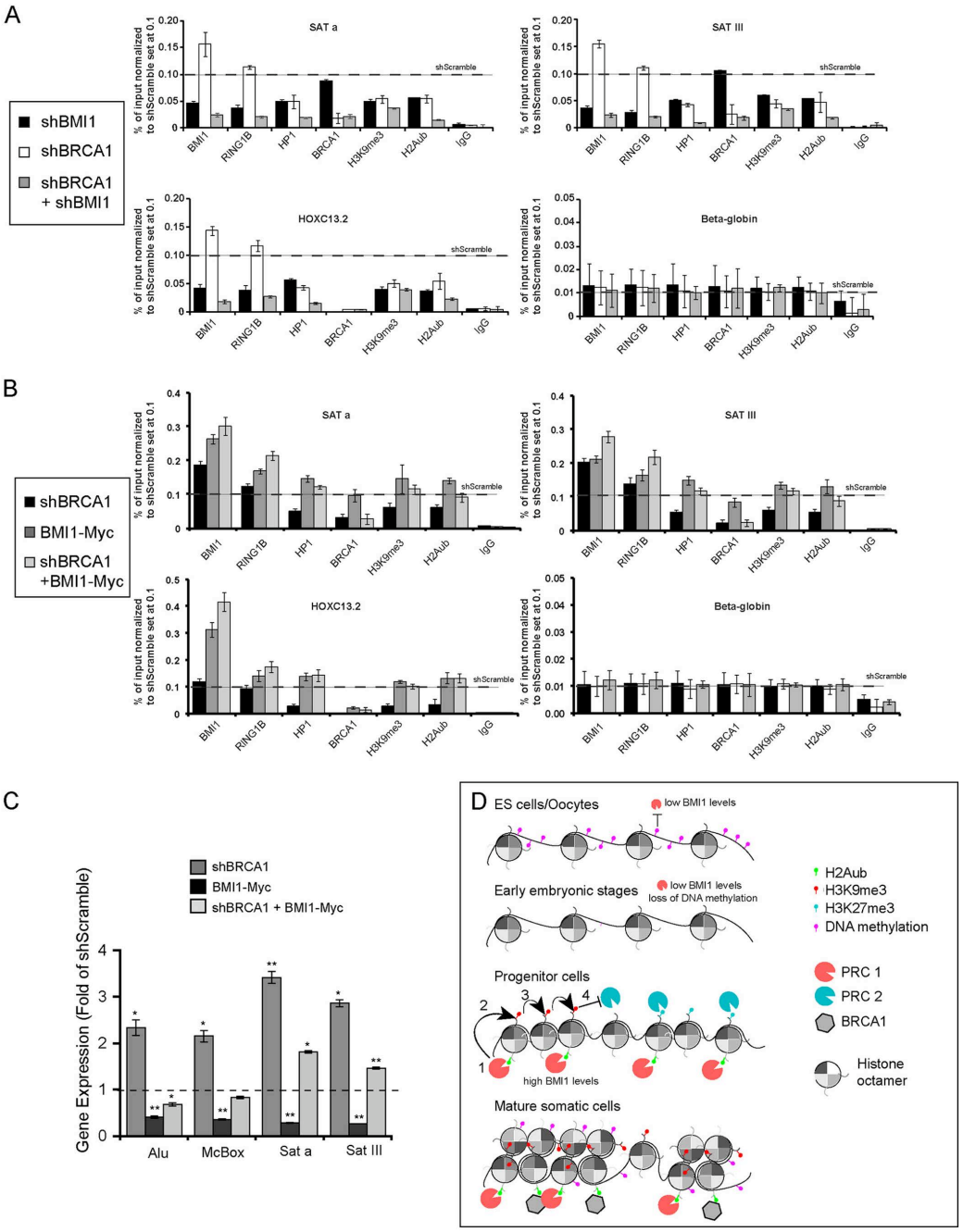

proteins are excluded from PCH in normal somatic cells (52). Using several methods, we demonstrated BMI1 enrichment at PCH and other repetitive elements in mouse neurons, human neural precursors, and immortalized human cells. Our cell fractionation assays further demonstrated that about 50% of the BMI1 pool was bound to the SDS-soluble chromatin fraction, which is enriched for constitutive heterochromatin. Interestingly, we also observed that: 1) BMI1 did not co-purify with EZH2 or H3K27^{me3}; 2) EZH2 and H3K27^{me3} were not enriched at constitutive heterochromatin; and 3) BMI1 accumulation at constitutive heterochromatin and *HOXC13* was *EZH2* independent. Although apparently surprising, these results are in agreement with numerous findings showing that PRC1 recruitment can be PRC2 independent, or that the PRC1 can work upstream of the PRC2 (29, 61, 62). It is also notable that RING1B knockdown could not mimic the BMI1-deficient phenotype. More specifically, whereas H2A^{ub} levels were reduced at *HOXC13* in RING1B knockdown cells, this was not accompanied by a corresponding reduction in HP1 and H3K9^{me3} levels, as observed in BMI1 knockdown cells. Furthermore, there was no apparent effect on H2A^{ub} levels at heterochromatin. This finding leaves us open with many explanations, one being functional compensation by RING1A for H2A^{ub} deposition, as shown in other context (50, 63–65). It is also possible that in addition to promote H2A^{ub} at silenced developmental genes and heterochromatin, BMI1 stimulates chromatin compaction and H3K9^{me3} loading through interactions and activities not shared by RING1A or RING1B (66).

Based on our findings and previously published work, we propose that PRC1 recruitment to PCH is highly dynamic and developmentally regulated (Fig. 7*D*). The highly variable DNA methylation states between ES cells/oocytes and progenitor cells/somatic cells, in combination with the distinct histone tail modifications and chromatin compactions levels, would explain the re-localization of PRC1 components to PCH in progenitor and somatic cells (67–69). Consistently, BMI1 expression levels are extremely low in human ES cells when compared with human neural progenitors and post-mitotic neurons.[5] Although PRC1 proteins are excluded from PCH in ES cells and oocytes, they would start to accumulate at PCH during mid-embryonic development coincidently with H3K9^{me3} deposition and progressive *de novo* DNA methylation (69). This is supported by the ChIP-Seq data showing that BMI1 is moderately enriched at PCH when compared with *HOX* and *p16^{INK4A}* canonical sites in human neural progenitors (Fig. 3). Interestingly, both H3K9^{me3} and H3K27^{me3} marks were also present at PCH but did not clearly overlap (Fig. 3), similarly as reported in DNA methylation-deficient mouse ES cells (30). The histone modification pattern of human neural progenitors at PCH is also distinct from that of mouse neurons where H3K27^{me3} is excluded (Fig. 2). This could be best explained by the robust accumulation of H3K9^{me3} at PCH in post-mitotic neurons, because H3K9^{me3} can prevent PRC2, but not PRC1 recruitment (30). Indeed, Bmi1 is highly enriched in mouse neurons at PCH when compared with canonical sites (Fig. 2). Taken together, these observations suggest a dynamic and developmentally regulated model of PcG occupancy at PCH (Fig. 7*D*). Because constitutive heterochromatin is intrinsically instable, we further propose that in somatic cells, the main biological function of BMI1 is to stabilize the repetitive genome by promoting chromatin compaction and silencing.

We observed that the *Bmi1*-null neuronal phenotype was associated with increased nuclear diameter and an irregular nuclear envelope. Human cells knockdown for BMI1 also presented anomalies in nuclear envelope architecture (Fig. 6, *B–E*). These anomalies are particularly interesting considering that loss of heterochromatin foci can result in disruption of the nuclear lamina (7). Perturbations of the nuclear envelope architecture is also a prominent feature of Hutchinson-Gilford Progeria cells carrying mutations in *LAMIN-A* and normal aging human cells (70). In most eukaryotes, constitutive heterochromatin perturbations result in genomic instability and premature aging or reduced lifespan (10, 16, 71–74). It is thus notable that *Bmi1*-deficient mice show reduced lifespan, genomic instability, neurodegeneration, and progeria features (38, 42–45, 75). Similar anomalies were also reported for *ATRx*-deficient mice (18, 20). Taken together, this raises the possibility that BMI1 requirement for constitutive heterochromatin formation and silencing could underlie the premature aging/senescence and genomic instability phenotypes observed in *Bmi1*-null mice and cells.

The BRCA1/BARD1 complex is required for heterochromatin formation and silencing through monoubiquitinylation of H2A at PCH, and the genomic instability phenotype of *BRCA1$^{-/-}$* cells could be rescued by overexpression of a histone H2A protein fused to an ubiquitin moiety in C terminus (22). How BMI1 or BRCA1-mediated H2A^{ub} deposition at repetitive DNA sequences can translate into H3K9^{me3} loading and heterochromatin spreading is unknown. One possibility is that H2A^{ub} induces allosteric changes in the histone H3 lysine trimethyltransferases SUV39H1/2 to promote their activity, such as proposed for H2B^{ub} and H3K4 methylation (76, 77).

[5] V. P., A. B., M. Abdouh, A. Flamier, and G. Bernier, unpublished data.

FIGURE 7. **BRCA1 and BMI1 display redundant activities in constitutive heterochromatin formation and silencing.** *A*, 293T cells were infected with shScramble or shBMI1 viruses. After selection with hygromycin, cells were transfected or not with an shBRCA1-encoding plasmid and analyzed by ChIP. Note the severe reduction for HP1, H3K9^{me3}, and H2A^{ub} at human Satellite repeats in shBMI1/shBRCA1 cells. All data where normalized to shScramble (*black horizontal bars*). *B*, 293T cells stably expressing BMI1^{Myc} or not were transfected with shScramble or shBRCA1 plasmids and analyzed by ChIP (*B*) and qPCR (*C*). *B*, endogenous and exogenous BMI1 was enriched in shBRCA1-treated cells at all tested loci. BMI1 overexpression also rescued HP1, H3K9^{me3}, and H2A^{ub} depletion in BRCA1 knockdown cells at human Satellite repeats. All data were normalized to shScramble (*black horizontal bars*). *C*, BMI1 overexpression rescues repeat-DNA sequences expression in BRCA1 knockdown cells; *, $p \leq 0.05$; **, ≤0.01. *D*, model depicting the dynamic and developmentally regulated PRC1 (BMI1) occupancy at PCH. In ES cells and oocytes, BMI1 is expressed at low levels and binding to PCH is prevented by DNA methylation. At pre-implantation stages, DNA methylation is erased coincidently with low levels of BMI1. During development, high BMI1 levels in progenitor cells stimulate PCR1-mediated H2A^{ub} (*1*), which promotes H3K9^{me3} deposition (*2*), and propagation (*3*). In turn, H3K9^{me3} prevents PRC2-mediated H3K27^{me3} activity on nucleosomal histones (*4*). PRC2 occupancy at PCH prior to PRC1 would allow deposition of the H3K27^{me3} mark (*right*) and the bivalent histone signature. In mature somatic cells, the PRC1 and BRCA1/BARD complexes are highly enriched at PCH, leading to heterochromatin compaction and silencing. DNA methylation at PCH may occur after spreading the H3K9^{me3} mark.

This would be consistent with previous observations that PRC1 components can interact with SUV39H1 (48). Alternatively, BMI1 may directly or indirectly regulate the transcription of H3 lysine methyltransferases or demethylases, thus operating in *trans*. We showed here that co-inactivation of BMI1 and BRCA1 induces more severe heterochromatin anomalies than individual BMI1 or BRCA1 deficiencies, and that BMI1 overexpression could rescue the BRCA1-deficient heterochromatin phenotype. These results suggest that BMI1 and BRCA1 are at least partially redundant for $H2A^{ub}$ deposition at constitutive heterochromatin, although the BRCA1/BARD1 complex targets H2A at lysines 127–129 (21). This would indicate that the commonly used anti-$H2A^{ub}$ antibody recognizes both the $H2AK119^{ub}$ and $H2AK127–129^{ub}$ motifs. The observation that BMI1 and BRCA1 proteins accumulation is mutually independent and that BMI1 levels are increased in BRCA1-deficient cells (and reciprocally) also suggests that both protein complexes possibly bind to very close substrates to catalyze H2A monoubiquitinylation. Structural analyses have indeed revealed a high degree of conservation between the nucleosome-binding loop of BRCA1 and the corresponding domain of RING1B (78). Notably, the reduced neuronal chromocenter number and size phenotype observed in *Bmi1*-null neurons is about identical to that reported for mouse cortical neurons conditionally deficient for *BRCA1*, thus further supporting our findings (22). Taken together, this suggests that although BMI1 and BRCA1 protein complexes target distinct lysine residues on histone H2A, the resulting biological effects on heterochromatin compaction and silencing are highly similar.

In conclusion, we demonstrated for the first time that BMI1 is highly enriched at intergenic repetitive elements and PCH of the mouse and human genomes in normal somatic cells, and required for constitutive heterochromatin formation and silencing. Because BM1 is also present at PCH in cancer cell lines and that several cancer cells were shown to be sensitive to BMI1 inhibition, this raises the possibility that BMI1 may be important to stabilize the transformed heterochromatic genome. BMI1 function at constitutive heterochromatin may be even more critical in *BRCA1*-deficient tumors, thus opening possibilities for the development of synthetic lethal strategies.

Author Contributions—M. A., R. H., and J. E. H. performed the experiments and analyzed the data. A. F. performed the bio-informatics analysis and wrote the corresponding section. G. B. supervised the experiments and wrote the manuscript. All authors reviewed the results and approved the final version of the manuscript.

Acknowledgments—We are grateful to S. Breault for technical assistance with electron microscopy and Dr. F. Rodier for the dermal fibroblast cell line and critical reading of the manuscript.

References

1. Fodor, B. D., Shukeir, N., Reuter, G., and Jenuwein, T. (2010) Mammalian Su(var) genes in chromatin control. *Annu. Rev. Cell Dev. Biol.* **26,** 471–501
2. Kim, M., Trinh, B. N., Long, T. I., Oghamian, S., and Laird, P. W. (2004) Dnmt1 deficiency leads to enhanced microsatellite instability in mouse embryonic stem cells. *Nucleic Acids Res.* **32,** 5742–5749
3. Kondo, Y., Shen, L., Ahmed, S., Boumber, Y., Sekido, Y., Haddad, B. R., and Issa, J. P. (2008) Downregulation of histone H3 lysine 9 methyltransferase G9a induces centrosome disruption and chromosome instability in cancer cells. *PLoS ONE* **3,** e2037
4. Peng, J. C., and Karpen, G. H. (2008) Epigenetic regulation of heterochromatic DNA stability. *Curr. Opin. Genet. Dev.* **18,** 204–211
5. Matsui, T., Leung, D., Miyashita, H., Maksakova, I. A., Miyachi, H., Kimura, H., Tachibana, M., Lorincz, M. C., and Shinkai, Y. (2010) Proviral silencing in embryonic stem cells requires the histone methyltransferase ESET. *Nature* **464,** 927–931
6. Rowe, H. M., Jakobsson, J., Mesnard, D., Rougemont, J., Reynard, S., Aktas, T., Maillard, P. V., Layard-Liesching, H., Verp, S., Marquis, J., Spitz, F., Constam, D. B., and Trono, D. (2010) KAP1 controls endogenous retroviruses in embryonic stem cells. *Nature* **463,** 237–240
7. Pinheiro, I., Margueron, R., Shukeir, N., Eisold, M., Fritzsch, C., Richter, F. M., Mittler, G., Genoud, C., Goyama, S., Kurokawa, M., Son, J., Reinberg, D., Lachner, M., and Jenuwein, T. (2012) Prdm3 and Prdm16 are H3K9me1 methyltransferases required for mammalian heterochromatin integrity. *Cell* **150,** 948–960
8. Towbin, B. D., González-Aguilera, C., Sack, R., Gaidatzis, D., Kalck, V., Meister, P., Askjaer, P., and Gasser, S. M. (2012) Step-wise methylation of histone H3K9 positions heterochromatin at the nuclear periphery. *Cell* **150,** 934–947
9. Black, J. C., and Whetstine, J. R. (2011) Chromatin landscape: methylation beyond transcription. *Epigenetics* **6,** 9–15
10. Wang, R. H., Sengupta, K., Li, C., Kim, H. S., Cao, L., Xiao, C., Kim, S., Xu, X., Zheng, Y., Chilton, B., Jia, R., Zheng, Z. M., Appella, E., Wang, X. W., Ried, T., and Deng, C. X. (2008) Impaired DNA damage response, genome instability, and tumorigenesis in SIRT1 mutant mice. *Cancer Cell* **14,** 312–323
11. Kappes, F., Waldmann, T., Mathew, V., Yu, J., Zhang, L., Khodadoust, M. S., Chinnaiyan, A. M., Luger, K., Erhardt, S., Schneider, R., and Markovitz, D. M. (2011) The DEK oncoprotein is a Su(var) that is essential to heterochromatin integrity. *Genes Dev.* **25,** 673–678
12. Maison, C., Bailly, D., Roche, D., Montes de Oca, R., Probst, A. V., Vassias, I., Dingli, F., Lombard, B., Loew, D., Quivy, J. P., and Almouzni, G. (2011) SUMOylation promotes de novo targeting of HP1α to pericentric heterochromatin. *Nat. Genet.* **43,** 220–227
13. Fan, Y., Nikitina, T., Zhao, J., Fleury, T. J., Bhattacharyya, R., Bouhassira, E. E., Stein, A., Woodcock, C. L., and Skoultchi, A. I. (2005) Histone H1 depletion in mammals alters global chromatin structure but causes specific changes in gene regulation. *Cell* **123,** 1199–1212
14. Iwase, S., Xiang, B., Ghosh, S., Ren, T., Lewis, P. W., Cochrane, J. C., Allis, C. D., Picketts, D. J., Patel, D. J., Li, H., and Shi, Y. (2011) ATRX ADD domain links an atypical histone methylation recognition mechanism to human mental-retardation syndrome. *Nat. Struct. Mol. Biol.* **18,** 769–776
15. Maison, C., and Almouzni, G. (2004) HP1 and the dynamics of heterochromatin maintenance. *Nat. Rev. Mol. Cell Biol.* **5,** 296–304
16. Peters, A. H., O'Carroll, D., Scherthan, H., Mechtler, K., Sauer, S., Schöfer, C., Weipoltshammer, K., Pagani, M., Lachner, M., Kohlmaier, A., Opravil, S., Doyle, M., Sibilia, M., and Jenuwein, T. (2001) Loss of the Suv39h histone methyltransferases impairs mammalian heterochromatin and genome stability. *Cell* **107,** 323–337
17. Prasanth, S. G., Shen, Z., Prasanth, K. V., and Stillman, B. (2010) Human origin recognition complex is essential for HP1 binding to chromatin and heterochromatin organization. *Proc. Natl. Acad. Sci. U.S.A.* **107,** 15093–15098
18. Huh, M. S., Price O'Dea, T., Ouazia, D., McKay, B. C., Parise, G., Parks, R. J., Rudnicki, M. A., and Picketts, D. J. (2012) Compromised genomic integrity impedes muscle growth after Atrx inactivation. *J. Clin. Invest.* **122,** 4412–4423
19. Law, M. J., Lower, K. M., Voon, H. P., Hughes, J. R., Garrick, D., Viprakasit, V., Mitson, M., De Gobbi, M., Marra, M., Morris, A., Abbott, A., Wilder, S. P., Taylor, S., Santos, G. M., Cross, J., Ayyub, H., Jones, S., Ragoussis, J., Rhodes, D., Dunham, I., Higgs, D. R., and Gibbons, R. J. (2010) ATR-X syndrome protein targets tandem repeats and influences allele-specific expression in a size-dependent manner. *Cell* **143,** 367–378
20. Watson, L. A., Solomon, L. A., Li, J. R., Jiang, Y., Edwards, M., Shin-ya, K., Beier, F., and Bérubé, N. G. (2013) Atrx deficiency induces telomere dys-

function, endocrine defects, and reduced life span. *J. Clin. Invest.* **123,** 2049–2063
21. Kalb, R., Mallery, D. L., Larkin, C., Huang, J. T., and Hiom, K. (2014) BRCA1 Is a histone-H2A-specific ubiquitin ligase. *Cell Rep.* **8,** 999–1005
22. Zhu, Q., Pao, G. M., Huynh, A. M., Suh, H., Tonnu, N., Nederlof, P. M., Gage, F. H., and Verma, I. M. (2011) BRCA1 tumour suppression occurs via heterochromatin-mediated silencing. *Nature* **477,** 179–184
23. Thakar, A., Parvin, J., and Zlatanova, J. (2010) BRCA1/BARD1 E3 ubiquitin ligase can modify histones H2A and H2B in the nucleosome particle. *J. Biomol. Struct. Dyn.* **27,** 399–406
24. Sparmann, A., and van Lohuizen, M. (2006) Polycomb silencers control cell fate, development and cancer. *Nat. Rev. Cancer* **6,** 846–856
25. Levine, S. S., Weiss, A., Erdjument-Bromage, H., Shao, Z., Tempst, P., and Kingston, R. E. (2002) The core of the polycomb repressive complex is compositionally and functionally conserved in flies and humans. *Mol. Cell. Biol.* **22,** 6070–6078
26. Dellino, G. I., Schwartz, Y. B., Farkas, G., McCabe, D., Elgin, S. C., and Pirrotta, V. (2004) Polycomb silencing blocks transcription initiation. *Mol. Cell* **13,** 887–893
27. Kuzmichev, A., Nishioka, K., Erdjument-Bromage, H., Tempst, P., and Reinberg, D. (2002) Histone methyltransferase activity associated with a human multiprotein complex containing the Enhancer of Zeste protein. *Genes Dev.* **16,** 2893–2905
28. Wang, H., Wang, L., Erdjument-Bromage, H., Vidal, M., Tempst, P., Jones, R. S., and Zhang, Y. (2004) Role of histone H2A ubiquitination in Polycomb silencing. *Nature* **431,** 873–878
29. Blackledge, N. P., Farcas, A. M., Kondo, T., King, H. W., McGouran, J. F., Hanssen, L. L., Ito, S., Cooper, S., Kondo, K., Koseki, Y., Ishikura, T., Long, H. K., Sheahan, T. W., Brockdorff, N., Kessler, B. M., Koseki, H., and Klose, R. J. (2014) Variant PRC1 complex-dependent H2A ubiquitylation drives PRC2 recruitment and polycomb domain formation. *Cell* **157,** 1445–1459
30. Cooper, S., Dienstbier, M., Hassan, R., Schermelleh, L., Sharif, J., Blackledge, N. P., De Marco, V., Elderkin, S., Koseki, H., Klose, R., Heger, A., and Brockdorff, N. (2014) Targeting polycomb to pericentric heterochromatin in embryonic stem cells reveals a role for H2AK119u1 in PRC2 recruitment. *Cell Rep.* **7,** 1456–1470
31. Kleer, C. G., Cao, Q., Varambally, S., Shen, R., Ota, I., Tomlins, S. A., Ghosh, D., Sewalt, R. G., Otte, A. P., Hayes, D. F., Sabel, M. S., Livant, D., Weiss, S. J., Rubin, M. A., and Chinnaiyan, A. M. (2003) EZH2 is a marker of aggressive breast cancer and promotes neoplastic transformation of breast epithelial cells. *Proc. Natl. Acad. Sci. U.S.A.* **100,** 11606–11611
32. Lassman, A. B., Dai, C., Fuller, G. N., Vickers, A. J., and Holland, E. C. (2004) Overexpression of c-MYC promotes an undifferentiated phenotype in cultured astrocytes and allows elevated Ras and Akt signaling to induce gliomas from GFAP-expressing cells in mice. *Neuron Glia Biol.* **1,** 157–163
33. Orian, J. M., Vasilopoulos, K., Yoshida, S., Kaye, A. H., Chow, C. W., and Gonzales, M. F. (1992) Overexpression of multiple oncogenes related to histological grade of astrocytic glioma. *Br. J. Cancer* **66,** 106–112
34. Valk-Lingbeek, M. E., Bruggeman, S. W., and van Lohuizen, M. (2004) Stem cells and cancer; the polycomb connection. *Cell* **118,** 409–418
35. Varambally, S., Dhanasekaran, S. M., Zhou, M., Barrette, T. R., Kumar-Sinha, C., Sanda, M. G., Ghosh, D., Pienta, K. J., Sewalt, R. G., Otte, A. P., Rubin, M. A., and Chinnaiyan, A. M. (2002) The polycomb group protein EZH2 is involved in progression of prostate cancer. *Nature* **419,** 624–629
36. Visser, H. P., Gunster, M. J., Kluin-Nelemans, H. C., Manders, E. M., Raaphorst, F. M., Meijer, C. J., Willemze, R., and Otte, A. P. (2001) The Polycomb group protein EZH2 is upregulated in proliferating, cultured human mantle cell lymphoma. *Br. J. Haematol.* **112,** 950–958
37. Bruggeman, S. W., Valk-Lingbeek, M. E., van der Stoop, P. P., Jacobs, J. J., Kieboom, K., Tanger, E., Hulsman, D., Leung, C., Arsenijevic, Y., Marino, S., and van Lohuizen, M. (2005) Ink4a and Arf differentially affect cell proliferation and neural stem cell self-renewal in Bmi1-deficient mice. *Genes Dev.* **19,** 1438–1443
38. Chatoo, W., Abdouh, M., David, J., Champagne, M. P., Ferreira, J., Rodier, F., and Bernier, G. (2009) The polycomb group gene Bmi1 regulates antioxidant defenses in neurons by repressing p53 pro-oxidant activity. *J. Neurosci.* **29,** 529–542
39. Jacobs, J. J., Kieboom, K., Marino, S., DePinho, R. A., and van Lohuizen, M. (1999) The oncogene and Polycomb-group gene bmi-1 regulates cell proliferation and senescence through the ink4a locus. *Nature* **397,** 164–168
40. Molofsky, A. V., Pardal, R., Iwashita, T., Park, I. K., Clarke, M. F., and Morrison, S. J. (2003) Bmi-1 dependence distinguishes neural stem cell self-renewal from progenitor proliferation. *Nature* **425,** 962–967
41. Sharpless, N. E., and DePinho, R. A. (1999) The INK4A/ARF locus and its two gene products. *Curr. Opin. Genet. Dev.* **9,** 22–30
42. Facchino, S., Abdouh, M., Chatoo, W., and Bernier, G. (2010) BMI1 confers radioresistance to normal and cancerous neural stem cells through recruitment of the DNA damage response machinery. *J. Neurosci.* **30,** 10096–10111
43. Ismail, I. H., Andrin, C., McDonald, D., and Hendzel, M. J. (2010) BMI1-mediated histone ubiquitylation promotes DNA double-strand break repair. *J. Cell Biol.* **191,** 45–60
44. Chagraoui, J., Hébert, J., Girard, S., and Sauvageau, G. (2011) An anticlastogenic function for the Polycomb Group gene *Bmi1*. *Proc. Natl. Acad. Sci. U.S.A.* **108,** 5284–5289
45. Liu, J., Cao, L., Chen, J., Song, S., Lee, I. H., Quijano, C., Liu, H., Keyvanfar, K., Chen, H., Cao, L. Y., Ahn, B. H., Kumar, N. G., Rovira, I. I., Xu, X. L., van Lohuizen, M., Motoyama, N., Deng, C. X., and Finkel, T. (2009) Bmi1 regulates mitochondrial function and the DNA damage response pathway. *Nature* **459,** 387–392
46. Hernández-Muñoz, I., Taghavi, P., Kuijl, C., Neefjes, J., and van Lohuizen, M. (2005) Association of BMI1 with polycomb bodies is dynamic and requires PRC2/EZH2 and the maintenance DNA methyltransferase DNMT1. *Mol. Cell. Biol.* **25,** 11047–11058
47. Saurin, A. J., Shiels, C., Williamson, J., Satijn, D. P., Otte, A. P., Sheer, D., and Freemont, P. S. (1998) The human polycomb group complex associates with pericentromeric heterochromatin to form a novel nuclear domain. *J. Cell Biol.* **142,** 887–898
48. Sewalt, R. G., Lachner, M., Vargas, M., Hamer, K. M., den Blaauwen, J. L., Hendrix, T., Melcher, M., Schweizer, D., Jenuwein, T., and Otte, A. P. (2002) Selective interactions between vertebrate polycomb homologs and the SUV39H1 histone lysine methyltransferase suggest that histone H3-K9 methylation contributes to chromosomal targeting of Polycomb group proteins. *Mol. Cell. Biol.* **22,** 5539–5553
49. Smigová, J., Juda, P., Cmarko, D., and Raška, I. (2011) Fine structure of the "PcG body" in human U-2 OS cells established by correlative light-electron microscopy. *Nucleus* **2,** 219–228
50. Leeb, M., Pasini, D., Novatchkova, M., Jaritz, M., Helin, K., and Wutz, A. (2010) Polycomb complexes act redundantly to repress genomic repeats and genes. *Genes Dev.* **24,** 265–276
51. Puschendorf, M., Terranova, R., Boutsma, E., Mao, X., Isono, K., Brykczynska, U., Kolb, C., Otte, A. P., Koseki, H., Orkin, S. H., van Lohuizen, M., and Peters, A. H. (2008) PRC1 and Suv39h specify parental asymmetry at constitutive heterochromatin in early mouse embryos. *Nat. Genet.* **40,** 411–420
52. Saksouk, N., Barth, T. K., Ziegler-Birling, C., Olova, N., Nowak, A., Rey, E., Mateos-Langerak, J., Urbach, S., Reik, W., Torres-Padilla, M. E., Imhof, A., Déjardin, J., and Simboeck, E. (2014) Redundant mechanisms to form silent chromatin at pericentromeric regions rely on BEND3 and DNA methylation. *Mol. Cell* **56,** 580–594
53. Gargiulo, G., Cesaroni, M., Serresi, M., de Vries, N., Hulsman, D., Bruggeman, S. W., Lancini, C., and van Lohuizen, M. (2013) In vivo RNAi screen for BMI1 targets identifies TGF-beta/BMP-ER stress pathways as key regulators of neural- and malignant glioma-stem cell homeostasis. *Cancer Cell* **23,** 660–676
54. Tadeu, A. M., Ribeiro, S., Johnston, J., Goldberg, I., Gerloff, D., and Earnshaw, W. C. (2008) CENP-V is required for centromere organization, chromosome alignment and cytokinesis. *EMBO J.* **27,** 2510–2522
55. Shumaker, D. K., Dechat, T., Kohlmaier, A., Adam, S. A., Bozovsky, M. R., Erdos, M. R., Eriksson, M., Goldman, A. E., Khuon, S., Collins, F. S., Jenuwein, T., and Goldman, R. D. (2006) Mutant nuclear lamin A leads to progressive alterations of epigenetic control in premature aging. *Proc. Natl. Acad. Sci. U.S.A.* **103,** 8703–8708
56. Hwang, W. L., Deindl, S., Harada, B. T., and Zhuang, X. (2014) Histone H4 tail mediates allosteric regulation of nucleosome remodelling by linker

DNA. *Nature* **512,** 213–217
57. Hewish, D. R., and Burgoyne, L. A. (1973) Chromatin sub-structure. The digestion of chromatin DNA at regularly spaced sites by a nuclear deoxyribonuclease. *Biochem. Biophys. Res. Commun.* **52,** 504–510
58. Kornberg, R. D., LaPointe, J. W., and Lorch, Y. (1989) Preparation of nucleosomes and chromatin. *Methods Enzymol.* **170,** 3–14
59. Wu, C. (1980) The 5′ ends of *Drosophila* heat shock genes in chromatin are hypersensitive to DNase I. *Nature* **286,** 854–860
60. Abdouh, M., Facchino, S., Chatoo, W., Balasingam, V., Ferreira, J., and Bernier, G. (2009) BMI1 sustains human glioblastoma multiforme stem cell renewal. *J. Neurosci.* **29,** 8884–8896
61. Schoeftner, S., Sengupta, A. K., Kubicek, S., Mechtler, K., Spahn, L., Koseki, H., Jenuwein, T., and Wutz, A. (2006) Recruitment of PRC1 function at the initiation of X inactivation independent of PRC2 and silencing. *EMBO J.* **25,** 3110–3122
62. Tavares, L., Dimitrova, E., Oxley, D., Webster, J., Poot, R., Demmers, J., Bezstarosti, K., Taylor, S., Ura, H., Koide, H., Wutz, A., Vidal, M., Elderkin, S., and Brockdorff, N. (2012) RYBP-PRC1 complexes mediate H2A ubiquitylation at polycomb target sites independently of PRC2 and H3K27me3. *Cell* **148,** 664–678
63. Buchwald, G., van der Stoop, P., Weichenrieder, O., Perrakis, A., van Lohuizen, M., and Sixma, T. K. (2006) Structure and E3-ligase activity of the Ring-Ring complex of polycomb proteins Bmi1 and Ring1b. *EMBO J.* **25,** 2465–2474
64. de Napoles, M., Mermoud, J. E., Wakao, R., Tang, Y. A., Endoh, M., Appanah, R., Nesterova, T. B., Silva, J., Otte, A. P., Vidal, M., Koseki, H., and Brockdorff, N. (2004) Polycomb group proteins Ring1A/B link ubiquitylation of histone H2A to heritable gene silencing and X inactivation. *Dev. Cell* **7,** 663–676
65. Román-Trufero, M., Méndez-Gómez, H. R., Pérez, C., Hijikata, A., Fujimura, Y., Endo, T., Koseki, H., Vicario-Abejón, C., and Vidal, M. (2009) Maintenance of undifferentiated state and self-renewal of embryonic neural stem cells by Polycomb protein Ring1B. *Stem Cells* **27,** 1559–1570
66. Francis, N. J., Kingston, R. E., and Woodcock, C. L. (2004) Chromatin compaction by a polycomb group protein complex. *Science* **306,** 1574–1577
67. Meshorer, E., Yellajoshula, D., George, E., Scambler, P. J., Brown, D. T., and Misteli, T. (2006) Hyperdynamic plasticity of chromatin proteins in pluripotent embryonic stem cells. *Dev. Cell* **10,** 105–116
68. Varley, K. E., Gertz, J., Bowling, K. M., Parker, S. L., Reddy, T. E., Pauli-Behn, F., Cross, M. K., Williams, B. A., Stamatoyannopoulos, J. A., Crawford, G. E., Absher, D. M., Wold, B. J., and Myers, R. M. (2013) Dynamic DNA methylation across diverse human cell lines and tissues. *Genome Res.* **23,** 555–567
69. Kohli, R. M., and Zhang, Y. (2013) TET enzymes, TDG and the dynamics of DNA demethylation. *Nature* **502,** 472–479
70. Scaffidi, P., and Misteli, T. (2006) Lamin A-dependent nuclear defects in human aging. *Science* **312,** 1059–1063
71. Oberdoerffer, P., Michan, S., McVay, M., Mostoslavsky, R., Vann, J., Park, S. K., Hartlerode, A., Stegmuller, J., Hafner, A., Loerch, P., Wright, S. M., Mills, K. D., Bonni, A., Yankner, B. A., Scully, R., Prolla, T. A., Alt, F. W., and Sinclair, D. A. (2008) SIRT1 redistribution on chromatin promotes genomic stability but alters gene expression during aging. *Cell* **135,** 907–918
72. Larson, K., Yan, S. J., Tsurumi, A., Liu, J., Zhou, J., Gaur, K., Guo, D., Eickbush, T. H., and Li, W. X. (2012) Heterochromatin formation promotes longevity and represses ribosomal RNA synthesis. *PLoS Genet.* **8,** e1002473
73. Pegoraro, G., Kubben, N., Wickert, U., Göhler, H., Hoffmann, K., and Misteli, T. (2009) Ageing-related chromatin defects through loss of the NURD complex. *Nat. Cell. Biol.* **11,** 1261–1267
74. Peng, J. C., and Karpen, G. H. (2009) Heterochromatic genome stability requires regulators of histone H3 K9 methylation. *PLoS Genet.* **5,** e1000435
75. van der Lugt, N. M., Domen, J., Linders, K., van Roon, M., Robanus-Maandag, E., te Riele, H., van der Valk, M., Deschamps, J., Sofroniew, M., and van Lohuizen, M. (1994) Posterior transformation, neurological abnormalities, and severe hematopoietic defects in mice with a targeted deletion of the bmi-1 proto-oncogene. *Genes Dev.* **8,** 757–769
76. Kim, J., Kim, J. A., McGinty, R. K., Nguyen, U. T., Muir, T. W., Allis, C. D., and Roeder, R. G. (2013) The n-SET domain of Set1 regulates H2B ubiquitylation-dependent H3K4 methylation. *Mol. Cell* **49,** 1121–1133
77. Wu, L., Lee, S. Y., Zhou, B., Nguyen, U. T., Muir, T. W., Tan, S., and Dou, Y. (2013) ASH2L regulates ubiquitylation signaling to MLL: trans-regulation of H3 K4 methylation in higher eukaryotes. *Mol. Cell* **49,** 1108–1120
78. McGinty, R. K., Henrici, R. C., and Tan, S. (2014) Crystal structure of the PRC1 ubiquitylation module bound to the nucleosome. *Nature* **514,** 591–596

The Polycomb Repressive Complex 1 Protein BMI1 Is Required for Constitutive Heterochromatin Formation and Silencing in Mammalian Somatic Cells

Mohamed Abdouh, Roy Hanna, Jida El Hajjar, Anthony Flamier and Gilbert Bernier

J. Biol. Chem. 2016, 291:182-197.
doi: 10.1074/jbc.M115.662403 originally published online October 14, 2015

Polycomb Repressive Complex 1 protein BMI1 is required for constitutive heterochromatin formation and silencing in mammalian somatic cells*

Mohamed Abdouh[1], Roy Hanna[1], Jida El Hajjar[1], Anthony Flamier[1], and Gilbert Bernier[1]

[1] From the Department of Neurosciences, University of Montreal, and The Stem Cell and Developmental Biology Laboratory, Hôpital Maisonneuve-Rosemont, 5415 Boul. l'Assomption, Montreal, Canada, H1T 2M4

*Running title: *BMI1 regulates heterochromatin compaction and silencing*

To whom correspondence should be addressed: Gilbert Bernier, Stem Cell and Developmental Biology Laboratory, Hôpital Maisonneuve-Rosemont, 5415 Boul. l'Assomption, Montreal, Canada, H1T 2M4. Tel: 514-252-3400 ext. 4648; Fax: 514-253-7626; E-mail: gbernier.hmr@ssss.gouv.qc.ca

Keywords: Polycomb; BMI1; BRCA1; heterochromatin; histone H2A

SUPPLEMENTAL INFORMATION

Content:

SUPPLEMENTAL EXPERIMENTAL PROCEDURES

Mouse RT-qPCR primers

Gene	Forward	Reverse
Hprt	5'-ACTGTAATGATCAGTCAACGGG-3'	5_-GGCCTGTATCCAACACTTGG-3'
Bmi1	5'-GGAGACCAGCAAGTATTGTCCTATTTG-3'	5'-CTTACGATGCCCAGCAGCAATG-3'
P16	5'-CAACGCCCCGAACTCTTTC-3'	5_-GCAGAAGAGCTGCTACGTGAAC-3'
Line	5′-TGGCTTGTGCTGTAAGATCG-3′	5′-TCTGTTGGTGGTCTTTTTGTC-3′
Sine	5′-GAGCACACCCATGCACATAC-3′	5′-AAAGGCATGCACCTCTACCACC-3′
Min. sat	5′-TTGGAAACGGGATTTGTAGA-3'	5′-CGGTTTCCAACATATGTGTTTT-3′
Maj. sat	5′-GGCGAGAAAACTGAAAATCACG-3′	5′-CTTGCCATATTCCACGTCCT-3′
IAP1	5′-CGCTCCGGTAGAATACTTAC-3′	5′-TGCCATGCCGGCGAGCCTGT-3′

Mouse ChIP-qPCR primers

Gene	Forward	Reverse
Line	5′-TGGCTTGTGCTGTAAGATCG-3′	5′-TCTGTTGGTGGTCTTTTTGTC-3′
Sine	5′-GAGCACACCCATGCACATAC-3′	5′-AAAGGCATGCACCTCTACCACC-3′
Min. sat	5′-TTGGAAACGGGATTTGTAGA-3'	5′-CGGTTTCCAACATATGTGTTTT-3′
Maj. sat	5′-GGCGAGAAAACTGAAAATCACG-3′	5′-CTTGCCATATTCCACGTCCT-3′
IAP1	5′-CGCTCCGGTAGAATACTTAC-3′	5′-TGCCATGCCGGCGAGCCTGT-3′
HoxA7.1	5'-GTGGGCAAAGAGTGGATTTC-3'	5'-CCCCGACAACCTCATACCTA-3'
Globin	5′-CAGTGAGTGGCACAGCATCC-3′	5′-CAGTCAGGTGCACCATGATGT-3′

Human RT-qPCR primers

Gene	Forward	Reverse
GAP-DH	5'-TCACCAGGGCTGCTTTTAAC-3'	5'-ATCCACAGTCTTCTGGGTGG-3'
BMI1	5'-AATCCCCACCTGATGTGTGT-3'	5'-GCTGGTCTCCAGGTAACGAA-3'
P16	5'-GGGTTTTCGTGGTTCACATC-3'	5'-CTGCCCATCATCATGACCT-3'
Alu	5'-CCTCAATCTCGCTCTCGCTC-3'	5'-CTCTAAGGCTGCTCAATGTCA-3'
McBox	5′-AGGGAATGTCTTCCCATAAAAACT-3′	5′-GTCTACCTTTTATTTGAATTCCCG-3′
Sat a	5′-AAGGTCAATGGCAGAAAAGAA-3′	5′-CAACGAAGGCCACAAGATGTC-3′
Sat III	5′-AATCAACCCGAGTGCAATCNGAATGGAATCG-3′	5′-TCCATTCCATTCCTGTACTCGG-3′

Human ChIP-qPCR primers

Gene	Forward	Reverse
HOXC13.2	5'-AGCAGAGCTCAGTGGGAGAG-3'	5'-AATTTCAGGCCCACCCTTAG-3'
Globin	5'-GGCTGTCATCACTTAGACCTC-3'	5'-GGTTGCTAGTGAACACAGTTG-3'
Alu	5'-CCTCAATCTCGCTCTCGCTC-3'	5'-CTCTAAGGCTGCTCAATGTCA-3'
McBox	5′-AGGGAATGTCTTCCCATAAAAACT-3′	5′-GTCTACCTTTTATTTGAATTCCCG-3′
Sat a	5′-AAGGTCAATGGCAGAAAAGAA-3′	5′-CAACGAAGGCCACAAGATGTC-3′
Sat III	5′-AATCAACCCGAGTGCAATCNGAATGGAATCG-3′	5′-TCCATTCCATTCCTGTACTCGG-3′

<u>Annexe II:</u> Differentiation of human embryonic stem cells into cone photoreceptors through simultaneous inhibition of BMP, TGFβ and Wnt signaling

L'annexe 2 vous présente un article n'étant pas en lien avec mon projet principal de doctorat mais faisant partie intégrante de ma formation. Cet article pour lequel je suis co-premier auteur est paru le 6 Aout 2015 dans le journal *Development*.

© 2015. Published by The Company of Biologists Ltd | Development (2015) 142, 3294-3306 doi:10.1242/dev.125385

RESEARCH ARTICLE

STEM CELLS AND REGENERATION

Differentiation of human embryonic stem cells into cone photoreceptors through simultaneous inhibition of BMP, TGFβ and Wnt signaling

Shufeng Zhou[1,*], Anthony Flamier[1,*], Mohamed Abdouh[1], Nicolas Tétreault[1], Andrea Barabino[1], Shashi Wadhwa[2] and Gilbert Bernier[1,3,4,‡]

ABSTRACT

Cone photoreceptors are required for color discrimination and high-resolution central vision and are lost in macular degenerations, cone and cone/rod dystrophies. Cone transplantation could represent a therapeutic solution. However, an abundant source of human cones remains difficult to obtain. Work performed in model organisms suggests that anterior neural cell fate is induced 'by default' if BMP, TGFβ and Wnt activities are blocked, and that photoreceptor genesis operates through an S-cone default pathway. We report here that *Coco* (*Dand5*), a member of the Cerberus gene family, is expressed in the developing and adult mouse retina. Upon exposure to recombinant COCO, human embryonic stem cells (hESCs) differentiated into S-cone photoreceptors, developed an inner segment-like protrusion, and could degrade cGMP when exposed to light. Addition of thyroid hormone resulted in a transition from a unique S-cone population toward a mixed M/S-cone population. When cultured at confluence for a prolonged period of time, COCO-exposed hESCs spontaneously developed into a cellular sheet composed of polarized cone photoreceptors. COCO showed dose-dependent and synergistic activity with IGF1 at blocking BMP/TGFβ/Wnt signaling, while its cone-inducing activity was blocked in a dose-dependent manner by exposure to BMP, TGFβ or Wnt-related proteins. Our work thus provides a unique platform to produce human cones for developmental, biochemical and therapeutic studies and supports the hypothesis that photoreceptor differentiation operates through an S-cone default pathway during human retinal development.

KEY WORDS: Coco, Dand5, Cerl2, Differentiation, Retina, Cone photoreceptors, hES cells, Mouse, Human

INTRODUCTION

Macular degenerations, retinitis pigmentosa and retinal dystrophies affect millions of people worldwide. In most cases, loss of visual function results from death of photoreceptors, the specialized cells involved in phototransduction (Pacione et al., 2003). Macular degenerations and cone dystrophies preferentially target the macula, a cone photoreceptor-rich retinal structure involved in color discrimination and high-resolution central vision. Cell replacement therapy may stop disease progression or restore visual function. However, a reliable and abundant source of human cone photoreceptors is not currently available. This limitation may be overcome using embryonic stem cells (ESCs). ESCs originate from the inner cell mass of the blastocyst and represent the most primitive stem cells. Human ESCs (hESCs) can develop into cells and tissues of the three primary germ layers and be expanded indefinitely (Reubinoff et al., 2000; Thomson et al., 1998).

Work performed in amphibians and chick suggests that primordial cells adopt a neural fate in the absence of alternative cues (Muñoz-Sanjuán and Brivanlou, 2002). The default model of neural induction has paved the way to the differentiation of ESCs into neurons (Tropepe et al., 2001). The retina and cerebral cortex originate from the anterior portion of the neural plate, and hESCs spontaneously adopt an anterior positional identity when induced to differentiate into neurons (Banin et al., 2006; Couly and Le Douarin, 1988). However, only a fraction of these cells actually differentiate into retinal neurons, possibly because active inhibition of bone morphogenetic protein (BMP), transforming growth factor β (TGFβ) superfamily (including Nodal and Activin), and Wingless (Wnt) signaling is normally required (Liu et al., 2010). In principle, this can be partially achieved by expressing noggin and chordin, two BMP antagonists, and dickkopf 1 (Dkk1), a Wnt antagonist. Furthermore, retinal fate can be promoted using insulin like growth factor 1 (IGF1) (Pera et al., 2001; Rorick et al., 2006). Application of this rationale has led to the differentiation of hESCs into retinal progenitor cells, where ~12% of cells express CRX (Lamba et al., 2006). CRX is expressed by photoreceptor progenitors, mature photoreceptors and a subset of bipolar neurons (Chen et al., 1997; Freund et al., 1997; Furukawa et al., 1997). Although ~4% of differentiated hESCs were reported to express rhodopsin, a marker of rod photoreceptors, fewer than 0.01% express S-opsin (OPN1SW – HUGO), a marker of cone photoreceptors. Notably, transplanted cells could adopt rod and cone photoreceptor phenotypes when grafted into the retina of normal and *Crx*-deficient mice (Lamba et al., 2009). The differentiation of hESCs into cone and rod photoreceptors at a frequency of 12-20% over a 150-200 day period was also achieved using Dkk1 and LEFTY, a Nodal antagonist, as well as retinoic acid (RA) and taurine, two factors that can promote the terminal differentiation of photoreceptors (Osakada et al., 2008). In addition, directed differentiation of hESCs into retinal pigment epithelium was performed using nicotinamide (Idelson et al., 2009). More recently, differentiation of human pluripotent stem cells into retinal organoids containing rod and cone photoreceptors was also achieved (Mellough et al., 2015; Nakano et al., 2012; Tucker et al., 2013).

We report here that ~60-80% of hESCs can be differentiated within 4-5 weeks into S-cone photoreceptors using human recombinant COCO, a multifunctional BMP, TGFβ and Wnt

[1]Stem Cell and Developmental Biology Laboratory, Maisonneuve-Rosemont Hospital, 5415 Boul. l'Assomption, Montréal, Canada H1T 2M4. [2]Department of Anatomy, All India Institute of Medical Sciences, New Delhi 110029, India. [3]Department of Neuroscience, University of Montréal, Montréal H3T 1J4, Canada. [4]Department of Ophthalmology, University of Montréal, Montréal H3T 1J4, Canada. *These authors contributed equally to this work

‡Author for correspondence (gbernier.hmr@ssss.gouv.qc.ca)

Received 13 April 2015; Accepted 6 August 2015

Development (2015) 142, 3294-3306 doi:10.1242/dev.125385

antagonist, supporting the hypothesis that photoreceptor development operates through an S-cone default pathway (Jadhav et al., 2006; Mears et al., 2001; Ng et al., 2001; Swaroop et al., 2010; Yanagi et al., 2002; Yaron et al., 2006). The short wave (S) and medium wave (M) cone subtype ratio can also be manipulated by the addition of thyroid hormone and the procedure is achieved without using the embryonic body (EB) induction step. Alternatively, a self-organized and polarized 3D cone photoreceptor sheet can be derived that shows evidence of connecting cilium and outer segment formation. This work might contribute to progress toward the use of hESCs for the treatment of macular degenerations and cone dystrophies, and provides a framework with which to study the biochemistry and developmental genetics of human cones in a culture dish.

RESULTS

Mouse *Coco* is expressed in the developing CNS and retina

Members of the Cerberus/Dan family of secreted inhibitors can block BMP, Nodal/TGFβ and Wnt activities simultaneously (Bouwmeester et al., 1996; Piccolo et al., 1999). In a search for a putative 'retinal promoting' factor of this family, we analyzed the expression pattern of the mammalian ortholog of *Coco* (also known as *Dand5* or *Cerl2* in mammals). In *Xenopus*, *Coco* is expressed maternally and ubiquitously within the ectoderm prior to neural induction, but expression is not detected after gastrulation (Bell et al., 2003). However, a search of the UNIGENE and EST databases reveals that mouse *Coco* and human *COCO* transcripts are present in the eye, brain and testis cDNA libraries at embryonic and adult stages.

Coco encodes two transcripts, with one lacking the 5′ coding sequence (supplementary material Fig. S1A). We analyzed mouse *Coco* expression by RNA *in situ* hybridization. Using the full-length mouse *Coco* cDNA (which recognizes both isoforms), we observed *Coco* expression in the optic vesicle and CNS at E9.5 (Fig. 1A), in the retina and hair follicles at E14.5 and P1 (Fig. 1A), and in the photoreceptor nuclear layer at P60 (supplementary material Fig. S1B). These observations were confirmed using quantitative RT-PCR (qPCR) analysis on tissues from neonates at P3 using

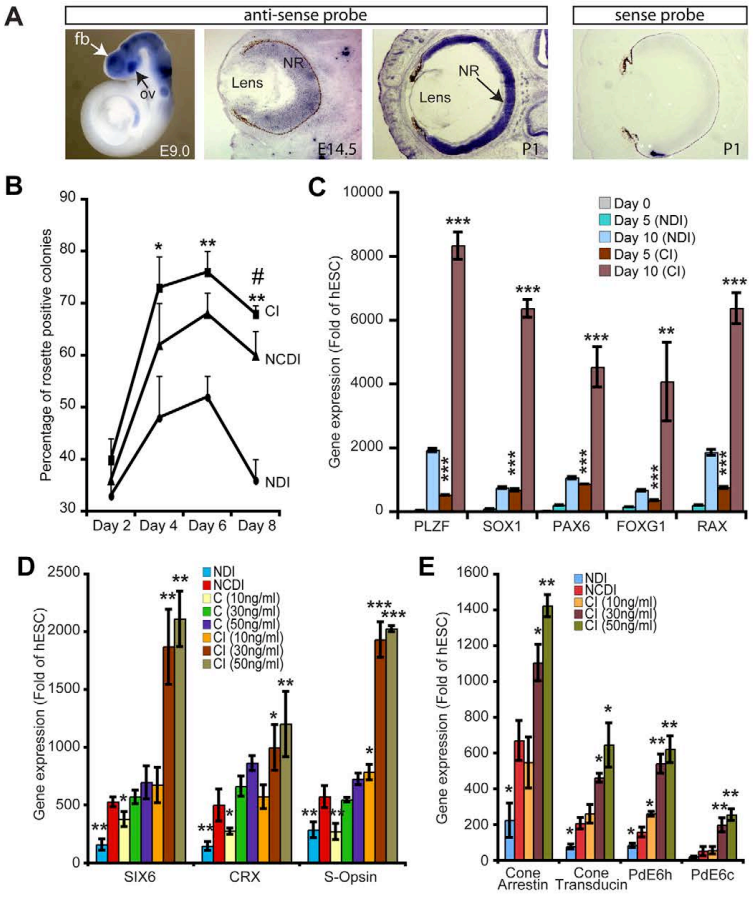

Fig. 1. COCO is a potent retinal and photoreceptor inducer. (A) *In situ* hybridization on E9.0 mouse embryos (whole mount) revealed *Coco* expression in the optic vesicle (ov), forebrain (fb) and neural tube, and in the neural retina (NR) at E14.5 and P1 (sections). The sense probe provides a negative control. (B) Analysis of neural rosette induction kinetics in NDI, NCDI, or COCO (30 ng/ml)+IGF1 (10 ng/ml) (CI) culture medium. *P<0.05 and **P<0.01 when compared with NDI-treated culture and $^{\#}P$<0.05 when compared with NCDI-treated culture. (C) hESCs were induced to differentiate in the presence of NDI or CI media for 5 and 10 days and analyzed by qPCR. Data are expressed as fold change over gene expression in undifferentiated hESCs. **P<0.01 and ***P<0.001 when comparing CI with NDI at both time points analyzed. (D,E) hESCs were induced to differentiate in the presence of NDI, NCDI, COCO alone or CI for 3 weeks. Differentiated hESCs were analyzed by qPCR. Data are expressed as fold change over gene expression in undifferentiated hESCs. *P<0.05, **P<0.01, ***P<0.001 as compared with gene expression levels in NCDI-treated cells. (B-E) Results are mean±s.d. (n=3).

Development (2015) 142, 3294-3306 doi:10.1242/dev.125385

oligonucleotide pairs that recognize either the 5′ coding isoform or both isoforms (supplementary material Fig. S1C).

COCO is a potent neural and photoreceptor inducer

Neural induction of hESCs can be achieved through the formation of floating EBs and subculture on a laminin or Matrigel substrate in serum-free media (supplementary material Fig. S2). Using the hESC line H9, we tested the putative neural/retinal-inducing activity of human recombinant COCO by morphological analysis of EBs maintained in suspension for 4-5 days and then subcultured on Matrigel. We quantified the frequency and kinetics of neural rosette formation (Fig. 1B). In these experiments, COCO (30 ng/ml) was used in combination with IGF1 and FGF2 (referred to as CI medium) or added at 10 ng/ml to the previously described NDI medium (referred to as NCDI medium), which contains noggin, Dkk1, IGF1 and FGF2. The original NDI medium was used as a positive control (Lamba et al., 2006). We found that although more colonies presented neural rosettes with the NCDI (~67%) than with the NDI (~50%) medium at day 6 of the differentiation protocol, this process was further improved with the CI medium (~76%). To directly compare the neural induction activity of the NDI and CI media, we analyzed the differentiated cells at early time points for the expression of neural rosette (*PLZF*; *ZBTB16* – HUGO), pan-neural (*SOX1*, *PAX6*), anterior neural/forebrain (*FOXG1*) and anterior neural/ventral forebrain/early retinal (*RAX*) cell fate markers using qPCR (Chambers et al., 2009; Mathers et al., 1997; Walther and Gruss, 1991). These results revealed that the CI medium provided robust neural and anterior neural/early retinal induction activity (Fig. 1C).

To evaluate the putative retinal-inducing activity of COCO, we tested whether COCO+FGF2 possessed early retinal (*SIX6*) and photoreceptor [*CRX*, rhodopsin (*RHO*), *NRL*, M-opsin (*OPN1MW* – HUGO) and S-opsin] inducing activity using qPCR analysis on colonies isolated at day 21 of the differentiation protocol (Gallardo et al., 1999; Jean et al., 1999). We found that COCO+FGF2 was very efficient at inducing *SIX6*, *CRX* and S-opsin gene expression, and that this effect was dose dependent (Fig. 1D). The retinal-inducing activity of COCO (30 ng/ml)+FGF2 was comparable to that of NCDI medium. When this was combined with 10 ng/ml IGF1 (the same concentration as in the NDI and NCDI media), the induction of *SIX6*, *CRX* and S-opsin was further enhanced. This effect was dose dependent, and maximal CI activity was obtained when COCO concentrations ranged between 30 and 50 ng/ml (Fig. 1D). Taken as a whole, the retinal- and photoreceptor-inducing activity of CI was ~10-fold more effective than the NDI medium and ~3- to 4-fold more effective than the NCDI medium. Expression of *RHO* and *NRL* (rods) and of M-opsin (M-cones) was not detected after 21 days of hESC differentiation in CI (supplementary material Fig. S3). However, timecourse analysis revealed weak induction (about 4-fold the hESC level) of the *NRL* and M-opsin genes at 1 week, and of *RHO* at week 2, suggesting that retinal progenitor cells might be potent to generate all types of photoreceptor cells at these early stages (supplementary material Fig. S3). Robust expression of the cone-specific genes cone arrestin [also known as arrestin 3 (*ARR3*) and X-arrestin], cone transducin (*GNAT2*), phosphodiesterase 6H (*PDE6H*) and phosphodiesterase 6C (*PDE6C*) was also observed in cells exposed to CI for 21 days (Fig. 1E) (Corbo et al., 2007), altogether suggesting a predominant S-cone photoreceptor cell population. Comparable results, but with variable efficiencies, were obtained with the hESC lines HUES1, HUES8 and HUES9 (supplementary material Fig. S4).

Generation of a highly enriched S-opsin-positive cell population

To further characterize the differentiated cell populations, we performed western blot analyses using extracts from hESCs exposed to NCDI or CI for 21 days. We observed robust expression of CRX and of the phototransduction proteins S-opsin, cone transducin and cone arrestin (Fig. 2A,B). Expression of rhodopsin and of M-opsin proteins was, however, not detected, even when thyroid hormone (T3) was added to the culture media (supplementary material Fig. S6A).

We performed intracellular labeling using an anti-S-opsin antibody combined with fluorescence activated cell sorting (FACS) analysis on cells exposed to CI for 21 days (Chatoo et al., 2010). We found that ~70±9% (n=5 independent cell differentiation experiments) of differentiated cells from the H9 cell line highly expressed S-opsin (Fig. 2C). Comparable results were obtained with the HUES1, HUES8 and HUES9 cell lines (supplementary material Fig. S6B). In a separate set of experiments, S-opsin-labeled cell populations were sorted and analyzed by qPCR for the expression of retinal, mesendodermal, ectodermal and ESC markers (Fig. 2D,E). We found that S-opsin^{high} cells (95% in experiment #1, 80% in experiment #2) expressed photoreceptor genes at levels several orders of magnitude higher than undifferentiated hESCs (Fig. 2E). The S-opsin^{low} cells (5% in experiment #1, 20% in experiment #2) were also positive for *CRX*, cone arrestin and S-opsin gene expression but at levels corresponding to 4-10% of those found in the S-opsin^{high} population (Fig. 2E, inset). Both populations were, however, negative for non-retinal lineage-specific genes (Fig. 2E).

Developmental kinetics of the differentiated cells

To study the developmental kinetics of the cell differentiation process, hESCs exposed to CI for 5, 10 and 21 days were analyzed by immunofluorescence (IF) microscopy for CHX10 (VSX1 – HUGO), SOX2, RAX and CRX expression (Burmeister et al., 1996; Ellis et al., 2004; Ferda Percin et al., 2000; Graham et al., 2003; Livne-Bar et al., 2006; Mathers et al., 1997; Taranova et al., 2006). At day 5, we observed that the large majority of the cells were positive for the retinal progenitor markers CHX10 (90%) and SOX2 (100%) (Fig. 3A,F,G). This proportion slightly declined at day 10, when numerous RAX-positive and CRX-positive cells also appeared (Fig. 3B,F,G). Yet, almost all CHX10-expressing cells also expressed SOX2 (Fig. 3D). At day 21, few cells positive for CHX10, SOX2 or RAX remained, being replaced by prospective photoreceptor cells expressing CRX (Fig. 3C,F).

Cells expressing S-opsin at the highest levels (40% of S-opsin^{high} cells) were generally located within neural rosettes (Fig. 3E). Most cells within rosettes also expressed βIII-tubulin (a marker of immature neurons) at low levels (Fig. 3E). Furthermore, ~3% of cells present in our cultures had a typical neuronal morphology and expressed βIII-tubulin at high levels (Fig. 3E). The subtype identity of these neurons remains to be established. These analyses revealed that, upon exposure to CI, the large majority of hESCs rapidly adopt a retinal progenitor cell identity, which is also rapidly lost toward a cone photoreceptor precursor cell identity.

Cone phenotype and cGMP degradation *in vitro*

In all experiments, hESCs were induced to differentiate into photoreceptors when at confluence, which in our hands improved cell survival and neural/photoreceptor induction. However, this procedure prevented the analysis of single cells. At first, we analyzed cells exposed to CI by high-resolution IF at day 21, which confirmed immunoreactivity for CRX (mean 72±7%) and ABCA4

Development (2015) 142, 3294-3306 doi:10.1242/dev.125385

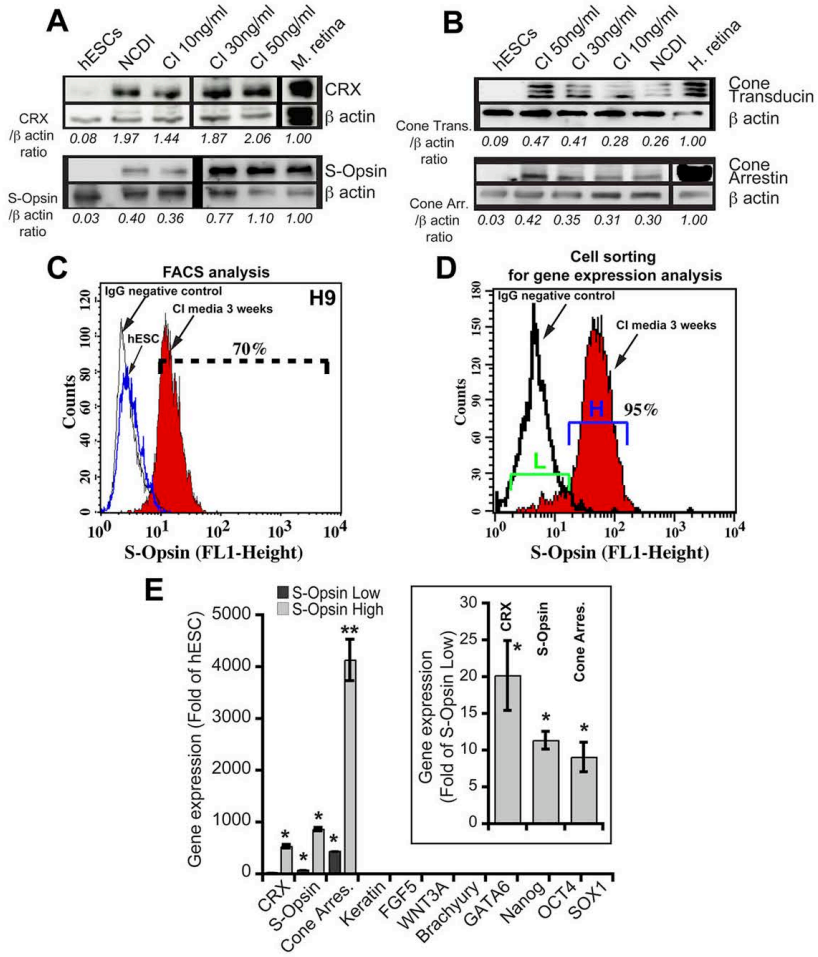

Fig. 2. COCO induces the generation of a highly enriched S-cone photoreceptor population. (A,B) hESCs cultured in NCDI or CI medium for 3 weeks were subjected to western blot analyses for the expression of CRX and S-opsin (A), or cone transducin and cone arrestin (B). β-actin was used to quantify protein loading. CRX, S-opsin, cone transducin or cone arrestin levels are expressed as a ratio over β-actin levels. Mouse or human retinas were used as positive controls. (C) Undifferentiated hESCs (blue line) or hESCs cultured in CI for 3 weeks (red) were analyzed by FACS for S-opsin expression. The black line represents the IgG isotypic control serum. (D) hESCs cultured in CI for 3 weeks were sorted by FACS for subsequent gene expression analysis on the basis of S-opsin expression levels [S-opsin^{low} (L) versus S-opsin^{high} (H)]. (E) Sorted cells were analyzed for gene expression by qPCR. Data are expressed as fold change over gene expression in undifferentiated hESCs. In the inset, a parallel analysis was performed in which gene expression in the S-opsin^{high} cell fraction is represented as fold change over that in the S-opsin^{low} cell fraction, which was set at 1. Results are mean±s.d. (n=2 cell sortings); *P<0.05 and **P<0.01 as compared with gene expression levels in undifferentiated hESCs and the S-opsin^{low} cell fraction, respectively.

(mean 67±12%) in densely packed cellular aggregates (Fig. 4A). *ABCA4* is mutated in Stargardt disease and is expressed by cone and rod photoreceptors (Allikmets et al., 1997; Molday et al., 2000). Cells differentiated for 21 days were next dissociated to single cells and plated on glass coverslips at low density. After an additional 7 days, they were analyzed by IF for the expression of cone markers. Under these conditions, most cells presented neurites and were positive for ABCA4 (mean 76±11%), S-opsin (mean 79±9%) and cone arrestin (mean 84.9±5%) (Fig. 4A). Although S-opsin immunoreactivity was diffused throughout the cell at this early stage, it was enriched in the proximal soma of the cells, suggesting possible S-opsin compartmentalization (Fig. 4A, inset).

Using the same experimental procedure, single cells were allowed to differentiate for 15 days. On rare occasions, we could observe the formation of more mature cones having an outer segment-like structure (Fig. 4A). These cells were immunoreactive

Development (2015) 142, 3294-3306 doi:10.1242/dev.125385

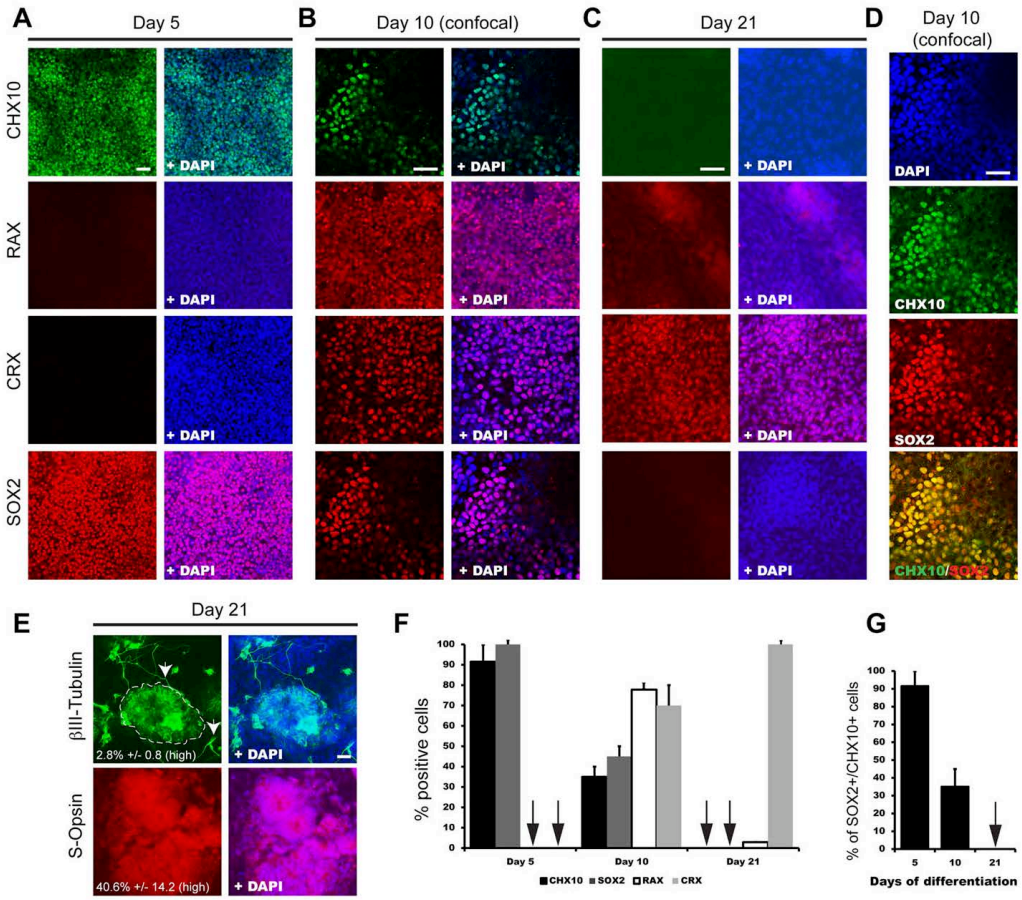

Fig. 3. Developmental kinetics of hESC differentiation into photoreceptors. (A-C) Representative immunofluorescence images of hESCs exposed to CI for 5 (A), 10 (B) or 21 (C) days using antibodies against CHX10, RAX, CRX and SOX2. (D) Co-expression of CHX10 and SOX2 after 10 days of differentiation, as revealed by confocal IF analysis. (E) Expression of βIII-tubulin and S-opsin after 21 days of differentiation. Arrowheads indicate neurons expressing βIII-tubulin at high levels. The dashed line delineates a neural rosette. Values indicate the percentage of cells expressing high levels of βIII-tubulin or S-opsin. (F) Quantitative analysis of cells positive for CHX10, SOX2, RAX or CRX. (G) Quantitative analysis of CHX10/SOX2 double-positive cells after 5, 10 and 21 days of differentiation. Results are mean±s.d. (n=3 experiments). Arrows (F,G) indicate the absence of positive cells for the corresponding antibody. Scale bars: 40 µm.

for ABCA4 at the presumptive junction between the inner and outer segments, a localization possibly corresponding to the nascent disk (Fig. 4A). We also observed polarized accumulation of S-opsin at one side of the cells, also suggesting cone maturation (Fig. 4A). Using scanning electron microscopy at day 35 of the differentiation protocol, we observed that cells within these aggregates displayed a buttonhead-like morphology reminiscent of the head-like morphology of week 15 human embryonic cones when viewed vertically (Fig. 4B). In immature cones, this structure corresponds to the apex of the inner segment (Narayanan and Wadhwa, 1998). The morphological similarity was also noticeable when cells were viewed in the horizontal plane, revealing the presence of an inner segment-like protrusion in the *in vitro* generated cones (Fig. 4B).

One of the unique properties of photoreceptors is to degrade cGMP in response to the activation of photosensitive opsin pigments by light. This process occurs through release of the α-transducin subunit, which can activate the cGMP phosphodiesterase, ultimately resulting in membrane hyperpolarization (Michaelides et al., 2006). To establish if cells could degrade cGMP in response to light exposure, we measured cGMP levels by immunoassay in cells differentiated for 35 days in NDI or CI medium (Jomary and Jones, 2008). Extracts were isolated from cells exposed to a bright light for 1 min or maintained in the dark for 2 days. No difference in cGMP levels was observed in undifferentiated hESCs between light and dark conditions, in contrast to hESCs differentiated with NDI or CI medium (Fig. 4C). To evaluate the total amount of cGMP

Development (2015) 142, 3294-3306 doi:10.1242/dev.125385

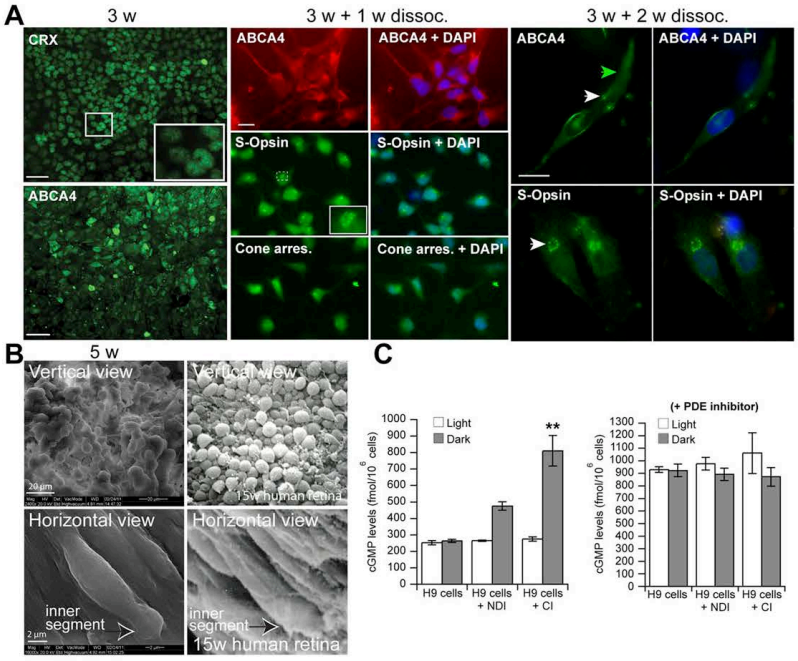

Fig. 4. Differentiated cells develop neurites and an outer segment-like structure and can degrade cGMP upon light exposure. (A) hESCs differentiated for 21 days (3 w) in CI medium were analyzed by IF. hESCs were differentiated for 3 weeks at confluence in CI medium and then dissociated to single cells and plated on glass coverslips at low density. Cells were analyzed 7 days later (3 w+1 w) by IF, revealing the broad cellular distribution of S-opsin at this early maturation stage but with stronger accumulation in the cell soma (inset), and expression of ABCA4 and cone arrestin. Note the presence of neurites. Cells were further analyzed 15 days later (3 w+2 w) by IF. Note the localization of ABCA4 at the presumptive inner/outer segment junction (white arrowhead) and the presence of an outer segment-like structure (green arrowhead). Note also the polarized accumulation of S-opsin (arrowhead). Scale bars: 5 µm, except 50 µm in 3 w. (B) hESCs differentiated for 35 days were analyzed by scanning electron microscopy. 15-week-old human embryonic retina is shown for comparison. (C) hESCs were cultured in NDI or CI medium for 35 days and cGMP concentrations were measured. (Left) Cells were kept in the dark or exposed to light. (Right) cGMP concentrations were measured in cells cultured in the presence of the PDE inhibitor IBMX. cGMP levels are presented as mean±s.d. (n=3); **P<0.01 as compared with cGMP levels in undifferentiated hESCs cultured in NDI medium.

hydrolyzed by all phosphodiesterases (PDEs) present in the cells, we applied a non-specific PDE inhibitor (IBMX). The addition of IBMX abolished the difference of cGMP levels between light and dark conditions (Fig. 4C). The level of cGMP hydrolyzed by light-sensitive PDE corresponds to the difference between the levels in light and dark conditions and represented 240 femtomoles/10^6 cells in NDI medium and 560 femtomoles/10^6 cells in CI medium. The total amount of cGMP hydrolyzed by all PDEs (the difference between the cGMP levels in the presence and absence of IBMX in the light) corresponds to 650 femtomoles/10^6 cells. Therefore, light-sensitive PDEs account for 36% (240/650) of the total PDE activity in NDI-differentiated cells and for 86% (560/650) in CI-differentiated cells.

Cone phenotype upon cell transplantation in mouse eyes

To test the capacity of the cells to migrate and adopt a cone phenotype *in vivo*, we performed cell transplantation experiments by injecting hESCs differentiated with CI for 2, 3 or 4 weeks into the vitreous of wild-type mouse pups (Lamba et al., 2009). A fraction of the cells that underwent differentiation for 2 weeks, but not for 3 or 4 weeks, could migrate into various layers of the host retina, as detected using a human-specific mitochondrial antigen antibody (1.4±0.5% from the 10,000 cells injected) (supplementary material Fig. S5A,B). Notably, rare human cells present in the photoreceptor nuclear layer were positive for S-opsin and adopted a morphology that was similar to that of endogenous photoreceptors (supplementary material Fig. S5B,B′). The non-rodent identity of the double-positive cells was further confirmed by the unique pattern of chromatin condensation and the larger nuclei of human cells, as visualized with DAPI (supplementary material Fig. S5B′). These features were not present in PBS-injected eyes (supplementary material Fig. S5C). These results suggested that a fraction of the immature human cone progenitors or precursors differentiated with CI could migrate into the mouse retina outer nuclear layer and adopt an S-cone photoreceptor fate *in vivo*.

Thyroid hormone signaling allows M-cone genesis

During mouse retinal development, cone differentiation into the M-cone subtype is induced by T3 through activation of the thyroid hormone receptor β2 (Thrβ2). Thrβ2 can repress the S-opsin promoter while activating the M-opsin gene (Roberts et al., 2006; Swaroop et al., 2010). In previous assays using the EB induction

Development (2015) 142, 3294-3306 doi:10.1242/dev.125385

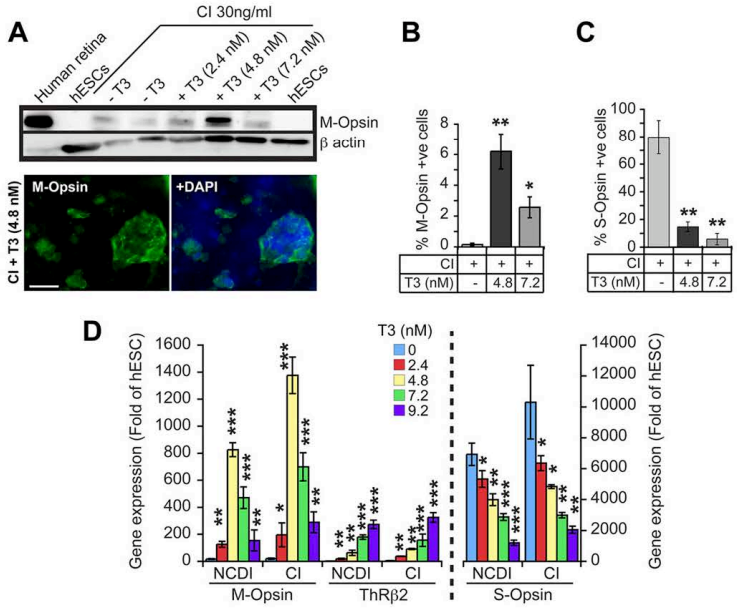

Fig. 5. Exposure to thyroid hormone can induce the generation of M-cone photoreceptors. (A) hESCs were cultured in CI medium with or without thyroid hormone (T3) for 3 weeks and analyzed by western blot and IF for M-opsin expression. Scale bar: 40 µm. (B,C) hESCs cultured as in A were labeled with anti-M-opsin (B) or anti-S-opsin (C) antibodies. The percentage of cells positive for M-opsin or S-opsin among total DAPI-stained nuclei are shown. Results are mean±s.d. (n=4); *P<0.05, **P<0.01 as compared with cells not treated with T3. (D) hESCs were cultured in NCDI or CI medium with or without T3, and analyzed by qPCR. Data are expressed as fold change over gene expression in undifferentiated hESCs. Results are mean±s.d. (n=3); *P<0.05, **P<0.01, ***P<0.001 as compared with gene expression levels in cells not treated with T3.

protocol and CI, we were unable to detect M-opsin and *Thrb2* expression by qPCR or western blot, even when cells were exposed to various concentrations of T3 (supplementary material Fig. S3 and Fig. S6A). To test if this limitation could be overcome, we induced hESCs predifferentiation by plating them directly on reduced growth factor Matrigel for 5-7 days in hESC medium until they reached confluence, and then added CI medium (thus bypassing the EB induction step) (Chambers et al., 2009). With this modification, addition of T3 to the CI medium resulted in a dose-dependent activation of M-opsin and *Thrb2* expression (Fig. 5A-D). M-opsin gene expression reached maximum levels at T3 concentrations of 4-5 nM, decreasing dramatically at higher concentrations (Fig. 5A-D). This result was expected since T3 is toxic for cones at high concentrations (Ng et al., 2010). In contrast to *Thrb2*, S-opsin gene expression decreased steadily with the addition of T3, which is suggestive of a binary cell fate choice between S- and M-cones (Fig. 5D). However, because the maximal proportion of M-cones generated (6%) never compensated for the observed reduction in S-cones at 4-5 nM T3 (Fig. 5B,C), S-cone differentiation might also be substantially inhibited by the addition of T3.

Spontaneous development of polarized cellular sheets containing cone photoreceptors

To test for self-organization of retinal tissue, we cultured COCO-exposed hESCs at confluence for 60 days, without additional manipulations (Fig. 6A). This generated a whitish and uniform cellular sheet (or tissue) that could be manipulated (see supplementary material Movie 1). The sheet could be grown to cover an entire well of a 6-well plate or cell culture dish, totaling ~6×10^6 cells. Pigmented cells were not observed on either side of the sheet, suggesting the absence of retinal pigment epithelium. Quantitative analyses revealed that ~80% of the cells were positive for CRX (Fig. 6B). Confocal IF combined with 3D reconstruction analyses revealed that the sheet was polarized and that peanut agglutinin (PNA) staining, which labels the inner and outer segment membrane of cones, was located at the opposite side of the DAPI-stained nuclear layer (Fig. 6C) (Blanks and Johnson, 1983). The presumptive PNA^+ outer segment of cones thus connected with the Matrigel-coated Petri dish surface (Fig. 6A). On average, the sheet was 150 µm thick and the nuclear layer was composed of ~5 nuclei, with additional sparse nuclei randomly distributed (Fig. 6C). Notably, immunolabeling for S-opsin was predominantly observed at the opposite side of the nuclei-rich layer (Fig. 6C).

Formation of the photoreceptor outer segment requires the presence of a connecting cilium (Novarino et al., 2011; Rachel et al., 2012). To test for this, we used three antibodies against proteins located at the connecting cilium, namely RP2, RPGR and acetylated α-tubulin (Ghosh et al., 2010; Hurd et al., 2010; Rachel et al., 2012). These antibodies, and especially RPGR, decorated a unique rod-shaped structure located in between the S-opsin-labeled outer segments and CRX-labeled nuclei (Fig. 6D). IF analyses of flat-mount P17 mouse retinas and human retinal sections were used to validate the specificity of all antibodies (supplementary material Fig. S7A-C). We used transmission electron microscopy to analyze cellular morphology and observed in longitudinal sections the presence of cells having a well-developed inner segment-like structure containing numerous mitochondria and a large Golgi apparatus (Fig. 6E). These cells had an additional protrusion resembling an immature outer segment, since membrane stacks were not present (Fig. 6E). The presence of a connecting cilium was not observed in the limited number of samples analyzed. In transverse sections and at the level of the mitochondria-rich inner segment, we also observed groups of cells with a rosette-like organization (Fig. 6E).

Development (2015) 142, 3294-3306 doi:10.1242/dev.125385

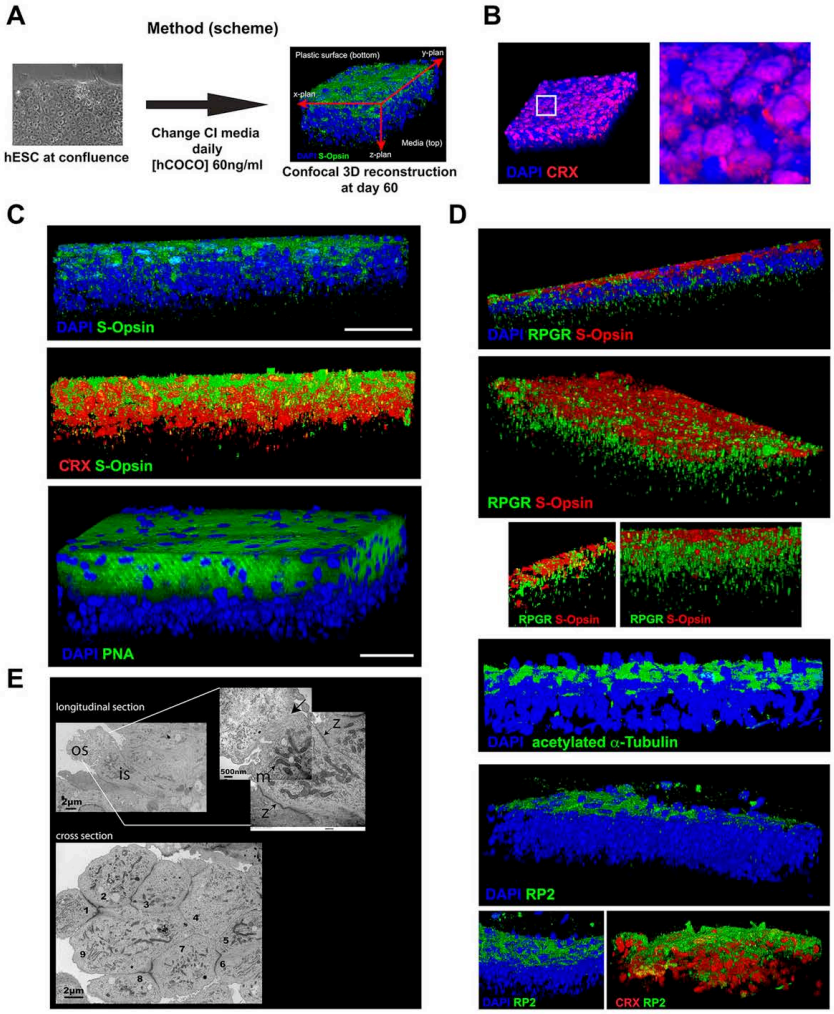

Fig. 6. Spontaneous development of a cellular sheet containing polarized cones. (A) Method for the derivation of a cellular sheet containing polarized cones. hESCs at confluence were exposed to CI medium (60 ng/ml COCO, daily media change) for 60 days and analyzed by confocal microscopy for 3D reconstruction, and by transmission electron microscopy. (B) Cellular sheet stained for CRX and analyzed by confocal microscopy. The boxed region is magnified to the right. (C) Cellular sheet stained for CRX, S-opsin and PNA. Scale bars: 40 µm. (D) Cellular sheet stained for connecting cilium markers (RPGR, acetylated α-tubulin and RP2). (E) Cellular sheets analyzed by transmission electron microscopy. Numbers on the transverse section reveal cells organized in a rosette-like conformation. Arrows indicate the junction between the inner (is) and outer (os) segment. m, mitochondria; z, stratum limitans junction.

Antagonism between COCO and BMP/TGFβ/Wnt activities

To address the mechanism of COCO activity, hESCs cultured under a constant concentration of FGF2, BMP4, activin A and WNT1 recombinant proteins were exposed, or not, to increasing concentrations of COCO, or of COCO+10 ng/ml IGF1, for a period of 7 days. Because SMAD2/3 proteins are stabilized through phosphorylation, we used β-actin to establish the phospho (p)-SMAD2/3 and p-SMAD1/5/8 ratio (Funaba et al., 2002). We found that phosphorylation of SMAD2/3 (a readout of BMP signaling) and of SMAD1/5/8 (a readout of TGFβ signaling) was inhibited in a dose-dependent manner by COCO, and that addition of IGF1 greatly increased COCO inhibitory activity (Fig. 7A).

p-β-catenin, which represents the β-catenin pool targeted for proteosomal degradation, was also greatly increased by the addition of COCO, while addition of IGF1 ultimately resulted in a net reduction in p-β-catenin (at 50 and 100 ng/ml COCO), which

Development (2015) 142, 3294-3306 doi:10.1242/dev.125385

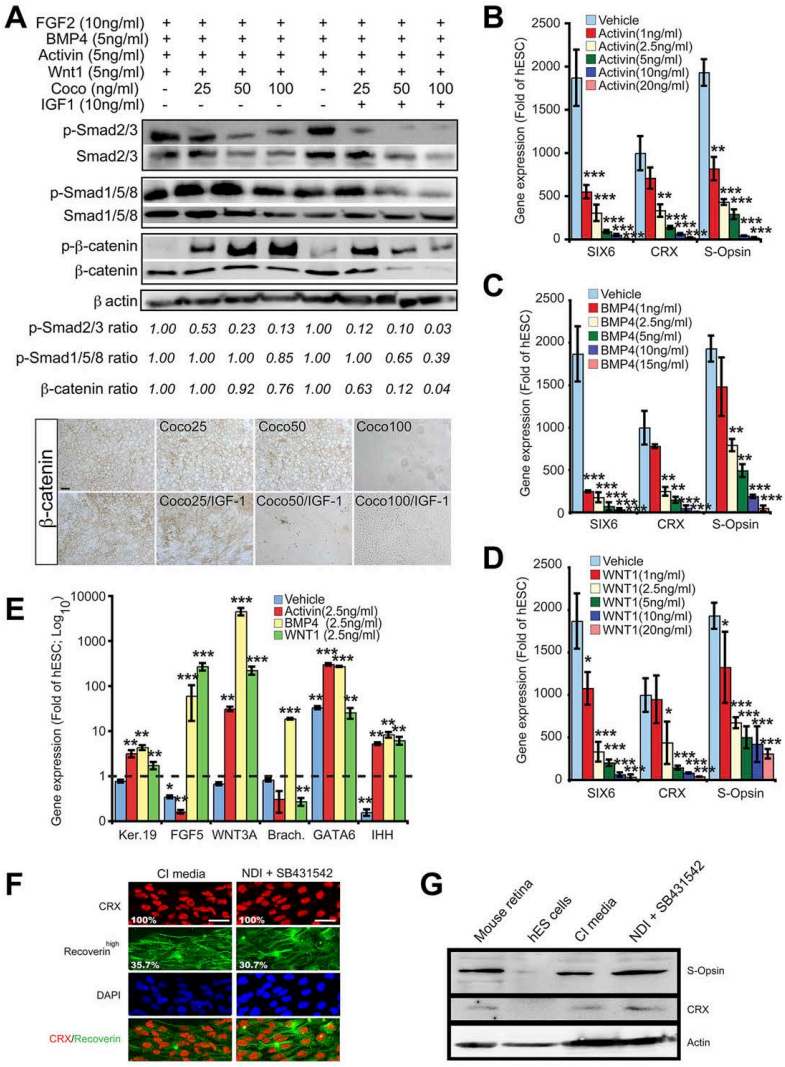

Fig. 7. COCO cooperates with IGF1 to inhibit BMP/TGFβ/Wnt activities. (A) hESCs cultured as indicated for 7 days were subjected to western blot (top) or immunohistochemistry (bottom) analyses. β-actin was used to quantify protein loading. p-SMAD2/3, p-SMAD1/5/8 or β-catenin levels are expressed as a ratio over β-actin levels. (B-D) hESCs were cultured for 21 days in CI without (vehicle, PBS) or with increasing concentrations of activin A, BMP4 or WNT1 and analyzed by qPCR. Data are expressed as fold change over gene expression in undifferentiated hESCs. Results are mean±s.d. (n=3); *P<0.05, **P<0.01, ***P<0.001 as compared with gene expression levels in vehicle-treated cells. (E) hESCs were cultured in CI for 21 days with the addition of 2.5 ng/ml activin A, BMP4 or WNT1, and then analyzed by qPCR. Data are expressed as fold change over gene expression in undifferentiated hESCs. Results are mean±s.d. (n=3); *P<0.05, **P<0.01, ***P<0.001 as compared with gene expression levels in undifferentiated cells. (F,G) hESCs cultured in CI or NDI+SB431542 (TGFβ inhibitor) for 21 days were analyzed by IF (F) or western blot (G). The percentage of positive cells is indicated (F). Scale bars: 40 µm.

is likely to reflect depletion of the β-catenin pool. Accordingly, the total level of β-catenin (a readout of Wnt signaling) progressively decreased with the addition of COCO, while β-catenin expression was nearly abolished with 50-100 ng/ml COCO+10 ng/ml IGF1 (Fig. 7A). Comparable results were also obtained by immunohistochemistry analysis (Fig. 7A, lower panel).

In converse experiments, hESCs differentiated with CI were exposed to increasing concentrations of activin A, BMP4 or WNT1

Development (2015) 142, 3294-3306 doi:10.1242/dev.125385

for 3 weeks. We observed that even 1 ng/ml BMP4, activin A or WNT1 was sufficient to inhibit CI retinal-inducing activity and that this effect was dose dependent (Fig. 7B-D). Accordingly, adding a fixed concentration (2.5 ng/ml) of activin A, BMP4 or WNT1 to CI-treated cells induced differentiation of hESCs toward the epidermal (*FGF5* and *KRT19*) and mesendodermal [*WNT3A*, brachyury (*T*), *GATA6* and *IHH*] cell lineages (Fig. 7E). Conversely, hESCs exposed to NDI+TGFβ inhibitor (SB431542) could differentiate as efficiently into S-cones as those exposed to CI when analyzed for CRX, recoverin and S-opsin expression (Fig. 7F,G).

Taken together, these results support the notion that COCO can promote neural and retinal cell fate from hESCs by simultaneous inhibition of BMP/TGFβ/Wnt signaling, and are consistent with the previously described inhibitory function of COCO on these pathways (Bell et al., 2003). They also suggest that IGF1 can greatly enhance the inhibitory activity of COCO on BMP/TGFβ/Wnt signaling.

DISCUSSION

We report on the rapid and efficient differentiation of hESCs into cone photoreceptors. ESCs were cultured under chemically defined, feeder-free conditions, and cell differentiation was induced under serum-free culture conditions without preselection procedures. Although COCO (+FGF2) displayed robust neuronal and retinal inducing activity, S-cone photoreceptor cell fate was induced to unprecedented levels when COCO was used in combination with IGF1. Differentiated cells expressed cone-specific genes and key proteins involved in phototransduction. After 35 days, *in vitro* generated cells were similar in morphology to week 15 human embryonic cones and could degrade cGMP when exposed to light. Bypassing the EB induction step also allowed manipulation of S- and M-cone cell fate by the addition of T3. After 60 days, *in vitro* generated cells self-organized into a cellular sheet with polarized cone photoreceptors and showing evidence of connecting cilium and outer segment formation.

In the developing mouse retina, photoreceptor development apparently follows an S-cone default pathway that is determined by Crx and Thrβ2; Crx induces the expression of S-opsin by default, whereas Thrβ2 suppresses it and instead induces the expression of M-opsin (Ng et al., 2001; Swaroop et al., 2010; Yanagi et al., 2002). Likewise, both Nrl and Notch1 inhibit cone formation to promote genesis of other retinal cell types (Jadhav et al., 2006; Mears et al., 2001; Yaron et al., 2006). We found here that most retinal progenitors derived from hESCs become S-cones upon exposure to COCO, FGF2 and IGF1. Notably, using a simplified neural induction protocol, M-cone genesis could also be induced by adding T3. During this process, 9-cis RA is, in principle, required to activate RA receptor γ (Rarγ), which cooperates with Thrβ2 to repress S-opsin expression (Roberts et al., 2006; Swaroop et al., 2010). Although we did not add RA to our cultures, the precursor of RA synthesis, retinyl acetate, is present in the B27 supplement.

We showed that antagonism between COCO and BMP4, Activin and WNT1 activities is required to allow hESC differentiation into retinal and photoreceptor cells. More surprisingly, we found that COCO (+FGF2) was sufficient to promote hESC differentiation into retinal and photoreceptor progenitors, with comparable efficiency to NCDI. This is notable because noggin and Dkk1 are unable to induce retinal cell fate from hESCs in the absence of IGF1 (Lamba et al., 2006). One explanation is that COCO, in contrast to noggin and Dkk1, is also able to block TGFβ signaling. Hence, pharmaceutical inhibition of TGFβ in combination with NDI provided comparable efficiency to CI (Fig. 7). Likewise, the relatively low efficiency of Dkk1 and LEFTY at inducing hESC differentiation into photoreceptors might be explained by the inability of LEFTY to block Activin signaling (Schier, 2009), combined with the absence of BMP inhibition (Osakada et al., 2008). This raises the possibility that Wnt, BMP and TGFβ/Nodal/Activin signaling also exert cone-inhibitory activities during normal retinal development. Accordingly, in the $Nrl^{-/-}$ mouse retina, which is composed of an excessively large number of cones, the *Bmp4*, *Smad4* and Wnt/Ca^{2+} signaling pathway genes are downregulated, and Nrl was found to directly activate these genes in order to promote rods genesis at the expense of cones (Yu et al., 2004). Finally, both Wnt and Activin can promote rod genesis (Davis et al., 2000).

These findings suggest a working model whereby inhibition of Wnt, BMP and TGFβ/Nodal/Activin is required to allow cone genesis at the expense of rods (and possibly of other retinal cell types), and suggest that S-cones are generated by default if all inhibitory factors are blocked. Our data also support the possibility that retinal cell fate can be actively promoted, as evidenced by the improved differentiation of hESCs into S-cones when IGF1 was used in combination with COCO. Likewise, although early neural induction efficiency was similar when using either COCO+IGF1 or COCO+FGF2, anterior neural and retinal induction was more efficient with IGF1. However, the mechanism by which IGF1 operates in this context is still unclear. IGF1 retinal fate-promoting activity may in part be through inhibition of Smad signaling (Pera et al., 2001). Indeed, we observed robust cooperation between COCO and IGF1 in blocking SMAD2/3 and SMAD1/5/8 phosphorylation, as well as in reducing β-catenin stabilization.

In eye diseases in which cones are severely affected, such as macular degenerations, cone dystrophies and cone-rod dystrophies, differentiation of hESCs into cones is of particular interest for cell therapy by transplantation (Michaelides et al., 2006). Although most forms of retinitis pigmentosa primarily affect rods, the disease is followed by loss of cones, possibly because of a reduction in the trophic support normally provided by rods to cones and/or increased metabolic stress (Mohand-Said et al., 2000; Punzo et al., 2009). Thus, the efficiency of cell replacement therapy to treat retinitis pigmentosa may also depend on our capacity to generate rods and cones. Using scanning electron microscopy, we observed that cells differentiated for 35 days developed a protruding inner segment and displayed morphological similarities to week 15 human embryonic cones. Prolonging the cell culture time to 60 days resulted in the formation of a cellular sheet composed of polarized cones with evidence of connecting cilium and outer segment formation. Self-organization of hESCs into a cone tissue sheet is reminiscent of the self-formation of hESCs into an optic cup (Nakano et al., 2012). Human cone tissue sheets may be used as a retinal patch for the treatment of macular degenerations, as shown for mouse retinal sheets transplanted into a retinitis pigmentosa mouse model (Assawachananont et al., 2014).

In conclusion, the availability of a highly enriched human cone photoreceptor population opens new avenues to study cone biochemistry and developmental genetics. Using induced pluripotent stem cell technology, it will also be possible to generate cones from cone-affected disease patients in order to study the disease mechanism and perform drug-screening assays (Jin et al., 2011).

MATERIALS AND METHODS

Ethics statement

The Animal Care Committee of the Maisonneuve-Rosemont Hospital Research Centre approved the use of the animals in this study. Post-mortem

Development (2015) 142, 3294-3306 doi:10.1242/dev.125385

human eyes (see the supplementary Materials and Methods) were provided by the Banque d'yeux du Québec du Centre Michel-Mathieu and were used with approbation of the Comité d'Éthique à la Recherche de l'Hôpital Maisonneuve-Rosemont. hESCs were used in accordance with Canadian Institute Health Research (CIHR) guidelines and approved by the Comité de Surveillance de la Recherche sur les Cellules Souches (CSRCS) of the CIHR.

Cell cultures

The hESC line H9 (WiCell) was cultured on a Matrigel-coated plate (BD Biosciences) with a daily change of mTeSR medium according to the manufacturer's instruction (Stemcell Technologies) (Thomson et al., 1998). The H9 hESC line was first established on mouse embryonic fibroblasts (MEFs) and then cultured on Matrigel in mTeSR medium. Undifferentiated hESC colonies were treated with dispase and induced to form EBs in ultra-low attachment plates (VWR) in neural induction medium, which consists of the NDI mix [DMEM-F12 medium (Invitrogen) containing 10% KnockOut serum, 2% B27, 1 ng/ml noggin, 1 ng/ml Dkk1 and 5 ng/ml IGF1], essentially as described (Lamba et al., 2006). Otherwise, cells were cultured in NCDI mix (NDI supplemented with 10 ng/ml COCO) using COCO alone or together with 10 ng/ml IGF1. EBs were plated 3 days later into Matrigel- or laminin-coated plates and cultured in DMEM-F12 medium supplemented with 2% B27, 1% N2, 10 ng/ml noggin, 10 ng/ml Dkk1, 10 ng/ml IGF1, 10 ng/ml COCO and 5 ng/ml FGF2 for an additional 4 weeks. The media were changed every 2 days. Unless otherwise stated, COCO was used at 30 ng/ml in CI media. Recombinant proteins were purchased from R&D Systems.

Western blot

Total protein extracts were prepared in the Complete Mini Protease Inhibitor Cocktail solution (Roche Diagnostics) and sonicated. Protein content was quantified using the Bradford reagent. Proteins in Laemmli buffer were resolved by SDS-PAGE and transferred to a nitrocellulose blotting membrane (Pall). Membranes were blocked for 1 h in 5% non-fat milk in 1×TBS containing 0.05% Tween 20 and incubated overnight with primary antibodies: mouse anti-CRX (1:1000; Genetex, GTX91782), rabbit anti-S-opsin (1:1000; Abcam, ab81017), mouse anti-rhodopsin (4D2) (1:50, provided by the Robert S. Molday Laboratory, University of British Columbia, Canada), rabbit anti-M-opsin (1:500; Chemicon, AB5405), rabbit anti-Smad1/5/8 (1:250; Santa Cruz, sc-6031-R), rabbit anti-p-Smad1/5/8 (1:250; #9516), rabbit anti-Smad2/3 (1:300; #8685), rabbit anti-p-Smad2/3 (1:300; #8828), rabbit anti-β-catenin (1:300; #8480), rabbit anti-p-β-catenin (1:300; #4176) (all from Cell Signaling), and mouse anti-β-actin (1:1000; Abcam, ab8226). Membranes were treated with the appropriate horseradish peroxidase-conjugated secondary antibodies (anti-rabbit, 1:15,000, A9169; anti-mouse, 1:10,000, A8924; Sigma) and developed using Immobilon western reagents (Millipore).

Immunohistochemistry

Fixed/permeabilized cells were incubated with primary antibodies overnight at 4°C, and analyzed using the Vectastain ABC Kit (Vector Laboratories); DAB (Sigma) was used as the peroxidase substrate. For grafting analyses, eye sections were incubated overnight with primary antibody solutions at 4°C, washed and incubated with Rhodamine-conjugated and FITC-conjugated secondary antibodies for 1 h at room temperature. Slides were mounted on coverslips in DAPI-containing mounting medium (Vector Laboratories). Observations were made under a Leica DMRE fluorescence microscope with a Retiga EX digital camera. For further details of sample preparation and the antibodies used, see the supplementary Materials and Methods.

In situ hybridization

For *in situ* hybridizations on slices, tissues were dissected in PBS, embedded in CRYOMATRIX embedding medium (Thermo Shandon), snap frozen in liquid nitrogen and sections (8 µm) were cut and dried onto Superfrost glass slides (Fisher Scientific). For *in situ* hybridizations on whole embryos, embryos were dissected in PBS, then fixed overnight in 4% paraformaldehyde at 4°C. Whole embryos and slices were hybridized with digoxigenin-labeled RNA probes [*Dand5* (*Coco*), accession #BC115659] and revealed with alkaline phosphatase-coupled anti-digoxigenin antibody (1:2000; Roche, 11093274910) and NBT/BCIP substrate (Boehringer) at pH 9.5.

RT-PCR

Total RNA (1 µg) was reverse transcribed with M-MLV reverse transcriptase (Invitrogen) and used in quantitative real-time PCR (qPCR) using Platinum SYBR Green SuperMix (Invitrogen) and an ABI Prism 7000 apparatus, with *GAPDH* as an internal standard. Experiments were performed at least in triplicate. For further details and primer sequences, see the supplementary Materials and Methods.

Phototransduction analysis

Phototransduction activity was assessed by measuring the light-induced hydrolysis of cyclic (c) GMP with an enzyme immunoassay kit (Biotrack EIA system) according to the manufacturer's instructions (Amersham Bioscience GE Healthcare). Undifferentiated H9 hESCs and cells cultured in NDI, COCO and IGF1 were kept in the dark or exposed to ambient light. The PDE inhibitor IBMX (3-isobutyl-1-methylxanthine, Sigma) was added (1 mM) 72 h before determination of cGMP levels.

Fluorescence-activated cell sorting

For cell membrane epitope staining, dispase-dissociated cells were stained with Rhodamine-coupled PNA (1:500; Vector Laboratories, RL-1072). Cells were then fixed/permeabilized with the CytoFix/Cytoperm Kit according to the manufacturer's instructions (BD Biosciences). Cells were incubated with rabbit anti-S-opsin antibody (1:2000; Chemicon, A5407) or Alexa-conjugated isotypic control goat anti-rabbit IgG antibody (1:500; Molecular Probes, A-11037). The primary antibody was visualized using FITC-conjugated goat anti-rabbit serum (1:500; Chemicon, AP124F). Sorting employed a FACSVantage flow cytometer (Becton-Dickinson) at a flow rate of less than 3000 cells/s. Dead cells and cell debris were excluded from acquisition by gating with FCS and SSC biparametric plot. After sorting, an aliquot of sorted cells was always reanalyzed to check for purity, which was usually greater than 95%.

Cell transplantation

Cell clamps (1 µl) containing ~10,000 cells were injected into the vitreous of anesthetized neonatal (P1) mice as described in the supplementary Materials and Methods.

Statistical analysis

Statistical differences were analyzed using Student's *t*-test for unpaired samples. An analysis of variance (ANOVA) followed by the Dunnett test was used for multiple comparisons with one control group. *P*-values are given in the figure legends.

Acknowledgements

We are grateful to D. Melton and the Harvard Stem Cell Institute for the HUES1, HUES8 and HUES9 cell lines, and to M. Nelea and S. Breault for technical assistance with electron microscopy.

Competing interests

The authors declare no competing or financial interests.

Author contributions

Conceived and designed the study and wrote the paper: G.B. Performed the experiments: S.Z., A.F., M.A., N.T., A.B., S.W. Analyzed the data: G.B., S.Z., A.F., M.A.

Funding

This work was supported by grants from the Foundation Fighting Blindness Canada, Turmel Family Foundation for Macular Degeneration Research, Canadian Stem Cell Network, C. Durand Foundation, the GO Foundation, and Natural Science and Engineering Research Council of Canada [grant #250970-2012]. A.F. was supported by fellowships from the Réseau Vision du Québec and from University of Montreal Molecular Biology Program. G.B. was supported by the Fonds de Recherche en Santé du Québec.

Supplementary material

Supplementary material available online at
http://dev.biologists.org/lookup/suppl/doi:10.1242/dev.125385/-/DC1

References

Allikmets, R., Singh, N., Sun, H., Shroyer, N. F., Hutchinson, A., Chidambaram, A., Gerrard, B., Baird, L., Stauffer, D., Peiffer, A. et al. (1997). A photoreceptor cell-specific ATP-binding transporter gene (ABCR) is mutated in recessive Stargardt macular dystrophy. *Nat. Genet.* **15**, 236-246.

Assawachananont, J., Mandai, M., Okamoto, S., Yamada, C., Eiraku, M., Yonemura, S., Sasai, Y. and Takahashi, M. (2014). Transplantation of embryonic and induced pluripotent stem cell-derived 3D retinal sheets into retinal degenerative mice. *Stem Cell Rep.* **2**, 662-674.

Banin, E., Obolensky, A., Idelson, M., Hemo, I., Reinhardtz, E., Pikarsky, E., Ben-Hur, T. and Reubinoff, B. (2006). Retinal incorporation and differentiation of neural precursors derived from human embryonic stem cells. *Stem Cells* **24**, 246-257.

Bell, E., Muñoz-Sanjuán, I., Altmann, C. R., Vonica, A. and Brivanlou, A. H. (2003). Cell fate specification and competence by Coco, a maternal BMP, TGFbeta and Wnt inhibitor. *Development* **130**, 1381-1389.

Blanks, J. C. and Johnson, L. V. (1983). Selective lectin binding of the developing mouse retina. *J. Comp. Neurol.* **221**, 31-41.

Bouwmeester, T., Kim, S.-H., Sasai, Y., Lu, B. and De Robertis, E. M. (1996). Cerberus is a head-inducing secreted factor expressed in the anterior endoderm of Spemann's organizer. *Nature* **382**, 595-601.

Burmeister, M., Novak, J., Liang, M.-Y., Basu, S., Ploder, L., Hawes, N. L., Vidgen, D., Hoover, F., Goldman, D., Kalnins, V. I. et al. (1996). Ocular retardation mouse caused by Chx10 homeobox null allele: impaired retinal progenitor proliferation and bipolar cell differentiation. *Nat. Genet.* **12**, 376-384.

Chambers, S. M., Fasano, C. A., Papapetrou, E. P., Tomishima, M., Sadelain, M. and Studer, L. (2009). Highly efficient neural conversion of human ES and iPS cells by dual inhibition of SMAD signaling. *Nat. Biotechnol.* **27**, 275-280.

Chatoo, W., Abdouh, M., Duparc, R.-H. and Bernier, G. (2010). Bmi1 distinguishes immature retinal progenitor/stem cells from the main progenitor cell population and is required for normal retinal development. *Stem Cells* **28**, 1412-1423.

Chen, S., Wang, Q.-L., Nie, Z., Sun, H., Lennon, G., Copeland, N. G., Gilbert, D. J., Jenkins, N. A. and Zack, D. J. (1997). Crx, a novel Otx-like paired-homeodomain protein, binds to and transactivates photoreceptor cell-specific genes. *Neuron* **19**, 1017-1030.

Corbo, J. C., Myers, C. A., Lawrence, K. A., Jadhav, A. P. and Cepko, C. L. (2007). A typology of photoreceptor gene expression patterns in the mouse. *Proc. Natl. Acad. Sci. USA* **104**, 12069-12074.

Couly, G. and Le Douarin, N. M. (1988). The fate map of the cephalic neural primordium at the presomitic to the 3-somite stage in the avian embryo. *Development* **103**, 101-113.

Davis, A. A., Matzuk, M. M. and Reh, T. A. (2000). Activin A promotes progenitor differentiation into photoreceptors in rodent retina. *Mol. Cell. Neurosci.* **15**, 11-21.

Ellis, P., Fagan, B. M., Magness, S. T., Hutton, S., Taranova, O., Hayashi, S., McMahon, A., Rao, M. and Pevny, L. (2004). SOX2, a persistent marker for multipotential neural stem cells derived from embryonic stem cells, the embryo or the adult. *Dev. Neurosci.* **26**, 148-165.

Ferda Percin, E., Ploder, L. A., Yu, J. J., Arici, K., Horsford, D. J., Rutherford, A., Bapat, B., Cox, D. W., Duncan, A. M. V., Kalnins, V. I. et al. (2000). Human microphthalmia associated with mutations in the retinal homeobox gene CHX10. *Nat. Genet.* **25**, 397-401.

Freund, C. L., Gregory-Evans, C. Y., Furukawa, T., Papaioannou, M., Looser, J., Ploder, L., Bellingham, J., Ng, D., Herbrick, J.-A. S., Duncan, A. et al. (1997). Cone-rod dystrophy due to mutations in a novel photoreceptor-specific homeobox gene (CRX) essential for maintenance of the photoreceptor. *Cell* **91**, 543-553.

Funaba, M., Zimmerman, C. M. and Mathews, L. S. (2002). Modulation of Smad2-mediated signaling by extracellular signal-regulated kinase. *J. Biol. Chem.* **277**, 41361-41368.

Furukawa, T., Morrow, E. M. and Cepko, C. L. (1997). Crx, a novel otx-like homeobox gene, shows photoreceptor-specific expression and regulates photoreceptor differentiation. *Cell* **91**, 531-541.

Gallardo, M. E., Lopez-Rios, J., Fernaud-Espinosa, I., Granadino, B., Sanz, R., Ramos, C., Ayuso, C., Seller, M. J., Brunner, H. G., Bovolenta, P. et al. (1999). Genomic cloning and characterization of the human homeobox gene SIX6 reveals a cluster of SIX genes in chromosome 14 and associates SIX6 hemizygosity with bilateral anophthalmia and pituitary anomalies. *Genomics* **61**, 82-91.

Ghosh, A. K., Murga-Zamalloa, C. A., Chan, L., Hitchcock, P. F., Swaroop, A. and Khanna, H. (2010). Human retinopathy-associated ciliary protein retinitis pigmentosa GTPase regulator mediates cilia-dependent vertebrate development. *Hum. Mol. Genet.* **19**, 90-98.

Graham, V., Khudyakov, J., Ellis, P. and Pevny, L. (2003). Sox2 functions to maintain neural progenitor identity. *Neuron* **39**, 749-765.

Hurd, T., Zhou, W., Jenkins, P., Liu, C.-J., Swaroop, A., Khanna, H., Martens, J., Hildebrandt, F. and Margolis, B. (2010). The retinitis pigmentosa protein RP2 interacts with polycystin 2 and regulates cilia-mediated vertebrate development. *Hum. Mol. Genet.* **19**, 4330-4344.

Idelson, M., Alper, R., Obolensky, A., Ben-Shushan, E., Hemo, I., Yachimovich-Cohen, N., Khaner, H., Smith, Y., Wiser, O., Gropp, M. et al. (2009). Directed differentiation of human embryonic stem cells into functional retinal pigment epithelium cells. *Cell Stem Cell* **5**, 396-408.

Jadhav, A. P., Mason, H. A. and Cepko, C. L. (2006). Notch 1 inhibits photoreceptor production in the developing mammalian retina. *Development* **133**, 913-923.

Jean, D., Bernier, G. and Gruss, P. (1999). Six6 (Optx2) is a novel murine Six3-related homeobox gene that demarcates the presumptive pituitary/hypothalamic axis and the ventral optic stalk. *Mech. Dev.* **84**, 31-40.

Jin, Z.-B., Okamoto, S., Osakada, F., Homma, K., Assawachananont, J., Hirami, Y., Iwata, T. and Takahashi, M. (2011). Modeling retinal degeneration using patient-specific induced pluripotent stem cells. *PLoS ONE* **6**, e17084.

Jomary, C. and Jones, S. E. (2008). Induction of functional photoreceptor phenotype by exogenous Crx expression in mouse retinal stem cells. *Invest. Ophthalmol. Vis. Sci.* **49**, 429-437.

Lamba, D. A., Karl, M. O., Ware, C. B. and Reh, T. A. (2006). Efficient generation of retinal progenitor cells from human embryonic stem cells. *Proc. Natl. Acad. Sci. USA* **103**, 12769-12774.

Lamba, D. A., Gust, J. and Reh, T. A. (2009). Transplantation of human embryonic stem cell-derived photoreceptors restores some visual function in Crx-deficient mice. *Cell Stem Cell* **4**, 73-79.

Liu, W., Lagutin, O., Swindell, E., Jamrich, M. and Oliver, G. (2010). Neuroretina specification in mouse embryos requires Six3-mediated suppression of Wnt8b in the anterior neural plate. *J. Clin. Invest.* **120**, 3568-3577.

Livne-Bar, I., Pacal, M., Cheung, M. C., Hankin, M., Trogadis, J., Chen, D., Dorval, K. M. and Bremner, R. (2006). Chx10 is required to block photoreceptor differentiation but is dispensable for progenitor proliferation in the postnatal retina. *Proc. Natl. Acad. Sci. USA* **103**, 4988-4993.

Mathers, P. H., Grinberg, A., Mahon, K. A. and Jamrich, M. (1997). The Rx homeobox gene is essential for vertebrate eye development. *Nature* **387**, 603-607.

Mears, A. J., Kondo, M., Swain, K. S., Takada, Y., Bush, R. A., Saunders, T. L., Sieving, P. A. and Swaroop, A. (2001). Nrl is required for rod photoreceptor development. *Nat. Genet.* **29**, 447-452.

Mellough, C. B., Collin, J., Khazim, M., White, K., Sernagor, E., Steel, D. H. and Lako, M. (2015). IGF-1 signaling plays an important role in the formation of three-dimensional laminated neural retina and other ocular structures from human embryonic stem cells. *Stem Cells* **33**, 2416-2430.

Michaelides, M., Hardcastle, A. J., Hunt, D. M. and Moore, A. T. (2006). Progressive cone and cone-rod dystrophies: phenotypes and underlying molecular genetic basis. *Surv. Ophthalmol.* **51**, 232-258.

Mohand-Said, S., Hicks, D., Dreyfus, H. and Sahel, J. A. (2000). Selective transplantation of rods delays cone loss in a retinitis pigmentosa model. *Arch. Ophthalmol.* **118**, 807-811.

Molday, L. L., Rabin, A. R. and Molday, R. S. (2000). ABCR expression in foveal cone photoreceptors and its role in stargardt macular dystrophy. *Am. J. Ophthalmol.* **130**, 689.

Muñoz-Sanjuán, I. and Brivanlou, A. H. (2002). Neural induction, the default model and embryonic stem cells. *Nat. Rev. Neurosci.* **3**, 271-280.

Nakano, T., Ando, S., Takata, N., Kawada, M., Muguruma, K., Sekiguchi, K., Saito, K., Yonemura, S., Eiraku, M. and Sasai, Y. (2012). Self-formation of optic cups and storable stratified neural retina from human ESCs. *Cell Stem Cell* **10**, 771-785.

Narayanan, K. and Wadhwa, S. (1998). Photoreceptor morphogenesis in the human retina: a scanning electron microscopic study. *Anat. Rec.* **252**, 133-139.

Ng, L., Hurley, J. B., Dierks, B., Srinivas, M., Saltó, C., Vennström, B., Reh, T. A. and Forrest, D. (2001). A thyroid hormone receptor that is required for the development of green cone photoreceptors. *Nat. Genet.* **27**, 94-98.

Ng, L., Lyubarsky, A., Nikonov, S. S., Ma, M., Srinivas, M., Kefas, B., St. Germain, D. L., Hernandez, A., Pugh, E. N., Jr and Forrest, D. (2010). Type 3 deiodinase, a thyroid-hormone-inactivating enzyme, controls survival and maturation of cone photoreceptors. *J. Neurosci.* **30**, 3347-3357.

Novarino, G., Akizu, N. and Gleeson, J. G. (2011). Modeling human disease in humans: the ciliopathies. *Cell* **147**, 70-79.

Osakada, F., Ikeda, H., Mandai, M., Wataya, T., Watanabe, K., Yoshimura, N., Akaike, A., Sasai, Y. and Takahashi, M. (2008). Toward the generation of rod and cone photoreceptors from mouse, monkey and human embryonic stem cells. *Nat. Biotechnol.* **26**, 215-224.

Pacione, L. R., Szego, M. J., Ikeda, S., Nishina, P. M. and McInnes, R. R. (2003). Progress toward understanding the genetic and biochemical mechanisms of inherited photoreceptor degenerations. *Annu. Rev. Neurosci.* **26**, 657-700.

Pera, E. M., Wessely, O., Li, S.-Y. and De Robertis, E. M. (2001). Neural and head induction by insulin-like growth factor signals. *Dev. Cell* **1**, 655-665.

Piccolo, S., Agius, E., Leyns, L., Bhattacharyya, S., Grunz, H., Bouwmeester, T. and De Robertis, E. M. (1999). The head inducer Cerberus is a multifunctional antagonist of Nodal, BMP and Wnt signals. *Nature* **397**, 707-710.

Punzo, C., Kornacker, K. and Cepko, C. L. (2009). Stimulation of the insulin/mTOR pathway delays cone death in a mouse model of retinitis pigmentosa. *Nat. Neurosci.* **12**, 44-52.
Rachel, R. A., Li, T. and Swaroop, A. (2012). Photoreceptor sensory cilia and ciliopathies: focus on CEP290, RPGR and their interacting proteins. *Cilia* **1**, 22.
Reubinoff, B. E., Pera, M. F., Fong, C. Y., Trounson, A. and Bongso, A. (2000). Embryonic stem cell lines from human blastocysts: somatic differentiation in vitro. *Nat. Biotechnol.* **18**, 399-404.
Roberts, M. R., Srinivas, M., Forrest, D., Morreale de Escobar, G. and Reh, T. A. (2006). Making the gradient: thyroid hormone regulates cone opsin expression in the developing mouse retina. *Proc. Natl. Acad. Sci. USA* **103**, 6218-6223.
Rorick, A. M., Mei, W., Liette, N. L., Phiel, C., El-Hodiri, H. M. and Yang, J. (2006). PP2A:B56epsilon is required for eye induction and eye field separation. *Dev. Biol.* **302**, 477-493.
Schier, A. F. (2009). Nodal morphogens. *Cold Spring Harb. Perspect. Biol.* **1**, a003459.
Swaroop, A., Kim, D. and Forrest, D. (2010). Transcriptional regulation of photoreceptor development and homeostasis in the mammalian retina. *Nat. Rev. Neurosci.* **11**, 563-576.
Taranova, O. V., Magness, S. T., Fagan, B. M., Wu, Y., Surzenko, N., Hutton, S. R. and Pevny, L. H. (2006). SOX2 is a dose-dependent regulator of retinal neural progenitor competence. *Genes Dev.* **20**, 1187-1202.
Thomson, J. A., Itskovitz-Eldor, J., Shapiro, S. S., Waknitz, M. A., Swiergiel, J. J., Marshall, V. S. and Jones, J. M. (1998). Embryonic stem cell lines derived from human blastocysts. *Science* **282**, 1145-1147.
Tropepe, V., Hitoshi, S., Sirard, C., Mak, T. W., Rossant, J. and van der Kooy, D. (2001). Direct neural fate specification from embryonic stem cells: a primitive mammalian neural stem cell stage acquired through a default mechanism. *Neuron* **30**, 65-78.
Tucker, B. A., Mullins, R. F., Streb, L. M., Anfinson, K., Eyestone, M. E., Kaalberg, E., Riker, M. J., Drack, A. V., Braun, T. A. and Stone, E. M. (2013). Patient-specific iPSC-derived photoreceptor precursor cells as a means to investigate retinitis pigmentosa. *Elife* **2**, e00824.
Walther, C. and Gruss, P. (1991). Pax-6, a murine paired box gene, is expressed in the developing CNS. *Development* **113**, 1435-1449.
Yanagi, Y., Takezawa, S. and Kato, S. (2002). Distinct functions of photoreceptor cell-specific nuclear receptor, thyroid hormone receptor beta2 and CRX in one photoreceptor development. *Invest. Ophthalmol. Vis. Sci.* **43**, 3489-3494.
Yaron, O., Farhy, C., Marquardt, T., Applebury, M. and Ashery-Padan, R. (2006). Notch1 functions to suppress cone-photoreceptor fate specification in the developing mouse retina. *Development* **133**, 1367-1378.
Yu, J., He, S., Friedman, J. S., Akimoto, M., Ghosh, D., Mears, A. J., Hicks, D. and Swaroop, A. (2004). Altered expression of genes of the Bmp/Smad and Wnt/calcium signaling pathways in the cone-only Nrl-/- mouse retina, revealed by gene profiling using custom cDNA microarrays. *J. Biol. Chem.* **279**, 42211-42220.

SUPPLEMENTARY MATERIALS AND METHODS

Quantitative RT-PCR

All primers were designed to flank individual exons and tested by PCR in RT+ and RT- control extracts. Total RNA was isolated using TRIzol reagent (Invitrogen). Reverse transcription (RT) was performed using 1 µg of total RNA and the MML-V reverse transcriptase (Invitrogen). Quantitative real-time PCR (qPCR) was performed using the Platinum SYBRGreen SuperMix (Invitrogen) and a real-time PCR apparatus (ABI Prism 7000). GAPDH was used as an internal standard for data calibration. The 2^{-DDCt} formula was used for the calculation of differential gene expression. All experiments were performed at least in triplicates. Primers sequences are: SIX3 (F; CCCACACAAGATGGCAACTG and R; GTTACCGAGAGGATGGAGGT), SIX6 (F; CCTGCAGGATCCATACCCTA and R; ACCTGCTGCTGGAGTCTGTT), CRX (F; CCTTCTGACAGCTCGGTGTT and R; CCACTTTCTGAAGCCTGGAG), S-opsin (F; TGTGCCTCTCTCCCTCATCT and R; GGCACGTAGCAGACACAGAA), PAX6 (F; AGATTTCAGAGCCCCATATTCG and R; CCATTTGGCCCTTCGATTAG), Cone Arrestin (F; CCCAGAGCTTTGCAGTAACC and R; CACAGGACACCATCAGGTTG), M-opsin (F; GCTACACCGTCTCCCTGTGT and R; ACCTGCTCCAACCAAAGATG), Rhodopsin (F; TAAGCCCATGAGCAACTTCC and R; GCTGCCCATAGCAGAAAAAG), PdEb (F; CAGTGATGAACACCGACACC and R; ATTTGACCAGGTCCAGTTCG), Arrestin3 (F; CCCAGAGCTTTGCAGTAACC and R; CACAGGACACCATCAGGTTG), PdE6h (F; TACTCTGCCTGCTCCAGCTT and R; GAGAGTGGCAGAACCTCTGG), PdE6c (F; TTGGGAACAAGGAGATCTGG and R; GGCTCCTCCTTCTTGCTTTT), Recoverin (F; AGCTCCTTCCAGACGATGAA and R; CAAACTGGATCAGTCGCAGA), Keratin19 (F; TTTGAGACGGAACAGGCTCT and R; AATCCACCTCCACACTGACC), FGF5 (F; CTTGGAGCAGAGCAGTTTCC and R;

ACAATCCCCTGAGACACAGC), Brachyury (F; CCGTCTCCTTCAGCAAAGTC and R; CACCGCTATGAACTGGGTCT), Indian Hedgehog (IHH) (F; CCTGAACTCGCTGGCTATCT and R; CGGTCTGATGTGGTGATGTC), WNT3A (F; CAAGATTGGCATCCAGGAGT and R; ATGAGCGTGTCACTGCAAAG), GATA6 (F; GCCAACTGTCACACCACAAC and R; AGTTGGAGTCATGGGAATGG), SOX1 (F; AAAGTCAAAACGAGGCGAGA and R; AAGTGCTTGGACCTGCCTTA), FOXG1 (F; GAACGGCAAGTACGAGAAGC and R; TCACGAAGCACTTGTTGAGG), RAX (F; GGCAAGGTCAACCTACCAGA and R; GCTTCATGGAGGACACTTCC), PLZF (F; CAAGGCTGACGCTGTATTGA and R; AGTGGGATGAAGACGTACGG), and GAPDH (F; TCACCAGGGCTGCTTTTAAC and R ATCCACAGTCTTCTGGGTGG). On the other hand, for 5'- and 3'-Coco (Dand5) transcripts amplification, the primers sequences used are: 5'-transcript (F; CTGCACAGCCAAGTGATGTT and R; CACTTCTTGAGGAGCCAAGG), and 3'-transcript (F; GCAGCTGCTAGGAAAACCTG and R; TTTATGGTTCCCACGGAATG).

Immunohistochemistry

Cells were fixed/permeabilized in 4% paraformaldehyde (PFA) containing 0.01% Tween 20 at room temperature for 15 minutes, and blocked with 5% horse serum in 1xPBS/0.1 % Tween 20 at room temperature for 1 hour. Slides were incubated with the primary antibodies overnight at 4°C, and analyzed using the Vectastain® ABC kit (Vector Laboratories, CA) according to the manufacturer instructions. DAB (Sigma) was used as the peroxidase substrate. For grafting analyses, eyes were immersed for 1 h at room temperature in 4% PFA/3% sucrose in 0.1 M phosphate buffer, pH 7.4. Samples were washed three times in PBS, cryoprotected in PBS/30% sucrose, and frozen in CRYOMATRIX embedding medium (CEM) (Thermo Shandon, Pittsburgh, PA). 7 µm thick sections were mounted on Super-Frost

glass slides (Fisher Scientific) and processed for immunofluorescence. Sections were incubated overnight with primary antibody solutions at 4ºC in a humidified chamber. After three washes in PBS, sections were incubated with secondary antibodies for 1 h at room temperature. Slides were mounted on coverslips in DAPI-containing mounting medium (Vector). Observations were made under a fluorescence microscope (Leica DMRE, Leica Microsystems) and images were captured with a digital camera (Retiga EX; QIMAGING; with OpenLab, ver.3.1.1 software; Open-Lab, Canada). Antibodies used in this study were: mouse anti-CRX (1:250; Genetex), mouse anti-S-opsin (1:500; Chemicon) and mouse anti-ABCA4 (1:25; SantaCruz Biotech.). For immunofluorescence, the secondary antibodies used were rhodamine-conjugated donkey anti-rabbit, and FITC-conjugated donkey anti-mouse (Chemicon).

Cell transplantation

Neonatal (P1) mice were anesthetized by hypothermia. The eyelid was opened using a scalpel, and a hole was made in the cornea using a 26G needle to have access to the vitreous. Cell clamps (1µl) containing ~10 000 cells were injected using a 5 µl Hamilton syringe with a 33G needle (Hamilton Company, Reno, NV). For the immunosuppressive regimen, mothers of neonatal pups were injected with Cyclosporine A (10 mg/kg/day) from the day before surgery until tissue preparation. For each experimental condition (2, 3 and 4 weeks of hES cell differentiation using CI at 30ng/ml of Coco (n = 15); and 2 weeks of hES cell differentiation using CI at 50ng/ml of Coco (n = 5)), pups were injected on the left eye. Animals were handled in accordance with the Animal Care Committee of Maisonneuve-Rosemont Hospital.

Human eyes specimens

Retinas were dissected and fixed in 4% paraformaldehyde, then cryopreserved in 30% sucrose. Retinas were frozen until use.

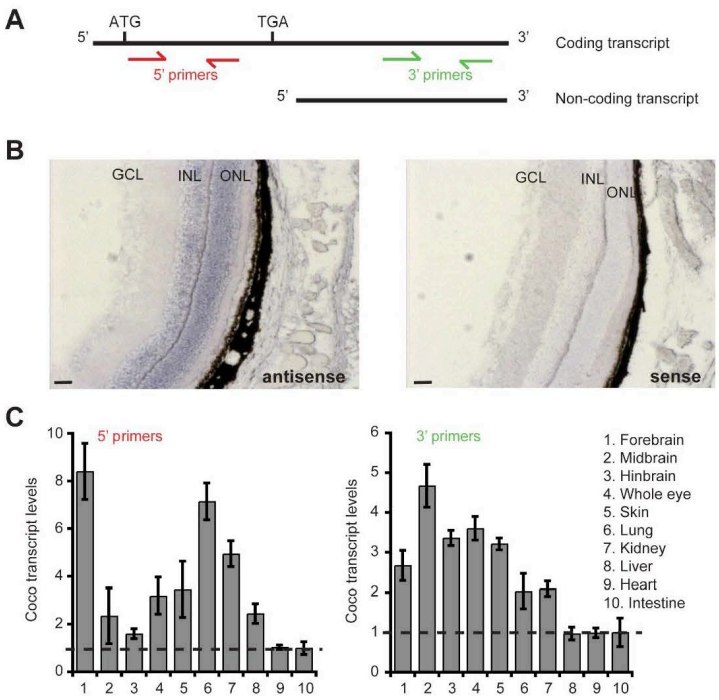

Figure S1. Coco/Cerl2 is expressed in the mouse retina

(A) Schematic representation of the coding and non-coding *Coco/Cerl2* transcripts. The PCR primers locations are highlighted, where the 5'primers (red) amplify only the coding transcript, while the 3'primers (green) amplify both transcripts. (B) *In situ* hybridization on adult mouse eye sections with antisense and sense *Coco/Cerl2* RNA probes showing robust expression of *Coco* transcripts in the photoreceptor nuclear layer (ONL; outer nuclear layer), and the inner nuclear layer (INL). *Coco* transcripts were not detected in the ganglion cell layer (GCL). (C) Post-natal day 3 mouse tissues were analyzed by qPCR for the expression of *Coco* transcripts using the 5'primers or the 3'primers. Data are expressed as fold change over gene expression in intestine, which was set at 1. Results are Mean +/- s.d. (n = 3). Scale bars: 30 µm.

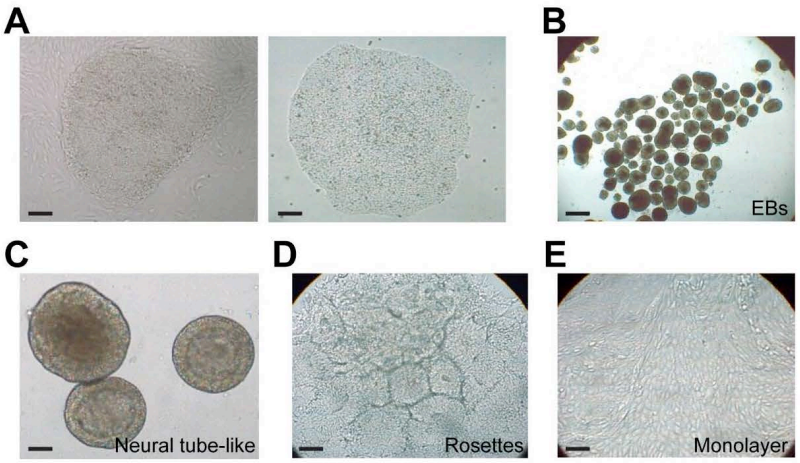

Figure S2. Stepwise neural induction of hES cells

(A) hES cultured on mouse fibroblasts feeders (left) or on matrigel (right). (B) Floating embryoid bodies (EBs). (C) EBs cultured on a matrigel surface showing neural tube-like appearance. (D) Neural rossettes. (E) Neuroepithelial monolayer. Scale bars: 50 μm (A and E), 100 μm (B and C), 200 μm (D).

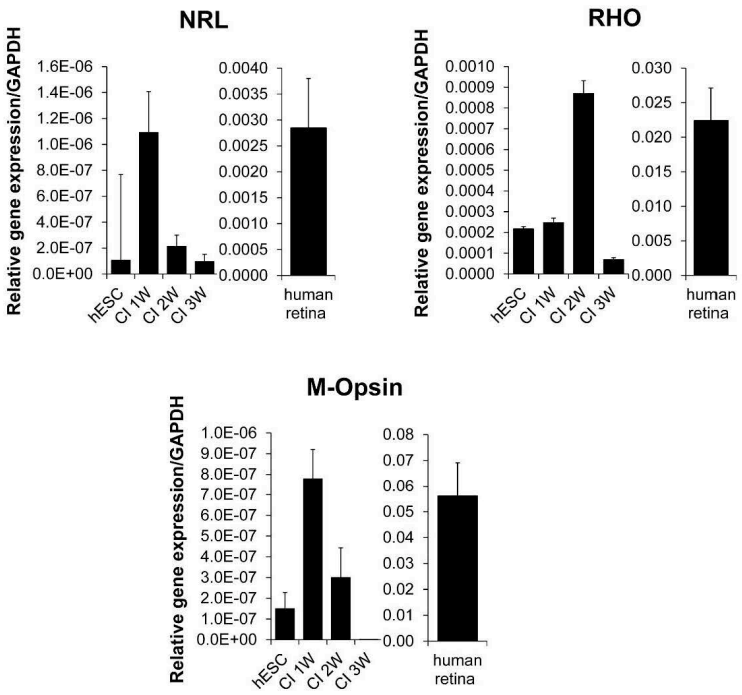

Figure S3. Analysis of rod and m-cone specific transcripts

hES cells were induced to differentiate in the presence of CI media for 1, 2 or 3 weeks and analyzed by qPCR. Data are expressed as relative gene expression over *GAPDH*. Whole human retina was used as positive control.

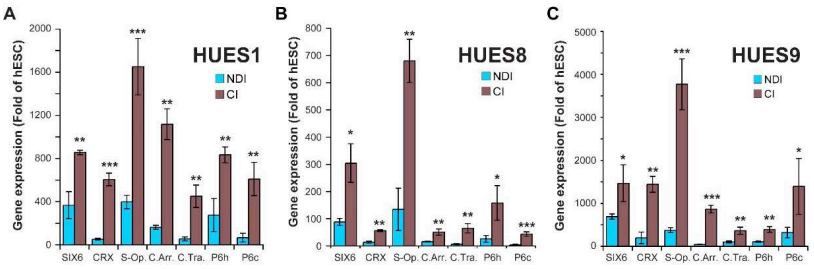

Figure S4. Expression of cone-specific transcripts across various hES cell lines

EBs derived from 3 hES cell lines (HUES1, HUES8 and HUES9) were differentiated in the presence of NDI or CI media for 3 weeks. Differentiated hES cells were analyzed by qPCR for the expression of *SIX6*, *CRX*, *S-Opsin* (*S-Op.*), *Cone Arrestin* (*C.Arr.*), *Cone transducin* (*GNAT2*), *PDE6h* (*P6h*) and *PDE6c* (*P6c*). Data are normalized over *GAPDH* and expressed as fold change of hESC. Results are Mean +/- s.d. (n = 3; *P<0.05; **P<0.01; ***P<0.001 as compared to gene expression levels in NDI-treated cells).

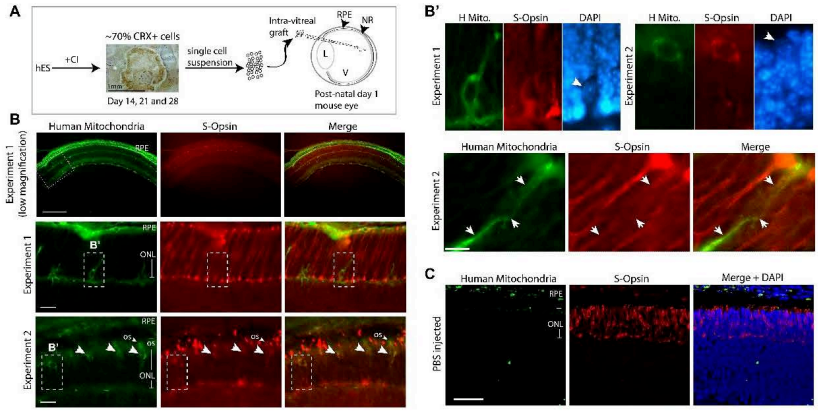

Figure S5. Differentiated hES can integrate the developing mouse retina

(A) Scheme describing the engraftment method. (B) 10 days (experiment 1) or 14 days (experiment 2) after transplantation, eye sections were labeled with anti-human mitochondria (H Mito.; green) and anti-S-Opsin (red) antibodies and mounted with DAPI (blue). Top: low magnification images from experiment 1. Percentage of grafted cells having migrated in the host retina was 1.4 +/- 0.5% in both experimental settings. Note that S-Opsin is mostly localized to the newly formed outer segment of endogenous cones in 14-day old grafted mice (experiment 2). Arrowheads point to grafted human cells that are S-Opsin positive. The smaller arrowhead in Experiment 2 indicates a human cell displaying S-Opsin immuno-reactivity in its outer segment. There may be more than a single human cell positive for S-Opsin in this particular region of the host retina. (B') The higher magnifications of cells selected in (B) revealed that double-positive cells have a larger nuclei and a unique chromatin condensation pattern (top arrowheads) when compared to that of endogenous mouse photoreceptors. They are also positive for S-Ospin. Bottom: high magnification images of engrafted cells (white arrows). (C) IF analysis of mouse eyes only injected with PBS (negative control). Scale bars: 800 µm (low magnification in B), 40 µm (higher magnification in experiments 1 and 2), 50 µm (PBS injected eyes in C). ONL: outer nuclear layer, RPE: retinal pigment epithelium, os: outer segment of photoreceptors.

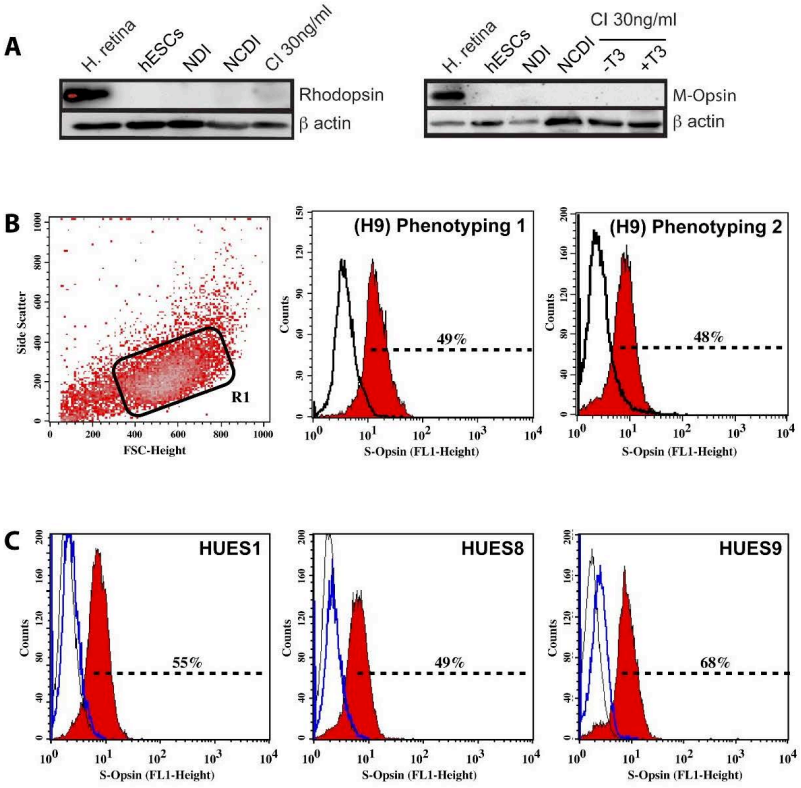

Figure S6. Generation of S-cones across various hES cell lines

(A) hES cell-derived EBs cultured in the NDI, NCDI, or CI media for 3 weeks were subjected to Western blot analysis for the expression of Rhodopsin. hES cell-derived EBs cultured in the presence or absence of thyroid hormone (T3; 4.8 nM) were subjected to Western blot analysis for the expression of M-Opsin. β actin was used for the quantification of protein loading. Human retinas were used as a positive control. (B-C) In the Side Scatter/Forward Scatter biparametric diagram, the R1 gate delineates the cell population analyzed. We analyzed by FACS using an anti-S-Opsin antibody either naive hES cells (blue line) or hES cells cultured in CI media for 3 weeks (red line). The isotypic control serum is represented by the black line. These uniparametric panels show data obtained with 4 different hES cell lines.

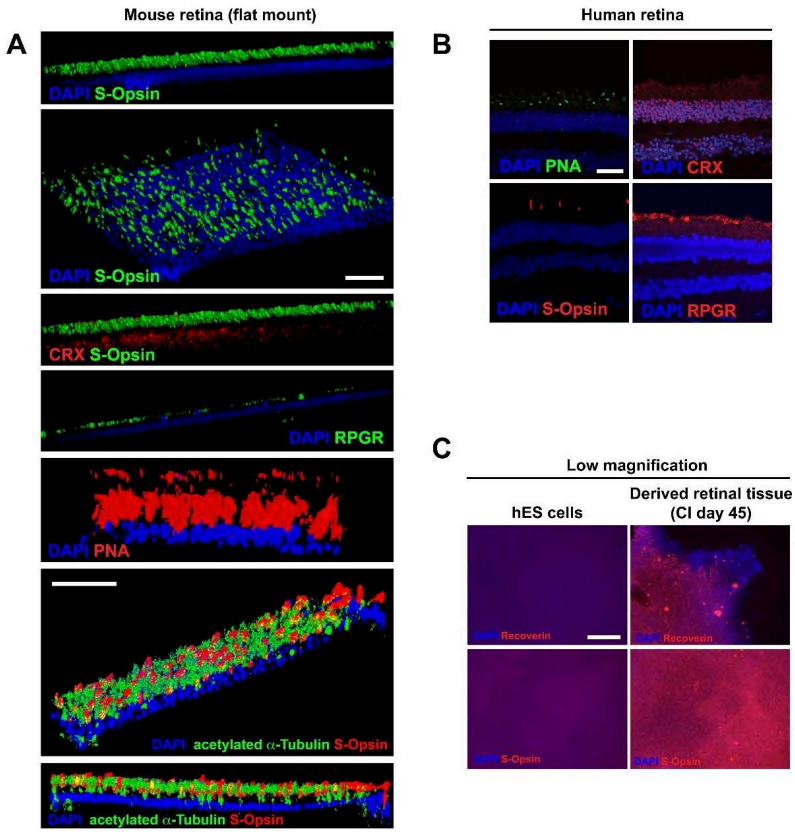

Figure S7. Antibodies specificity validated on mouse and human retinas

(A) Immunofluorescence on whole mount P17 mouse retina for photoreceptor markers (CRX, S-Opsin and PNA) and connecting cilium markers (RPGR and acetylated α-Tubulin). Tissues were reconstructed in 3D using confocal microscopy. (B) Immunofluorescence on adult human retina for the photoreceptor markers CRX, S-Opsin and PNA, and the connecting cilium marker RPGR using confocal microscopy. (C) Immunofluorescence on undifferentiated hES cells and cellular sheet obtained after 45 days with the CI media (10X magnification). Scale bars: 40µm (3D images) and 400µm (low magnification in C).

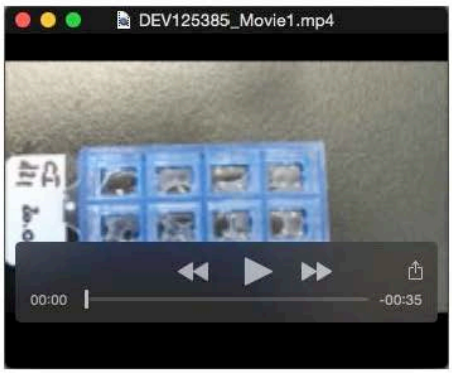

Supplementary Movie 1. Manipulation of hES cells-derived retinal sheet

hES cells were differentiated for 60 days in CI media with a daily media change. Cellular sheets are then detached from the chamber slides using nippers and placed on a microscopy slide.